Novel Electrochemical Patterning of Titanium Alloy to Control Osteogenesis at the Bone-Implant Interface

Sarah Johnson-Lynn

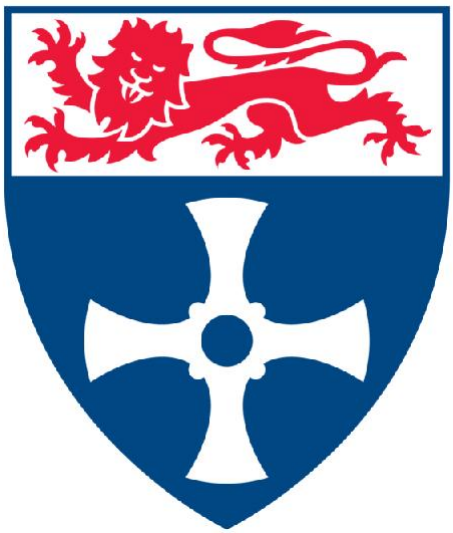

A Thesis submitted in partial fulfilment of the requirements for the degree of Doctor of Philosophy

Institute of Cellular Medicine

Newcastle University

September 2013

Abstract

The aims of this thesis were to fully characterise the surface properties of titanium alloy treated with a novel process of electrochemical etching and to assess the effect of these surfaces on osseointegration and the behaviour of osteoblasts.

In vitro investigation was performed using rat osteoblasts and human mesenchymal cells. Significant differences were observed in cell polarity and cell area between cells cultured on 3V and 5V and those treated at 9V. Significantly greater mean focal adhesion area and mean number of focal adhesions per unit cell area were also observed between the 3V and 5V treated surfaces compared to the 9V treated surfaces.

Longer term experiments revealed no significant changes in the levels of alkaline phosphatase activity between cells cultured on the different surfaces. After 28 days in culture, cells were stained for mineralised deposits and no significant differences were seen in the total area of bone nodules found on the experimental surfaces.

To assess the influence of the treated surfaces on bone cell biology, immunofluorescence was used to localise cadherin-11 and activity and inhibition assays were performed for small GTPases of the Rho family. On the 9V treated surfaces, significantly increased staining for cadherin-11 was seen, as well as significantly greater RhoA activity.

In vivo experiments were performed with electrochemically treated titanium implants in a rat tibia model. Analysis of micro-CT images of retrieved tibias revealed a significantly greater area of mineralised bone matrix in contact with the implant surface for the 9V treated surfaces and the same trend was observed on histomorphometric analysis. High variability in the mechanical testing data meant that no significant differences were seen, but a trend for greater load to failure of the bone-implant interface was observed for the 3V treated surfaces.

Table of contents

Acknowledgments

This work was carried out within the Musculoskeletal Research Group in the Institute of Cellular Medicine at Newcastle University.

The project was generously funded by Arthritis Research UK and the Royal College of Surgeons of Edinburgh.

I would like to say a huge thank you to my supervisors – firstly Mark Birch, without whose daily support this surgeon could never have dreamed of completing any scientific work at all. Thank you for your incredible patience and unflagging optimism. Professor Andrew McCaskie, for believing in me in the first place and giving me a chance with an academic training post and providing continuing invaluable guidance on the big picture. Also Sudipta Roy from the Centre for Electrochemistry and Advanced Materials, who managed to make at least a small part of the baffling world of electrochemistry comprehensible to a complete beginner.

I would also like to give a mention to the rest of our group, particularly Lynette Spalding who gave up her valuable time to teach me the basics of cell culture and molecular biology techniques.

The chemical engineers Jeet Varia and Jose Portoles provided much needed support to the project with materials fabrication and analysis.

Dr Matt German in Dental Materials was kind enough to spend time with me explaining the intricacies of AFM and materials testing.

The wonderful staff of the Newcastle University Centre for Comparative Biology were so accommodating and generous in allowing an orthopaedic surgeon into their midst for the first time in many years.

Finally, I couldn't possibly have completed this work without the love and support of my husband Gavin and I have to give a special mention to my tiny daughter Mina for allowing me to get at least some sleep so I could finish writing up.

List of Figures

Figure 44: 50µm^2 2D image of 3V180s surface obtained in contact mode using JPK Nanowizard II atomic force microscope with HYDRA6V-200WG SI_3N_4 probe tips

Figure 45: 5µm^2 3D image of 3V180s surface obtained in contact mode using JPK Nanowizard II atomic force microscope with HYDRA6V-200WG SI_3N_4 probe tips

Figure 46: Sample height profile taken from horizontal measurements on 3V180s surface over 5µm.

Figure 47: 50µm^2 2D image of 5V60s surface obtained in contact mode using JPK Nanowizard II atomic force microscope with HYDRA6V-200WG SI_3N_4 probe tips.

Figure 48: 5µm^2 3D image of 5V60s surface obtained in contact mode using JPK Nanowizard II atomic force microscope with HYDRA6V-200WG SI_3N_4 probe tips.

Figure 49: Sample height profile taken from horizontal measurements on 5V60s surface over 5µm.

Figure 50: 50µm^2 2D image of 5V120s surface obtained in contact mode using JPK Nanowizard II atomic force microscope with HYDRA6V-200WG SI_3N_4 probe tips.

Figure 51: 5µm^2 3D image of 5V120s surface obtained in contact mode using JPK Nanowizard II atomic force microscope with HYDRA6V-200WG SI_3N_4 probe tips.

Figure 52: Sample height profile taken from horizontal measurements on 5V120s surface over 5µm.

Figure 53: 50µm^2 2D image of 5V180s surface obtained in contact mode using JPK Nanowizard II atomic force microscope with HYDRA6V-200WG SI_3N_4 probe tips.

Figure 54: 5µm^2 3D image of 5V180s surface obtained in contact mode using JPK Nanowizard II atomic force microscope with HYDRA6V-200WG SI_3N_4 probe tips.

Figure 55: Sample height profile taken from horizontal measurements on 5V120s surface over 5µm.

Figure 56: 50µm^2 2D image of 9V60s surface obtained in contact mode using JPK Nanowizard II atomic force microscope with HYDRA6V-200WG SI_3N_4 probe tips.

Figure 57: 5µm^2 3D image of 9V60s surface obtained in contact mode using JPK Nanowizard II atomic force microscope with HYDRA6V-200WG SI_3N_4 probe tips.

Figure 58: Sample height profile taken from horizontal measurements on 9V60s surface over 5µm.

Figure 59: 50µm^2 2D image of 9V120s surface obtained in contact mode using JPK Nanowizard II atomic force microscope with HYDRA6V-200WG SI_3N_4 probe tips.

Figure 75: Anti-vinculin immunofluorescence of rat calvarial osteoblasts cultured on a machined Ti6Al4V surface for 24 hours.

Figure 76: Anti-vinculin immunofluorescence of rat calvarial osteoblasts cultured on a polished Ti6Al4V surface for 24 hours.

Figure 77: Anti-vinculin immunofluorescence of rat calvarial osteoblasts cultured on a 3V180s treated Ti6Al4V surface for 24 hours.

Figure 78: Anti-vinculin immunofluorescence of rat calvarial osteoblasts cultured on a) 5V60s, b) 5V120s and c) 5V180s treated Ti6Al4V surfaces for 24 hours.

Figure 79: Anti-vinculin immunofluorescence of rat calvarial osteoblasts cultured on a) 9V60s, b) 9V120s and c) 9V180s treated Ti6Al4V surfaces for 24 hours.

Figure 80: Bar chart illustrating the mean number of cells counted during immunofluorescence of rat osteoblasts cultured for 24 hours on the control and modified surfaces for 24 hours (results combined from 3 independent experiments).

Figure 81: Bar chart demonstrating mean cell area (μm^2) of primary rat calvarial osteoblasts cultured on control and modified surfaces for 24 hours (data from 1 experiment representative of 3 independent experiments; n=10).

Figure 82: Bar chart recording cell polarity of rat calvarial osteoblasts cultured for 24 hours on control and modified surfaces as a ratio of long to short cell axis (data from 1 experiment representative of 3 independent experiments; n=10).

Figure 83: Bar chart illustrating mean area of focal adhesions measured from anti-vinculin immunofluorescence in rat osteoblasts cultured for 24 hours on control and modified surfaces (data from 1 experiment representative of 3 independent experiments; n=10).

Figure 84: Bar chart demonstrating the number of focal adhesion complexes found per unit of cell area from anti-vinculin immunofluorescence after rat calvarial osteoblasts cultured for 24 hours on control and modified surfaces (data from 1 experiment representative of 3 independent experiments; n=10).

Figure 85: Graph demonstrating the area of rat primary calvarial osteoblasts cultured on polycaprolactone moulds of the treated surfaces (μm^2) for 24 hours, error bars representing standard error of the mean (data from 1 experiment representative of 3 independent experiments; n=10).

Figure 86: Graph showing the polarity of rat primary calvarial osteoblasts cultured on polycaprolactone moulds of the treated surfaces for 24 hours (as a decimal ratio), error bars expressing standard error of the mean (data from 1 experiment representative of 3 independent experiments; n=10).

Figure 87: Anti-vinculin immunofluorescence of human mesenchymal cells cultured on a glass surface for 24 hours.

Figure 88: Anti-vinculin immunofluorescence of human mesenchymal cells cultured on a machined Ti6Al4V surface for 24 hours.

Figure 89: Anti-vinculin immunofluorescence of human mesenchymal cells cultured on a mechanically polished Ti6Al4V surface for 24 hours.

Figure 90: Anti-vinculin immunofluorescence of human mesenchymal cells cultured on a 3V180s treated Ti6Al4V surface for 24 hours.

Figure 91: Anti-vinculin immunofluorescence of human mesenchymal cells cultured on a) 5V60s, b) 5V120s and c) 5V180s treated Ti6Al4V surfaces for 24 hours.

Figure 92: Anti-vinculin immunofluorescence of human mesenchymal cells cultured on a) 9V60s, b) 9V120s and c) 9V180s treated Ti6Al4V surfaces for 24 hours.

Figure 93: Bar chart illustrating the mean number of cells counted during immunofluorescence of human mesenchymal stromal cells cultured for 24 hours on the control and modified surfaces for 24 hours (results combined from 3 independent experiments).

Figure 94: Bar chart demonstrating mean cell area (μm^2) of primary human mesenchymal stromal cells cultured on control and modified surfaces for 24 hours (data from 1 experiment representative of 3 independent experiments; n=10).

Figure 95: Bar chart recording cell polarity of human mesenchymal stromal cells cultured for 24 hours on control and modified surfaces as a ratio of long to short cell axis (data from 1 experiment representative of 3 independent experiments; n=10).

Figure 96: Bar chart illustrating mean area of focal adhesions measured from anti-vinculin immunofluorescence in human mesenchymal stromal cells cultured for 24 hours on control and modified surfaces (data from 1 experiment representative of 3 independent experiments; n=10).

Figure 97: Bar chart demonstrating the number of focal adhesion complexes found per unit of cell area from anti-vinculin immunofluorescence after human mesenchymal stem cells were cultured for 24 hours on control and modified surfaces (data from 1 experiment representative of 3 independent experiments; n=10).

Figure 98: Bar chart displaying the absorbance measured at 405nm from p-nitrophenol assay for quantification of alkaline phosphatase activity of rat primary calvarial osteoblasts cultured for 21 days on glass control and modified surfaces (results of 1 experiment, representative of 3 independent experiments).

Figure 99: Bar chart displaying the absorbance measured at 405nm from p-nitrophenol assay for quantification of alkaline phosphatase activity of human mesenchymal cells

cultured for 21 days on glass control and modified surfaces (results of 1 experiment, representative of 3 independent experiments).

Figure 100: Incident light photomicrographs of bone nodules stained with alizarin red on a) 3V180s, b) 9V180s and c) machined surfaces.

Figure 101: Area of bone nodule formed on treated surfaces following 28 days culture in osteogenic media, measured from digital photographs of surfaces (results of a single experiment representative of 3 independent experiments).

Figure 102: Absorbance at 520nm following culture of rat primary calvarial osteoblasts for 28 days and staining with alizarin red (results of the same single experiment as in Figure 101, representative of 3 independent experiments).

Figure 103: Absorbance at 520nm following culture of rat primary calvarial osteoblasts for 28 days and staining with alizarin red.

Figure 104: Graph of mean CT values for Runx2 taken from 3 separate real-time PCR runs (GAPDH used as housekeeping gene) after culture of cells on modified surfaces for 7 days in osteogenic media (error bars represent standard error of the mean).

Figure 105: Graph of mean CT values for osterix taken from 3 separate real-time PCR runs (GAPDH used as housekeeping gene) after culture of cells on modified surfaces for 7 days in osteogenic media (error bars represent standard error of the mean).

Figure 106: Graph of mean CT values for osteocalcin taken from 3 separate real-time PCR runs (GAPDH used as housekeeping gene) after culture of cells on modified surfaces for 7 days in osteogenic media (error bars represent standard error of the mean).

Figure 107: Graph of mean CT values for cadherin-2 taken from 3 separate real time PCR runs (GAPDH used as housekeeping gene) after culture of cells on modified surfaces for 7 days in osteogenic media (error bars represent standard error of the mean).

Figure 108: Graph of mean CT values for cadherin-11 taken from 3 separate real time PCR runs (GAPDH used as housekeeping gene) after culture of cells on modified surfaces for 7 days in osteogenic media (error bars represent standard error of the mean).

Figure 109: FITC Anti-cadherin-11 and DAPI immunofluorescence of rat osteoblasts on glass (a), machined (b) Ti6Al4V and mechanically polished (c) surfaces

Figure 110: Anti-cadherin-11 and DAPI immunofluorescence of rat osteoblasts on a 3V180s treated Ti6Al4V surface

Figure 111 : Anti-cadherin-11 and DAPI immunofluorescence of rat osteoblasts on 5V60s (a), 5V120s (b) and 5V180s (c) treated Ti6Al4V surfaces

Figure 112: Anti-cadherin-11 and DAPI immunofluorescence of rat osteoblasts on 9V60s (a), 9V120s (b) and 9V180s (c) treated Ti6Al4V surface

Figure 113: Graph of mean length of cell perimeter stained positive for cadherin-11 (μm) per cell, as a mean of 5 measurements taken from the results of one experiment, representative of three independent experiments in which rat osteoblasts were cultured for 7 days (error bars represent standard error of the mean).

Figure 114: Graph of absorbance at 490nm, measuring RhoA activity in rat osteoblasts cultured in osteogenic media for 7 days. Results from 1 experiment, representative of 2 independent experiments (error bars represent standard error of the mean).

Figure 115: Graph of absorbance at 490nm, measuring Rac1 activity in rat osteoblasts cultured in osteogenic media for 7 days. Results from 1 experiment, representative of 2 independent experiments (error bars represent standard error of the mean).

Figure 116: Graph of the mean focal adhesion area per unit of cell area measured on photomicrographs of anti-vinculin immunofluorescence stained surfaces following 48 hours of culture, 24 of which after addition of Y27632, a ROCK inhibitor.

Figure 117: Graph of the mean focal adhesion area per unit of cell area measured on photomicrographs of anti-vinculin immunofluorescence stained surfaces following 48 hours of culture, 24 of which after addition of NSC23766, a RAC1 inhibitor.

Figure 118: Light microscopy of histomorphometry section, stained with silver nitrate and Giemsa stain, of rat tibia bone surrounding rod with mechanically polished surface

Figure 119: Light microscopy of histomorphometry section, stained with silver nitrate and Giemsa stain, of rat tibia bone surrounding rod treated with 3V180s surface

Figure 120: Light microscopy of histomorphometry section, stained with silver nitrate and Giemsa stain, of rat tibia bone surrounding rod treated with 5V180s surface

Figure 121: Light microscopy of histomorphometry section, stained with silver nitrate and Giemsa stain, of rat tibia bone surrounding rod treated with 9V180s surface

Figure 122: Bar chart displaying the percentage of implant surface in contact with mineralised bone matrix (n=5).

Figure 123: Example tracing of application of load (N) to failure against displacement (mm). Arrow indicates point of failure of the bone-implant interface.

Figure 124: Bar chart illustrating the yield strength of the bone-implant interface during mechanical push-out testing for each of the modified surfaces.

Figure 125 (a-d): Micro-CT slice longitudinally through experimental implant treated with a) mechanical polishing, b) 3V180s, c) 5V180s and d) 9V180s and surrounding bone.

Figure 126: Graph displaying the percentage of the experimental implant surfaces in direct contact with trabeculae of mineralised bone on a sample of micro-CT slices (n=10). Asterisked bracket indicates a significant difference ($p<0.05$).

List of Abbreviations

AFM	Atomic Force Microscopy
ANOVA	Analysis Of Variance
BMPs	Bone Morphogenetic Factors
BSA	Bovine Serum Albumin
cDNA	Complementary DNA
DMEM	Dulbecco's Modified Eagle Medium
Dlx5	Distal-less homeobox 5 (Dlx5)
DMSO	Dimethyl Sulfoxide
DNA	Deoxyribonucleic Acid
ECM	Extra Cellular Matrix
GAPDH	Glyceraldehyde 3-Phosphate Dehydrogenase
GDF-8	Growth Differentiation Factor-8 (Myostatin)
IL	Interleukin
MCSF	Macrophage Colony Stimulating Factor
mRNA	Messenger RNA
Msx2	msh homeobox homologue 2
PBS	Phosphate Buffered Saline
PCR	Polymerase Chain Reaction
PDGF	Platelet Derived growth Factor
RANKL	Receptor activator of nuclear factor kappa-B ligand
RNA	Ribonucleic acid
Runx2	Runt-related Transcription factor 2
SDS	Sodium Dodecyl Sulphate
SEM	Scanning Electron Microscopy
TGF-β	Transforming Growth Factor β
TNF-α	Tumour Necrosis Factor α

VEGF	Vascular Endothelial Growth Factor
XPS	X-ray Photoelectron Spectoscopy

Chapter 1. Introduction

1.1. Biomaterials in orthopaedics and dentistry

The development of biomaterials over the past several decades has been integral to the wider application and greater success of integration of metallic components into the body for many uses including vascular stents, dental implants and orthopaedic applications for fracture fixation and arthroplasty. Innovations in biomaterials research have driven the increased use of uncemented and hybrid arthroplasty solutions, particularly for the hip. The long term success of uncemented implants in bone is dependent upon osseointegration, or direct bonding of bone into the skeleton without the interposition of tissue types other than bone.

1.1.1. Arthroplasty

There were almost 90,000 hip and over 93,000 knee replacements recorded in the National Joint Registry in the UK in 2010 (NJR). This figure is predicted to increase by 40% over the next 30 years due to the changing population demographics. Hip and knee replacements are some of the most successful elective operations being performed today in terms of increasing patient quality of life, as measured by Quality Adjusted Life Years (QUALYs) (Rasanen et al. 2007). Despite the success of total joint arthroplasty, failure of the implants is a recognised problem and revision joint replacements are now forming an increasing proportion of all arthroplasties performed. Failure of implants may be caused by infection or fracture but aseptic loosening, caused by implants that do not successfully integrate with bone, is currently an unsolved problem. Revision rates for total hip arthroplasties from the 9th annual report of the National Joint Registry are 0.7% at 1 year rising to 3.9% at 8 years. Results for knee arthroplasties are very similar with 0.45% revised at 1 year and 2.4% at 7 years (National Joint Registry). Revision rates seen globally, as recorded in national joint registries suggest average revision rates of 12% at 10 years for both hip and knee arthroplasty (Labek et al. 2011).

Historically most arthroplasty components have been secured using polymethylmethacrylate bone cement; however, more recently the majority of components for hip arthroplasty have been uncemented. A theoretical advantage of uncemented components is that the number of interfaces where failure can occur are

reduced and the problem of polyethylene particles causing bone resorption at the cement-bone interface is avoided. The long-term success of these implants is determined by initial integration of the implants with the bone (Sychterz 2002). Uncemented implants appear to yield similar revision rates to cemented implants in patients under 60 years old (National Joint Registry, 2012).

The material selected for implant manufacture is an important determinant of biocompatibility; the tolerance of the body's immune system to the material. It is also important to match the strength and stiffness characteristics of the material to that of the surrounding bone, to prevent the problems of bone loss due to stress shielding. The macroscale design features of all arthroplasty components have already undergone many years of iterative evolution based on biomechanical and human studies using radiology, survival analysis and implant retrieval to arrive at components with the best long term survival (Bauer 1999).

Surface modification of prostheses is an important part of the manufacturing process. Articulating surfaces require a high degree of polishing to eliminate imperfections which could hasten the progress of wear. The stems and keels of prostheses are treated according to their fixation method. Stems to be cemented are often polished, which allows a small degree of settling into the cement, improving the long-term fixation through 'taper-lock' whereby subsidence increases transmission of radial forces through the prosthesis-cement interface (Norman et al, 2001). Matt femoral stems do not subside to the same extent as polished stems but no difference between the surface finishes, in cement fatigue damage, has been demonstrated in experimental models (Lennon et al, 2003). Clinical results suggest a slightly higher rate of loosening of matt finished stems (Howie et al, 1998). Uncemented stems on the other hand are usually roughened with grit blasting and may be treated with hydroxyapatite coating to improve early bone formation. It appears that there may be a short-term advantage to hydroxyapatite-coated stems in preventing subsidence of uncemented implants during the first year after surgery but this advantage does not necessarily translate to the longer term (Hamadouch et al, 2001).

1.1.2. Fracture repair

Both stainless steel and titanium alloys are common materials for the manufacture of fracture fixation implants. The advantages of titanium over stainless steel include improved biocompatibility, improved resistance to fatigue and greater yield strength. However, titanium exhibits low tensile strength and low modulus of elasticity, requiring plates to be bulkier than their equivalents made from stainless steel. In certain circumstances plates are routinely removed (dorsal distal radius, olecranon, paediatric applications) and bony ingrowth onto titanium plates can complicate this (Bates and Ramachandran 2007).

1.1.3. Dental implants

Dental implants are becoming increasingly common in the treatment of edentulous patients. These are uncemented implants and, as with orthopaedic implants, similar concerns exist regarding adequate bone-implant fixation. Commercially pure (cp.) titanium and Ti6Al4V are materials commonly used in dental implants. Several different designs exist, some of which are hollow or contain pores to allow macroscopic ingrowth of bone. Implant surfaces are often treated to increase surface roughness with processes such as acid etching, grit blasting and sputter-coating. Rougher implants in animal models have generally been found to increase the volume of bone in contact with the implant during healing and increase the torque required to remove threaded implants (Buser et al. 2001, Wennerburg et al. 1998). Hydroxyapatite-coated implants, however, have not achieved anticipated levels of clinical success, mostly due to de-bonding between the surface treatment and bulk of the material in an aqueous environment with repeated cyclical loading (Reis et al.1994).

1.2. Osseointegration

Osseointegration is a term first used by Swedish orthopaedic surgeon and researcher Professor Brånemark (Brånemark 1983). He used it to describe the direct healing of bone onto titanium implants during his experiments in rabbits. Prior to this work, it was not thought to be possible for metal implants to be directly incorporated into bone. Most foreign objects placed into the body initiate a foreign body response, causing the object to be walled off by poorly vascularised fibrous tissue. For implants placed into bone this results in the implants being surrounded by a layer of fibrous tissue which has poor mechanical properties when compared with bone and can contribute to loosening of the

implant when loaded. With certain materials this foreign body response is not seen (titanium, niobium, zirconium and hydroxyapatite), and bone can be found in direct contact with the implant (Figure 1). The implant material is not the only variable affecting how the body responds to the implant. Other important factors include implant shape, surface topography, surgical technique and the quality of the host tissue where the implant will be placed (Albrektsson and Albrektsson 1987).

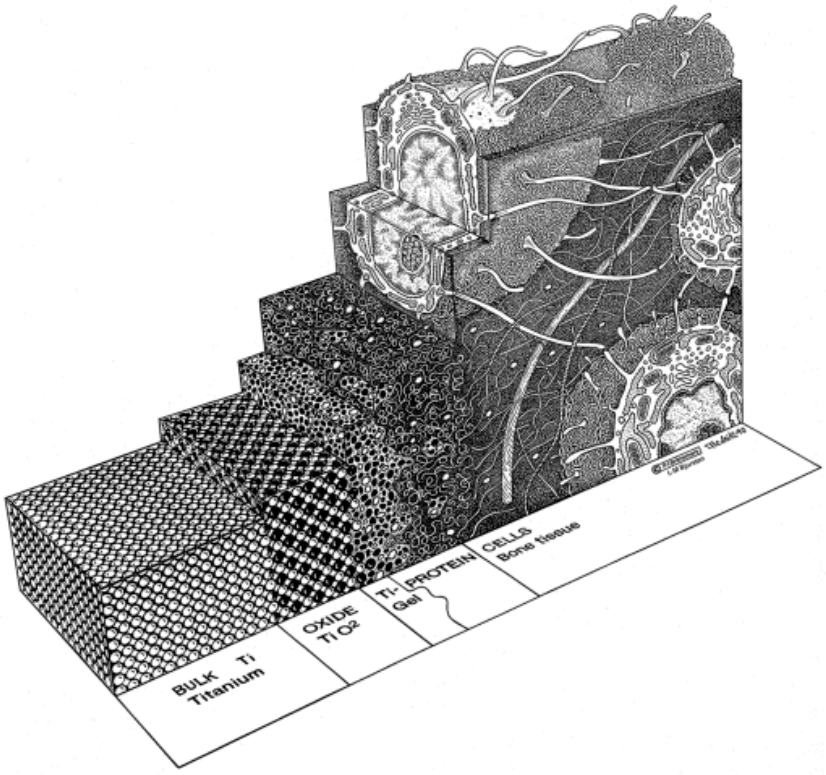

Figure 1: The bone-titanium interface (from Brånemark et al. 2001)

Osseointegration has been defined as 'a direct structural and functional coexistence, possibly in a symbiotic manner, between differentiated, adequately remodelled, biologic tissues and strictly defined and controlled synthetic components, providing lasting, specific clinical functions without initiating rejection mechanisms' (Brånemark et al. 2001). An implant can be said to be osseointegrated when there is no relative movement between the implant and surrounding bone when loaded (Brånemark 1983). It has become the basis for the stable fixation of uncemented orthopaedic and dental/maxillofacial implants (Albrektsson et al 1981). The resolution of x-rays (100μm) are such that they cannot be used to provide evidence of osseointegration and

the gold-standard for determining osseointegration of implants is retrieval and histomorphometry of bone-implant sections (Albrektsson and Johansson 2001).

A key part of the initial attachment of cells to the surfaces of biomaterials is the adsorption of serum proteins such as fibronectin and vitronectin to the material, which begins when blood comes into contact with the implant surface (Figure 1). The amino acid sequence Arginine-Glycine-Asparic acid (RGD) is present in many extracellular matrix proteins including fibronectin and forms the ligand for interaction with the extracellular domain of cell membrane - spanning components such as integrins. Howlett et al. (1994) demonstrated that depleting culture media of fibronectin and vitronectin reduced the attachment and spreading of human bone-derived cells on biomaterials including titanium. A layer, 20-500nm thick, most likely comprised of collagen and other mineralised matrix components is seen in immediate contact with titanium implants with electron microscopy of the interface (Albrektsson and Johansson 2001), on which the bone cells attach. It has been observed that the oxide layer of titanium implants increases in thickness with long term implantation into the body (to 1000-2000Å after 7 years compared to 60Å on control surfaces that were not implanted) (Albrektsson et al. 1987). This led to the theory that osseointegration was a dynamic process resulting from the local reaction to surgical trauma producing reactive oxygen species that caused the increased thickness of the oxide layer, along with incorporation of calcium and phosphate from the bone into the oxide (Ehrenfest et al. 2010). As is the case with fracture healing, the bonding of bone to the surface of an implant can only occur in mechanically favourable situations, i.e. with limited micromotion at the interface (Kuzyck and Schemitsch 2011).

Gene expression in the bone around titanium implants placed into rat tibias was studied by Omar and colleagues in 2011. There was found to be greater torque required for removal of implants with anodically oxidised surfaces compared to control machined surfaces. This corresponded with increased expression of the osteoblast differentiation markers Runx2, and osteocalcin at the oxidised surfaces and decreased expression of the pro-inflammatory cytokines IL-1β and TNF-α, suggesting less inflammatory response and greater bone formation. Molecular mechanisms underpinning cell adhesion and behaviour on biomaterial surfaces are discussed further in section 1.16.

1.3. Titanium and Titanium alloys

Titanium is an excellent biomaterial due to a combination of its mechanical properties, resistance to corrosion and the fact that it is relatively inert in the body. Titanium forms a surface layer of oxide (TiO_2) in any environment with a supply of oxygen, thereby forming a stable, corrosion-resistant layer on its surface. However, a small degree of corrosion in the human body appears to occur, with TiO_2 having been isolated from tissues surrounding an implant (Woodman et al. 1984). It is also easy to machine and process if the low Young's modulus (causing back springing), relatively low thermal conductivity (causing high thermal stress at the cutting edge) and tendency to stick to tools are taken into account (Black and Hastings 1998).

It has a high affinity for oxygen which causes a stable oxide layer (TiO_2) to form on the surface, preventing further reaction with body tissues. The major form of oxide important in commercial applications is rutile (Figure 2). The building blocks of this crystal are units of 1 titanium atom surrounded by 6 oxygen atoms in an octahedral formation. These units then stack with their long axis alternating 90° to each other (Diebold 2003).

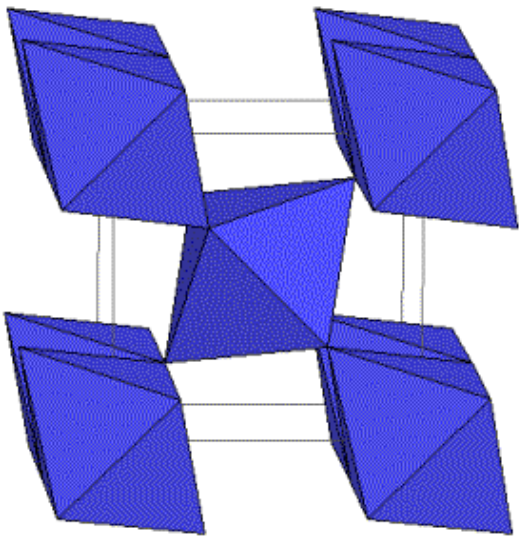

Figure 2: Rutile structure of titanium oxide

Commercially pure (cp.) titanium is used in a number of biomedical applications including dental and craniomaxillofacial implants. However, the alloy Ti6Al4V (containing 6% aluminium and 4% vanadium) is most commonly used for orthopaedic

applications due to its superior mechanical properties (Lutjering and Williams 2003) (Table 1). Pure titanium exists in two phases:-

- Alpha – close-packed hexagonal crystalline form
- Beta – body-centred cubic arrangement

Pure titanium transitions from alpha to beta phase when heated above 883°C. Titanium alloys contain elements which stabilise the alpha phase to higher temperatures or the beta phase to lower temperatures. There are three categories of titanium oxides:-

- Alpha – usually contain tin or an alpha stabiliser such as aluminium or oxygen. These alloys are suitable for welding but are not heat treatable. They have low to medium strength and have good mechanical properties at cryogenic temperatures.
- Alpha + beta – contain a combination of alpha and beta stabilisers. Can be heat treated to varying degrees and have high strength. Ti4Al6V is a member of this group.
- Beta – contain beta stabilisers such as molybdenum, silicon, iron or vanadium and are most suitable for heat treatment.

	Ti6Al4V	Cortical bone	Cancellous bone
Young's modulus (GPa)	105-110	17-20	17-18
Hardness	310	0.3-0.7	0.2-0.5
Tensile yield strength (MPa)	830-870	130-160	0.1-30

Table 1: Summary of mechanical characteristics of Ti6Al4V and bone (Turner et al. 1999; Rho et al. 1993; Morgan and Keaveny 2001)

There have been concerns that Ti6Al4V is not as biocompatible in the body as commercially pure titanium. Titanium particles have been observed around Ti6Al4V implants in the work of Albrektsson and Jacobsson in 1987, although they did not appear to be causing a tissue reaction. It has also been found that metals leach out of the implants into the tissues of the host, despite the inert surface oxide layer. Levels of titanium and aluminium were studied in baboons for up to 8 years after Ti6Al4V segmental femoral replacement implants. It was found that titanium levels were elevated

in the sacrificed animals' lungs, spleen, draining lymph nodes and muscle adjacent to the implants, elevated urinary titanium levels were also noted in the remaining live animals. Raised serum aluminium levels were also seen and increased aluminium was present in lungs, adjacent muscle and lymph nodes compared to controls. None of the levels found in live or sacrificed animals were in the known harmful range (Woodman et al. 1984).

1.4. Electrochemistry

Electrochemistry is the study and application of charge transfer reactions, which occur at electrified interfaces. In an electrochemical cell, these occur between an electron conductor (e.g. metal) and an ionic conductor (e.g. salt solution). Transfer of electrons at the electrodes forms the basis of this reaction. Reduction, or gain of electrons by a reactant occurs at the cathode (negative electrode) and oxidation, or loss of electrons occurs at the anode (positive electrode).

The study of chemical engineering seeks to evaluate chemical (and electrochemical) reactions to elucidate the rate limiting step in the reaction and therefore optimise the efficiency of the reaction. To model this process the reaction is considered to occur at one of the electrodes in an electrochemical cell (the working electrode). The reaction occurring at the electrified interface surrounding the working electrode can then be modelled in several stages at the different layers of the interface (Figure 3). These are the bulk substrate of the electrode, the Herlmotz inner layer, the Herlmotz outer layer, the Nernst diffusion layer and the bulk electrolyte. The Herlmotz inner layer represents the first 10Å outside the surface of the electrode and is where charge transfer occurs. The Nernst diffusion layer represents the next 10-100 microns and is the area in which reactants from the bulk electrolyte travel to and from the inner layer by the process of diffusion along their concentration gradients. In the bulk of the electrolyte, the predominant method of movement of the reactants is by convection (which can be increased in efficiency by stirring).

In the case of a titanium working electrode there is a duplex salt film layer of 40-120Å at the surface of the bulk material, with the inner compact layer being predominantly TiO_2 and the outer porous layer being made up mainly of titanium-sulphate and titanium-methanoic-sulphate complexes (Koryta et al, 1993).

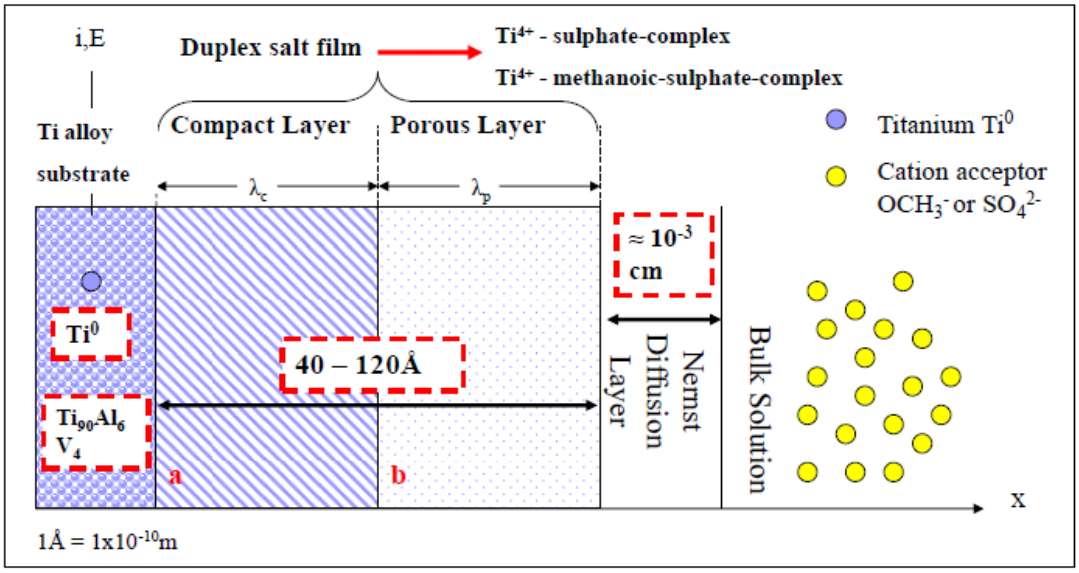

Figure 3: Diagrammatic representation of the electrical interface in the titanium alloy/methanol-suphuric acid cell system. (By J. Varia 2010).

The reaction at the electrified interface can be considered in a number of steps with O representing cation acceptors in the electrolyte (OCH_3^- or SO_4^{2-} in the case of the sulphuric acid/methanol electrolyte), ne^- representing electrons involved in the reaction and R representing the product of the reaction at the charged interface:-

$O_{(bulk)} \rightarrow O_{(Nernst)}$	Reactant O from bulk to Nernst layer by convection
$O_{(Nernst)} \rightarrow O_{(Hermoltz)}$	Reactant O from Nernst to Hermoltz layer by diffusion
$O_{(Outer\ Hermoltz)} \rightarrow O_{(Inner\ Hermoltz)}$	Reactant O from outer to inner Hermoltz layer
$O_{(Inner\ Hermoltz)} \rightarrow O_{(adsorbed)}$	Reactant O adsorbed onto electrode surface
$O_{(adsorbed)} + ne^- \rightarrow R_{(adsorbed)}$	Charge transfer
$R_{(adsorbed)} \rightarrow R_{(bulk)}$	Transfer of product R back to bulk electrolyte

Once the rate-limiting step in the above representation is identified it is possible to manipulate reaction conditions in order to optimise the speed of this step and therefore the reaction as a whole (Bockris et al. 1974).

1.5. Surface roughness

Several methods have been used to produce microscale features on implant surfaces including grit blasting, acid etching and sputter coating. Porous coating is already used on implant surfaces in a clinical setting. This produces large surface features which allow macroscale bone interlocking and ingrowth (Simmons et al 1999). They tend to

be used when there is a large amount of bone loss – such as in revision arthroplasty. Hydroxyapatite (HA) coating is also already in clinical use in uncemented arthroplasty components. The purpose of this surface modification is to create a surface with not only microscale surface roughness, but also a surface chemistry very similar to that of the mineralised components of bone. There have been concerns raised regarding this approach, particularly in the field of dental implants, where HA coated implants have been withdrawn from clinical use. The two main issues are that HA coating has been shown to delaminate and failure of bonding can occur between the coating and the bulk implant (Svehla 2005) and these coatings have also been shown to resorb in *in vivo* models (Radl 2000).

Several methods are available for production of nanoscale features on surfaces including compacting nanophase particles (Palin 2005), lithography (using resists to impart patterns and features) (Biggs et al 2007b) and polymer demixing (Berry et al 2006). The current definition of nanoscale features is of topography with features in the range of 1-100nm or materials created out of components of this size (Christenson 2007).

Nanoscale surface features can influence the adsorption of proteins onto surfaces, which in turn affects the ability of osteoblasts to attach to these surfaces. This leads to long lasting changes in cell behaviour, including differentiation. Biggs et al in 2006 demonstrated that nanoscale surface patterns with a slightly disordered near-square format were effective in increasing osteoblast focal adhesion complexes whereas those with a square format were not. Hexagonal formats actually decreased overall adhesion (Biggs et al 2007a). In general, rougher surfaces are more favourable for protein adsorption due to increased surface area. The oxidised surfaces that form on many metals when implanted into the body usually carry an overall positive charge due to the loss of electrons during oxidation, which is favourable to protein adsorption via the increased affinity for negatively charged protein side groups.

Regularly spaced grooved features of 350-700nm in width were found to decrease the density of F-actin stress fibres in human mesenchymal stem cells. Focal adhesion kinase was also found to be downregulated and focal adhesions were seen to be distributed less widely throughout the cell periphery (Yim et al, 2010).

The average length of an osteoblast is 20-50 microns so any surface features larger than this would be seen by the cells as a smooth surface. Fewer studies have focused on the effect of nanoscale features than on the effect of microscale features but the available studies (Anselme et al 2002, Bigerelle et al 2002) have produced results indicating that osteoblastic cells attach more successfully to surfaces with submicron-scale features than to those that are smooth at this scale. Focal adhesion complexes on cell filopodia enter nanoscale pores providing enhanced and guided initial attachment. Rice in 2003 concluded that cells can be affected by structures as small as 8-10nm (comparable to single collagen fibre). However Hallgren in 2001 revealed no difference in osteoblast behaviour between nanoscale patterned and control implants (Hallgren et al. 2001). The diameter of the pillar, pits or grooves is likely to be a more important determinant of adhesion than the distance between features as cell-surface integrin subunits are 20-30nm in size and below this threshold would not provide increased binding area.

In a paper by Anselme et al. (2002), it was concluded from their experiments that on surfaces with microscale grooves, cells react to discontinuities on the surfaces when spreading and proliferating and these provide contact guidance which determine in which direction the cells grow. 100 micron grooves have been demonstrated to increase osteoblast-specific differentiation of human osteoblasts via focal adhesion kinase-mediated activation of the ERK/MAPK signalling pathway (Biggs, 2009).

Surface roughness has effects on cell morphology as cells growing on smooth surfaces tend to produce a rounded morphology, whereas those on rougher surfaces show a more elongated pattern with lamellipodia and filopodia spreading out across the surfaces which can span surface features such as craters using focal adhesions and form a three-dimensional network (Schmidt 2002). There is also greater production of actin, a component of the cytoskeleton which is involved in cell locomotion, shaping and cleavage during reproduction. This is further evidence that cells on rougher surfaces tend to take up a more differentiated phenotype compared to those on smoother surfaces (Kim et al 2005). This is confirmed by the enhanced production of alkaline phosphatase (a marker of mineralisation) by osteoblasts on rougher surfaces in response to activated vitamin D (Boyan et al 1998).

Growing osteoblasts on surfaces with microscale geometric patterns, including grooves and gap-cornered boxes, appears to enhance differentiation through modulation of focal adhesion kinases and the ERK pathway of intracellular signalling. ERK phosphorylation promotes nuclear translocation after activation by ligands, including fibroblast growth factor 2 (Hamilton and Brunette 2007). Grooved surfaces also alter the profile of matrix metalloproteinase expression and the quantity of collagen produced by mesenchymal cells (Brydone et al, 2011).

Surfaces produced with nanoscale pillars have been shown to cause disruption to the cytoskeleton of the cells and changes to cytoskeletal components clathrin and dynamin in keeping with attempted endocytosis (Dalby et al, 2004). Further work by this team demonstrated similar findings on surfaces created by polymer demixing (spontaneous phase separation when spun onto silicon wafers) (Berry et al, 2006). These surfaces caused cells to put out very long processes which sensed the nanoscale features but did not necessarily attach to them and substances were produced which are involved in endocytosis, suggesting that the cells may have been attempting to internalise the features.

Nanoscale features may increase the adhesion of osteoblast selectively over that of fibroblasts and bacterial adhesion may be decreased on nanotopography (Colon et al. 2006). These are both advantageous features when considered in the context of osseointegration which can be seen as a race between osteoblasts and bacteria to adhere to the implant surface first.

1.6. Surface chemistry

Several aspects of the chemical composition of biomaterial surfaces have also been found to affect cell behaviour including charge, hydrophobicitiy and surface energy. Cell-surface interactions can be due to receptor-ligand, hydrophobic interactions and electrostatic van der Waals forces (Senaratne, Andruzzi and Ober 2010).

Positively charged surfaces have been seen to increase cell adhesion but reduce differentiation in a rat bone marrow stromal cell model on indium tin oxide (Qiu et al. 1998). An optimum balance between hydrophilic and hydrophobic surface properties is likely to promote greatest cell adhesion. Protein adsorption is affected by the

hypdrophobicity of the surfaces with increased fibronectin binding to hydrophobic surfaces, but greater biological activity on hydrophilic surfaces (Grinnell and Feld, 1982).

Nakaoka et al. in 2010 studied the effect of coating surfaces with several different functional groups on the growth and differentiation of human osteoblasts. They found that cell proliferation was reduced on surfaces with methyl groups in comparison with those with hydroxyl, amino, carboxyl, sulphate and phosphate groups. This effect, however, did not appear to be mediated by changes in the gap junction complexes, which were not found to be significantly different between groups. Park and colleagues in 2010 demonstrated that strontium-containing titanium alloys increased bone-implant contact and removal torque of implants when compared to untreated implants in a rat model. The in vitro studies also demonstrated increased alkaline phosphatase activity and increased expression of mRNA for osteocalcin, osterix and bone sialoprotein on these strontium containing surfaces.

Curran and colleagues in 2006 demonstrated that different functional groups attached to glass surfaces altered the differentiation profile of human mesenchymal cells. They found that control glass and methyl groups maintained a stem cell phenotype whereas amino and silane groups promoted differentiation along the osteoblast lineage. Work by Benoit and colleagues showed that small charged phosphate groups suspended in polyethylene glycol gels guided the differentiation of human mesenchymal cells down the osteogenic lineage while controlling the physical characteristics of the gel to demonstrate the independent effect of changing substrate chemistry (Benoit et al, 2008).

Zreiqat and colleagues in 2005 studied the effect on signalling in human osteoblasts of treatment of a titanium alloy substrate with magnesium and hydroxyl carbonate apatite. c-fos, which is associated with osteoblast proliferation was up-regulated on the treated surfaces as was the MAP kinase pathway, suggesting the surface treatments may increase cell growth.

Both surface roughness and surface chemistry control the adsorption of biomolecules, which in turn affects the adhesion and function of cells on biomaterial surfaces. This is reflected in the particular circumstances of bone-bonding of titanium implants. Berry

and colleagues in 2007 demonstrated the concept of manipulation of cell behaviour on surfaces using a combination of lithography and electrostatic self-assembly to create surfaces with different nanotopographies which also had different surface chemical properties, in regard to the affinity of proteins for the surfaces. The nanoscale features increased cell adhesion, whereas the areas with different surface chemistry appeared to disrupt cytoskeletal organisation and focal adhesion complex formation, in fibroblasts and bone marrow stromal cells.

1.7. Bone Biology

An appreciation of the biology of the skeleton, the behaviour of specialised bone cells and the biochemical processes involved in cell-cell and cell-surface contact are central to the understanding of osseointegration at the titanium-bone interface. Bones form an internal support structure for vertebrates, provide a large pool of inorganic ions, such as calcium and phosphate and contain bone marrow, which supplies progenitor cells for the mesenchymal lineage and blood cells. The human skeleton is typically made up of 206 bones (Bilzekian 2002). These can be divided into five types:-

- Long (e.g. femur)
- Short (e.g. carpal bones)
- Flat (e.g. bones of the skull)
- Irregular (e.g. ethmoid)
- Sesamoid bones (those embedded in tendons e.g. patella)

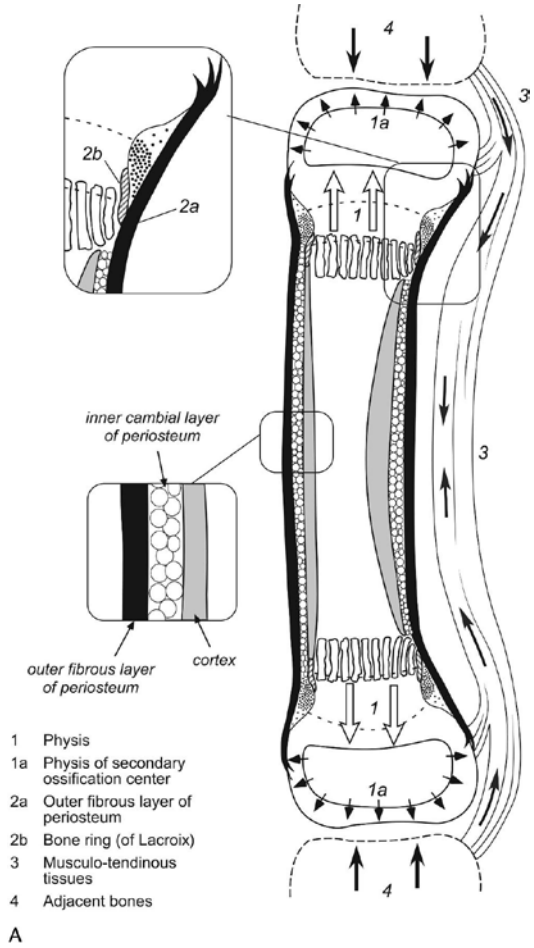

Figure 4: Structure of a long bone. (From Forriol and Shapiro, 2006)

Long bones (Figure 4) are characterised by distinct structural areas, with a central cylinder (the diaphysis) and expansions at the ends for joints (epiphyses). The transition areas between are the metaphyses. The whole bone, other than regions covered with articular cartilage has an outer fibrous covering – the periosteum. This is a dual-layered structure with an outer tough layer of fibroblasts, carrying blood vessels and nerves and an inner layer containing osteogenic progenitor cells. The major blood supply of long bones comes from 1-2 nutrient arteries that pass through the cortex and anastomose with the territories of smaller vessels supplying the epiphyseal and metaphyseal regions (Laing, 1953). There is also a blood supply running in the periosteum which supplies the outer region of the cortex. Short and irregular bones are supplied by the vessels of the periosteum and some also have small nutrient arteries (Kurana 2009).

1.7.1. Cortical Bone

Cortical bone forms the outer layer of the cylinder, which makes up the diaphysis of long bones and also the thin outer layer of flat and irregular bones. It is made up of tightly organised lamellar bone, arranged into units called osteons or Haversian systems. These are concentric rings of lamellar bone, laid down around a central canal containing capillaries, venules, lymphatic vessels, loose connective tissue and osteoprogenitor cells (Figure 5). Volkmann's canals comprise a vascular system connecting the Haversian canals to each other and the blood supply of the periosteum. Osteocytes are specialist bone cells that can be found in the lacunae between the lamella layers and their processes spread out in branching canaliculi, allowing communication with each other and cells at the surface. Osteons are mainly formed in the direction of the longitudinal axis in long bones due to the response to prevailing tension, compression and torsional forces on the bone (Bilezikian 2002). The components of the individual layers making up the concentric rings, however, do not align uniformly and the direction of the collagen fibrils in each layer is at an angle to those adjacent to it forming a 'twisted plywood' structure (Weiner et al. 1999).

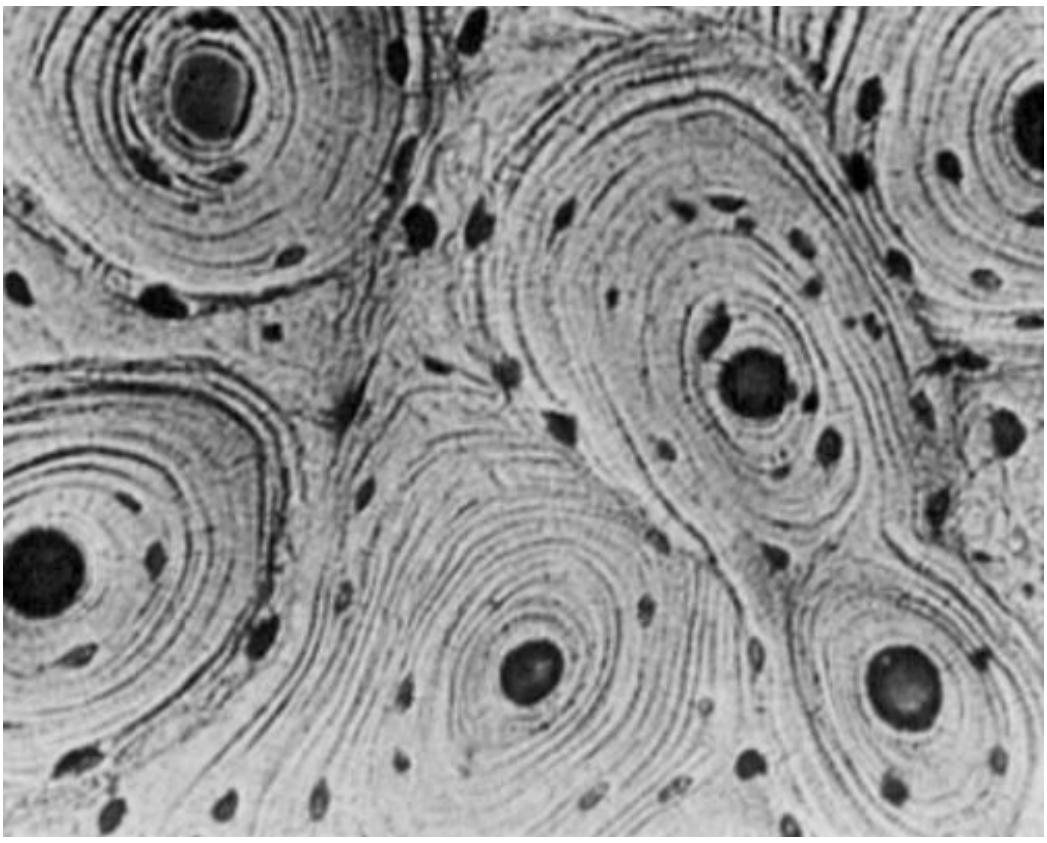

Figure 5: Micrograph of osteons. (From Biomechanics in Dentistry)

The major inorganic component of mineralised bone is hydroxyapatite, forming 39.9% of wet bone mass. The crystals are arranged parallel to collagen fibres to form a mechanical structure most resistant to the prevailing forces acting on that part of the bone. Water forms 15.5% and 41.8% is made up of organic molecules. The most common organic component is collagen, with type I being the most common, although small amounts of types III and IV are present. Non-collagenous proteins make up 10% of the organic material and include osteocalcin, osteonectin, osteopontin and bone sialoprotein (Black and Hastings 1998).

1.7.2. Cancellous bone

Cancellous bone makes up the inside of the diaphyseal and metaphyseal regions and centre of other bone types. It is formed from irregularly oriented trabecular bone elements, making up a scaffold for the fat and haematopoietic cells of the bone marrow. It is more metabolically active than cortical bone, with bone-forming osteoblasts and bone-resorbing osteoclasts residing in a layer of endosteum on the trabeculae (Kurana 2009).

Cancellous bone is formed of lamellar bone in the form of irregular rods and plates making up trabeculae 100-200 microns in width. The composition is slightly different to that of cortical bone with water making up 27%, organic material 35% and inorganic material 38%. Cancellous bone has improved resistance to compression and shear forces than cortical bone but lower resistance to torque (Black and Hasting 1998).

1.8. Bone growth and development

The skeleton is formed from three lineages of embryonic cells. The craniofacial skeleton from cranial neural crest cells, the axial skeleton from paraxial mesoderm and the appendicular skeleton from lateral plate mesoderm. Formation of the axial skeleton from paraxial mesoderm begins with segmentation of somites, which is driven in a sequential fashion in a cranial to caudal direction by the expression of genes that are part of the molecular segmentation clock (including *Notch* and *Delta*, which have been associated with segmentation abnormalities in the human axial skeleton). The cells making up the somites then differentiate into the ventromedial sclerotomes (making up

the vertebral column and part of the ribs) and the dorsolateral dermatomyotomes (making up the paraspinal musculature and dorsal skin) (Sadler 1995). Once the sclerotome has formed, bone morphogenic protein activity induces chondrocyte differentiation (Ehlen et al, 2006).

The embryonic limb buds develop from lateral plate mesoderm in a proximal to distal order. The bones initially form as continuous cylinders with condensation of the precartilage mesenchyme in response to the accumulation of fibronectin in the extracellular matrix (Zhu et al, 2010). Joints and the separate bones of the hands and feet are formed by apoptosis controlled by BMP signalling (Olsen, Reginato and Wang 2000). Proximal-distal patterning of the limb is regulated by fibroblast growth factor originating from the apical ectodermal ridge.

Limb buds appear at the end of the 4th week of gestation, with hand and footplates developing at the distal extents in the 6th week. The outgrowth of the limb bud is directed by fibroblast growth factor and Wnt signals, which confine the cartilage pattern to a central bar of the paddle-shaped limb. Indian hedgehog and Sonic hedgehog secreted proteins are involved in coordinating several patterning processes during embryonic development, acting through the cell surface receptor Patched-1, which in turn releases suppression of activity of the transmembrane protein Smoothened (Ehlen et al, 2006). Sonic hedgehog signalling is responsible for anterior-posterior patterning in the limb, controlled by a small group of cells in the distal, posterior area of the limb bud in the zone of polarising activity producing a temporal and spatial signalling gradient (Olsen, Reginato and Wang 2000). During the 7th week of gestation the limb buds rotate by 90° in opposite directions, with the arm buds rotating laterally to orient the extensor muscles on the posterior aspect and leg buds rotating medially to place the extensor muscles on the anterior aspect (Sadler 1995).

1.8.1. Enchondral ossification

Most of the bones of the axial and appendicular skeleton are formed in this way (Figure 6). An initial template of chrondroblasts differentiates into chondrocytes secreting type II collagen, controlled by the transcription factor SOX9. Indian hedgehog signalling regulates differentiation of hypertrophic chondrocytes (Karsenty and Wagner, 2002).

An initial collar of bone is then formed by local intramembranous ossification in the perichondrium. Matrix calcification and chondrocyte hypertrophy with production of type X collagen follow in this region of the diaphysis. The bone collar is pierced by blood vessels responding to VEGF, bringing osteoprogenitor cells to the region, which adhere to the calcified matrix forming the primary ossification centre (Kumana 2009). Secondary ossification centres then form at the bone ends in a similar way, producing the epiphyses of long bones.

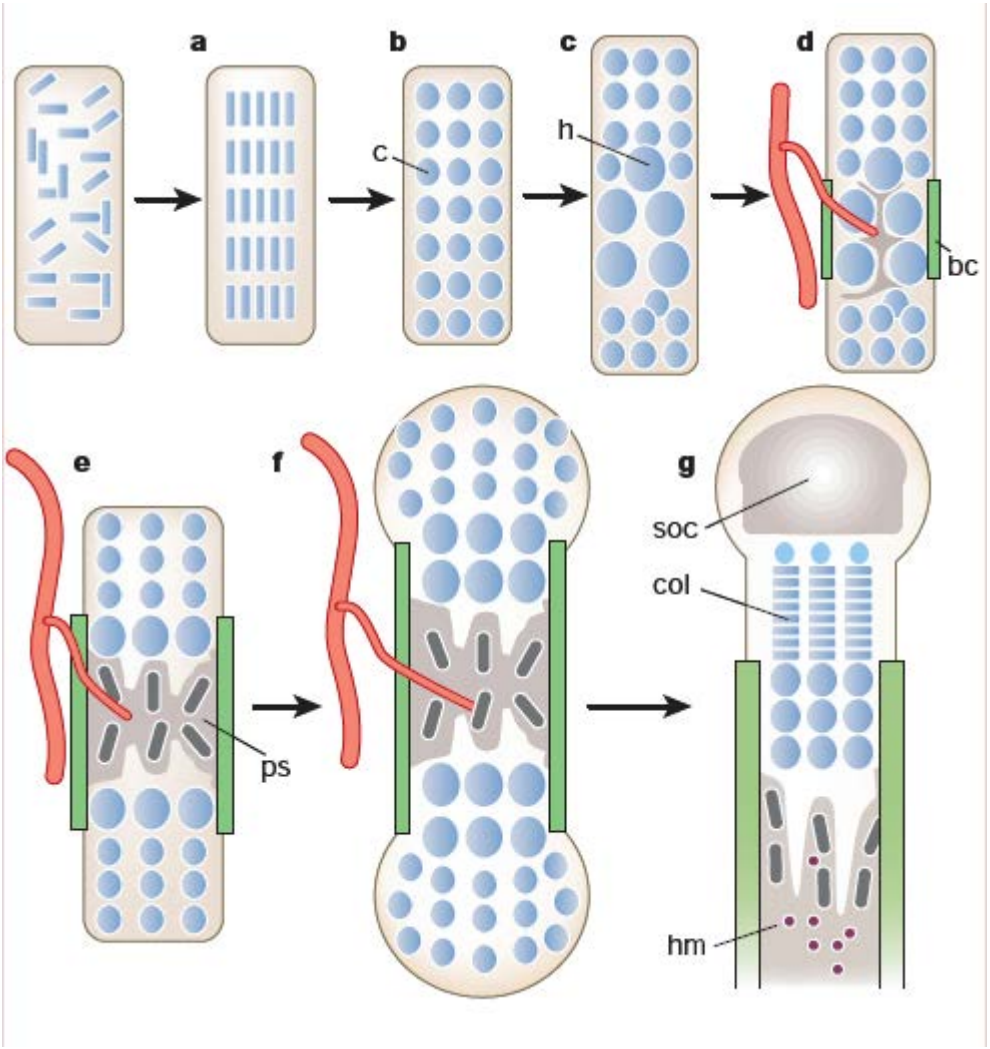

Figure 6: Enchondral ossification. (From Kronenberg, 2003)

Cartilage remains around the secondary ossification centres as articular cartilage and the growth plate. The growth plate is responsible for the increase in length of the long bones. The cartilage in this region forms four zones and a zone of ossification (Figure 7):-

- Resting zone – hyaline cartilage with no morphological changes
- Proliferative zone – rapidly dividing chondrocytes, stacking in columns. This area is managed by the action of Indian hedgehog signalling, which acts on parathyroid hormone-related peptide to prevent chondrocyte hypertrophy and maintain a pool of proliferating cells.
- Zone of hypertrophy – enlarged chondrocytes with increased stores of glycogen and reduced abundance of matrix. Synthesis of type X collagen.
- Zone of calcification – hydroxyapatite is deposited on the small amount of remaining matrix
- Zone of ossification – osteoprogenitor cells originating from the periosteum arrive in the spaces left by chondrocytes and begin to produce matrix (Bilezikian 2002).

Figure 7: Histology of the growth plate. (Naski and Ornitz, 1998)

1.8.2. Intramembranous ossification

This is the process responsible for formation of the flat bones of the skull and some of the facial bones. Following condensation of the mesenchymal cells, there is differentiation of a group of these cells into osteoblasts (primary ossification centre). Production of bone matrix by these cells is followed by calcification and transformation of encapsulated osteoblasts into osteocytes. Ossification centres expand radially, replacing the connective tissues. In the flat bones of the skull, inner and outer layers of bone are formed around a centre of connective tissue and blood vessels (Kumana 2009).

1.8.3. Bone remodelling

This process occurs not only during bone growth but also throughout life (Figure 8). It is important in body mineral homeostasis, fracture repair and response of bone to applied loads and forces (Curry 2003). Without bone remodelling, microfractures are not removed, producing structural weakness, which can lead to pathological fractures, as seen in patients on bisphosphonate therapy (Isaacs et al. 2010). The remodelling process is initiated by osteocyte intercellular signalling responding to cues such as mechanical stress or hormones. Bone lining cells retract away from the area to allow matrix metalloproteinases to remove the mineralised matrix. Osteoblasts adjacent to the area of remodelling express RANKL to promote local differentiation of preosteoclasts into mature osteoclasts. RANKL also causes downregulation of preosteoclast receptors for sphingosine-1 phosphate (S1P), which maintains osteoclast precursors in the remodelling area by desensitising them to S1P gradients that would otherwise cause their chemoattraction back into the circulation. Mononuclear osteoclast precursors fuse together to form polynuclear mature osteoclasts, this process of fusion is in part controlled by the expression of dendritic cell-specific transmembrane protein (DC-STAMP), which allow the preosteoclasts to identify each other (Nakahama 2010). This is then filled with osteoblasts differentiated from the mesenchymal stem cells of the endosteal sinus, forming new bone after the apoptosis of local osteoclasts (Datta 2008).

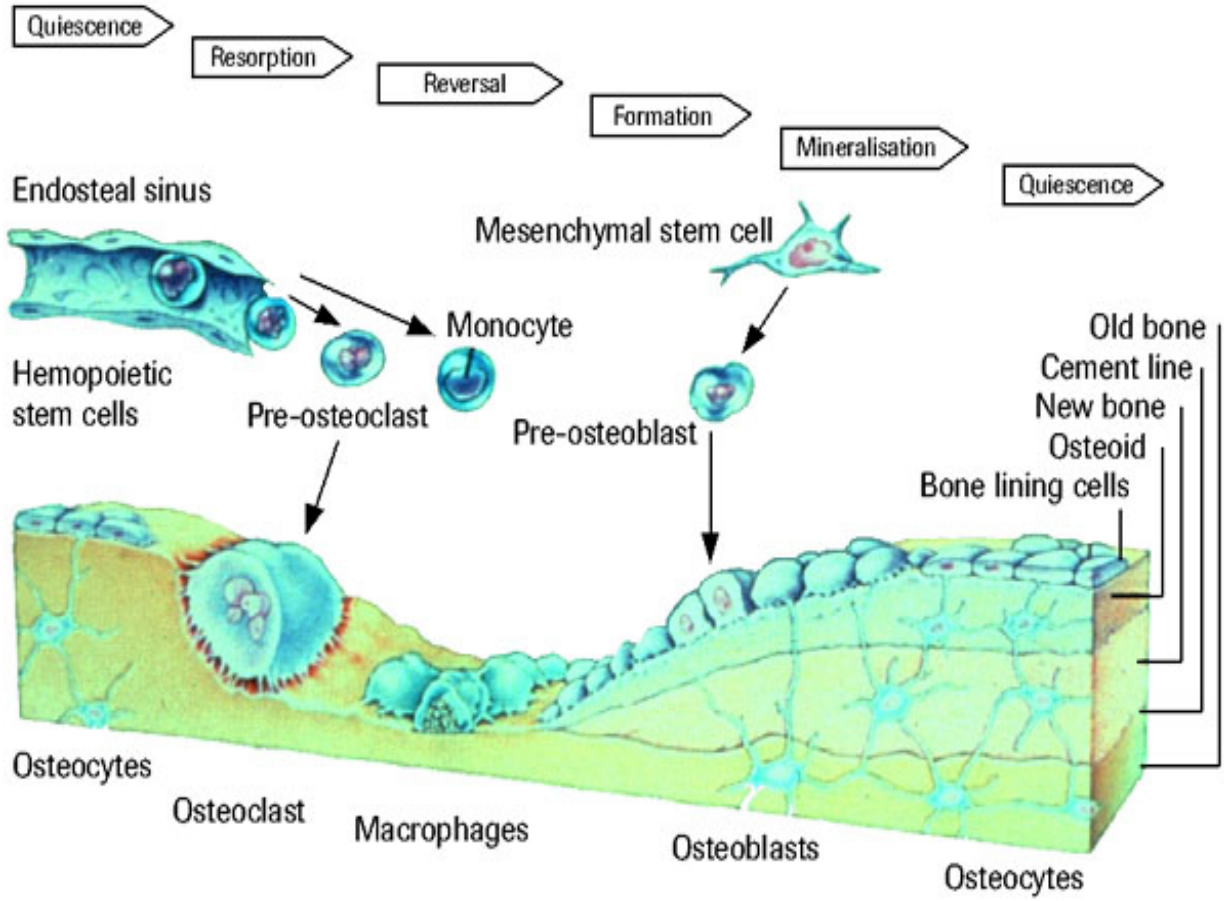

Figure 8: The bone remodelling cycle (Adapted from Roche.com)

Bone remodelling, as well as being under the control of local factors such as prevailing mechanical stress and paracrine factors, is at least in part centrally regulated. Leptin is a hormone that appears to be involved in bone homeostasis, with leptin-deficient mice displaying a high bone mass phenotype as well as obesity and hyperinsulinism. Infusion of leptin into the cerebrovascular circulation in these animals normalises their bone phenotype despite no leptin appearing in the general circulation (Ducy, Schinke and Karsenty 2000). Sclerostin levels, controlled by the maturation of osteocytes is a likely candidate for the termination of bone remodelling as rising levels antagonise the effect of BMP-2 (Nakahama 2010).

1.9. Specialised Bone Cells

1.9.1. Osteoblasts

Osteoblasts are derived from the fibroblast lineage. In culture they are morphologically identical and osteoblasts express all genes typically expressed by fibroblasts. Only the genes for Runx2 and Osteocalcin are specific to osteoblasts, as well as mineralisation of

the extracellular matrix (Ducy, Schinke and Karsenty 2000). As well as its role in osteoblast differentiation, Runx2 also plays a role in control of terminally differentiated osteoblasts, through its negative modulation of Osteocalcin expression, which inhibits bone formation by osteoblasts.

1.9.2. Osteoclasts

These are the predominant resorbing cell involved in bone remodelling. They are formed by the fusion of cells from the monocyte/macrophage lineage into multinucleated cells. Maturation into osteoclasts is regulated by Macrophage Colony Stimulating Factor (M-CSF) and Receptor for Activation of Nuclear factor Kappa B Ligand (RANKL), produced by osteoblasts or their bone marrow stromal cell precursors. The balance between RANKL and the soluble inhibitor osteoprotegerin determines the rate of bone resorption. Both parathyroid hormone and activated vitamin D exert their effects on osteoclastogenesis via control of expression of RANKL on osteoblasts (Teitelbaum 2000).

Osteoclast resorption of bone begins with tight attachment of the osteoclast to the bone surface with a characteristic 'sealing zone' formed of F-actin. The cell membrane in contact with the bone forms a 'ruffled border' which allows the creation of a specific microenvironment between the cell and the bone surface that can be acidified through the H^+-ATPase transporters located in the plasma membrane. This promotes dissolution of the mineral component of bone and cathepsin K and matrix metalloproteinases digest the remaining demineralised matrix, which is then endocytosed (Väänänen et al. 2000). Tartrate Resistant Acid Phosphatase (TRAP) is present in the vesicles transporting encytosed products and is capable of producing reactive oxygen species which can break down collagen (Halleen et al, 1999). This process leaves behind a pit or resorptive lacuna in the surface of the bone.

1.9.3. Osteocytes

Osteocytes are the most common cell type in mature bone, making up 90-95% of cells. They are formed by the terminal differentiation of osteoblasts and are found within lacunae in lamellar bone. Their branching cytoplasmic processes, found throughout a canalicular network, maintain connections with other osteocytes and osteoblasts through

gap junctions (Kamioka et al. 2007). Most osteocyte processes are found in the direction of the long axis of the bone and are believed to help act as mechanoreceptors in inducing a bone remodelling response to prevailing shear forces transmitted through the fluid flow through the canaliculi (Knothe-Tate 2004). They recruit osteoblasts to their local area during bone remodelling, by the expression of osteoblast stimulating factor 1 (OSF-1) (Bilezikian 2002), prostaglandins and nitric oxide (Chow 2000). Mature osteocytes express osteocalcin, osteopontin and osteonectin but little alkaline phosphatase. Apoptosis of osteocytes following disruption of the canalicular network in their immediate area, perhaps through bone microfractures, also appears to be an event that causes signals to begin bone remodelling (Rochefort, Pallu, Benhamou 2010).

Differentiation of osteoblasts into osteocytes may be partially dependent on the hypoxic conditions in the bone canalicular system in which they are found. Oxygen tension in bone marrow is 1-7% and it has been observed that there is greater expression of osteocyte-specific markers (DMP-1, FGF-23, MEPE) in cultures of osteoblasts in hypoxic conditions compared to those in normoxic conditions (Hirao et al. 2007). DMP-1 (Dentin Matix Protein-1) is produced by osteocytes in response to mechanical signalling and loss of function mutations are seen to cause low bone mineralisation (Noble 2008).

1.9.4. Bone lining cells

These are flat cells which are regarded as being resting osteoblasts or osteocytes. They cover the majority of endosteal bone surfaces (75% of cancellous bone surfaces, 95% of endosteal surfaces of cortical bone), in areas where there is neither resorption or formation. They play a role in transfer of mechanical loading signals from osteocytes to osteoclasts to initiate local bone modelling and control substrate transfer across the bone endosteal surfaces to and from the bone marrow. Bone lining cells may also have a more direct catabolic role and they express matrix metalloproteinases (MMPs) and tissue inhibitors of matrix metalloproteinases (TIMPs) (Dierkes et al. 2009).

1.10. Hydroxyapatite

Hydroxyapatite is the mineral component of bone and has the chemical formula $(Ca_{10}(PO_4)_6(OH)_2$ – although in 4-6% of molecules, carbonate replaces the phosphate

group). Hydroxyapatite (dahllite) has unusual crystalline properties with the crystals microscopically showing hexagonal symmetry but on the macroscopic scale forming flat plates (Weiner and Traub 1992) (Figure 9). The crystals are oriented in parallel along collagen fibrils and this organised structure spans several fibrils (Weiner, Traub and Wagner 1999). Mineralisation occurs through the transformation of soluble calcium and phosphate in pores within collagen fibrils forming mineral deposits which fill the remaining spaces in the organic matrix. Hydroxyapatite is responsible for the compressive strength of bone and forms a reservoir for 99% of total body calcium, 85% of phosphate and 40-60% sodium and potassium (Bates and Ramachandran 2007).

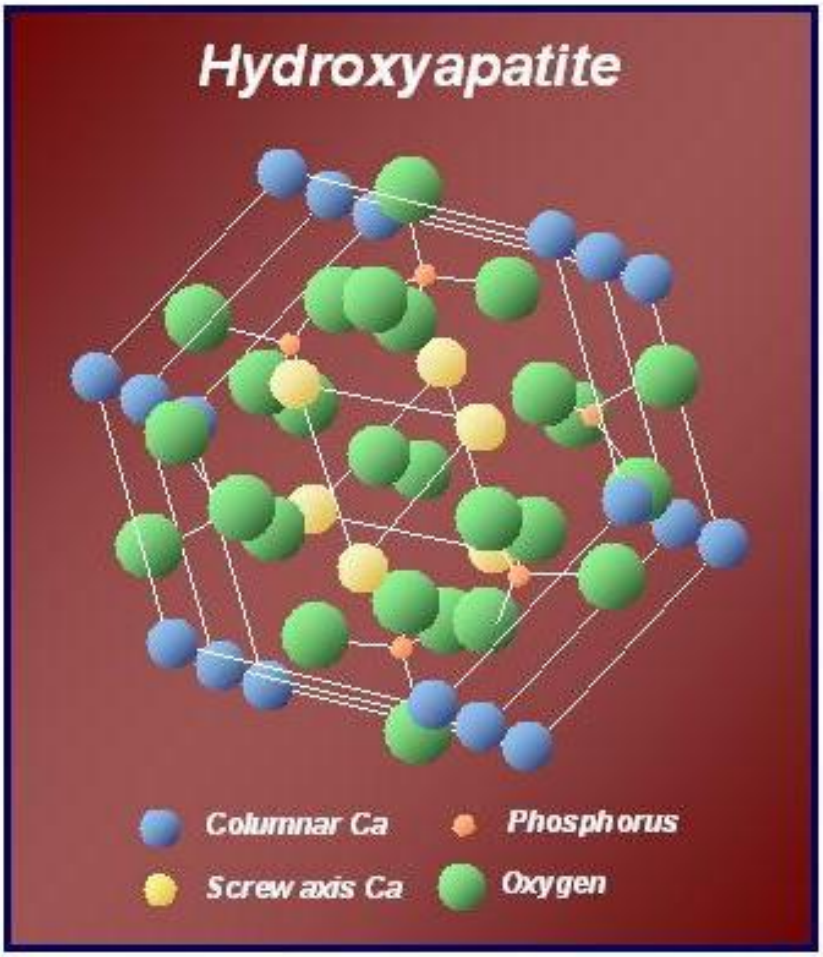

Figure 9: The molecular structure of hydroxyapatite (Adapted from The Division of Chemical Engineering, Osaka University)

1.11. Extracellular Matrix

1.11.1. Collagens

Collagen type I is the predominant form in bone with type II being the primary component of the extracellular matrix in cartilage. Type I collagen is a heterotrimeric

molecule with the two α1 and one α2 chains being coded for by the genes *COL1A1* and *COL1A2* respectively.

As well as articular cartilage, collagen type II is also found in the nucleus pulposus of the intervertebral discs, the vitreous humour of the eye and the tectorial membrane in the ear. It is encoded by the gene *COL2A1* and forms a heterotrimeric molecule. The minor collagens IX, X, and XI (fibril associated collagens) are also present in cartilage and appear to perform regulatory functions. Collagen IX molecules are found on the surface of collagen II fibrils and cross-link to the collagen II molecules. Type X collagen is a short chain molecule, which is expressed by hypertrophic chondrocytes during enchondral ossification. Type XI collagen polymerises with type II collagen and the ratio of the two proteins appears to regulate fibril diameter (Olsen, Reginato and Wang 2000).

Collagen I self assembles into fibrils according to the position of hydrophobic and charged groups on the surface of the molecules. Production of type I collagen by osteoblasts is regulated by growth factors such as TGF-β, IGF-I and –II, cytokines such as IFN-γ, TNF-α and IL-1 and other circulating substances vitamin D, PTH and corticosteroids.

1.11.2. Non-collagenous proteins

1.11.2.1. Osteocalcin

Osteocalcin is an osteoblast-specific protein, secreted at the onset of matrix mineralisation and it is involved in promotion of bone formation and metabolic regulation. It is produced as a pre-promolecule and secreted into circulation and undergoes post-translational modification by carboxylation of glutamic acid residues. Transcription of the gene during osteoblast differentiation is in part controlled by Runx2. In its undercarboxylated form, osteocalcin acts as a hormone on pancreatic islet cells to increase release of insulin and adiponectin from adipose tissue (Fulzele et al. 2010). Osteocalcin-null mice display unusually large amounts of visceral fat, supporting the role of osteocalcin in metabolism.

1.11.2.2. Osteopontin

Is a protein of around 300 amino acids in length, which as well as being a non-collaganous protein in bone is present in several other organs and in plasma. It plays a role in regulation of osteoclast activity and bone architecture. The actions of osteopontin on intracellular signalling and cytoskeletal structure are mediated via binding to the ECM receptor $\alpha_v\beta_3$ integrin. Osteopontin deficient mice show a normal bone phenotype at birth and throughout growth but they show an increase in osteoclast numbers, which may be compensatory for their slight hypocalcaemia. Osteopontin has been identified in the cement line attaching osteoclasts to the underlying bone during resorption. Osteopontin has also been found in osteoblasts and its production is induced by mechanical stress, furthermore, osteopontin-deficient mice are protected from decreased bone density resulting from unloading, providing evidence for its significant role in modulating bone turnover (Bilezikian, 2002).

1.11.2.3. Osteonectin

Osteonectin was one of the first non-collagenous proteins to be identified in bone and is also transiently present in other connective tissues during growth, development and repair. It binds calcium with several low affinity and two high affinity binding sites and can also bind sodium, hypdroxyapatite and collagen. Osteonectin-deficient mice develop cataracts and osteoporosis. It is believed that osteonectin is secreted by osteoblasts during formation of mineralised matrix, initiating hydroxyapatite deposition. Its main role is in matrix mineralisation but also has functions in cell-matrix interactions, cell adhesion and regulating the cell cycle (Bilezikian 2002).

1.11.2.4. Proteoglycans

These are made up of core proteins with glycosaminoglycans covalently attached to serine residues. Glycosaminoglycans contain repeating carbohydrate units, which are extensively sulphated. Proteoglycans have varying roles including binding to collagen and TGF-β and are involved in nucleation of hydroxyapatite crystallisation. They also bind cations such as sodium and calcium and regulate the movement of molecules through the extracellular matrix.

The proteoglycans associated with bone include versican, decorin and biglycan. Versican is a large proteoglycan, found mainly in mesenchymal tissue during very early bone formation and is progressively replaced during osteogenesis. Decorin and biglycan are part of the group of small leucine-rich repeat proteoglycans which interact with collagen. Biglycan facilitates the action of BMP-4 in bone formation and decorin promotes formation of collagen fibrils (Bilezikian 2002).

1.11.2.5. Alkaline phosphatase (ALP)

In humans, four different ALP isoenzymes are coded by separate genes. Tissue non-specific ALP is a tetromeric glycoprotein found in all body tissues but particularly in the kidney, liver, biliary duct system and bone. Alkaline phosphatase is bound to the cell membrane of osteoblasts and can be used as a serum marker of bone turnover. It is a zinc-metalloenzyme, which requires magnesium as a co-factor and acts to hydrolyse phosphoesters, increasing local phosphate concentrations to interact with calcium held by ostecalcin, osteopontin and osteonectin (Bilezikian, 2002).

1.12. Hormones and calcium homeostasis

1.12.1. Parathyroid hormone

Parathyroid hormone (PTH) is one of the major modulators of calcium homeostasis through direct effects on the kidney and bone and indirect action on the gastrointestinal tract. PTH is released in response to low serum calcium and acts to enhance re-absorption of calcium in kidneys and release calcium from the skeleton by bone resorption. It also increases formation of activated vitamin D which increases calcium uptake in the gastrointestinal tract.

1.12.2. Vitamin D

Vitamin D is made in the skin and activated to 1,25 dihydroxy-vitamin D in the kidneys and liver, has a primary purpose of increasing absorption of calcium in the small intestine. It also acts to increase the release of calcium from bone in order to increase serum calcium levels.

1.12.3. Calcitonin

Calcitonin is a 32 amino acid peptide produced by the C cells of the thyroid. Its action is specific to osteoclasts and in culture has been shown to cause loss of the ruffled border and reduction in motility. Over the longer term there is a reduction in total osteoclast number. Calcitonin also affects secretion of acid via modulation of carbonic anhydrase activity and secretion of TRAP. Overall calcitonin is a powerful inhibitor of bone resorption and has the net effect of lowering serum calcium. Exogenous calcitonin is used in the clinical treatment of osteoporosis, Paget's disease and hypercalcaemia of malignancy (Bilezikian, 2002).

1.13. Osteoblast Lineage and Differentiation

Adhesion and differentiation of osteoblast precursor cells at the bone-implant interface is a key component of osseointegration. Mature osteoblasts differentiate from mesenchymal precursor cells, which are pluripotent and also differentiate into the adipocyte, myoblast and chondroblast lineages. Differentiation down the osteoblast pathway is controlled by several transcription factors, one of the earliest of which is Runx2.

1.13.1. Runx2

Runt-related Transcription factor 2 (Runx2) is also referred to as Cbfa1. This is present in cells from chondrogenic and osteogenic lineages, promoting hypertrophy and maturation of chondrocytes and differentiation of preosteoblasts. Its expression is upregulated by the action of bone morphogenetic proteins (BMPs), particularly 2 and 4. Runx2-null mice are born with cartilaginous skeletons without any osteoblasts and showing abnormal cartilage with delayed maturation of chondrocytes. Expression of Runx2 precedes osteoblast differentiation by 4-5 days due to initial co-expression of the inhibitors Twist 1 and 2 (Karsenty 2007). Twist 2 is regulated by insulin receptor signalling and it has been shown in a mouse model lacking insulin receptors on osteoblasts that these mice have decreased numbers of osteoblasts and reduced bone formation (Fulzele et al. 2010).

Runx2 expression is regulated by a wide array of other transcription regulators with those such as Smad1, Smad5, Menin, BAPX-1 and HoxA10 enhancing Runx2 expression and others (Sox8, Sox9, Stat1, YAP and MEF) inhibiting expression. Fibroblast Growth factor 18 (FGF18) is an essential regulator of bone development and is induced via the canonical Wnt signalling pathway by Runx2 (Reinhold and Naski, 2007).

1.13.2. Osterix

Osterix is a zinc-finger containing protein that acts downstream of Runx2, which is itself induced by the action of BMP2. Interaction of osterix with NFATc1 upregulates *COL1A1* expression and activates the Wnt pathway which, via Frizzled and LRP5/6 interactions and β-catenin phosphorylation, in turn activates Runx2, Osterix and Dlx5. Osterix-null mice are also born with cartilaginous skeletons but they contain normal chondrocytes. Osterix is not expressed in Runx2-null mice (Gordeladze et al 2010).

1.13.3. Dlx and Msx

Distal-less homeobox (Dlx) and msh homeobox homologue (Msx) transcription factors also have roles in early osteoblast differentiation. They are key transcription factors in intramembranous ossification and, from in vitro studies, appear to have roles as both activators and suppressors of transcription (Harada and Rodan 2003). Mice deficient in Msx1 or Msx2 have abnormalities of cranial bone formation and Msx2 appears to play a role in promoting osteoblast differentiation and proliferation. Dlx5 and 6 are transcription factors belonging to the homeobox group of proteins and are present in osteoblasts. Deficiency of Dlx5 causes craniofacial abnormalities and fusion of fore and hind digits in mice models. Embryonic limb ossification is also significantly slowed and chondrocyte maturation is also affected (Komori 2006).

1.14. Fracture Healing

Other than arthroplasty, the major use for biomaterials in orthopaedics is in fracture fixation with metallic and bioabsorbable materials in use in devices such as plates, screws, wires and intramedullary nails. An appreciation of the normal process of fracture healing is important for the fixation of fractures with attention to the biology of the fracture site and to an understanding of the processes underlying non-union of fractures.

1.14.1. Direct and Indirect fracture healing

The process of fracture healing is dependent on the strain experienced by the local tissues. Two forms of bone healing are seen

- Direct
- Indirect

Direct (or primary) bone healing only occurs in the presence of absolute stability at the fracture site where there is no gap between the bone ends, which can be achieved by interfragmentary screw fixation and compression plating. This produces almost no strain at the bone ends, preventing callus formation and allowing, instead, direct remodelling of the Haversian systems. In a situation of relative stability (bridging plate, intramedullary nail, casting) there is greater strain experienced by the tissues, promoting callus formation and indirect (secondary) bone healing. In grossly unstable fractures, the strain may overcome the ability of callus tissue to form, causing a situation predisposing to non-union (Bates and Ramachandran 2007). The four phases of callus formation in secondary bone healing (Figure 10) are described below:-

1.14.2. Haematoma and inflammation

Over the first week following fracture, a fibrin clot initially forms around the ruptured blood vessels at the fracture site. GDF-8 is a member of the TGF-β superfamily and operates only in the first day following fracture, suggesting a role in cell proliferation. Osteoclasts and macrophages resorb necrotic bone tissue. IL-1, IL-6 and TNF-α are the pro-inflammatory cytokines that initiate the cascade of events leading to fracture healing, beginning with the migration into the clot of polymorphonuclear neutrophils and macrophages. These are followed by fibroblasts and osteoprogenitor cells as well as

ingrowth of capillaries, which are attracted by cytokines and growth factors such as BMP-2, TGF-β and PDGF (Al-Aql et al. 2008).

1.14.3. Cartilage callus

For several weeks following organisation of the haematoma and mobilisation of osteoprogenitor cells to the fracture site, there is callus formed by production and mineralisation of type I collagen by osteoblasts in the periosteum under the control of BMP-5 and BMP-6 (intramembranous ossification). This forms new woven bone, which does not cross the fracture site. Callus that bridges the fracture site is formed from the differentiation of mesenchymal stem cells in the callus into chondroblasts and fibroblasts, whose actively is controlled by a peak in TGF-β2, TGF-β3 and GDF-5 (enchondral ossification). These produce mineralised matrix which forms calcified fibrocartilage (Al-Aql et al. 2008).

1.14.4. Mineralisation

TNF-α, Macrophage Colony Stimulating Factor (MCSF) and RANKL mediate resorption of calcified cartilage via apoptosis of hypertrophic chondrocytes (Gerstenfeld et al, 2003). There is invasion of new blood vessels, initiated by angiopoietins and VEGFs. VEGF also promotes osteoclast recruitment (Kanczler and Oreffo 2008). BMP-3, -4, -7 and -8 act to recruit osteoprogenitor cells to the region and these cells differentiate and begin to produce bone matrix. Callus formation is also continued peripherally by the osteoprogenitor cells in the periosteum (Al-Aql et al. 2008).

1.14.5. Reorganisation

Once the fracture is successfully bridged with hard callus, the process of reorganising the woven bone to mature lamellar bone begins and can continue for several years. Osteoclasts resorb the woven bone and it is replaced by osteoblasts in Haversian systems which reorient in the direction of prevailing stresses. This process is associated with an increase in local IL-1 and IL-6 and a reduction in MCSF and RANKL. The medullary cavity is also reformed by the same process in the context of reduced levels of members of the TGF-β superfamily (Bates and Ramachandran 2007).

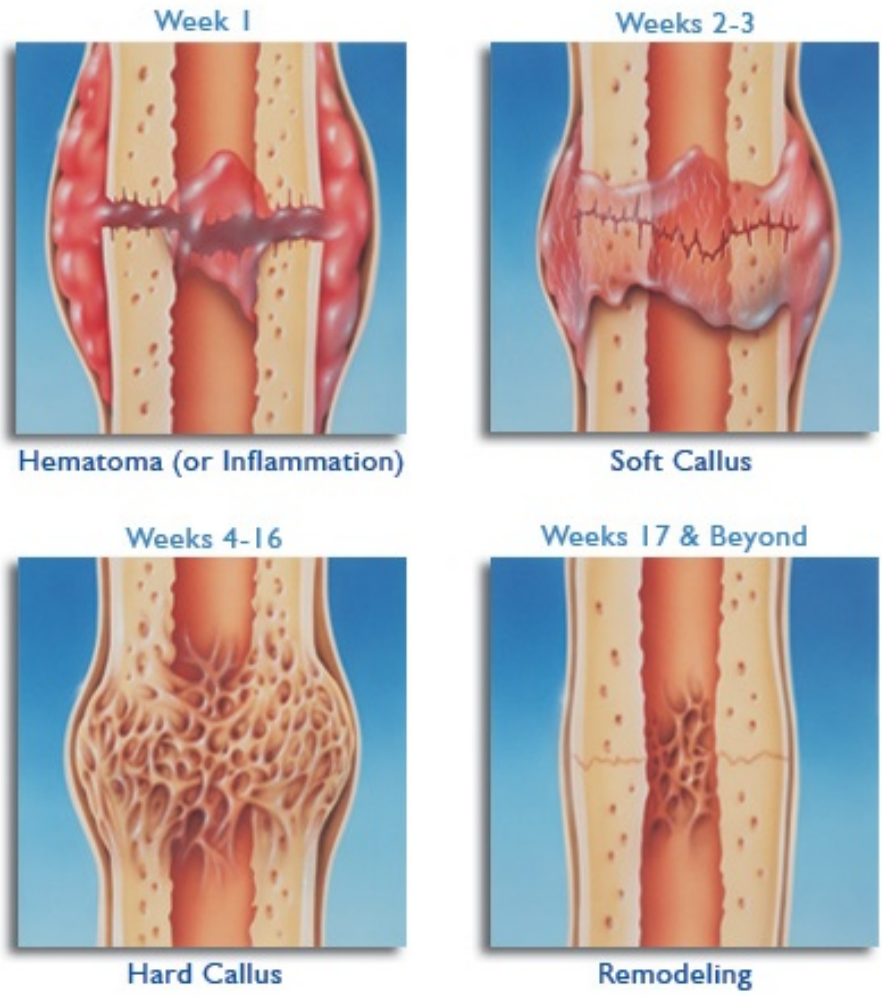

Figure 10: The stages of fracture healing. (Adapted from medical-definitions.com)

1.15. The role of bone cells in diseases of the bone

There are several metabolic, genetic and inflammatory diseases of bones and joints, which are of significance to orthopaedic surgery. Osteoporosis, osteopetrosis, Paget's disease and osteomalacia are causes of pathological fractures and complicate fracture fixation. Rheumatoid arthritis and osteoarthritis cause joint destruction and result in the need for arthroplasty.

1.15.1 Osteoporosis

Osteoporosis is the most common disease of bone and is defined in a consensus statement as 'characterised by low bone mass and microarchitectural deterioration of bone tissue, leading to enhanced fragility and a consequent increase in fracture incidence'. The World Health Organisation defines osteoporosis as a bone density,

measured in the lumbar vertebrae, of more than 2.5 standard deviations below the young adult mean (T score). It affects 1:3 women over the age of 60 years and results in an increased risk of fracture, particularly of the distal radius, neck of femur, proximal humerus and spine. Bone loss is accelerated in females after the menopause for several years and bone density is lost with age in both sexes, due to an imbalance between bone resorption by osteoclasts and new bone formation by osteoblasts. Lack of oestrogen increases the cytokines IL-1, IL-6 and Tumour Necrosis Factors, which have been liked to bone resorption. Risk factors for osteoporosis include low body mass index, high alcohol intake, smoking, European or Asian descent, early menopause, low dietary calcium and immobility. Secondary causes of osteoporosis include certain medications such as steroids, phenytoin and anticoagulants, multiple myeloma, Turners syndrome, rheumatoid arthritis, systemic mastocytosis, adrenal disease and hyperthyroidism. Dual energy x-ray absorptiometry (DEXA) is the most common method of diagnosis but CT scanning can also be used. Serum calcium, phosphate and alkaline phosphatase are usually found to be in the normal range (Khurana 2009).

Treatment of osteoporosis includes excluding secondary causes, supplementation of dietary calcium and vitamin D and pharmacological therapies to reduce bone turnover such as bisphosphonates, calcitonin and strontium and anabolic agents such as parathyroid hormone (Miller 2004).

1.15.2. Osteomalacia

This is a disorder of mineralisation, resulting in production of large amounts of unmineralised osteoid. Due to vitamin D deficiency, there is inadequate calcium and phosphate for mineralisation. This may be due to dietary deficiency, lack of sunlight, disorders of intestinal absorption (coeliac disease, Crohn's disease, short bowel syndrome) and renal osteodystrophy. Abnormal blood test results include low calcium and phosphate, high alkaline phosphatase and high pararthyroid hormone. Histology of bone in osteomalacia shows areas of unmineralised osteoid surrounding mineralised trabeculae with mineralisation lag often greater than 100 days (80-90 days is normal). Treatment strategies include calcium, vitamin D and its active metabolites (Khurana 2009).

1.15.3. Osteopetrosis

This is a group of disorders caused by decreased osteoclast function, often associated with a lack of the normal ruffled border, preventing bone resorption. This results in loss of the medullary cavities of long bones, which are filled with necrotic calcified cartilage. The infantile form may lead to hepatosplenomegaly and aplastic anaemia and may require bone marrow transplantation with osteoclast precursors. The adult autosomal dominant form causes generalised sclerosis and fractures due to brittleness of bone (Miller, 2004).

1.15.4. Paget's disease

Or osteitis deformans is a disease of bone turnover, which may occur in one bone or several and has a strong genetic component. Pagets lesions are initiated following bone resorption by increased numbers of abnormal osteoclasts, with larger numbers of nuclei. This produces multiple resorptive pits, resulting in the characteristic radiological appearances of the lytic phase. Following this is the mixed phase, in which osteoblasts join osteoclasts at the bone surfaces. The blastic phase then follows with formation of irregular, woven bone. Trabeculae become broad and coarse and cortices are irregularly remodelled. Blood tests demonstrate increased alkaline phosphatase. The axial and proximal appendicular skeleton are most frequently involved and pain is the most frequent presenting symptom. Treatment is aimed at decreasing bone turnover with agents such as bisphosphates (Khurana 2009).

1.15.5. Rheumatoid Arthritis

Rheumatoid arthritis is the most common inflammatory joint disease, affecting 3% of women and 1% of men globally. Genetic predisposition (including HLA-DR4) interacts with environmental cues to produce a multi-system autoimmune disease which causes destruction of joints that is usually symmetrical and often affects the small joints of the hands and feet initially. A 'pannus' of fibroblast-like synovial cells adheres to articular cartilage, degrading it and the underlying bone. This synovial overgrowth is driven by upregulation of c-Fos/AP-1 and the synoviocytes produce the pro-inflammatory cytokine IL-1. The synovial cells then present antigen to T cells, modifying the course of subsequent inflammation. The collagenous matrix of bone and cartilage becomes vulnerable to degradation after initial attack by matrix metalloproteinases that remove

proteoglycan. The normal balance of MMPs and their inhibitors TIMPs is disordered in rheumatoid arthritis as pro-inflammatory cytokines such as IL-1 up-regulate MMPs. Bone resorption in periarticular regions occurs early in the disease process due to increased differentiation of osteoclasts and the action of MMP9 and cathepsin K. New bone formation in these areas is also suppressed by the action of TNF-α via Dickopf-1 (Shiozawa et al. 2011).

1.15.6. Osteoarthritis

Osteoarthritis is the most common joint disease, affecting over 50% of the population at some time. The condition presents with pain and joint stiffness but normal inflammatory markers. The large weight-bearing joints are commonly affected, along with the thumb metacarpophalangeal joints and the distal interphalangeal joints of the fingers. An imbalance between cartilage degradation and repair occurs, with increased cellularity of the cartilage and extracellular matrix that is less resistant to mechanical stress. Matrix metalloproteinases and aggrecanases mediate cartilage degradation and cartilage debris initiates synovial inflammation with increased numbers of synovial macrophages and upregulation of catabolic mediators. Small areas of collapse and necrosis of subchondral bone lead to cysts and reactive growth of subchondral bone, causes subchondral sclerosis and marginal osteophytes. Subchondral bone changes appear early in the disease process and may initiate some of the cartilage damage (Bijlsma, Berenbaum and Lafeber 2011).

1.16. Cell adhesion, Mobility and Communication

1.16.1. Mechanisms of bone cell response to the local environment

Bone cell adhesion, communication and response to changes in the local environment are mediated through a series of connections. These begin outside the cell with extracellular matrix proteins, through complexes of cell membrane-spanning adhesion molecules (focal adhesions and gap junctions) to intra-cellular signalling molecules and direct connections with the cytoskeleton and on to the nucleus, affecting gene transcription (Pavalko 2003).

Focal adhesions are complexes of proteins which connect the cell cytoskeleton with the extracellular matrix, thereby mediating cell adhesion and signalling. They are also

involved in cell sensing and migration by their formation in lamellipodia, the finger-like projections of cell membrane formed at the leading edge of a mobile cell during migration (Cavalcanti-Adam et al 2007).

Focal adhesion complexes and gap junctions are linked to the actin cytoskeleton by proteins such as vinculin, paxillin and fimbrin. There are also signalling molecules that effect changes to cytoskeletal organisation, such as MAP kinase, focal adhesion kinase, Rho and Rac (Pavalko 2003) and by these cellular mechanisms, gap junctions facilitate intercellular communication.

1.16.2. Connexins

Connexins are a family of related proteins that make up the hexameric transmembrane complexes (connexons) which connect with those on neighbouring cells forming channels known as gap junctions and therefore play a crucial role in cell-cell signalling (Civitelli 2008). Gap junctions allow the passage of ions and signalling molecules between cells, the size of the molecules determined by the type of connexin. Connexin-43 (Cx-43) is particularly associated with osteoblasts and osteocytes, although Cx-45 is also present (Ddouk et al 2009) and Cx-43 is involved in bone growth and remodelling via transmission of mechanical load, growth factor and hormones (Lima et al. 2009). In humans, defects in the gene Gja1, which codes for Cx-43, result in Oculodentodigital dysplasia, a rare disorder characterised by small teeth, small eyes, syndactyly of the 4^{th} and 5^{th} fingers and neurological disturbances.

Its roles in the regulation of osteoblast differentiation have been elucidated in the study by Li et al in 2006, in which immortalised human foetal osteoblasts were transfected with anti-sense cDNA for Cx-43. A 50% reduction in gap junctions was observed and an almost total absence of alkaline phosphatase activity was found in these cells in comparison to controls. A relative decrease in osteocalcin and increase in osteopontin was also observed. Whilst there was no change to collagen type I production, these results suggest that Cx-43 activity is important in the ability of bone cells to produce mineralised matrix. This is supported by the observation that mice with a selective deletion of Cx-43 in osteoblasts show decreased bone mass and reduced new bone

formation response to exogenously introduced parathyroid hormone (Chung et al. 2006).

Cx-43 is also implicated in the response of osteoblasts to circulating levels of PTH, with continuous intermittent administration resulting in no overall change to the quantity of Cx-43 but an increase in its expression in connexons on the cell surface (Cherian et al. 2008). PTH also regulates the signalling in the osteocyte network, which occurs through gap junction connections (Civitelli 2008). Intercellular signalling via gap junctions is regulated by the binding of the carboxyl terminal and cytoplasmic loop domains of connexins to several molecules including ZO1, β-tubulin and the Src family of tyrosine kinases (Kang et al. 2009).

Cx-43 appears also to play a role in modulating the response of bone to applied forces. Cx-43 null mice show an attenuated bone formation response to strain applied to long bones (Grimston et al. 2006), which may be mediated by modulation of sclerostin production (Lin et al. 2009). Cx-43 deficit bone marrow stromal cells also produce reduced levels of osteoprotegerin, resulting in increased bone resorption by osteoclasts and disruption of normal osteoblast differentiation, forming abnormal bone in response to loading (Watkins et al. 2011).

1.16.3. Cadherins

Cadherins, particularly -2 and -11 play important roles in osteoblast function and differentiation. Cadherins are transmembrane glycoproteins that regulate calcium-dependent cell-cell adhesion by linking the cytoskeletons of adjacent cells via their extracellular domains (Figure 11). They are also important in intracellular signalling through binding to β-catenin, which both links to the actin cytoskeleton via α-catenin and also forms part of the Wnt signalling pathway (Castro et al. 2004).

Cadherin-2 is important in osteoblast homeostasis (Lai et al. 2006) and relatively increased levels of cadherin-2 and -11 are present in mature osteoblasts as compared with other mesenchymal cells (Kawaguchi et al. 2006). Cadherin-2 is present in all cells of mesenchymal derivation but the expression of different cadherin profiles is characteristic of commitment to specific lineages.

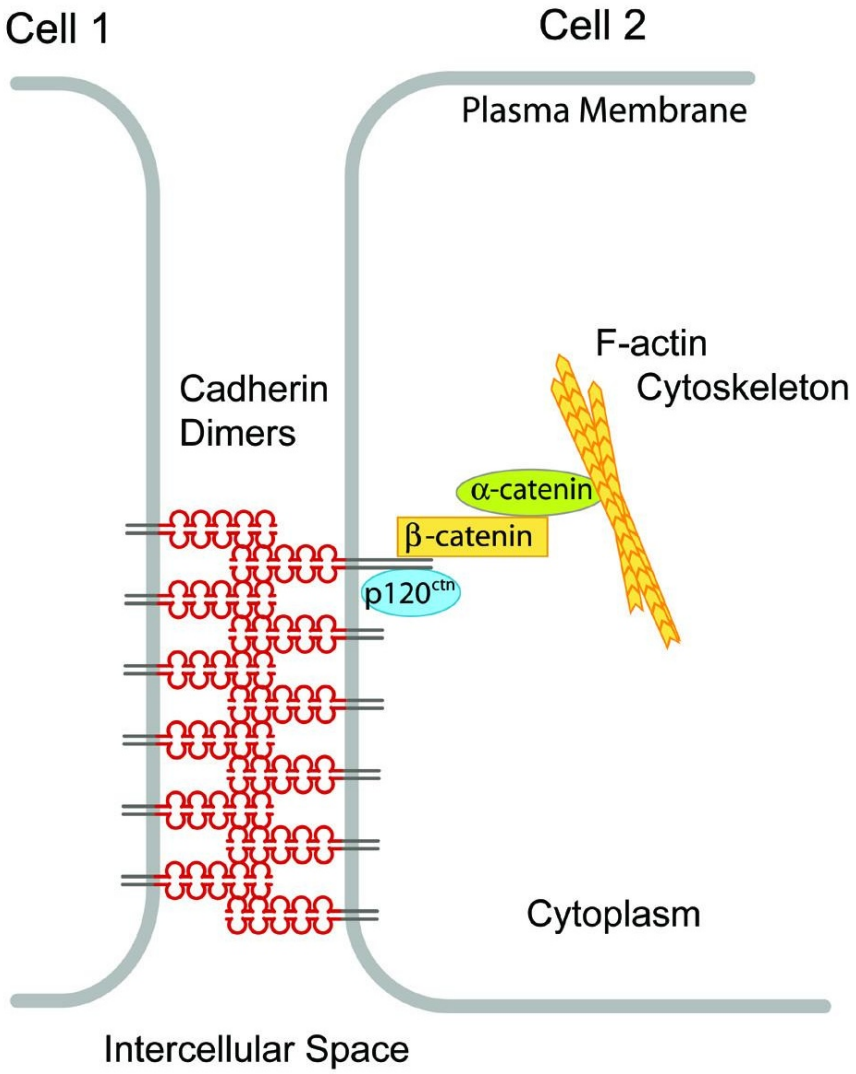

Figure 1: Cadherin-11 forming a gap junction. (Adapted from Kiener and Brenner, 2005)

Osteoblasts are characterised by the expression of cadherin-2 and -11. A mouse model with a dominant-negative cadherin-11 mutation showed decreased numbers of osteoblasts with resultant increased commitment of bone marrow stromal cells to the adipogenic lineage. The mechanism of this action was interference with normal β-catenin signalling with knock-on downstream effects on the Wnt signalling pathway (Castro et al. 2004). Mice with cadherin-2 ablation display increased age-related osteopenia and reduced bone strength. Double knockdown of Cadherin-2 and Cadherin-11 results in decreased numbers of bone precursor cells, severely decreased bone mass and decreased bone strength (Di Benedetto et al, 2010). Cadherin-2 and cadherin-11 therefore appear to have synergistic roles in skeletal development and maintenance of bone mass through their effects on cell adhesion and communication.

1.16.4. Rho / Rac

These are part of the Rho family of small GTPases, which are present in all eukaryotic cells and are involved in many intracellular events such as cell proliferation, apoptosis and adhesion and appear to be key regulators of signalling between cell membrane receptors and the cytoskeleton. Rho and Rac are both required for the formation of cadherin-based adherens junctions and gap junctions formed from connexins. These GTPases regulate gene expression through their effects on cellular communication through adherens junctions and also more directly by activating the MAP kinase pathway. They regulate the structure of the actin cytoskeleton and the formation of actin stress fibres in response to extracellular signals (Hall 1998). The Rho-like subfamily is involved in cell contractility and focal adhesion formation and the Rac-like subfamily are all involved in the formation of membrane ruffles and lamellipodia. Rho-mediated formation of actin stress fibres and focal adhesions occurs via increased myosin light chain phosphorylation and the downstream effector ROCK (Rho-associated kinase) depressing the action of MLC phosphatase, causing increased cytoskeletal tension. Both Rho and Rac promote cell adhesion to the extracellular matrix through the clustering of integrins and their connection to the actin cytoskeleton. Rho and Rac are upregulated by the presence of several effector molecules including insulin, platelet derived growth factor and epidermal growth factor (Burridge and Wennerberg 2004).

Anderson and colleagues in 2002 demonstrated that inhibition of Rho and its downstream effector ROCK caused changes in connexin expression and gap junctions in cultures of rabbit corneal epithelial cells. Inhibition of Rho caused decreased expression of Cx-43 positive gap junctions, however inhibition of ROCK resulted in increased gap junction formation.

Rac plays a role in animal cell motility, particularly observed in chemotaxis of neutrophils, as it is found in the leading edge of the cell, involved in polymerisation of actin filaments creating protusions of the cell membrane causing forward propulsion. Rho is found at the rear edge of the mobile cell, acting via ROCK to phosphorylate myosin light chain light chains, resulting in contractile forces being generated (Jaffe and Hall 2005).

In a previous study, it has been observed that inhibition of RhoA and ROCK decreases the contact guidance observed in mesenchymal stem cells and osteoblasts cultured on nanometre grooved Ti6Al4V substrates, with the cells treated with inhibitors C3 transferase and hydroxyfasudil displaying significantly decreased orientation in the direction of the grooves (Calzado-Martín et al. 2011).

1.17 Summary

Metallic biomaterials play an important role in the surgical treatment of a range of conditions; of particular interest being implants for orthopaedic use in fracture fixation and arthroplasty. The surface structure and chemistry of titanium alloys used in orthopaedics and dentistry have been extensively researched and there is an understanding of the effect of these features on osteoblast behaviour and function. The electrochemical technique used in this project, however, is novel and its effects on osteoblast behaviour and osseointegration uncertain. Much is already understood regarding the role of bone cells in terms of bone structure, growth and contribution to disease. The role of molecules involved in cell adhesion and cell-cell communication, which may underlie the observed differences in osteoblast behaviour has not been fully explored.

1.18 Aims

- Characterisation of surface roughness and surface chemistry produced by electrochemical modification
- Investigation of osteoblast adhesion, differentiation and behaviour on the modified surfaces
- Demonstration of the molecular mechanisms underlying the observed differences in cell behaviour
- Investigation of osseointegration of the modified surfaces *in vivo*

1.19 Objectives

- Produce treated titanium alloy surfaces using a novel electrochemical etching technique with a sulphuric acid and methanol electrolyte.

- Use optical microscopy and profiling, scanning electron microscopy, atomic force microscopy and x-ray photoelectron spectroscopy to fully characterise the surface chemistry and roughness of the electrochemically treated surfaces.
- Use immunofluorescence on rat calvarial osteoblasts and human mesenchymal stromal cells, with anti-vinculin primary antibody, to measure parameters of early cell adhesion and growth including cell number, cell area, cell polarity and focal adhesion area and density.
- Characterise later cell differentiation and growth using an alkaline phosphatase activity assay and staining for calcified bone nodules.
- Investigate the molecular mechanisms underpinning the observations of cell behaviour using real-time quantitative PCR, RhoA and Rac activity assays and functional studies of the effect of inhibition of Rho-family proteins on focal adhesion complexes.
- Investigation of osseointegration of the treated surfaces in an animal model using cylindrical pins in rat tibias, which are then extracted and subjected to micro-CT imaging, mechanical push-out testing or histomorphometry.

Chapter 2. Materials and Methods

Experimental Flow Chart

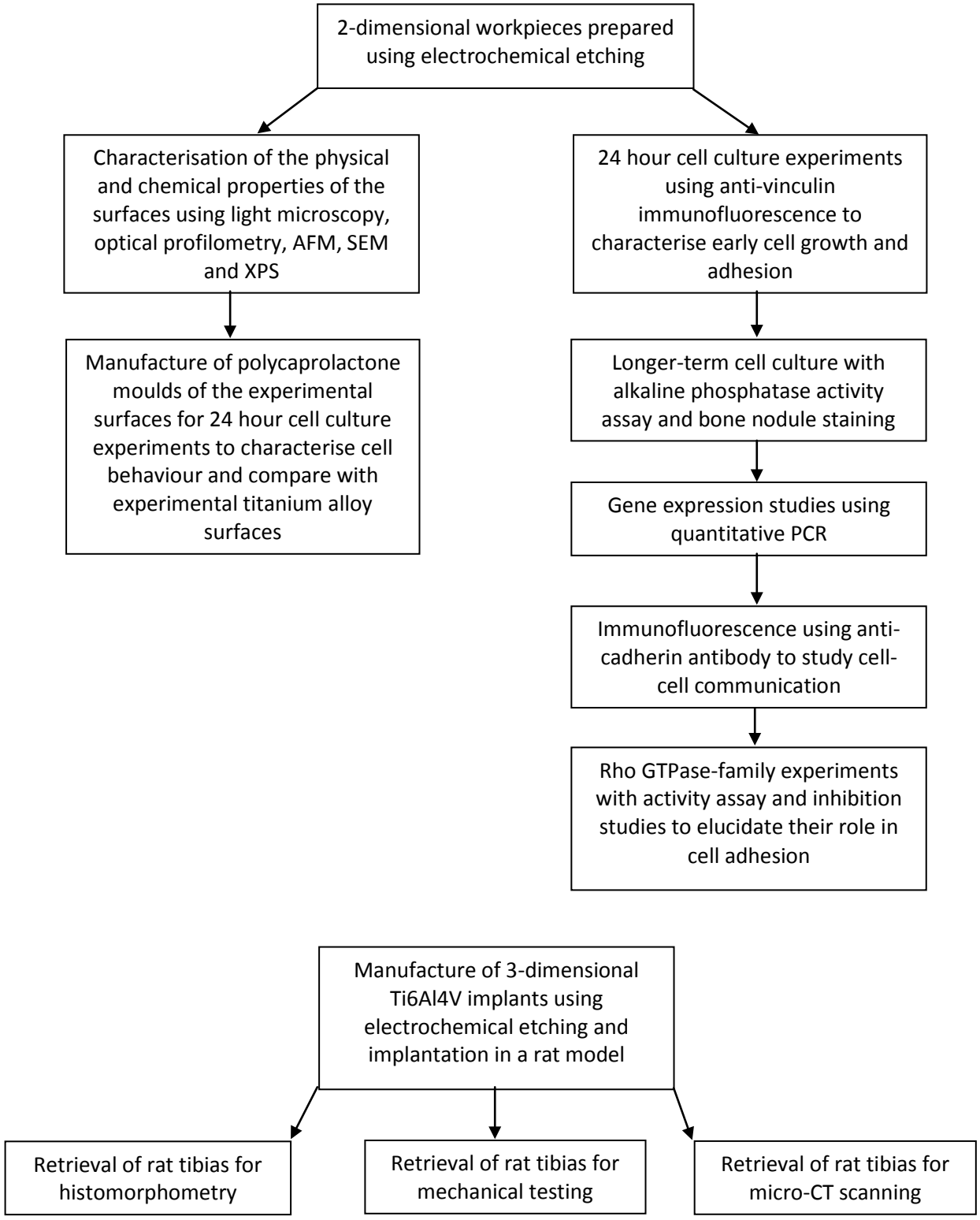

2.1. Workpiece preparation

2.1.1. Grinding and polishing

5mm thick samples were cut from 12.7mm diameter Ti6Al4V rods (Goodfellows, UK) using a low speed diamond-edged circular saw. Plane grinding was performed on a grinding wheel (Struers DAP-7 wet grinding machine) with 400 grit paper and water lubrication. Sequential fine polishing was achieved using 1200, 2400 and 4000 grit papers (Struers) to achieve a mirror finish, again with water lubrication, according to Struers metalography guide to polishing (Stuers knowledge). Progressively finer grit papers allow the polishing out of the rougher striations caused by the coarser grit papers until the surface is uniformly smooth and reflective to the naked eye (mirror finish).

2.1.2. Electrochemical surface modification of flat workpieces

A custom glass cell was fabricated as illustrated below (Figure 12), with copper and platinum mesh electrodes (Meuleman and Roy, 2003; Birch et al, 2012). The ionic conductor was a 3M solution of 98% H_2SO_4 (VWR) in methanol (VWR), (pH of 2) which has been demonstrated by previous experiments to be the optimum concentration for surface modification of Ti6Al4V (Nouraei, 2008). This was produced in 1 litre quantities using 163ml sulphuric acid in 837ml methanol, made by adding one drop of sulphuric acid at a time to the methanol to manage the exothermic nature of the reaction.

The samples were placed in the cell one at a time and the copper electrode backplate was affixed to hold the samples in place. Steady state chronoamperometric polarisation was performed at 25°C, using the Autolab PGSTAT 30 and GPES (General Purpose Electrical System) control software. Chronoamperometry allows a constant voltage to be applied across the cell (and therefore to the workpieces) during the electrochemical process by adjusting the applied current according to measurements from the reference electrode. A saturated calomel electrode (SCE) was used as a reference in these experiments and all voltages stated in this work refer to values from this electrode. Care was taken to avoid any water in the system as this affects the conductivity of the electrolyte solution and therefore the current profile and characteristics of the resulting surface modification.

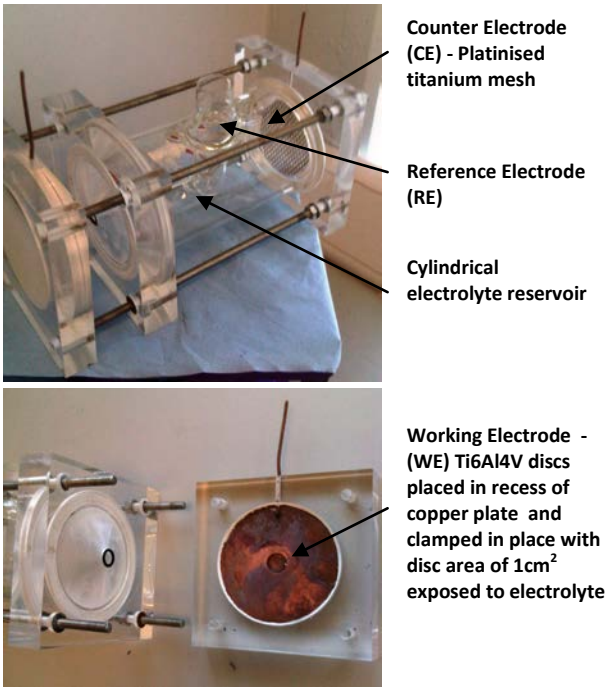

Figure 12: Glass cell for electrochemical modification (photographs from J. Varia with permission)

2.1.3. Electrochemical surface modification of in vivo implants

This was performed in a cylindrical cell manufactured from a simulation using design software (ElSyCa, Belgium) (Figure 13). The implants were made from Ti6Al4V rods supplied by Goodfellow, UK of 2mm diameter and 100mm length. Before electrochemical modification, the rods were mechanically polished on a metalworking lathe to a mirror finish. The ionic conductor was again a 3M solution of 98% H_2SO_4 (VWR) in methanol (VWR), produced in 1 litre quantities using 163ml sulphuric acid in 837ml methanol. Steady state chronoamperometric polarisation was performed using the Autolab PGSTAT 30 and GPES (General Purpose Electrical System) control software. A saturated calomel electrode (SCE) was used as a reference in these experiments and all voltages stated in this work refer to values from this electrode.

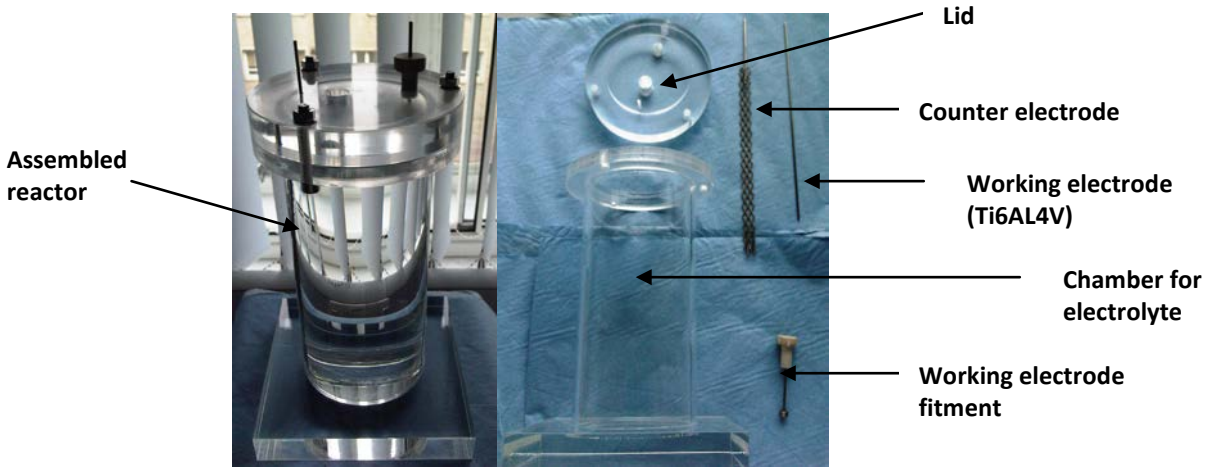

Figure 13: Electrochemical cell for electrochemical modification of in vivo implants

2.2. Preparation of polycaprolactone reproductions of titanium alloy surfaces

Moulds were taken of the titanium alloy surfaces in order to culture cells on surfaces that reproduced the topography of the alloy but had identical surface chemistry. Titanium alloy workpieces were placed into wells of the same diameter and Microset silicone rubber curing compound (Microset Products UK) was injected onto the top using the manufacturer's injection gun. Microset fluid is used to take impressions of surfaces in the engineering, aerospace and manufacturing industries, usually to analyse mechanisms of component damage and failure, due to its excellent resolution for surface features (Rollins, 2001). The curing compound was left to set for 20 minutes before being carefully removed from the wells with the workpieces, producing a negative impression of the surface of the workpieces. Polycaprolactone pellets (Aldrich Chemistry, typical molecular weight 14000) were melted in a laboratory oven at 120°C for 30 minutes. Polycaprolactone was used as the substrate for reproducing the titanium alloy surfaces as it is an FDA approved biomaterial with a long history of safe use to support cell growth. The microset negative moulds were then placed into wells and the molten polycaprolactone was poured onto them and left to set for 30 minutes. These were then removed with the microset moulds.

2.3. Surface characterisation

2.3.1. Metallurgical microscopy and optical profilometry

Light microscopy was performed at a magnification of ×20, using an Olympus BX41 digital camera system microscope with Soft Imaging System GmbH 2004 (ETrainFIVE0605). A Zygo 2416A optical profiler was then used for non-contact 3-D measurements to assess the surface profile of the Ti6Al4V workpieces.

2.3.2. Atomic force microscopy

Samples were rinsed in 70% ethanol to remove surface grease and loose debris. They were attached with cyanoacrylate to ferro-magnetic bases to provide a firm couple to the microscope stage. Images were recorded in contact mode, using JPK Nanowizard II atomic force microscope with HYDRA6V-200WG SI_3N_4 probe tips. 1 image of each surface was taken over a large scale (50μm^2) and 5 further images of each surface over 5μm^2 were taken and 5 vertical and 5 horizontal cross-sections from each of these images was used to make roughness measurements using Gwyddion software.

2.3.3. Scanning Electron Microscopy

Workpieces were rinsed in 70% ethanol to remove surface grease and loose debris. Images of the workpiece surfaces were taken at 2500 and 20,000 magnification with an FEI XL30 ESEM-FEG at high vacuum, 10kV, for visual analysis.

2.3.4. X-ray Photoelectron Spectroscopy

X-ray photoelectron spectroscopy was performed using a VG ESCALAB 250 XPS at the Leeds Nanotechnology Centre (Leeds, UK) to determine the surface chemistry of the electropolished samples. The pass energy for the survey scans (whole spectrum) was 150eV and for the detailed scans (single peaks) was 20eV. Fifty passes were made to ensure detection of each element due to the low quantities of vanadium and aluminium present in the alloy. Depth profiling of the samples was conducted using a 3 kV 1mA Ar ion beam rastered over a 3mm x 3mm square, concentric with the x-ray spot. This provided an etch rate of approximately 2-2.5 Å/s. This was performed to confirm the chemical composition several nanometres below the alloy surface.

2.4. Cell culture

2.4.1. Culture of primary rat calvarial osteoblasts

Primary isolation of rat calvarial osteoblasts was performed by the initial collection of calvariae from 3-4 day old pups using sharp dissection and ensuring removal of all attached soft tissue. The tissue was washed in Hanks' Balanced Salt Solution (Sigma) and cut into 2-3mm wide strips. These were digested at 37°C for 15 minutes with shaking in 1mg/ml sterile collagenase (Sigma C-9891, crude Type IA) made up in Hanks' Balance Salt Solution with 0.1% BSA. The supernatant was then discarded to remove the initially released surface cells, as these are more likely to be fibroblasts from the soft tissue. The collagenase digestion was repeated for 30 minutes and this supernatant was reserved as Fraction 1. The calvariae were washed twice with sterile PBS and these washes were added to Fraction 1. 4mM EDTA (Sigma), made up in PBS was then added to the calvariae and shaken at 37°C for 15 minutes. The supernatant was then reserved as Fraction 2. Two washes with Hanks' Balanced Salt Solution were then added to Fraction 2. Collagenase digestion was repeated for 30 minutes and the supernatant reserved as Fraction 3 with two washes of Hanks' solution. All fractions were kept on ice after harvesting then centrifuged at 300G for 5 minutes and re-suspended in 1ml of DMEM. All three fractions were then pooled and added to 12ml of Dulbecco's Modified Eagle Medium in one 75cm^2 culture flask. Media was changed at 24 hours. DMEM was supplemented with 10% foetal bovine serum, 1mM glutamine and antibiotics (100U/ml penicillin, 100µg/ml streptomycin). Osteogenic media was made up as above, with the addition of 10nm dexamethasone (Sigma), 100µg/ml L-ascorbic acid phosphate (Sigma) and 5mM β-glycerophosphate (Sigma). Primary rat calvarial osteoblasts were cultured in 75cm^2 flasks (Corning Costar) in DMEM at 37^{o}C in a humidified atmosphere with 5% CO_2.

2.4.2. Culture of human mesenchymal stromal cells

Human mesenchymal cells retrieved from bone marrow from bone trimmed and discarded or retrieved from aspiration of the reaming cavities at the time of hip and knee arthroplasty were also cultured in the same manner. Previous work by the musculoskeletal group has demonstrated the multipotency of these cells in culture producing cells of osteogenic, chondrogenic and adipogenic lineages.

2.4.3. Passage and cell quantification

When cells reached 80-90% confluence in culture flasks they were passaged. In order to retain osteoblastic characteristics, no cells were used above passage 3. The cell monolayer in the flasks was washed thoroughly with PBS to remove all traces of media which may inhibit the action of trypsin. 2ml 0.5% trypsin solution was then added to each flask and incubated at room temperature until cells began to dissociate. 20ml pre-warmed DMEM media was then added to the flask to stop further trypsin action and the media was split between 2 new flasks for continued culture or seeding onto experimental surfaces. A Newbauer haemocytometer was used for cell counting, with 300µl culture media being added under the tightly applied coverslip.

2.5. Immunofluorescence

2.5.1. Vinculin

Primary rat osteoblasts or human mesenchymal cells were seeded at 5000 cells per well on metal workpieces or glass control cover slips (3 per experimental surface) in 24-well plates (Corning Costar) and cultured for 24 hours. Media was aspirated from wells and three washes with PBS (Dulbecco's Phosphate Buffered Saline) were performed. 4% (w/v) paraformaldehyde (Sigma) in PBS was used to fix the cells for 30 minutes at room temperature. Three further washes with PBS-Tween (0.1% v/v – Tween-20 from Sigma-Aldrich) were performed and blocking with 3% goat serum (v/v) (Sigma) in PBS-Tween was performed for 40 minutes. Anti-vinculin primary antibody, raised in mouse (Sigma), was added to the goat serum at a concentration of 1:400. This was left for 2 hours. Three further washes with PBS-Tween were performed and the secondary antibody – goat-anti-mouse (Sigma) was added in a concentration of 1:400 in PBS-Tween and left for 1 hour. Following this, washes were performed twice with PBS-Tween and once with deionised water and samples were mounted with Vectashield + DAPI (Vector Laboratories) and glass coverslips were applied. Microscopy was performed and photographs taken and analysed (Image J) using nuclei for cell counts and cells for morphology, area, polarity and focal adhesion mean area.

2.5.2. Cadherin-11

Rat primary osteoblasts were seeded at 10,000 cells per well on metal workpieces or glass control cover slips in 24-well plates (Corning Costar) and cultured until 80%

confluent, which usually occurred by 48 hours. Media was then changed to osteogenic media (as defined above) and cultured continued for a further 5 days. Medium was aspirated from wells and three washes with PBS (Dulbecco's Phosphate Buffered Saline) were performed. 4% (w/v) paraformaldehyde (Sigma) was used to fix the cells for 30 minutes at room temperature. Three further washes with PBS-Tween (0.1% v/v – Tween-20 from Sigma-Aldrich) were performed and blocking with 3% (v/v) goat serum (Sigma) in PBS-Tween was performed for 40 minutes. Anti-cadherin-11 primary antibody, raised in mouse (Abcam, UK), was added to the goat serum at a concentration of 1:250. This was left for 2 hours. Three further washes with PBS-Tween were performed and the secondary antibody – goat-anti-mouse (Sigma) was added in a concentration of 1:400 in PBS-Tween and left for 1 hour. Following this, washes were performed twice with PBS-Tween and once with deionised water and samples were mounted with Vectashield + DAPI (Vector Laboratories) and glass coverslips were applied. Microscopy was performed and photographs taken and analysed (Image J) to assess the proportion of cell perimeter stained positive for cadherin-11 per cell.

2.5.3. Toluidine blue

Polycaprolactone surfaces were seeded at 5000 cells per well in 24 well plates and cultured for 24 hours. Media was aspirated from wells and three washes with PBS (Dulbecco's Phosphate Buffered Saline) were performed. 4% paraformaldehyde (Sigma) was used to fix the cells for 30 minutes at room temperature. Three further washes with PBS-Tween (0.1% v/v – Tween-20 from Sigma-Aldrich) were performed. A 1% (w/v) Toluidine blue (Sigma) stock solution was made up in 70 % ethanol (VWR) then a working solution was made by diluting to 0.1% in a 1% (w/v) sodium chloride (Sigma) solution. 500µl of the working solution was added to each well and left at room temperature for 5 minutes. Further washes with PBS were performed until the waste solution ran clear. Photomicrographs were taken of the surfaces dry with incident light to analyse cell number, area and polarity.

2.6. Assays

2.6.1. RhoA and Rac1 assays

Primary rat calvarial osteoblasts were seeded at 100,000 cells per well in a 24–well plate onto metal workpieces and glass control surfaces and cultured in standard media for 24 hours. A commercial G-LISA™ assay kit from Cytoskeleton was used for measurement of RhoA and Rac1 activity. Cell lysates were obtained by washing surfaces with ice-cold PBS followed by the addition of 40µl ice-cold lysis buffer per well. A cell scraper was used to lyse the cells and the lysates were aspirated and transferred into eppendorf tubes, which were kept on ice then centrifuged at 10 000G at 4°C for 2 minutes. 20µl of each supernatant was transferred to another eppendorf tube with 1ml of Precision Red™ Advanced Protein Assay Reagent and incubated for 60 seconds. Protein concentrations were measured using a Sunrise spectrophotometer at 600nm and the concentrations in each sample were normalised to the lowest value by dilution with ice-cold lysis buffer.

A blank buffer sample was made using 60µl of lysis buffer, diluted with 60µl of ice-cold binding buffer in a microcentrifuge tube (Corning). A positive control sample was made by diluting 12µl of RhoA/Rac1 control protein with 48µl of cell lysis buffer and 60µl binding buffer. Both control samples were stored temporarily on ice. 100µl of ice-cold water was added to the required sample wells in the Rho plate from the kit to dissolve the precipitate within these wells. This water was removed from the plate with a vigorous flick. 50µl of sample cell lysates were added to the wells and 50µl of both blank buffer control and the RhoA/Rac1 positive control were added to duplicate wells. The plate was then placed on an orbital microplate shaker at 400rpm at 4°C for 30 minutes. The solution was removed from the plate and the wells were washed twice with 200µl of wash buffer.

200µl of the antigen presenting buffer was added to each well and incubated for 2 minutes. The solution was removed and wells washed with 200µl of wash buffer. 50µl of anti-RhoA/Rac1 antibody in a 1:250 dilution with the antibody dilution buffer was added to each well and incubated on the orbital microplate shaker at 400rpm at room temperature for 45 minutes. The solution was removed and wells washed with 200µl of wash buffer. 50µl of the secondary antibody was added to each well and incubated on

the orbital microplate shaker at 400rpm at room temperature for 45 minutes. The solution was removed and wells were washed with 200µl of wash buffer. A further incubation was performed at room temperature for 15 minutes following the addition of 50µl of HRP detection reagent to each well then 50µl of HRP stop buffer was added to stop the reaction. The plate was then read on a Sunrise spectrophotometer at 490nm.

2.6.2. ROCK inhibition

Osteoblasts were seeded at 50000 cells per well in a 24-well plate and incubated for two days in standard medium and a further 5 days in osteogenic medium. On day 7, specific inhibitors of ROCK were added and incubation continued for a further 24 hours. The inhibitor used was Y27632 (TOCRIS) at 0.1µM. Previous experiments using serial dilutions of the inhibitor demonstrated the effectiveness of this concentration without lethal effects on the cells, as demonstrated by MTT assay.

2.6.3. Rac1 inhibition

Osteoblasts were seeded at 50000 cells per well in a 24-well plate and incubated for two days in standard medium and a further 5 days in osteogenic medium. On day 7, specific inhibitors of Rac1 were added and incubation continued for a further 24 hours. The inhibitors used were NSC23766 (TOCRIS, US) at 10µmol concentration. Previous experiments using serial dilutions of the inhibitors demonstrated the effectiveness of these concentrations without lethal effects on the cells, as demonstrated by MTT assay.

2.6.4. Alkaline phosphatase assay (p-nitrophenol)

Cells were cultured on metal workpieces or glass cover slips in 24-well plates, initially in standard DMEM media then for 14 days following change to osteogenic media. Media was aspirated and three washes with PBS were performed. 1ml of 4% (w/v) paraformaldehyde was added to each well and left for 10 minutes to achieve fixation. Two further washes with PBS were then carried out, followed by one with 0.1M Tris at pH 8.3 to alkalinise the samples. 500µl Alkaline phosphatase substrate (pNPP) (Sigma-Aldrich) was then added to each well of the plate and left to incubate for 15 minutes until a yellow colour developed. Two samples of 100µl of this liquid were then transferred to wells in a 96 well plate, which were read at 405nm in a Sunrise plate reader (Tecum). Surfaces were then washed again twice with PBS and mounted with

Vectashield + DAPI (Vector Laboratories) and glass coverslips were applied for fluorescence microscopy to count cell nuclei per field.

A standard curve for absorbance, allowing calculation of amount of p-nitrophenol from known absorbance was constructed using serial dilutions of p-nitrophenol in a 96 well plate. Dilutions were of 1:2 of the contents of the preceding well diluted with 0.1M Tris pH 8.3. This was read at 490nm with a Sunrise plate reader.

2.6.5. Bone nodule assay (alizarin red)

Cells were cultured on metal workpieces or glass cover slips in 24-well plates, initially in standard DMEM media then for 28 days following change to osteogenic media. Media was aspirated and three washes with PBS were performed. 1ml of 4% (w/v) paraformaldehyde was added to each well and left for 15 minutes to achieve fixation. Three further washes with PBS were carried out then 200µl of alizarin red stain was added to each well. The stain was left on for 5 minutes, followed by repeated washes with PBS until the wash remained clear then the samples were left to dry before being photographed for assessment of percentage surface coverage with bone nodules. The dry samples were moved to new 24-well plates. 500µl 2% sodium dodecyl sulphate (SDS) was added to each well and left for 12 hours. 100µl from each well was then aspirated and added to a 96 well plate, which was read at 520nm on a Sunrise plate reader.

2.7. Molecular biology

2.7.1. Total RNA extraction

Cells were cultured on metal workpieces or glass control cover slips in 24-well plates. Medium was aspirated from wells and three washes with PBS were performed. 1ml of Trizol reagent was added to the top line of wells and repeatedly pipetted onto the surfaces to encourage homogenisation of the cell components. The procedure was repeated using the initial measure of Trizol in the other wells containing the workpieces with the same surface treatment. Following the last well, the Trizol was pipetted into an Eppendorf tube and incubated at room temperature for 2 minutes. 200µl chloroform was then added to each Eppendorf and the tubes were agitated by hand for 15 seconds. They were then centrifuged at 12,000rpm for 15 minutes. The colourless aqueous phase

containing the RNA was then carefully removed by pipette and added to new Eppendorf tubes. 500µl propan-2-ol was then added to each tube and they were stored in the -20°C freezer.

2.7.2. RNA quantification

RNA samples extracted using the method above were removed from -20°C storage and thawed. They were then centrifuged at 13,000rpm for 15 minutes. The supernatant was aspirated leaving the RNA pellet, to which 1ml of 70% ethanol was added. The samples were then centrifuged again at 13,000rpm for 3 minutes. The supernatant was again aspirated and the RNA pellet was left to air dry, before adding 20µl of DEPC-treated water. The samples were placed in a water bath at 65°C for 5 minutes to re-suspend the RNA. At this stage 1 µl of each sample was added to another Eppendorf tube and made up to 50µl with DEPC-treated water. The concentration of RNA in the samples was then measured on the Nanodrop equipment in order to calculate the necessary volume of RNA to make 2µg of cDNA.

2.7.3. cDNA synthesis

This calculated volume of RNA sample was added to new tubes and made up to 9µl total volume with DEPC-treated water. 1µl of oligo(DT) primer (Invitrogen $Oligo(dt)_{12-18}$ primer 0.5µg/µl) and 2µl of dNTP (Invitrogen Nucleotide kit 10mM) were added to each tube. The tubes were then placed in a water bath at 65°C for 5 minutes and then into ice. 4µl of cDNA synthesis buffer (Invitrogen 5× cDNA synthesis buffer), 1µl of DTT (Invitrogen 0.1M), 1µl of RNAse inhibitor (Invitrogen RNaseOUT recombinant RNAse inhibitor 40U/µl), 1µl of cloned AMV reverse transcriptase (Invitrogen 15U/µl) and 1µl of DEPC-treated water were added to each tube and they were incubated at 50°C for 60 minutes. Following this, 30µl of DEPC-treated water was added and they were placed in the -20°C freezer for storage.

2.7.4. Real-time polymerase chain reaction

cDNA samples were retrieved from the -20°C freezer and thawed at room temperature. Real-time PCR reaction mixture was made up according to the manufacturers instructions to a total volume of 20µl for each reaction in each well of a 96-well microamp plate (Applied Biosystems, UK) using 2µl of cDNA, 7.2µl distilled water,

0.4µl of each primer (5µM) (Sigma-Aldrich) and 10µl SYBR green Advantage PCR mix (Clontech). Distilled water was used instead of cDNA for the negative control. The plate was then covered with an adhesive lid (Applied Biosystems, UK) and placed in the real-time thermal cycler 7900HT Fast Sequence Detector (Applied Biosystems, UK). The cycle conditions were as follows:-

- 10s at 95°C
- 40 cycles of 5s at 95°C and 30s at 60°C

The following conditions were used to produce a dissociation curve at the end of the run, ensuring experimental values represented amplification of a single product only:-

- 15s at 95°C
- 1 min at 60°C
- 15s at 95°C

Gene	5' primer	3' primer
GAPDH	GCAAGAGAGAGGCCCTCAG	TGTGAGGGAGATGCTCAGTG
Runx2	GATGATGACACTGCCACCTCT	AAAAAGGGCCCAGTTCTGA
Osterix	TCACACCCGGGAGAAGAA	GCTGATGTTTGCTCAAGTGG
Osteocalcin	GAGCTCACACACCTCCCTGT	CTACCTCAACAATGGACTTGGA
Cadherin-2	CAGAGAGTCGCCAAATGTCA	TTCACAAGTCTCGGCCTCTT
Cadherin-11	GCCAACAGCCCAATAAGGTA	TGTGGATTTCTGCTGCAAAG

Table 1: Sequences for primers used in SYBR green real-time PCR (rat cells)

For analysis of the real-time PCR data, a cycle threshold (Ct) value, within the reaction exponential phase, of 50 relative fluorescent units (RFU) was set for all assays. Transcript expression was normalised relative to a reference gene (GAPDH). To calculate normalised expression, the ΔCt method was used:-

$$\text{Relative transcript level} = 2^{-(\text{control reference gene Ct-control target gene Ct})}$$

2.8. In vivo experiments

In vivo experiments were performed to study the osseointegration of the experimental surfaces in a living model.

2.8.1. Rat model

24 male CD rats (Figure 14) of 400-500g weight were used in this project. CD rats were chosen due to ease of obtaining specimens of the requisite size. They were procured from Charles Rivers 14 days prior to surgery for acclimatisation. They were housed in groups of 4 and fed a standard diet.

Figure 14: CD rat

2.8.2. Animal surgery

Induction of anaesthesia was by inhaled isoflurane in an enclosed box (Figure 15).

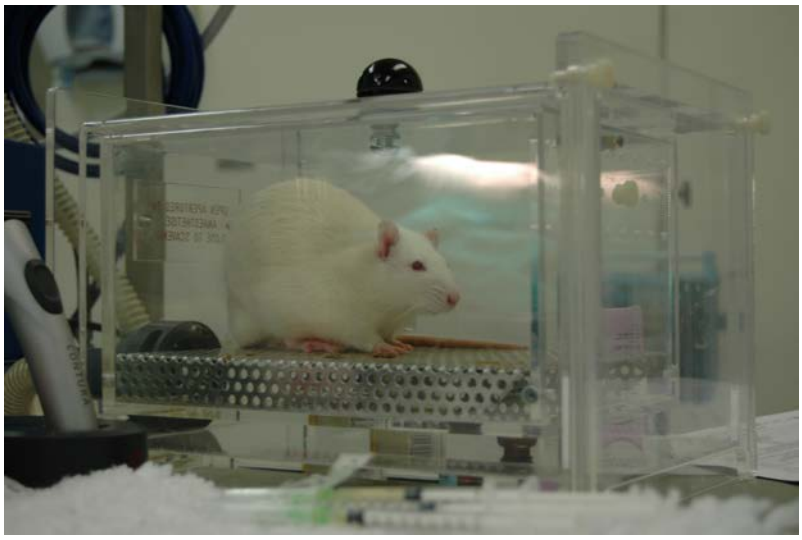

Figure 15: Induction of anaesthesia

Depth of anaesthesia was maintained using inhaled isoflurane through a face mask (Figure 16).

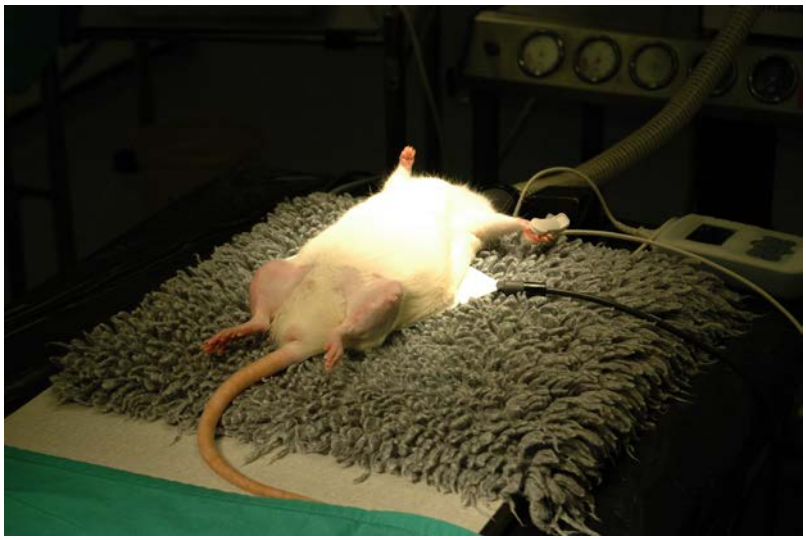

Figure 16: Rat under anaesthesia on a face mask

Analgesia using buprenorphine 0.05mg/kg (Vetagesic Multidose 0.03mg/ml, Reckitt Benkeiser) and meloxicam 1mg/kg (Metacam 5mg/ml, Boehringer Ingelheim) was administered at the time of induction, intraperitoneally. The legs were shaved bilaterally from groin to ankle. Skin preparation was with chlorhexidine in alcohol solution. A 2cm incision was made over the medial aspect of the knee joint (Figure 17). The joint line was identified and the gastrocnemius muscle reflected subperiosteally in a posterior direction.

Figure 17: Skin and muscle dissection

The tibial tuberosity was identified and used as a landmark for the drill hole (Figure 18). A 2mm drill hole was made horizontal to the joint line through both cortices.

Figure 18: Pilot hole for implant drilled with 2mm drill

The experimental implant was then inserted and trimmed flush with the bone (Figure 19).

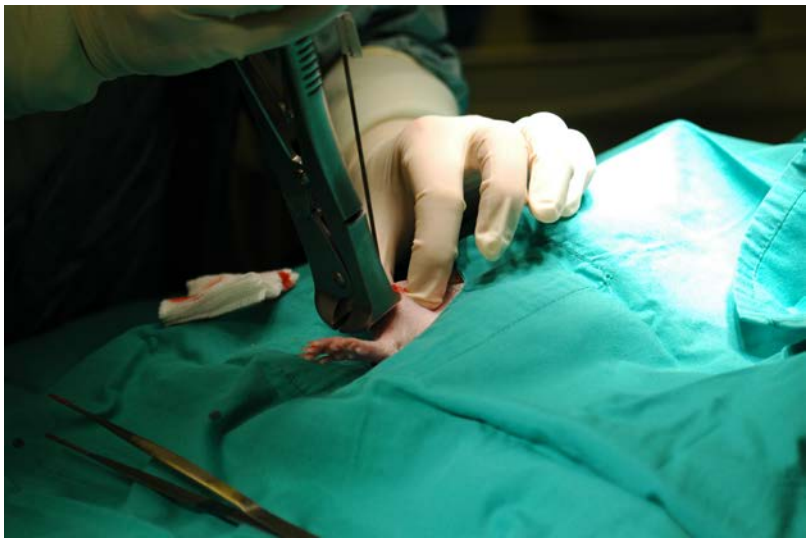

Figure 19: Implant insertion and trimming with wire cutters

Haemostasis was achieved (Figure 20).

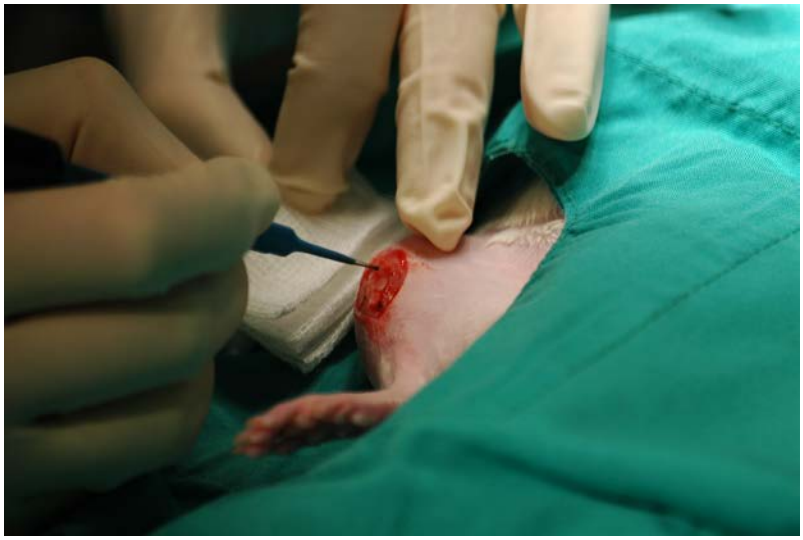

Figure 20: Haemostasis with bipolar diathermy

Muscle edges and skin were closed in layers with 4-0 vicryl (Ethicon Inc.) and 9mm skin staples (Ethicon) (Figure 21).

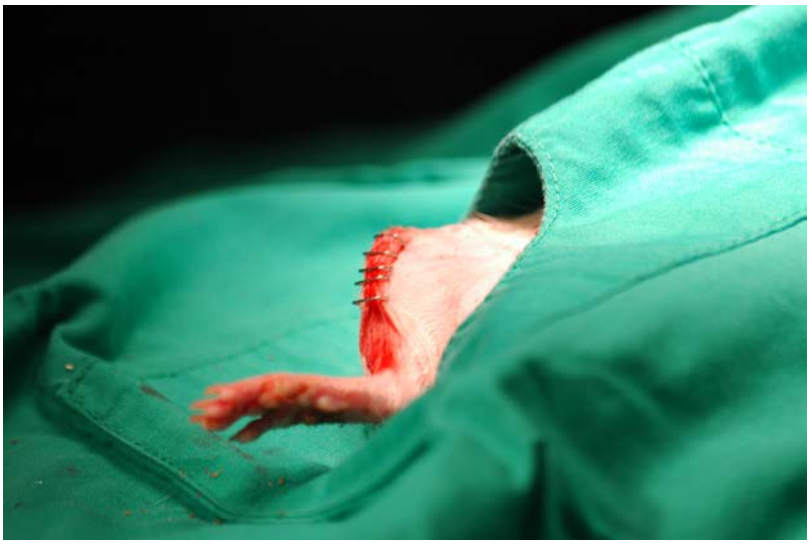

Figure 21: Closure with Ethicon skin staples

The procedure was then repeated on the opposite tibia (Figure 22).

Figure 22: Rat following procedure completion

Instrument tips were sterilised using a hot bead steriliser between cases. Rats were recovered in incubators at 30°C for 2 hours. Skin clips were removed at 5 days. Experimental implants with two different surface finishes were implanted in each tibia to minimise disruption to the experimental design if animals were lost during the time course.

Animals were marked using sequential ear notching to signify which surfaces had been implanted. Further analgesia with buprenorphine 0.05mg/kg was administered 12 hours and 24 hours post procedure. Animals were inspected daily in the post-operative period for behaviour indicating distress and weighed every 2 days with plans in place for euthanasia if behaviour or weight loss outside of that specified in the project license was observed.

Animals were euthanised at the end of 3 weeks and both tibias retrieved by extension of the original surgical incision, disarticulation at the knee and transaction of the tibia and fibula above the ankle. Samples for mechanical testing were stored fresh in normal saline-soaked gauze for immediate testing. Samples for histomorphometry and micro-CT were fixed in 10% formalin (Sigma).

2.8.3. Histomorphometry

Explanted tibias were fixed in 10% formalin (Sigma) overnight. The samples were then dehydrated with increasing concentrations (v/v) of ethanol (25%, 50%, 75%, and 90%) for 30 minutes at each concentration. This was followed by 3 changes of 100% ethanol for 30 minutes each.

For resin embedding, the samples were agitated in a 1:1 mixture of 100% ethanol and methylacrylate resin (75% methyl methacrylate, 25% butyl methacrylate – Sigma Aldrich) for 72 hours. Further agitation for 48 hours was performed in 100% methacrylate resin. This was then changed to 100% methacrylate resin containing 1% w/v benzoyl peroxide (Sigma Aldrich) and the samples were incubated overnight at 60°C for the resin to polymerise. 500µm sections were cut perpendicular to the axis of the bone using a diamond-edged cutting blade (Accutom-5, Struers). The sections were then stained with giemsa and silver nitrate.

2.8.4. Micro-CT

Computerised tomography scans were performed by Mr Nick Corps on a SkyScan 1176 high resolution in-vivo scanner at 90kV and 150µA with a 1mm Al / 0.1mm Cu filter, producing a reconstructed pixel size of 9µm. Samples were scanned in formalin, stored in micro-centrifuge tubes (Corning).

2.8.5. Mechanical testing

Rat tibias were recovered using sharp dissection following euthanasia of the experimental animals by CO_2 inhalation. The samples were trimmed to fit an adjustable clamp and positioned with the implant perpendicular to the apparatus base. Mechanical push-out testing was performed using an Instron mechanical testing apparatus with a 2mm diameter indenting tip (Figure 23). The tip was advanced using at 1mm per minute. Stress/strain curves were produced and force required for failure of the bone-implant interface recorded.

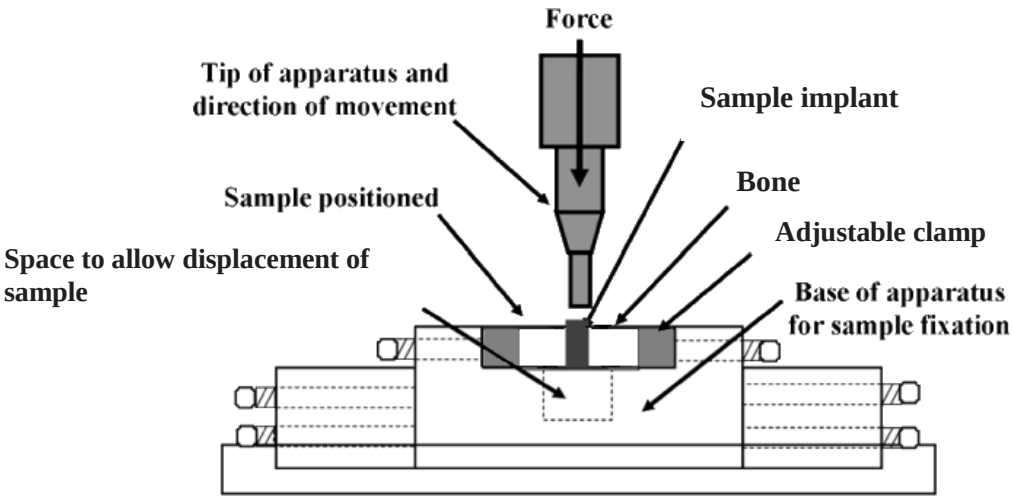

Figure 23: Mechanical testing apparatus. Image adapted from Teixeira et al. Journal of Applied Oral Science, 2009.

2.9. Statistical analysis

Minitab version 15 was used for all statistical analysis. All data was found to be normally distributed as tested using the Shapiro-Wilk test. One way analysis of variance was used with Tukey's pairwise comparisons at 95% confidence to compare the means of the data sets.

Chapter 3. Results 1 – Electrochemical modification of Ti6Al4V produces structured surfaces that influence cell morphology

3.1. Introduction

Electrochemical modification provides an economical and scalable method of forming reproducible changes to topography and chemistry on the surface of a bulk metal. Previous work by others in the group has provided data for optimisation of the electrolyte composition and identified a useful range of time and voltage parameters (Nouraei, 2008). Initial experiments during the development of the process began with a 2M sulphuric acid in methanol electrolyte at 3 and 5 V. The workpieces used were commercially pure titanium foils without mechanical polishing to a mirror finish, therefore the existing topography on the surfaces before electrochemical modification made a significant contribution to the resultant topography (Birch et al, 2012). The titanium alloy most frequently used in orthopaedic implants was used in the current series of experiments to improve the applicability of the results to a clinical situation. Further, the workpieces used in the current experiments were cylinders, which allowed improved mechanical polishing. The first step is plane grinding – so called because it leave the surface all on one level, removing pre-existing imperfections and the effects of previous treatment and machining. This is achieved using coarse grit silicon oxide papers. This was followed by fine grinding, using progressively finer grits of paper to achieve a macroscopically mirror finish (Struers Knowledge). Further experiments demonstrated improved polishing conditions and reproducibility with a 3M sulphuric acid and methanol electrolyte and higher voltages (7-9V) (Yang 2005, Ngalim 2007).

This process produces features on the titanium surface at the submicron and nanometre scales, altering the roughness characteristics of the surface as a whole, which can be demonstrated using SEM, AFM and optical profilometry.

Several previous papers have demonstrated effects of modifying titanium and titanium alloy surfaces on the growth and differentiation of osteoblasts. Surface micron-scale topography presents cells with features that are larger than the area of a single cell and can physically prevent cell-cell communication behaviour (Kirmizidis and Birch 2009). Topography of this scale has been demonstrated to influence early cell attachment (Bowers et al. 1992), cell morphology (Anselme et al. 2002) and mineralised matrix

deposition (Boyan et al. 2002). Increased mineralised matrix deposition has been observed in osteoblasts cultured on nanophase titanium alloy, in comparison to those cultured on microphase alloy (Ward and Webster 2006). Titanium surfaces which can modulate the behaviour of osteoblasts have potential clinical applications in orthopaedics and implant dentistry. Many existing implants already employ acid etching or grit-blasting processes in order to create larger features that promote macroscopic ingrowth of bone. Electrochemical modification can be applied to manipulate cell behaviour at a smaller scale.

Cell morphology is one of several modalities that can give insight into the effect of biomaterial surface properties on cell activity and hence tissue response. Vinculin is a cytoskeletal protein found at focal adhesion complexes, which acts to link integrin adhesion molecules with the actin cytoskeleton. Immunofluorescence staining for vinculin therefore allows an appreciation of both the cell morphology as a whole and more specifically the size and distribution of focal adhesion complexes. These are collections of large molecules which connect the cell with the extracellular matrix, transduce mechanical stress and influence other regulators and are therefore likely to be implicated in any cellular response to the underlying surface. Both rat osteoblasts and human mesenchymal cells from multiple donors were used in these experiments. Rat osteoblasts are a commonly used in vitro model found in the existing literature on cell-surface interactions and allow us to assay the ability of cells to lay down mineralised matrix on the surface, whereas human mesenchymal cells provide further insight into cell behaviour in potential clinical applications.

The effect of surface treatment on bone cell behaviour can also be studied through the quantification of alkaline phosphatase activity. This is an enzyme which is a marker of osteoblast activity due to its role in matrix mineralisation. Formation of mineralised bone nodules is a demonstration of the presence and activity of mature osteoblasts and can be investigated with analysis of images of macroscopic bone nodules and by quantification by spectrophotometer of solubilised alizarin red dye, which stains mineralised matrix present in the bone nodules.

Both surface topography and surface chemistry have been found to independently influence cell growth and behaviour on modified surfaces. Very rough surfaces allow macroscopic ingrowth of bone. Several studies have suggested a role for micron-scale roughness in improved osteoblast proliferation and differentiation (Anselme et al, 2002; Boyan et al, 2002; Att et al, 2007). Defined nano-scale topographies have been shown to improve adsorption of protein onto treated surfaces and improve osteoblast adhesion (Biggs et al, 2007b; Dalby et al, 2007).

In this chapter, the modified titanium alloy surfaces are characterised with regard to surface morphology using light microscopy and optical profilometry, Scanning Electron Microscopy, Atomic Force Microscopy and using X-ray Photoelectron Spectroscopy to elucidate the chemistry of the surface oxide layers. The short term morphology and behaviour of osteoblasts are investigated using immunofluorescence. Polymer casts of modified titanium alloy surfaces have been used in these experiments to attempt to delineate the effects, on cell morphology, of surface topography in isolation from changes to surface alloy chemistry. Longer term osteoblast behaviour is determined using alkaline phosphatase assay and alizarin red staining for bone nodules.

The aims of this section of experiments were:-

- To characterise the topography and chemistry of the modified titanium alloy surfaces using light microscopy, SEM, AFM and XPS
  To characterise changes in cell morphology of rat osteoblasts and human mesenchymal cells cultured on the modified surfaces using immunofluorescence
- To measure differentiation of rat osteoblasts and human mesenchymal cells on the modified surfaces using alkaline phosphatase and bone nodule assays

3.2. Surface characterisation

3.2.1. Current profiles

Chronoamperometry was the electrochemical method used to perform the electrochemical modification of the titanium alloy surfaces. This required a three electrode system, with use of a reference electrode for measurement of current, at the working electrode, required to maintain a constant voltage, against time. The graphs below (Figure 24) use current density as a function of time to allow a meaningful comparison between the current profiles during modification of the 2D and 3D alloy substrates, controlling for the different cross-sectional areas.

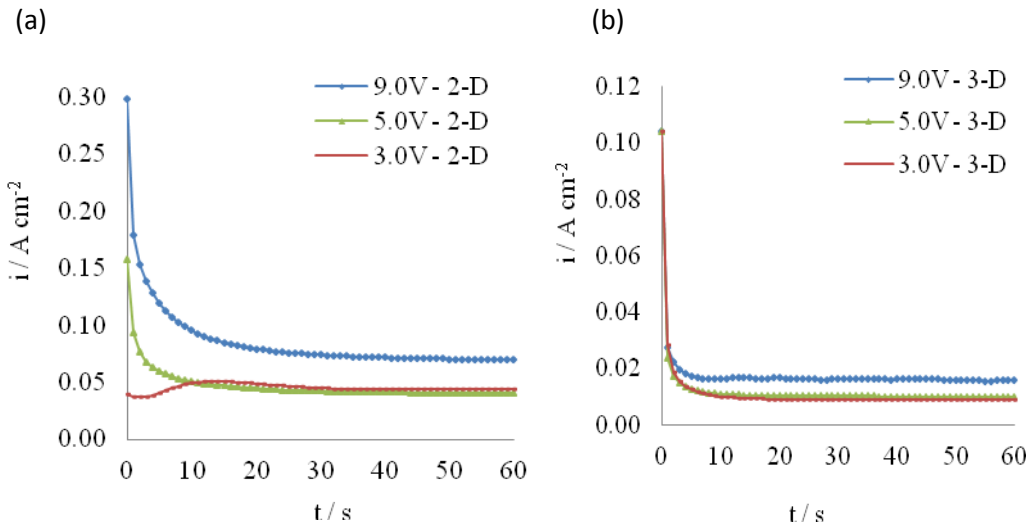

Figure 24: Chronoamperometry data for 3,5 and 9V electropolishing on (a) 2D substrates and (b) 3D substrates

These graphs (Figure 24) plot the current density against time, during polishing at 3, 5 and 9V, as a result representative of 3 experiments. As anticipated with a pulsed electrochemical technique, there is a high charging current, which decays exponentially with time. By comparing the two graphs it is possible to demonstrate that the current densities seen when polishing at 3 and 5V on the 2D and 3D surfaces were very similar. Although the shape of the chronoamperometry curve was the same for 2D and 3D electropolishing at 9V, the current density was higher at all time points for 2D polishing. The shape of the curve represents a high initial charging current falling to a plateau due to the formation of the surface oxide layer.

3.2.2. Light microscopy and optical profilometry

To assess the surface topography of the titanium alloy samples produced in the study, reflected light microscopy and optical profilometry analysis was performed.

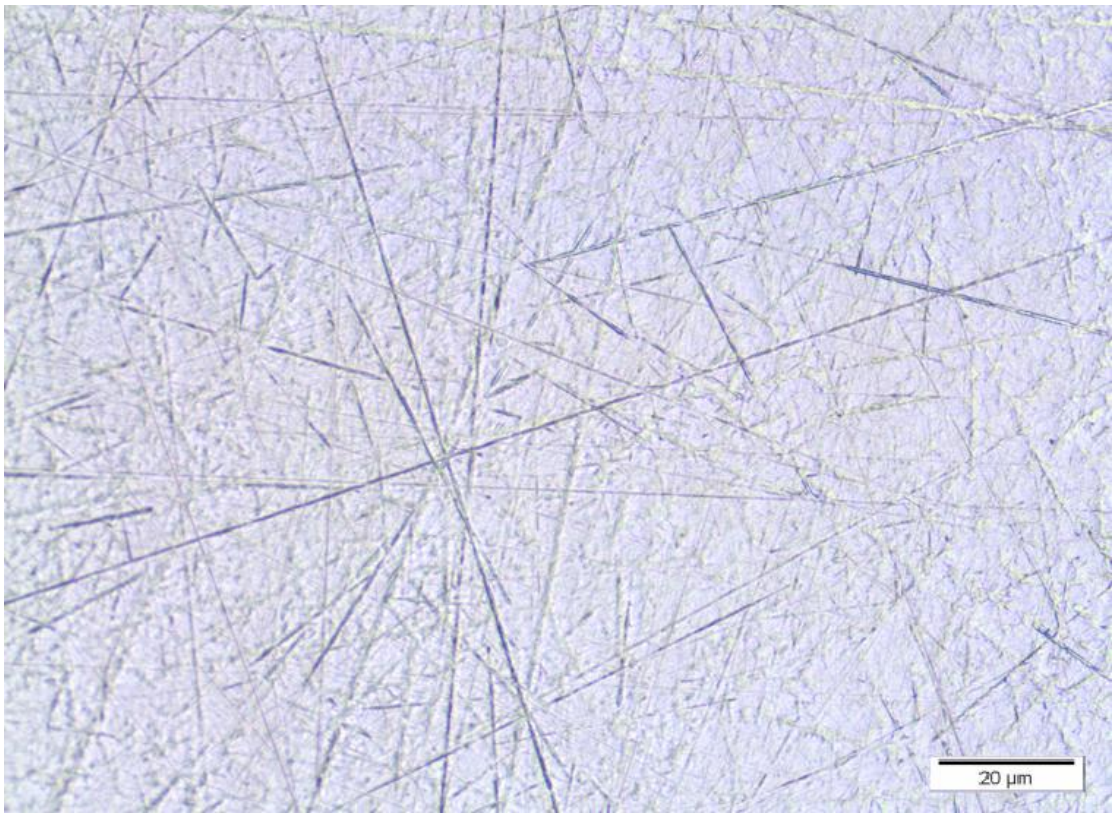

Figure 25: Photomicrograph of mechanically polished surface with reflected light microscopy

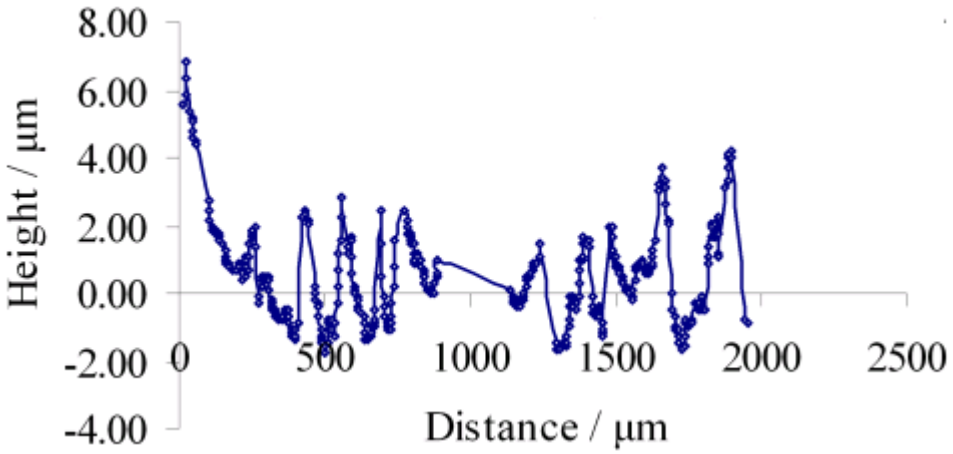

Figure 26: Optical profile of mechanically polished surface (representative of 5 independent experiments)

Analysis of the polished specimens (Figure 25) illustrates the presence of grooves due to the mechanical polishing process. Even with the use of sequential grinding papers

down to a very fine grit of 4000, it was not possible to eliminate these grooves completely, simply using the mechanical process. The optical profile (Figure 26) confirms the morphology of these grooves, there being 11 over the distance of 2mm in this profile, with most being between 4 and 6μm in depth.

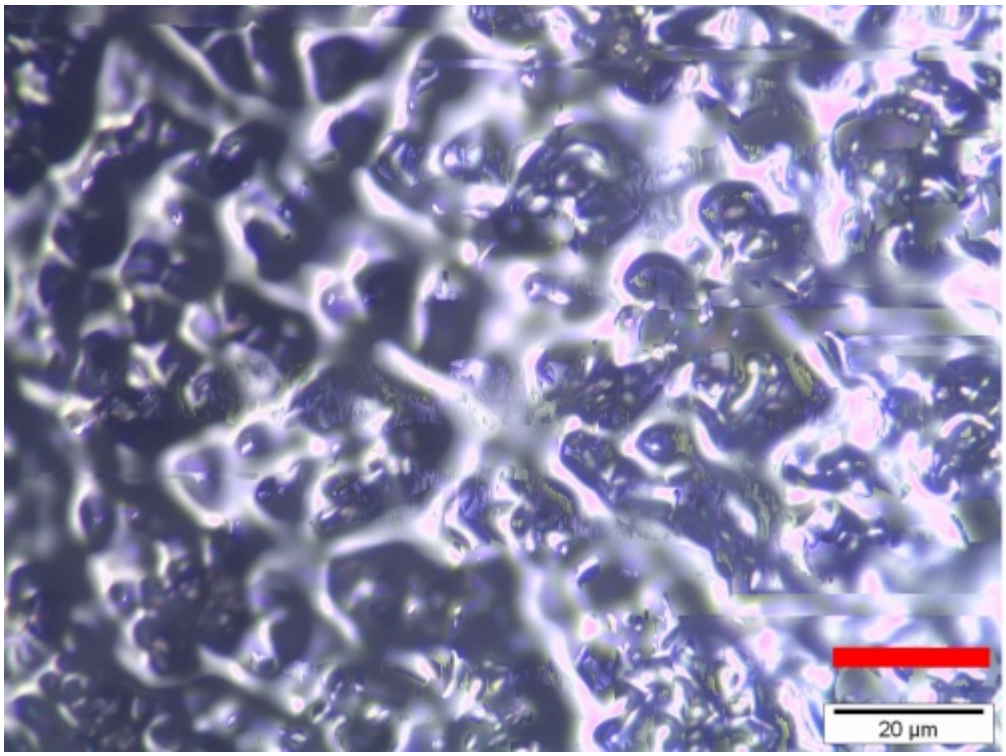

Figure 27: Photomicrograph of 3V180s surface with reflected light microscopy

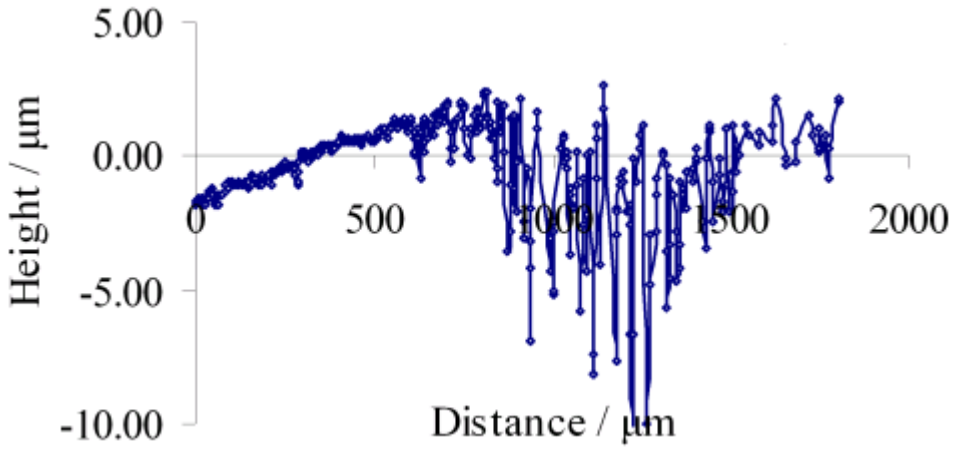

Figure 28: Optical profile of 3V180s surface

Analysis of specimens treated at 3V for 180 seconds (Figure 27) demonstrates a surface which is amorphous in character with large features of peaks and valleys of around 10-

12µm in height which are superimposed with smaller features of less than 1µm (Figure 28).

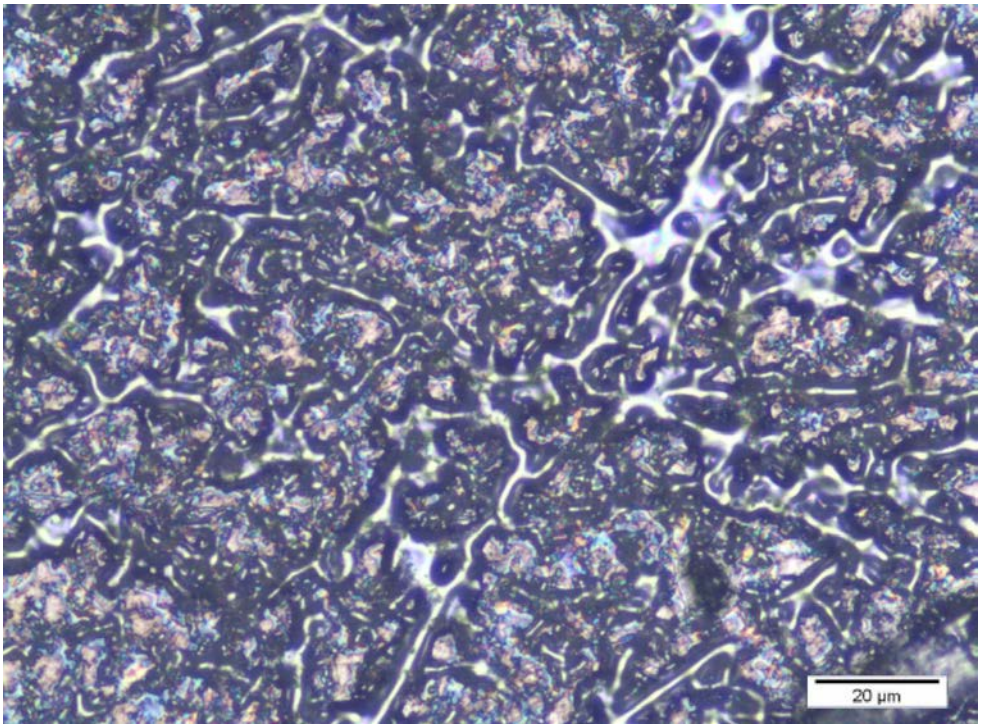

Figure 29: Photomicrograph of 5V60s surface with reflected light microscopy

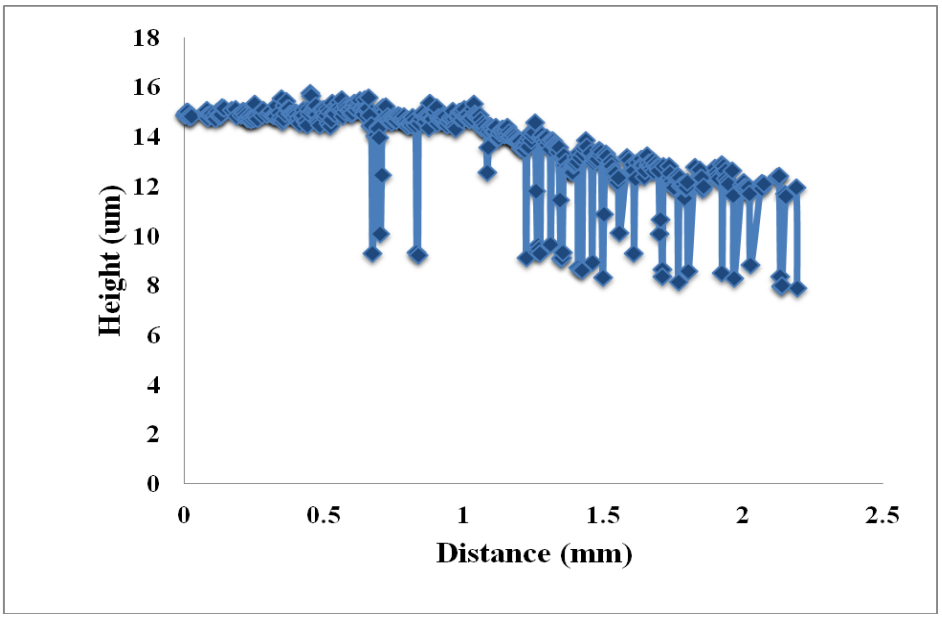

Figure 30: Optical profile of 5V60s surface

Reflected light microscopy of surfaces treated at 5V for 60 seconds again reveals amorphous surface features (Figure 29) with peak and trough features of 4-6µm spaced

several microns apart, interspersed with smaller features of less than 1µm in height (Figure 30).

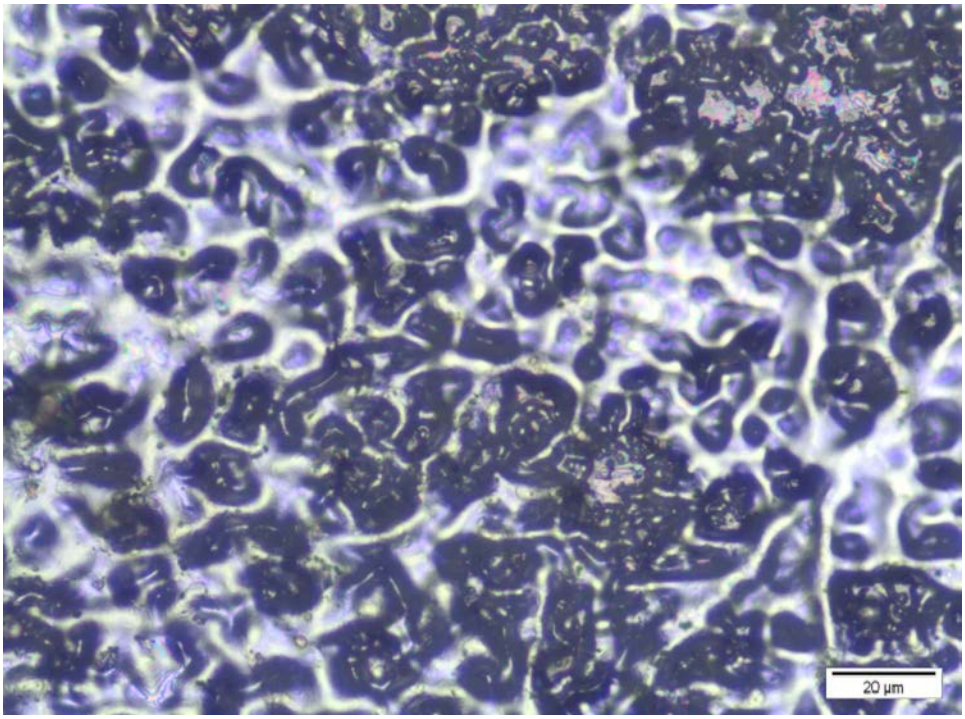

Figure 31: Photomicrograph of 5V120s surface with reflected light microscopy

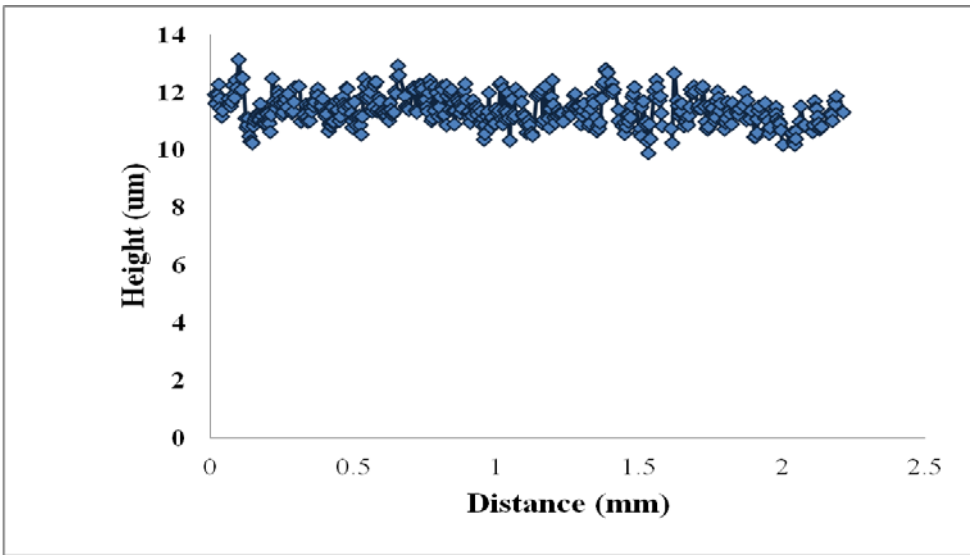

Figure 32: Optical profile of 5V120s surface

The amorphous features of 5V120s treated surfaces (Figure 31) are smaller and smoother, with most features being measured in the 1-3µm range (Figure 32).

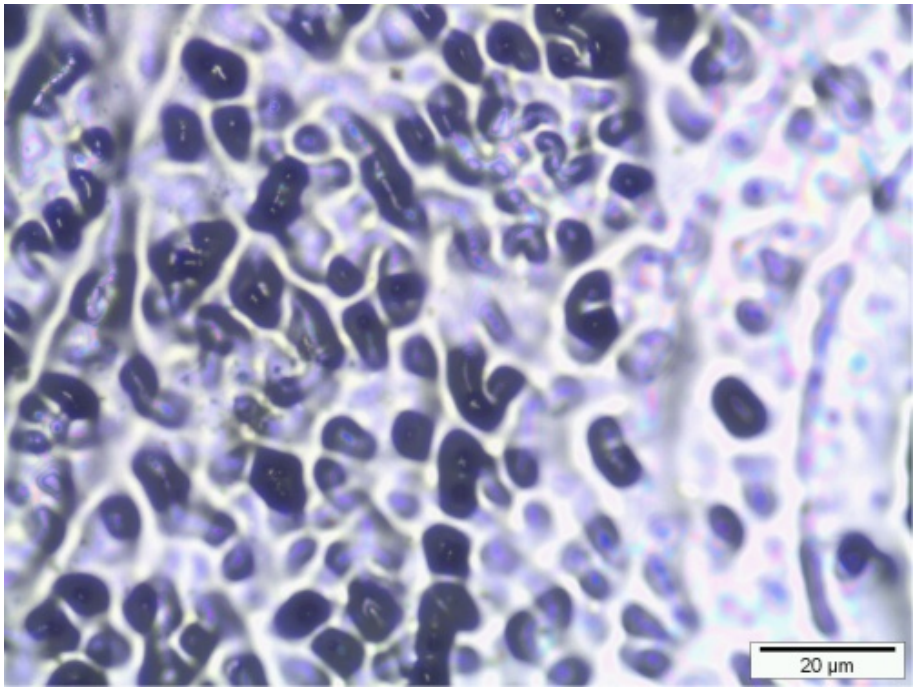

Figure 33: Photomicrograph of 5V180s surface with optical microscope

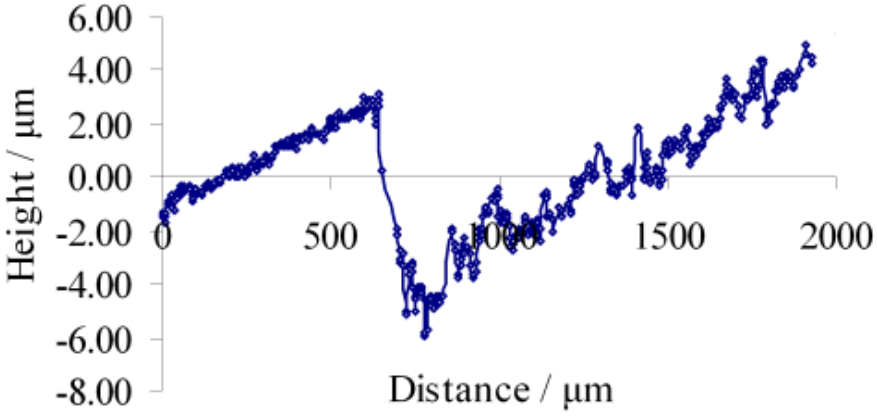

Figure 34: Optical profile of 5V180s surface

Figure 33 illustrates the appearance of the 5V180s treated surfaces, which are smoother overall than the 5V60s treated surfaces. Figure 34 demonstrates this smoother transition of the larger features of 8-12µm, with fewer appearing per 2mm profile and fewer smaller peaks of less than 1µm.

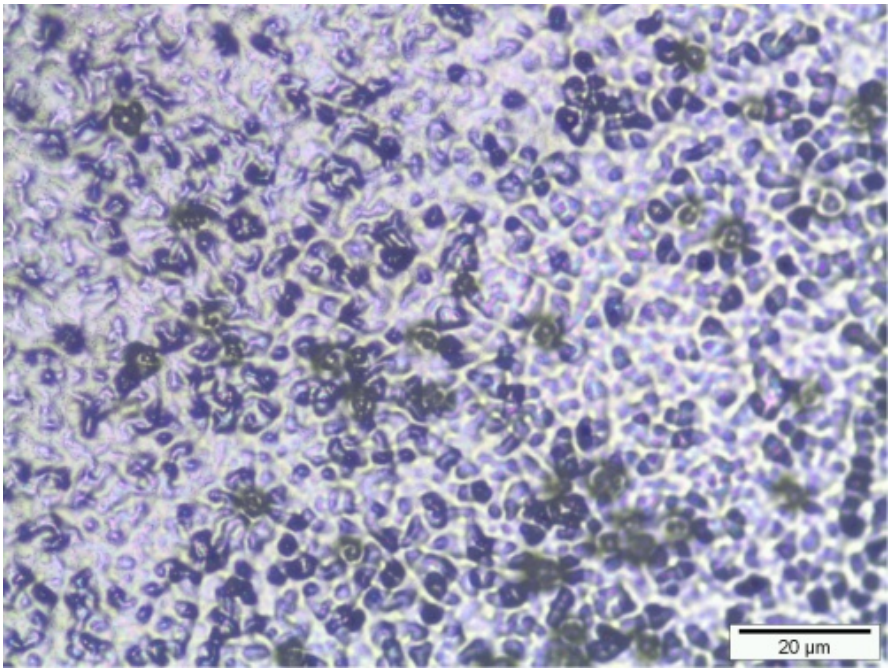

Figure 35: Photomicrograph of 9V60s surface with optical microscope

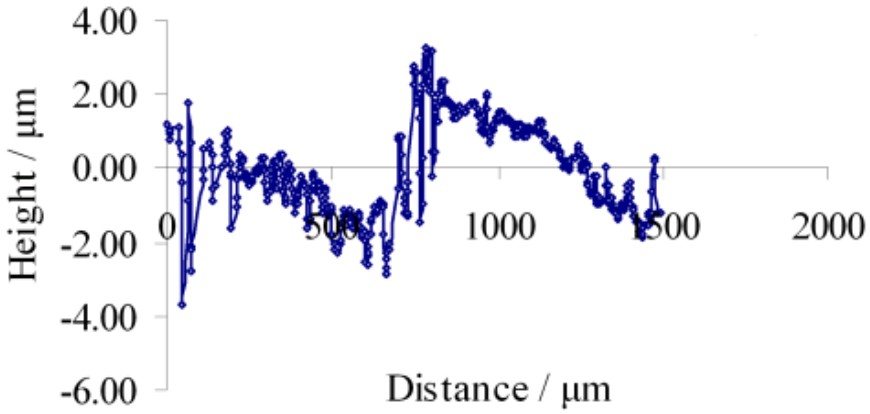

Figure 36: Optical profile of 9V60s surface

Most of the features present on the 9V60s treated surface (Figure 35) are smaller in height (1-6 µm) and there were more small features per 2mm profile than those produced on the 5V treated surfaces (Figure 36).

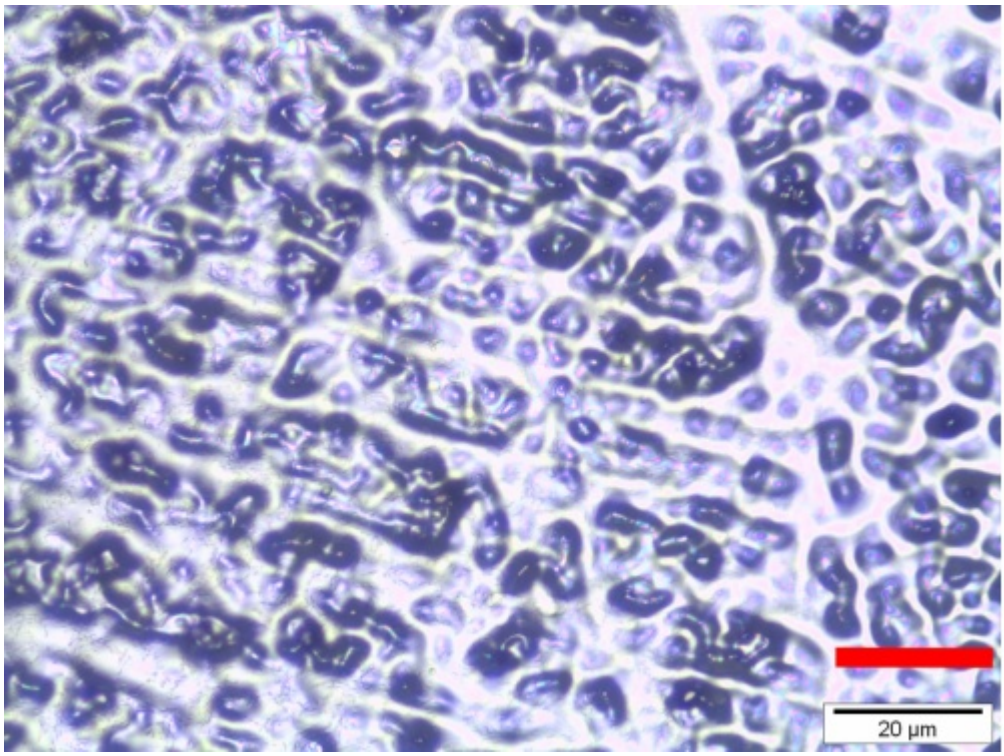

Figure 37: Photomicrograph of 9V120s surface with optical microscope

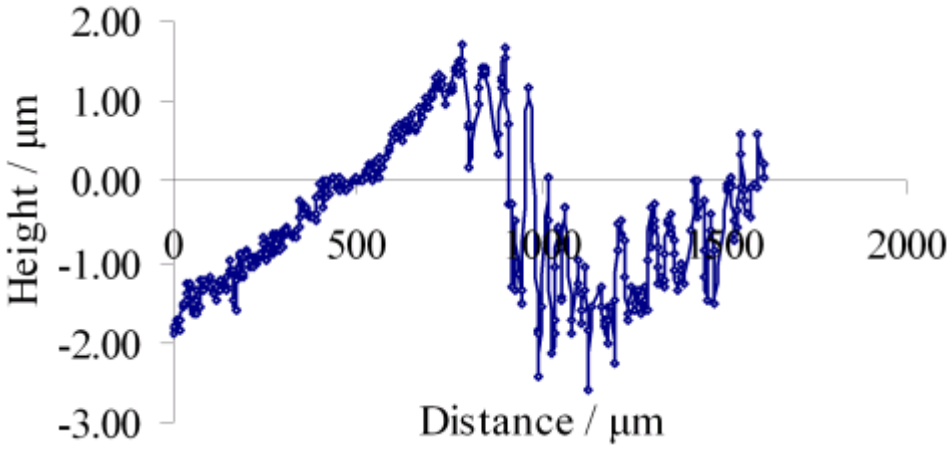

Figure 38: Optical profile of 9V120s surface

Surfaces treated at 9V for 120s are smoother (Figure 37), with the larger features 4-5µm in height and 500-1000µm in width and multiple smaller features of less than 1µm (Figure 38).

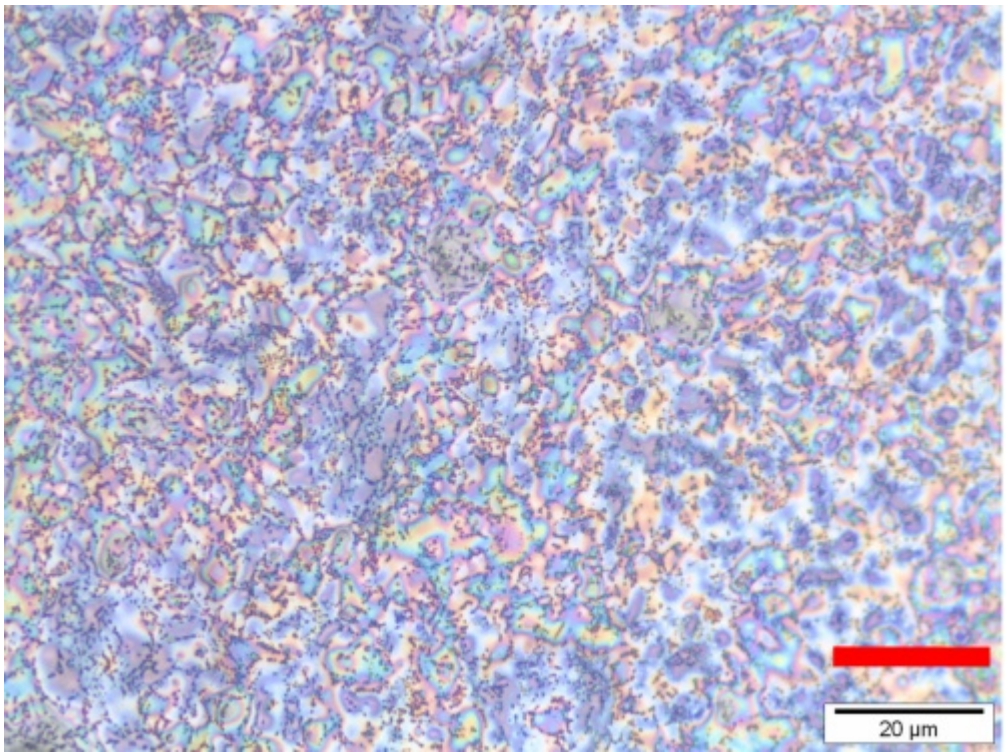

Figure 39: Photomicrograph of 9V180s surface with optical microscope

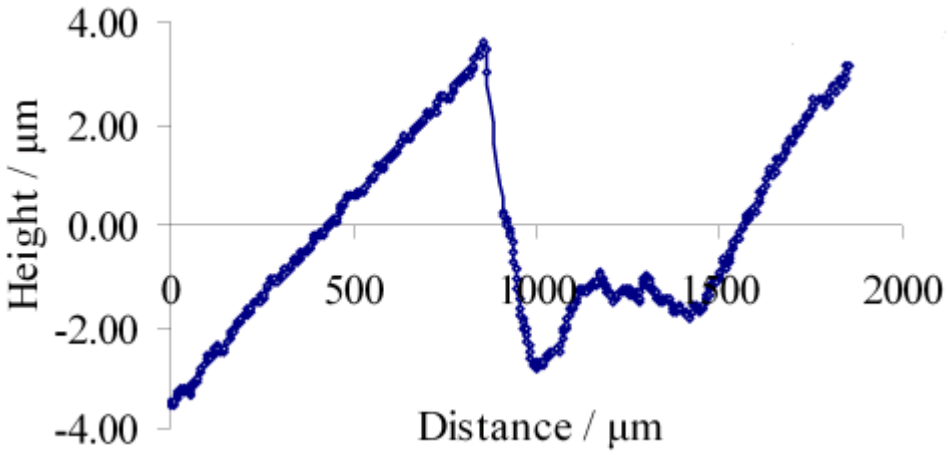

Figure 40: Optical profile of 9V180s surface

When surfaces were treated at 9V for 180s, the surface had much smaller features with altered reflection of visible spectrum light (Figure 39). The average roughness of the surfaces was lower, with fewer 1µm features between the larger 6-8µm features (Figure 40).

3.2.3. Atomic Force Microscopy

Atomic force microscopy (AFM) was used to provide a visual interpretation of the features of the titanium alloy surfaces at the submicron level. This technique could also be used to produce height profiles of the surfaces, with all profiles below being representative of 10 profiles (5 taken in 2 orthogonal directions).

Figure 41: 50µm^2 2D image of mechanically polished surface obtained in contact mode using JPK Nanowizard II atomic force microscope with HYDRA6V-200WG SI_3N_4 probe tips.

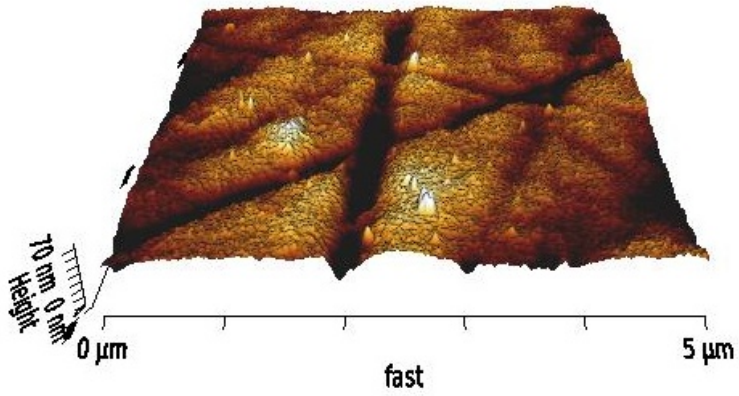

Figure 42: 5µm^2 3D image of mechanically polished surface obtained in contact mode using JPK Nanowizard II atomic force microscope with HYDRA6V-200WG SI_3N_4 probe tips.

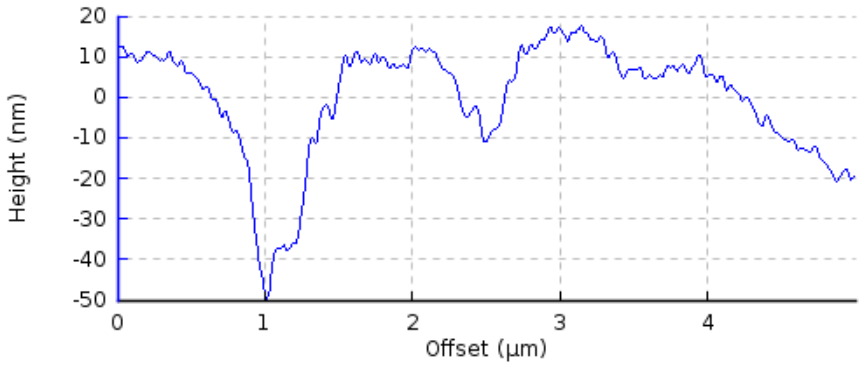

Figure 43: Sample height profile taken from horizontal measurements on a mechanically polished surface over 5µm.

The above profiles generated by atomic force microscopy of the mechanically polished surface show that the grooves produced by the polishing are also seen at the sub-micrometre scale. In depth, these grooves were between 10 and 60nm and were randomly distributed in orientation and spacing.

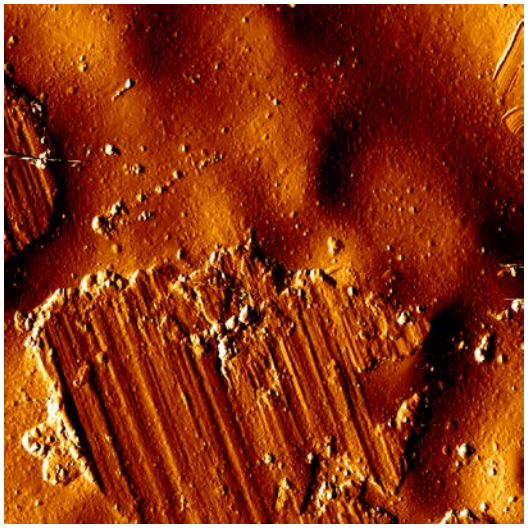

Figure 44: 50µm^2 2D image of 3V180s surface obtained in contact mode using JPK Nanowizard II atomic force microscope with HYDRA6V-200WG SI_3N_4 probe tips

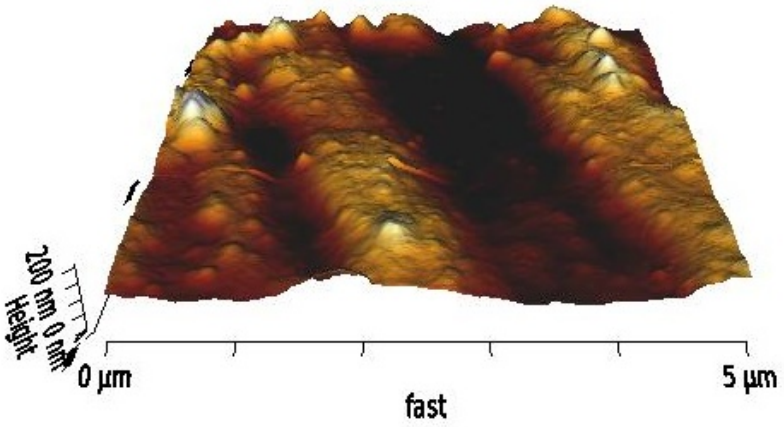

Figure 45: 5µm^2 3D image of 3V180s surface obtained in contact mode using JPK Nanowizard II atomic force microscope with HYDRA6V-200WG SI_3N_4 probe tips

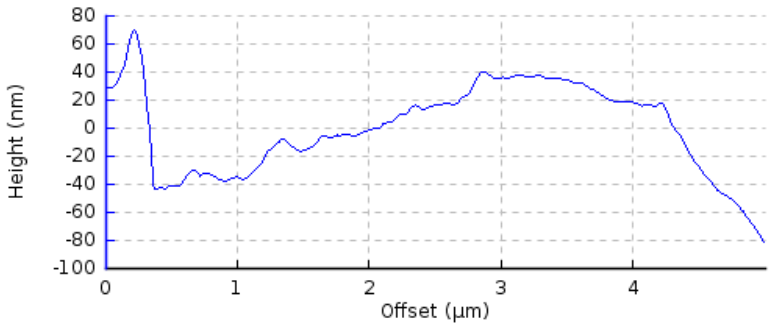

Figure 46: Sample height profile taken from horizontal measurements on 3V180s surface over 5µm.

The surfaces treated at 3V180s demonstrated infrequent, large (2-3 µm) features, and an underlying relatively smooth undulation of the surface. There was little in the way of nanometre-scale features observed.

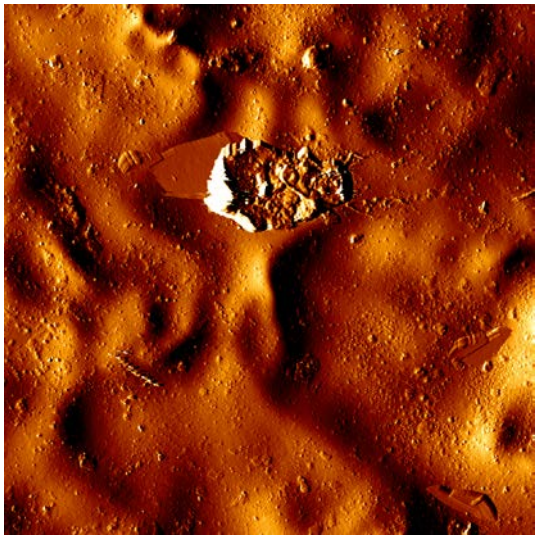

Figure 47: 50µm^2 2D image of 5V60s surface obtained in contact mode using JPK Nanowizard II atomic force microscope with HYDRA6V-200WG SI_3N_4 probe tips.

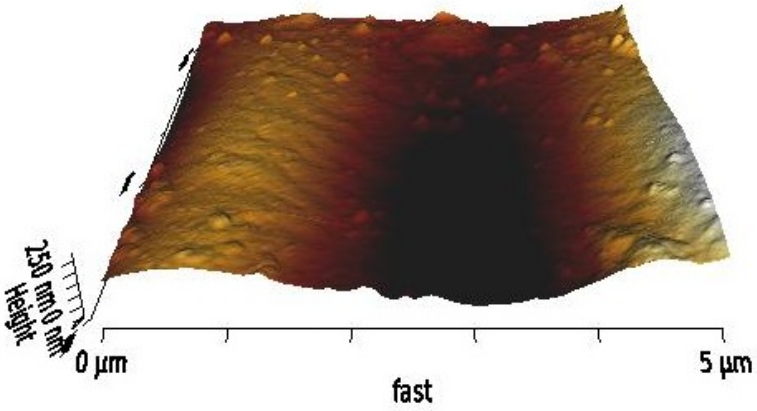

Figure 48: 5µm^2 3D image of 5V60s surface obtained in contact mode using JPK Nanowizard II atomic force microscope with HYDRA6V-200WG SI_3N_4 probe tips.

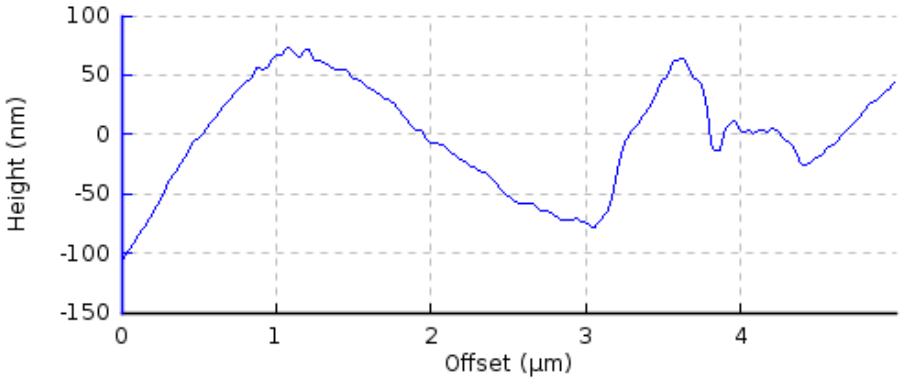

Figure 49: Sample height profile taken from horizontal measurements on 5V60s surface over 5µm.

The 5V60s treated surfaces were shown to have the highest RA values of all the surfaces. This was due to a combination of underlying undulation of the surface over 50-100nm in height and 2-3µm between peaks and also the presence of quite closely distributed features of 100-150nm in diameter, which were raised above the surrounding surface.

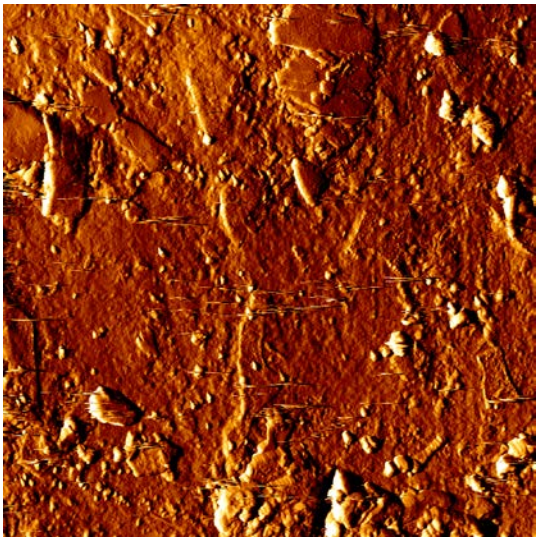

Figure 50: 50µm^2 2D image of 5V120s surface obtained in contact mode using JPK Nanowizard II atomic force microscope with HYDRA6V-200WG SI_3N_4 probe tips.

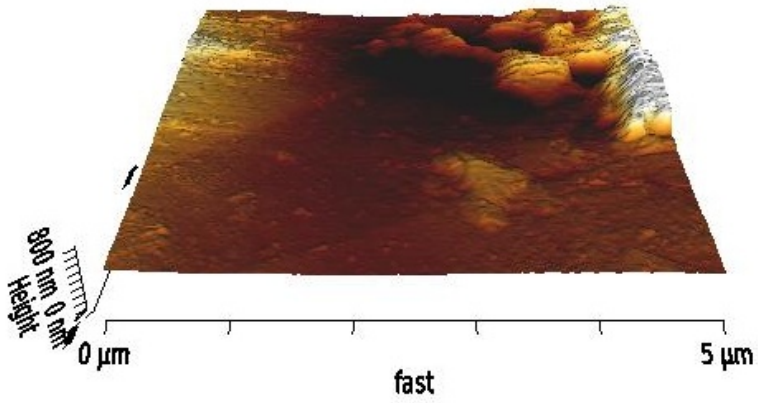

Figure 51: 5µm^2 3D image of 5V120s surface obtained in contact mode using JPK Nanowizard II atomic force microscope with HYDRA6V-200WG SI_3N_4 probe tips.

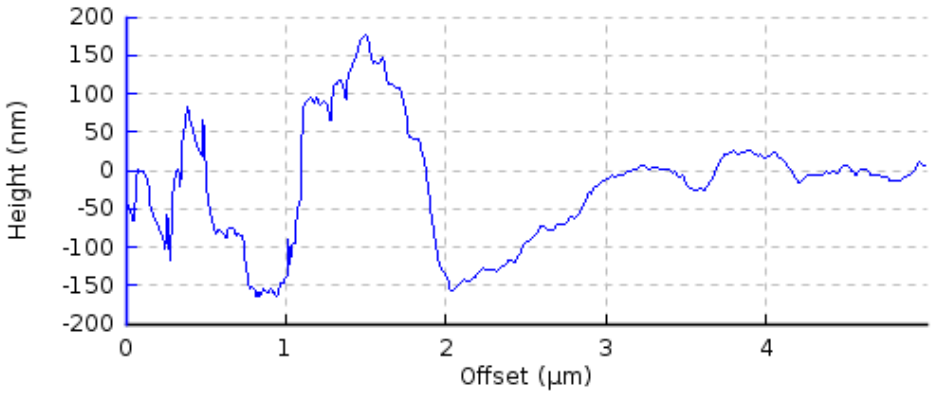

Figure 52: Sample height profile taken from horizontal measurements on 5V120s surface over 5µm.

The surfaces treated at 5V120s were observed to have lower RA values than those treated at 5V for 60s. The large undulations of the surface were no longer apparent and the baseline level of the surface as a whole was observed to be more on one level. Irregular features of 1-2µm in diameter and 200-400nm in height were seen with more frequency across the surface.

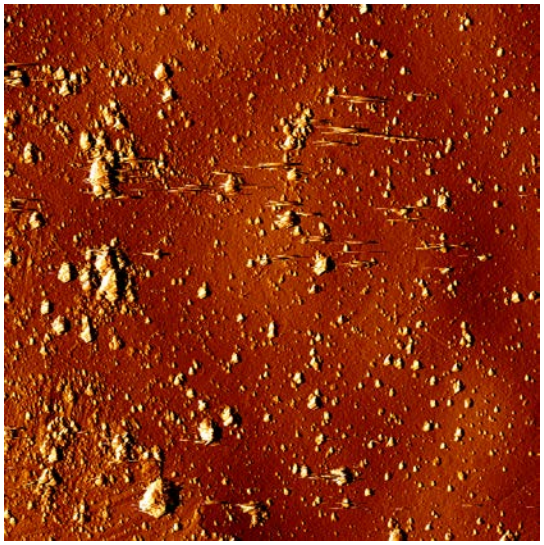

Figure 53: 50µm^2 2D image of 5V180s surface obtained in contact mode using JPK Nanowizard II atomic force microscope with HYDRA6V-200WG SI_3N_4 probe tips.

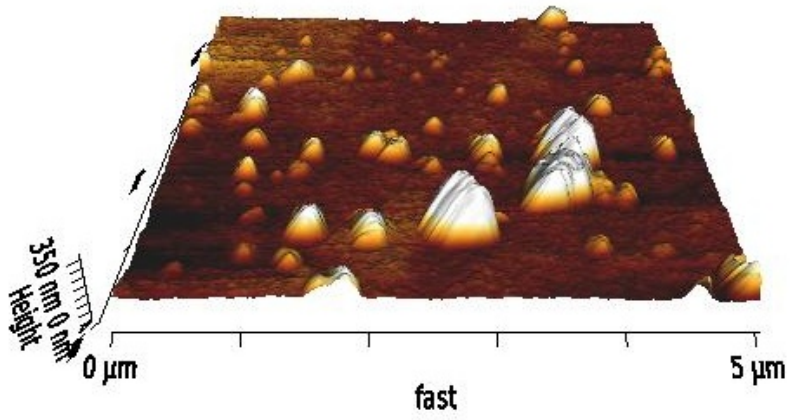

Figure 54: 5µm^2 3D image of 5V180s surface obtained in contact mode using JPK Nanowizard II atomic force microscope with HYDRA6V-200WG SI_3N_4 probe tips.

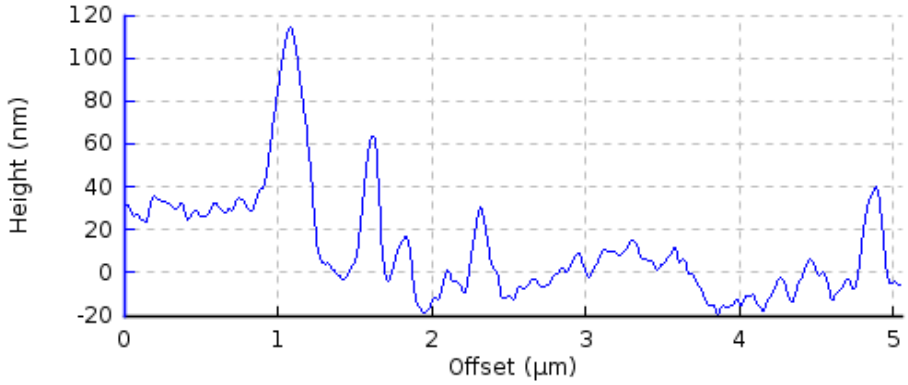

Figure 55: Sample height profile taken from horizontal measurements on 5V120s surface over 5µm.

The trend for smaller, more frequent, smoother features became more apparent from the profiles of the 5V180s treated surface. This demonstrated a flatter surface overall with more numerous small, smooth sided features of 200-300nm in diameter and 30-100nm in height.

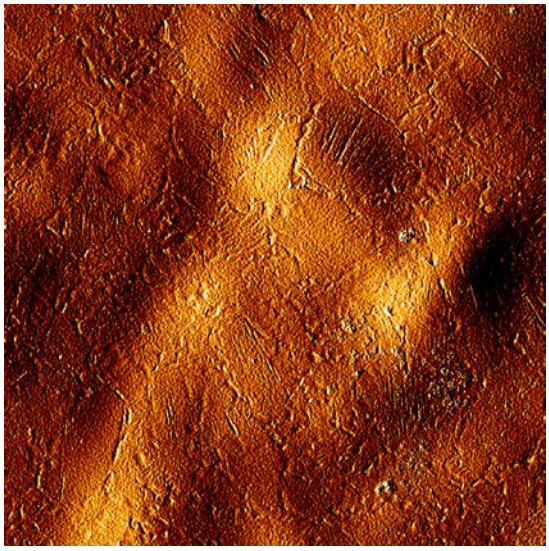

Figure 56: 50µm^2 2D image of 9V60s surface obtained in contact mode using JPK Nanowizard II atomic force microscope with HYDRA6V-200WG SI_3N_4 probe tips.

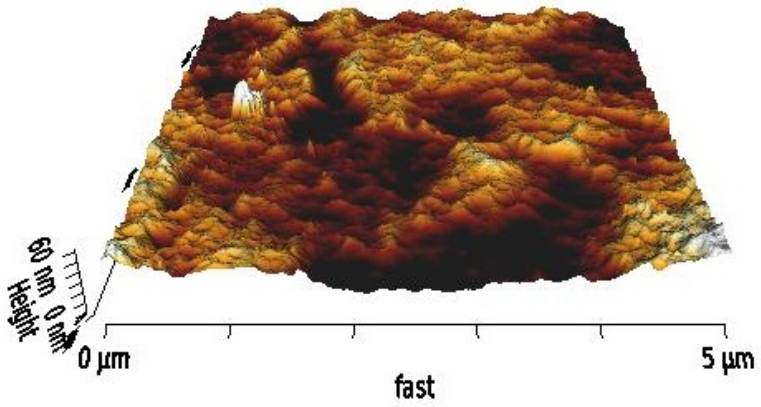

Figure 57: 5µm^2 3D image of 9V60s surface obtained in contact mode using JPK Nanowizard II atomic force microscope with HYDRA6V-200WG SI_3N_4 probe tips.

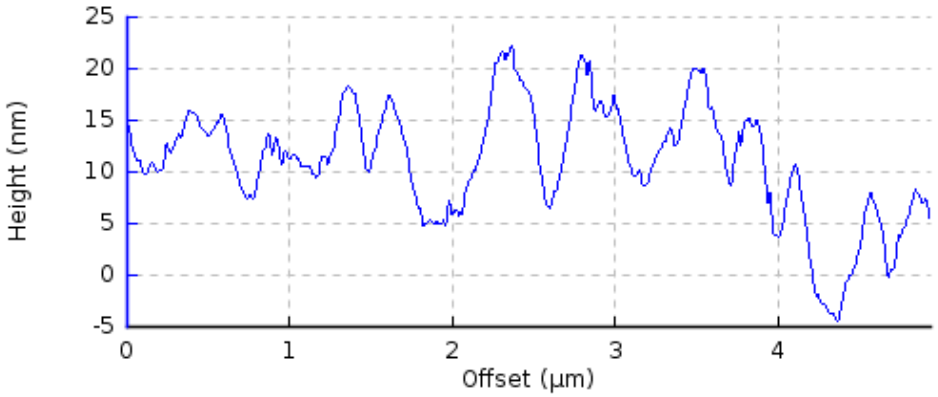

Figure 58: Sample height profile taken from horizontal measurements on 9V60s surface over 5µm.

The surfaces treated at 9V all had smaller RA values than those treated at 3V and 5V. There was an absence of large features elevated above the surrounding surface and a more regular peak and trough pattern was seen. These peaks and troughs at 9V60 were 10-30nm in height and varied between 100 and 600nm in width.

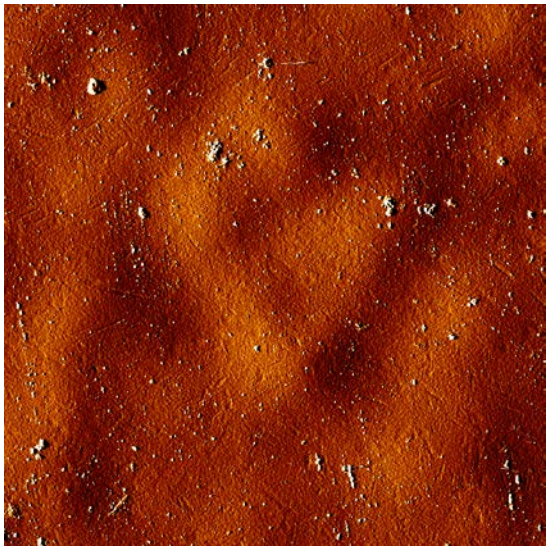

Figure 59: 50µm^2 2D image of 9V120s surface obtained in contact mode using JPK Nanowizard II atomic force microscope with HYDRA6V-200WG SI_3N_4 probe tips.

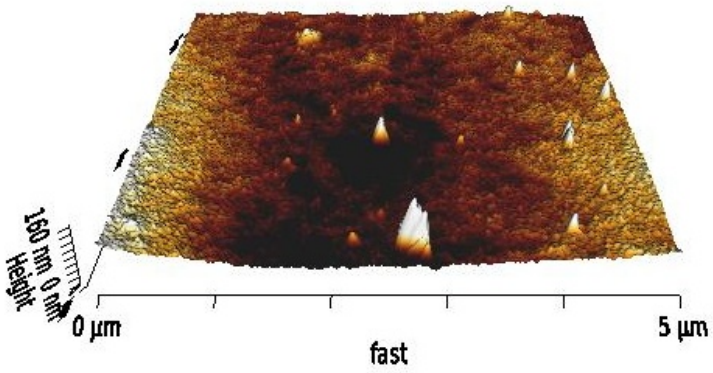

Figure 60: 5µm^2 3D image of 9V120s surface obtained in contact mode using JPK Nanowizard II atomic force microscope with HYDRA6V-200WG SI_3N_4 probe tips.

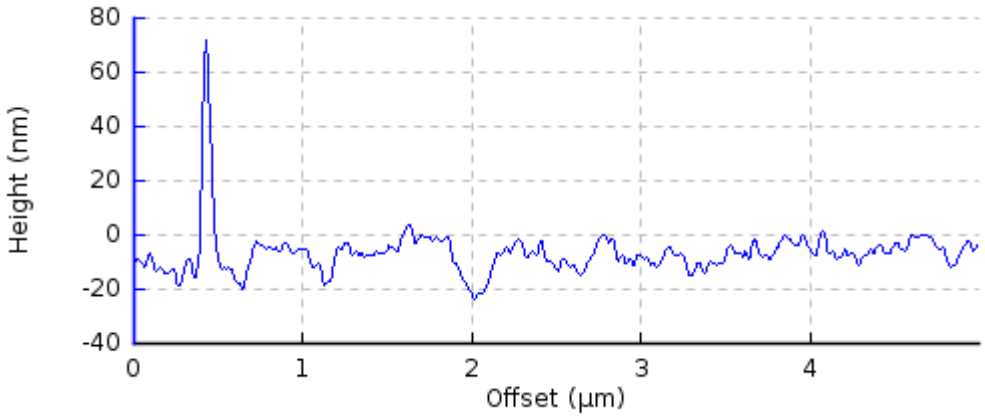

Figure 61: Sample height profile taken from horizontal measurements on 9V120s surface over 5µm.

When treated at 9V120s, the surfaces were observed as displaying very small amplitude peaks and troughs of 5-20nm in height and width. There were also some infrequent, larger, smooth sided features, which reached 80-100nm in height, although were similar in width to the small, baseline peaks.

Figure 62: 50µm^2 2D image of 9V180s surface obtained in contact mode using JPK Nanowizard II atomic force microscope with HYDRA6V-200WG SI_3N_4 probe tips.

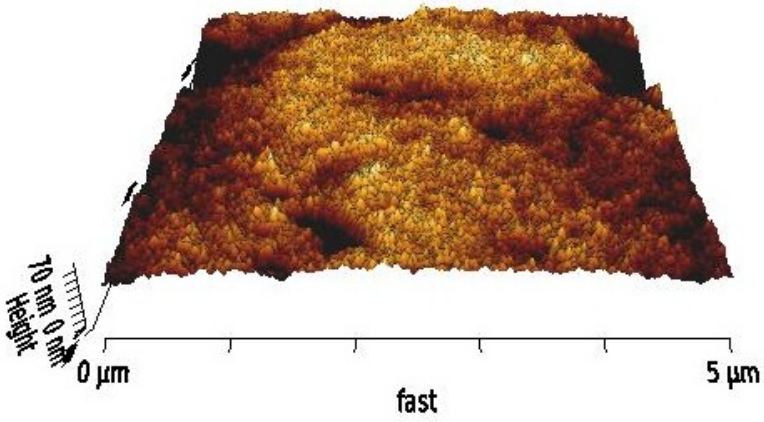

Figure 63: 5µm^2 3D image of 9V180s surface obtained in contact mode using JPK Nanowizard II atomic force microscope with HYDRA6V-200WG SI_3N_4 probe tips.

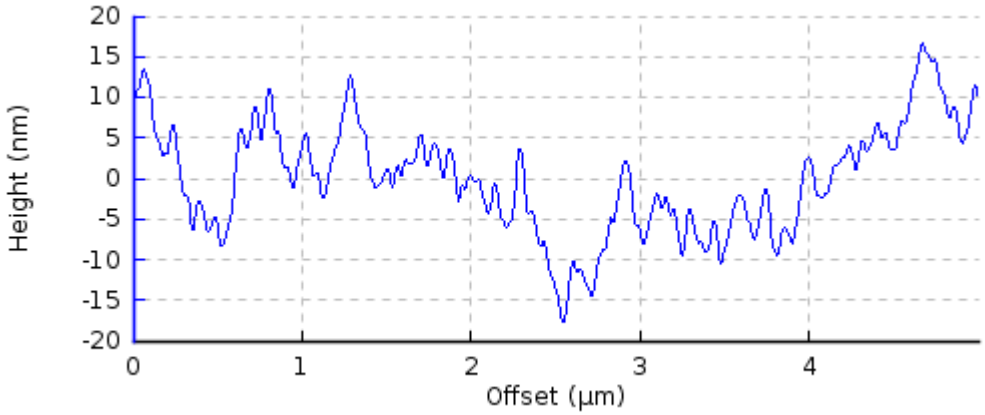

Figure 64: Sample height profile taken from horizontal measurements on 9V180s surface over 5µm.

The profiles of the surfaces treated at 9V180s were seen to be very similar to those of the 9V120s treated surfaces, with small amplitude peaks and troughs 2-30nm in height and 10-50nm in width, however no features of larger amplitude were observed, resulting in surfaces with the lowest RA values.

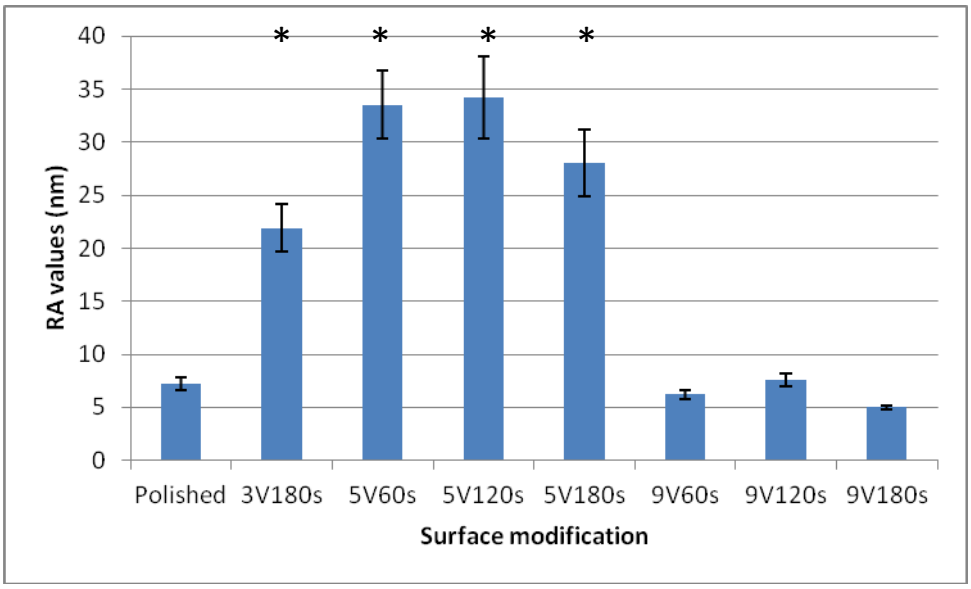

Figure 65: RA values taken from AFM profiles in nm (representing mean results of 10 independent measurements), error bars express standard error of the mean. RA of surfaces marked with * were significantly greater than the unmarked surfaces ($p<0.05$).

Pairwise comparisons using Tukey's 95% simultaneous confidence intervals demonstrate that there are statistically significant differences in RA values between the

treated surfaces. The mechanically polished surface and all three surfaces treated at 9V had significantly lower RA values than the 3V180s treated surface and all surfaces treated at 5V(*).

3.2.4. Scanning Electron Microscopy

Scanning Electron Microscopy (SEM) provides images of the experimental surfaces at the submicron scale, allowing a qualitative assessment of surface features.

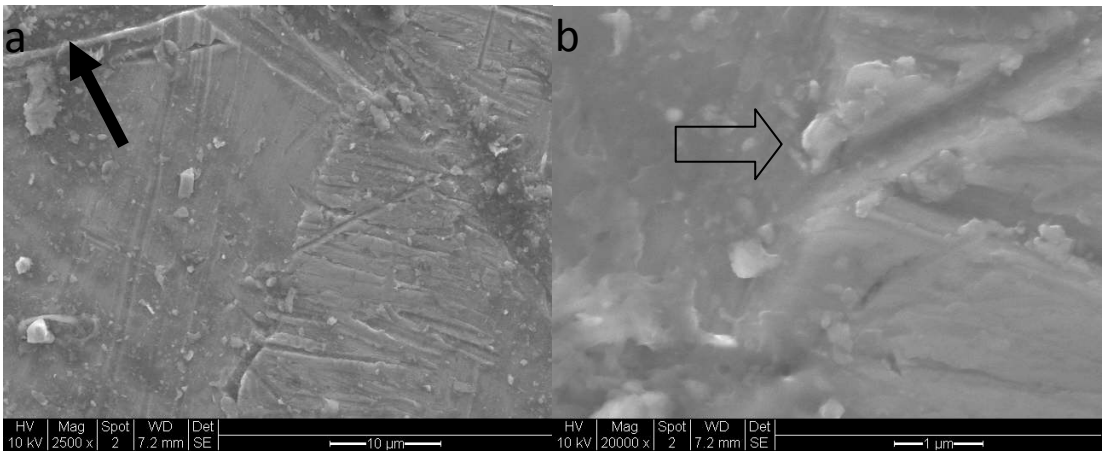

Figure 66: Images at 2500 and 20,000 × magnification taken with FEI XL30 ESEM of machined Ti6Al4V surface

SEM images of the machined Ti6Al4V surface show the deep circumferential machine tooling marks only in the top left corner of the 2500 × magnified image (Figure 66a – solid arrow). The small area visualised otherwise demonstrated the unpolished surface with crystals of the alloy formed in room air on the exposed surfaces after they were cut to size (Figure 66b – open arrow).

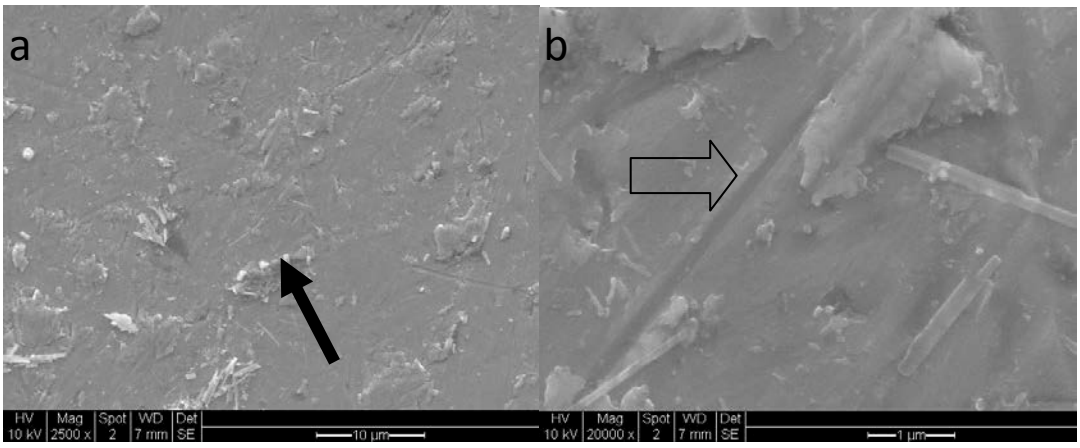

Figure 67 : Images at 2500 and 20,000 × magnification taken with FEI XL30 ESEM of mechanically polished Ti6Al4V surface

The appearance of the mechanically polished surface is smooth at the micrometre scale, with a combination of crystalline and more irregular, rounded alloy features formed in

air (Figure 67a – solid arrow), as well as the presence of small, shallow grooves created by the mechanical polishing process (Figure 67b – open arrow).

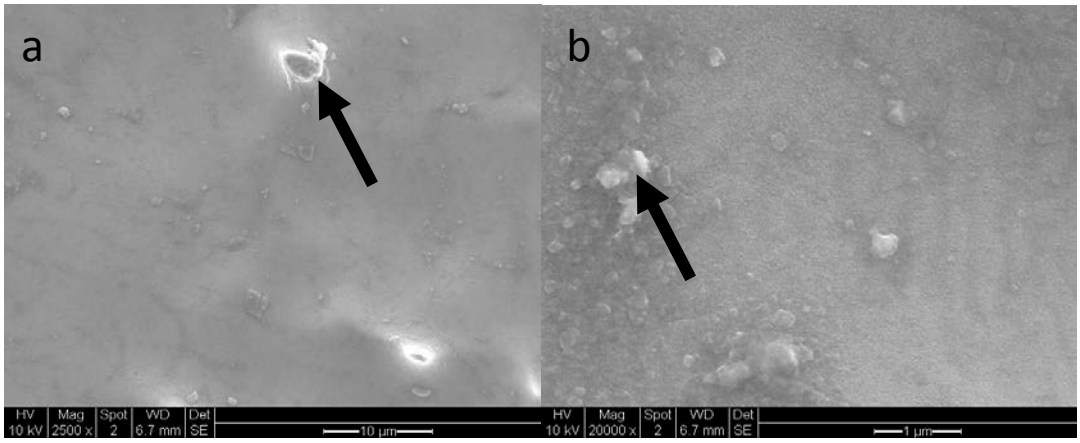

Figure 68: Images at 2500 and 20,000 × magnification taken with FEI XL30 ESEM of 3V180s treated Ti6Al4V surface

As observed on AFM imaging, the 3V180s treated surfaces display an undulating morphology with few features (Figure 68a). Those that are present are irregular and rounded in character and tend to be peaks on the surface, rather than troughs etched out of the oxide (Figure 68a and b – solid arrows).

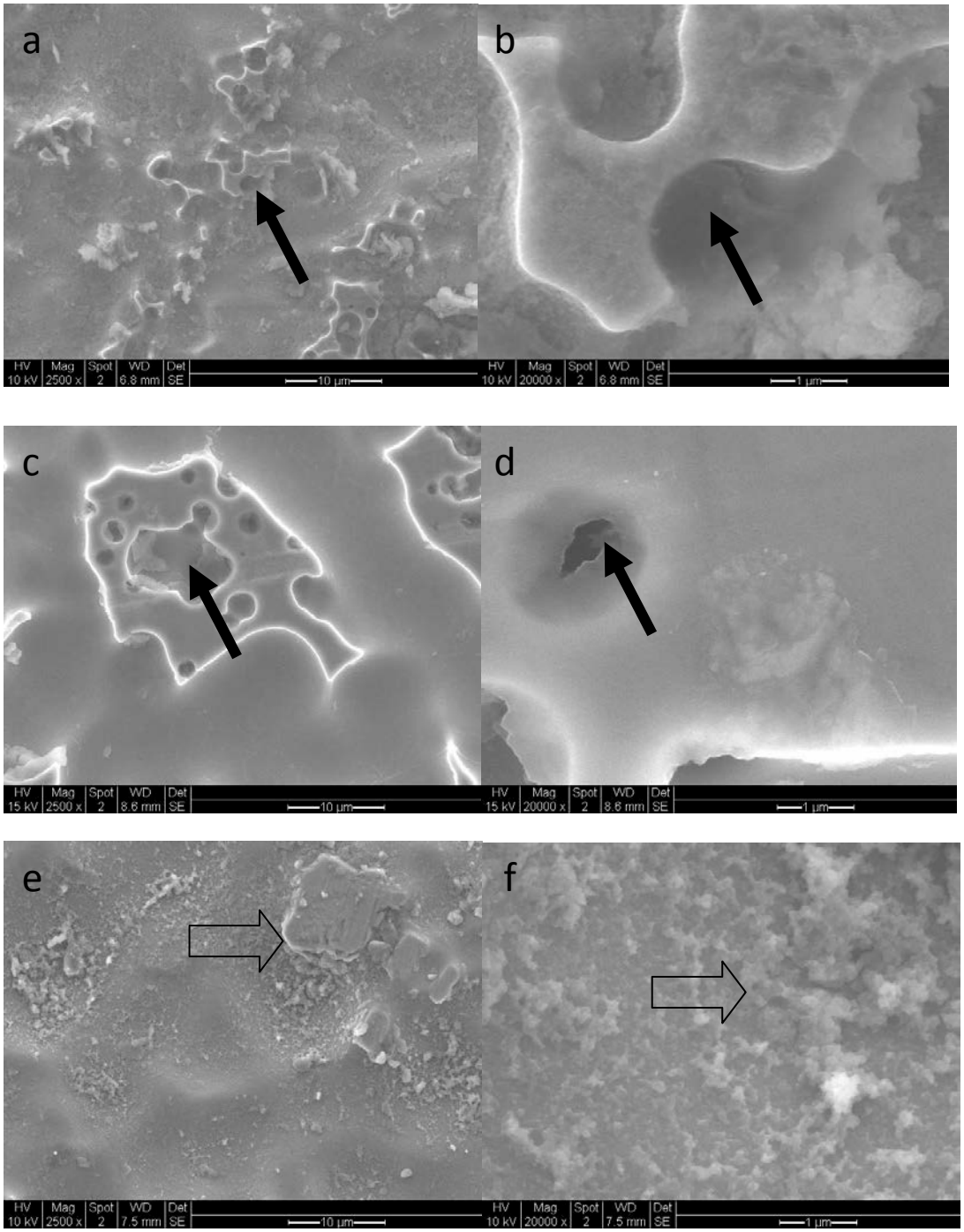

Figure 69: Images at 2500 and 20,000 × magnification taken with FEI XL30 ESEM of 5V60s, 5V120s and 5V180s treated Ti6Al4V surface

At 5V60s and 5V120s (Figures 69a-d), the electropolishing tends to produce relatively large, etched out features below the base level of the oxide surface, resulting in high levels of average roughness (solid arrows). With further etching time, at 5V180s (Figures 69e and f), the surface again appears smoother, with the appearance of smaller, irregular, built up features (open arrows).

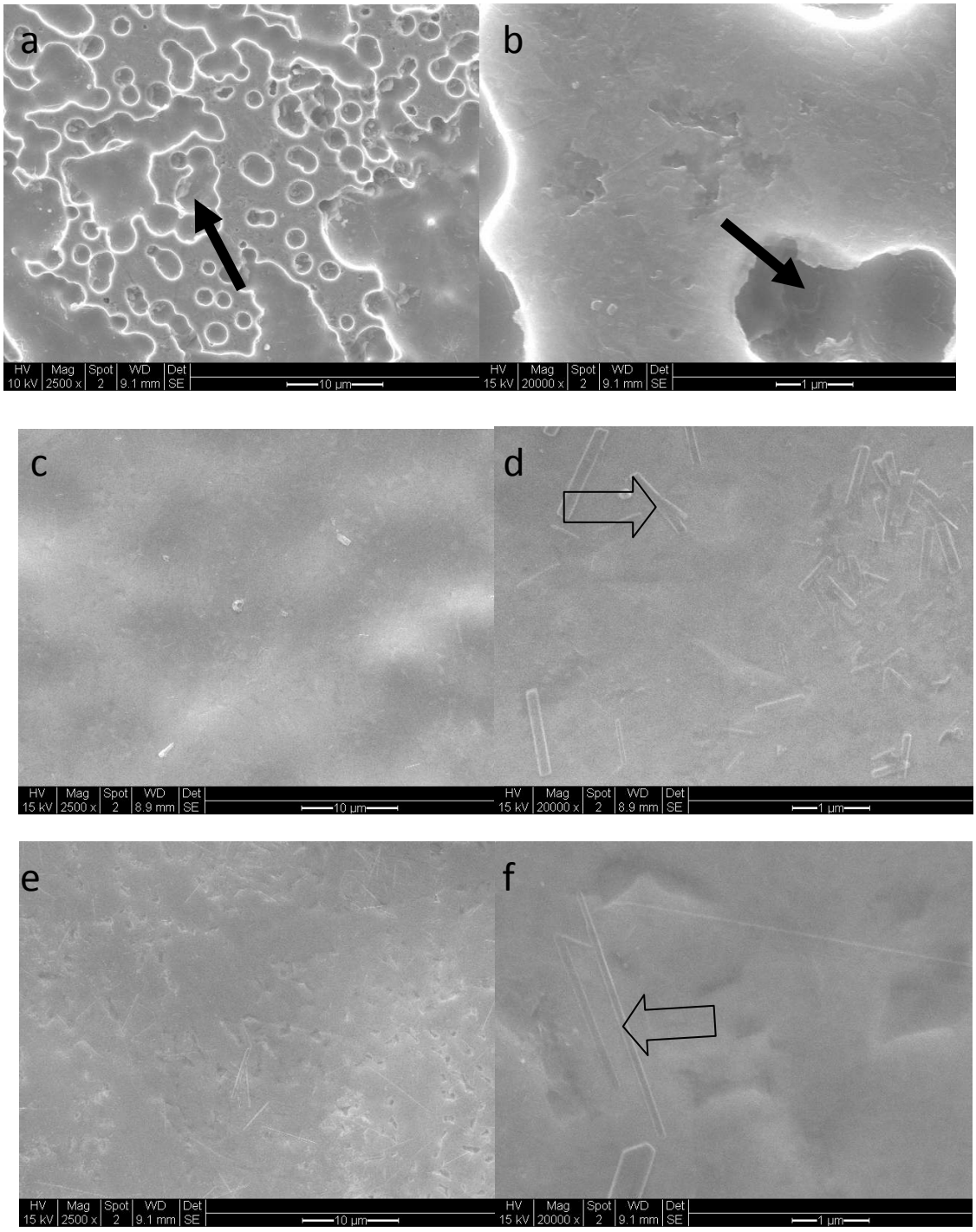

Figure 70: Images at 2500 and 20,000 × magnification taken with FEI XL30 ESEM of 9V60s, 9V120s and 9V180s treated Ti6Al4V surface

Treatment at 9V60s produces a surface very similar to those produced with polishing voltages of 5V (Figures 70a and b), with etched out features (solid arrows). At longer polishing times, almost featureless surfaces were observed, with oxide crystals becoming a more predominant appearance over the previously observed pits (Figures 70c-f, open arrows).

3.2.5. X-ray Photoelectron Spectroscopy

XPS was performed in order to assess the chemical composition of the surface oxide layer on the modified titanium alloy surfaces according to polishing voltage and time. Argon milling was performed for 1 and 2 seconds allowing the composition of the oxide layer at levels below the surface to be quantified (with 2-2.5 Å of surface depth removed for each second of milling).

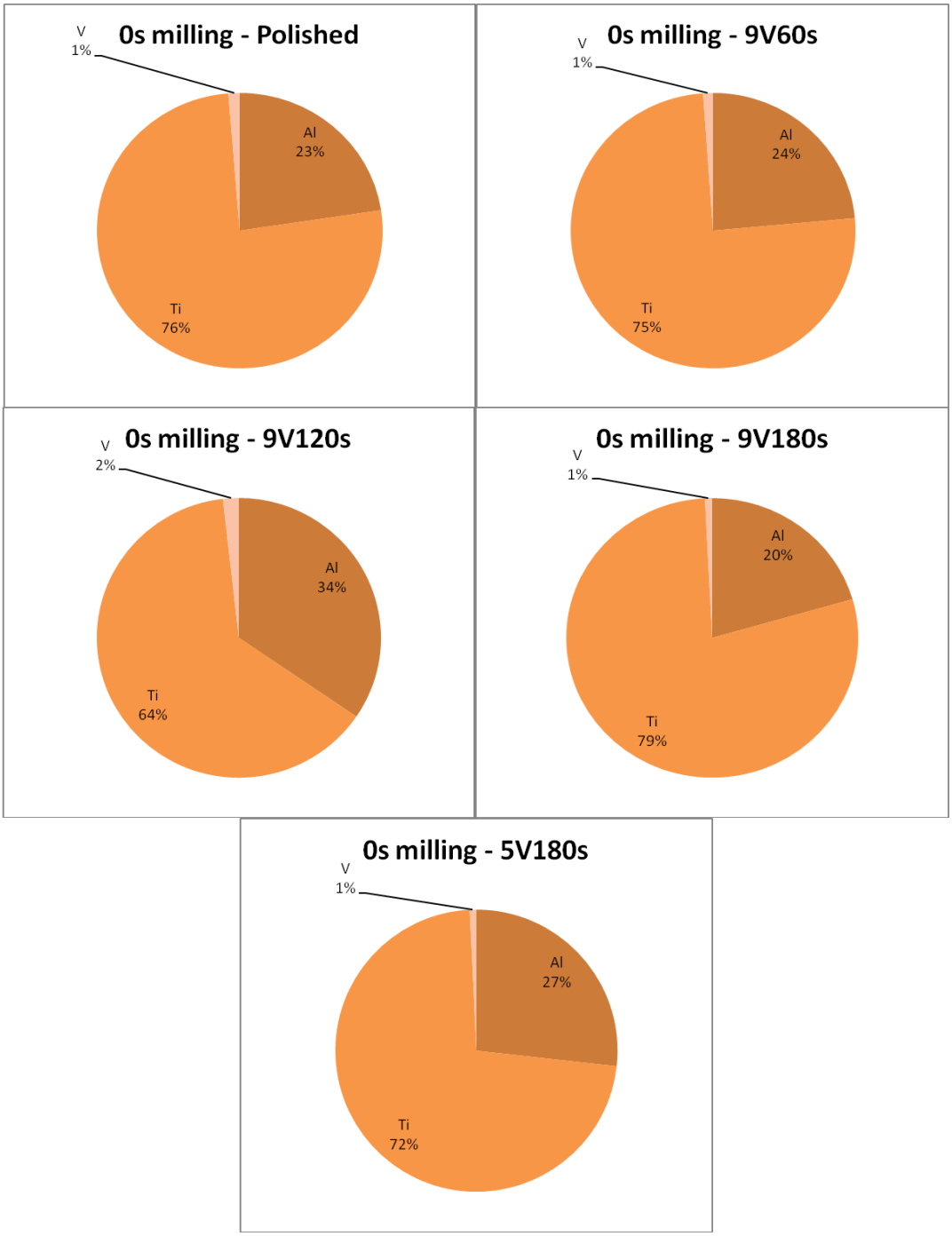

Figure 71: Pie charts of the atomic percentage of different metal oxides present on the surface of the alloy oxide layer on x-ray photoelectron spectroscopy (20eV pass energy) (without argon milling), for the mechanically polished, 5V and 9V treated surfaces.

Figure 72: Pie charts of the atomic percentage of different metal oxides present in the alloy oxide layer on x-ray photoelectron spectroscopy (20eV pass energy) following 1s of argon milling at 3 kV 1mA, for the mechanically polished, 5V and 9V treated surfaces.

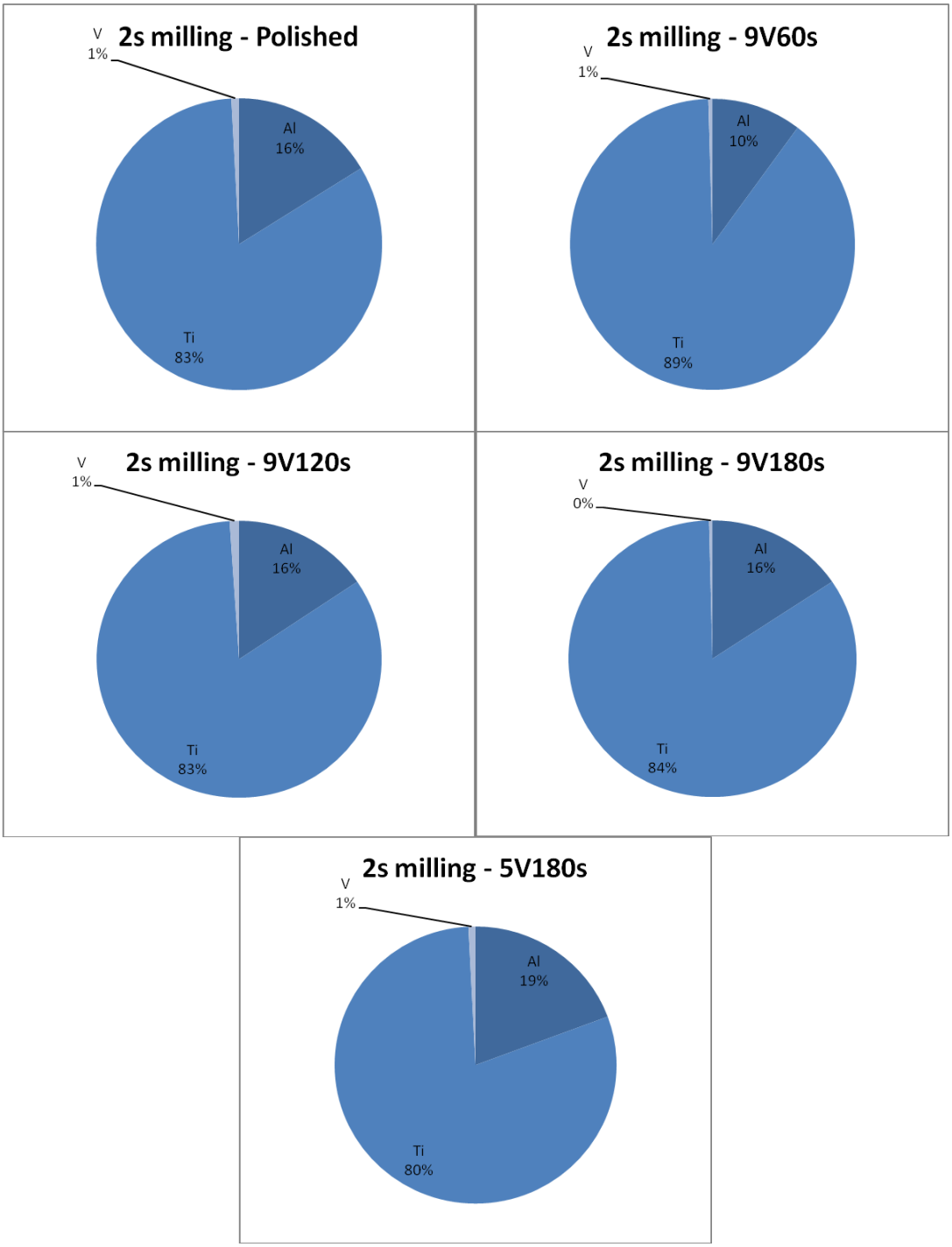

Figure 73: Pie charts of the atomic percentage of different metal oxides present in the alloy oxide layer on x-ray photoelectron spectroscopy (20eV pass energy) following 2s of argon milling at 3 kV 1mA, for the mechanically polished, 5V and 9V treated surfaces.

The pie charts above demonstrate the percentage of the component metal oxides present in the oxide layer at the surface (Figure 71) then with sequential argon milling for 1

(Figure 72) and 2s (Figure 73); therefore depths of 2-5Å. At each of the levels measured, a general trend for decreasing percentage of aluminium in the oxide is apparent with increasing voltage and increasing time of polishing. A similar trend is illustrated as occurring with decreasing abundance of vanadium in the oxide layer with increasing time and voltage used in the polishing process. This is apparent at all three levels where measurements were obtained.

3.3. Cell adhesion and morphology of rat calvarial osteoblasts on Titanium alloy surfaces

3.3.1. Immunofluorescence with anti-vinculin

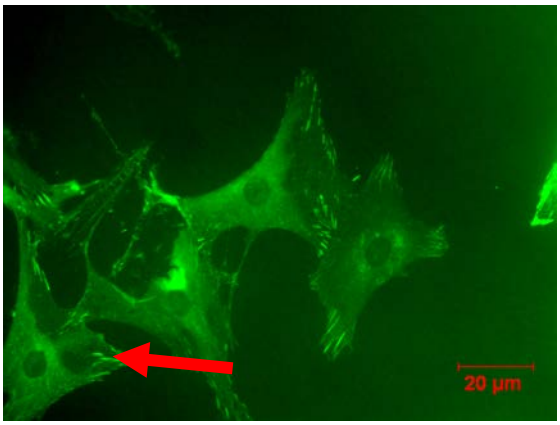

Figure 74: Anti-vinculin immunofluorescence of rat calvarial osteoblasts cultured on a glass surface for 24 hours.

Cells cultured on glass (Figure 74) provided a control against which any changes in morphology observed on the treated surfaces could be compared. These cells were observed to be large, well spread and randomly oriented. They displayed numerous, large focal adhesions around the perimeter of the cells. The solid arrow indicates typical vinculin-positive plaque at cell perimeter.

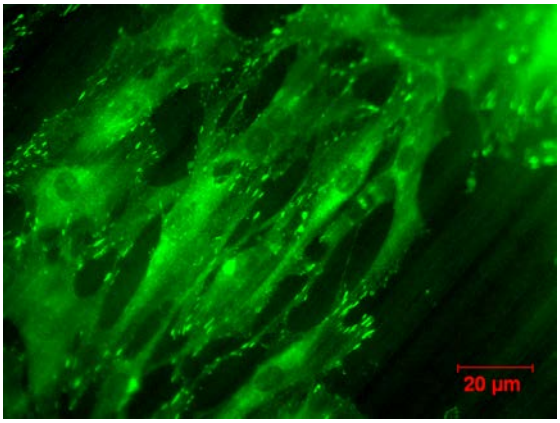

Figure 75: Anti-vinculin immunofluorescence of rat calvarial osteoblasts cultured on a machined Ti6Al4V surface for 24 hours.

Osteoblasts cultured on unpolished Ti6Al4V with machine tooling marks (Figure 75), were noted to exhibit contact guidance, with their long axes aligned parallel to the

direction of the tooling marks. Focal adhesions appeared smaller than those in the cells cultured on glass and distributed towards the ends of the long axis of the cells.

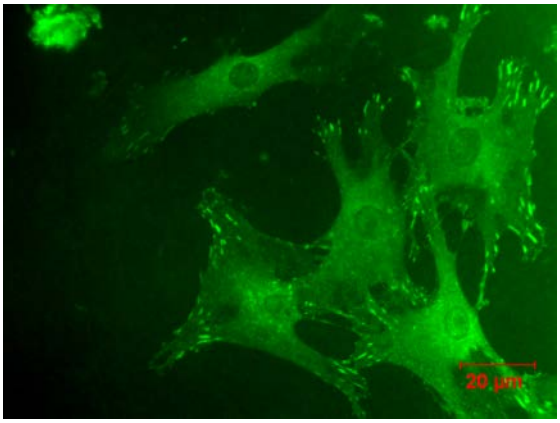

Figure 76: Anti-vinculin immunofluorescence of rat calvarial osteoblasts cultured on a polished Ti6Al4V surface for 24 hours.

Rat osteoblasts cultured on mechanically polished Ti6Al4V surfaces (Figure 76) were well spread with no orientation of their axes and numerous focal adhesions.

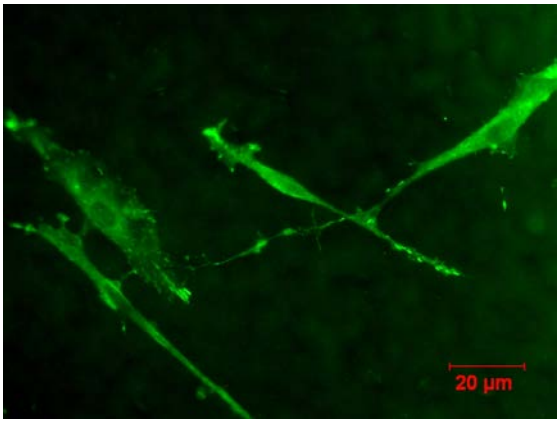

Figure 77: Anti-vinculin immunofluorescence of rat calvarial osteoblasts cultured on a 3V180s treated Ti6Al4V surface for 24 hours.

Rat osteoblasts on 3V180s treated surfaces (Figure 77) displayed a more elongated morphology with long filopodia in contact with the titanium alloy surface with small focal adhesion complexes mostly confined to the leading edges of the filopodia. Although elongated, the cells appeared randomly oriented on the surface.

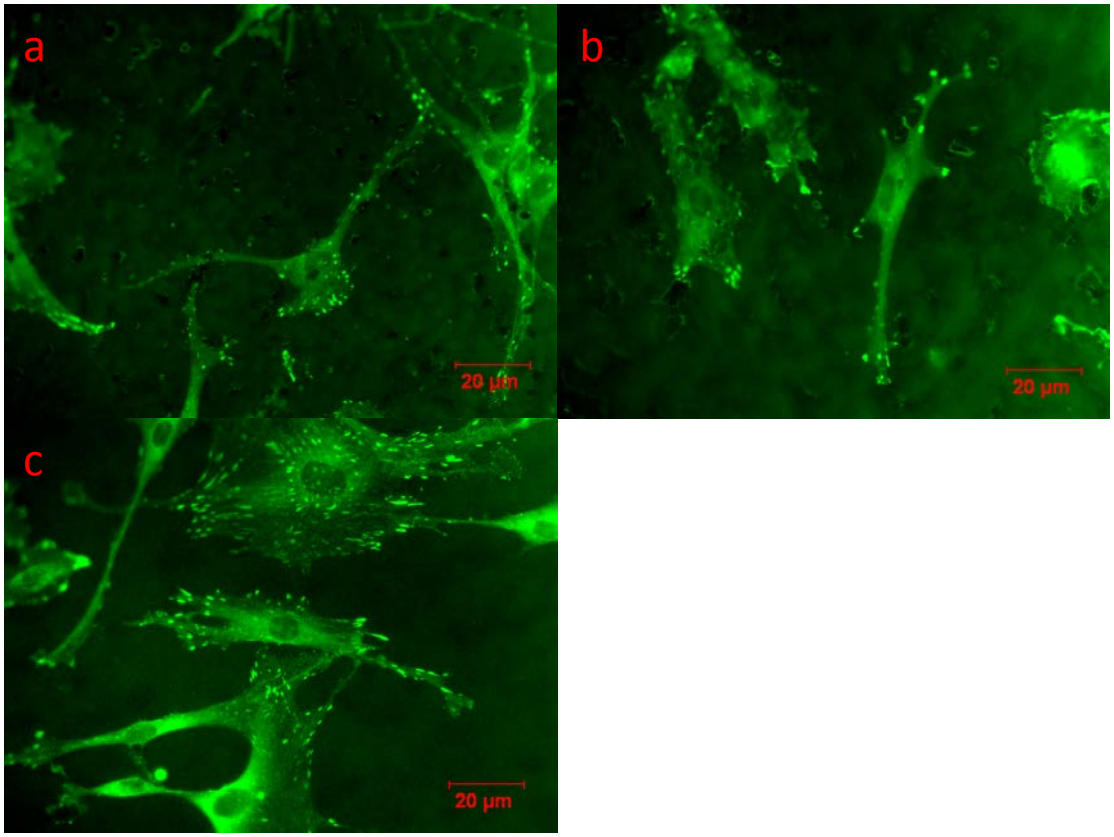

Figure 78: Anti-vinculin immunofluorescence of rat calvarial osteoblasts cultured on a) 5V60s, b) 5V120s and c) 5V180s treated Ti6Al4V surfaces for 24 hours.

The rat osteoblasts cultured on surfaces treated at 5V (Figures 78a-c) for increasing time periods displayed progressively more spread morphology with larger and more numerous focal adhesion complexes being observed in the cells cultured on the 5V180s (Figure 78c) surfaces and smaller focal adhesions distributed on longer filopodia present in the cells cultured on the 5V60s surfaces (Figure 78a). The long axes of the cells were randomly oriented with respect to the surface.

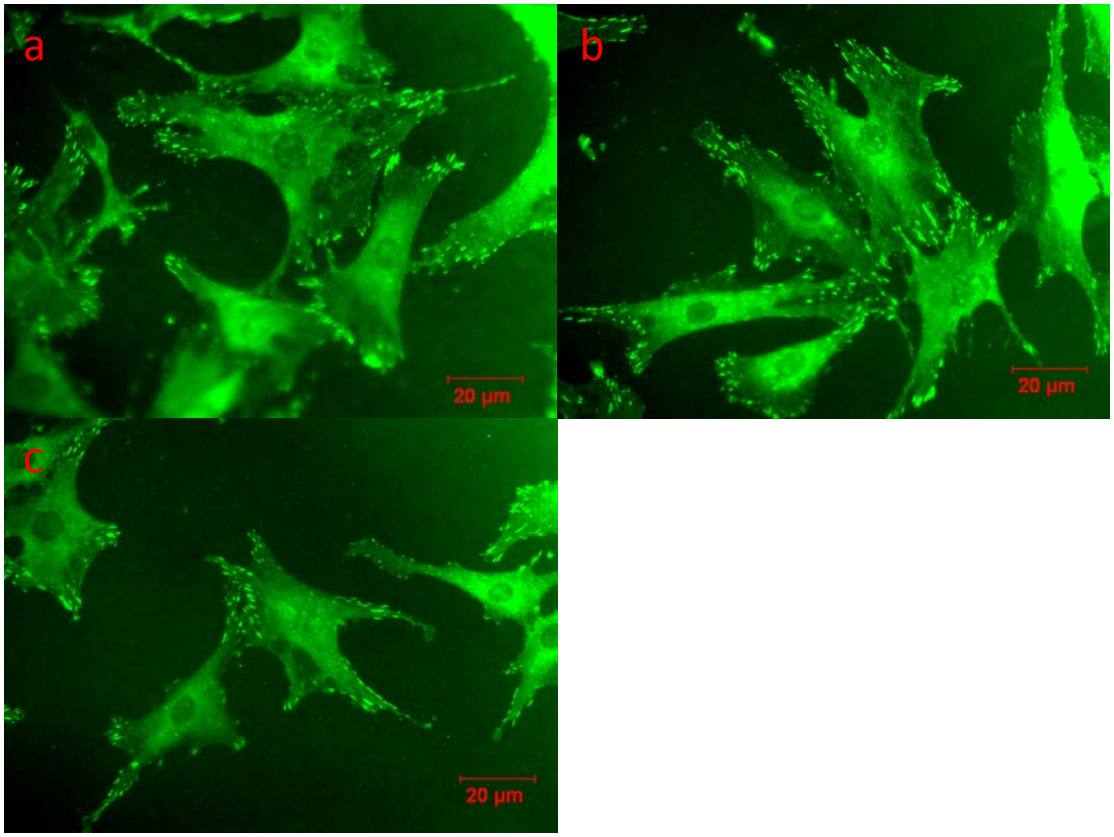

Figure 79: Anti-vinculin immunofluorescence of rat calvarial osteoblasts cultured on a) 9V60s, b) 9V120s and c) 9V180s treated Ti6Al4V surfaces for 24 hours.

Cells cultured on surfaces treated at 9V were randomly oriented with respect to the surface and well spread with large, numerous focal adhesions around the perimeter of the cells, particularly those cultured on the 9V120s and 9V180s surfaces. Some short filopodia were observed on some of the cells cultured on the 9V60s surfaces.

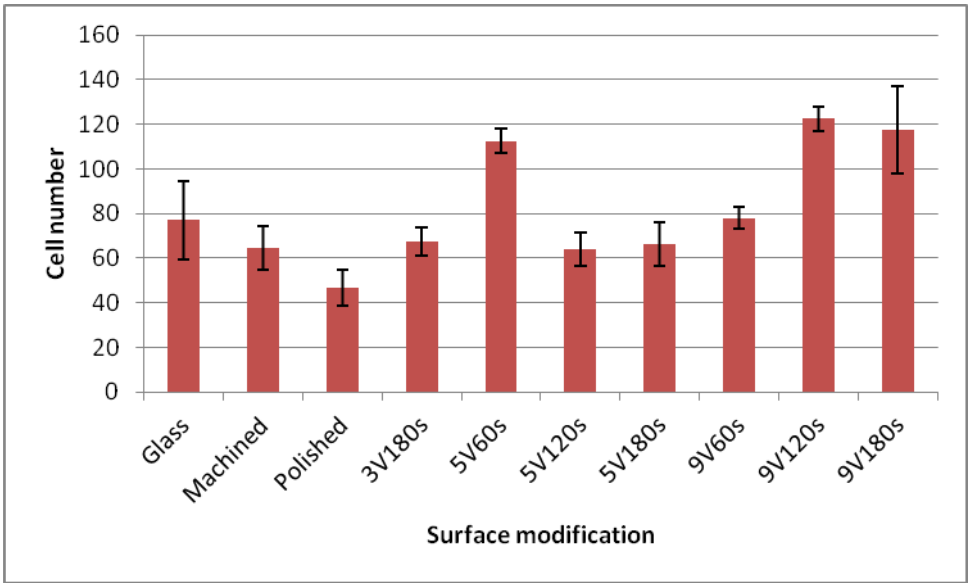

Figure 80: Bar chart illustrating the mean number of cells counted during immunofluorescence of rat osteoblasts cultured for 24 hours on the control and modified surfaces for 24 hours (results combined from 3 independent experiments).

Broadly similar numbers of cells were apparent on all surfaces. A clear pattern of change in cell number with change in surface properties was not observed and the same pattern of cell numbers was not present in all three independent experiments.

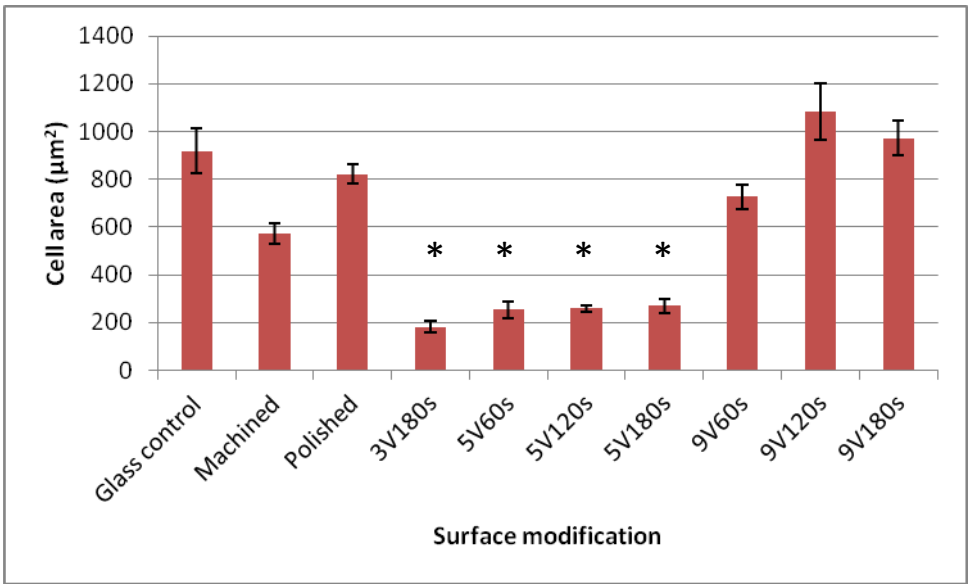

Figure 81: Bar chart demonstrating mean cell area (µm^2) of primary rat calvarial osteoblasts cultured on control and modified surfaces for 24 hours (data from 1 experiment representative of 3 independent experiments; n=10).

Cell area was significantly smaller for the cells cultured on the 3V180s, 5V60s, 5V120s and 5V180s surfaces (Figure 81; marked with *), than for those cultured on the glass control, polished, 9V60s, 9V120s and 9V180s treated surfaces ($p<0.05$).

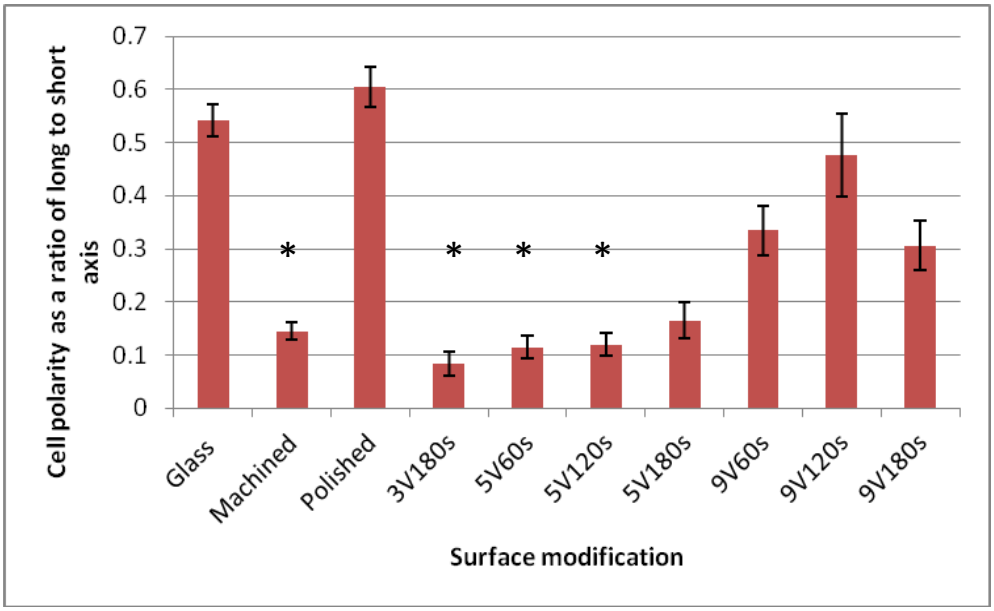

Figure 82: Bar chart recording cell polarity of rat calvarial osteoblasts cultured for 24 hours on control and modified surfaces as a ratio of long to short cell axis (data from 1 experiment representative of 3 independent experiments; n=10).

Cell polarity was measured as a ratio of the longest to the shortest axis of the cell. This was used as a measure of the degree of contact guidance and spreading of cells on the experimental surfaces. Polarity was found to be significantly smaller for the cells cultured on the machined, 3V180s, 5V60s and 5V120s surfaces (Figure 82, marked with *) than those on the glass control, polished and 9V treated surfaces ($p<0.05$).

3.3.2. Focal adhesion quantification

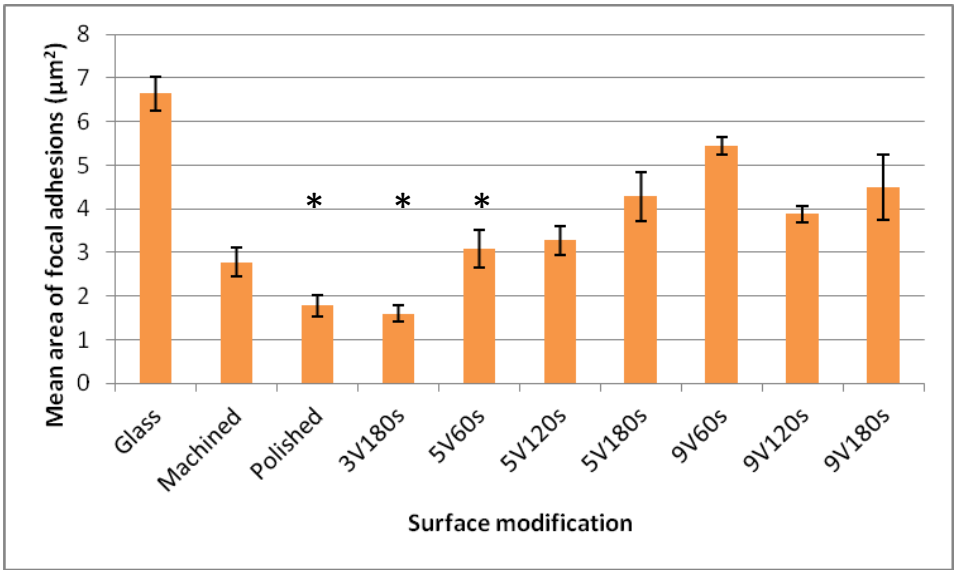

Figure 83: Bar chart illustrating mean area of focal adhesions measured from anti-vinculin immunofluorescence in rat osteoblasts cultured for 24 hours on control and modified surfaces (data from 1 experiment representative of 3 independent experiments; n=10).

A further analysis of the focal adhesion complexes visualised by anti-vinculin immunofluorescence revealed that the mean size of focal adhesions was significantly larger on the glass control, 9V60s and 9V180s treated surfaces than on the polished, 3V180s and 5V60s (Figure 83, marked with *) treated surfaces ($p<0.05$).

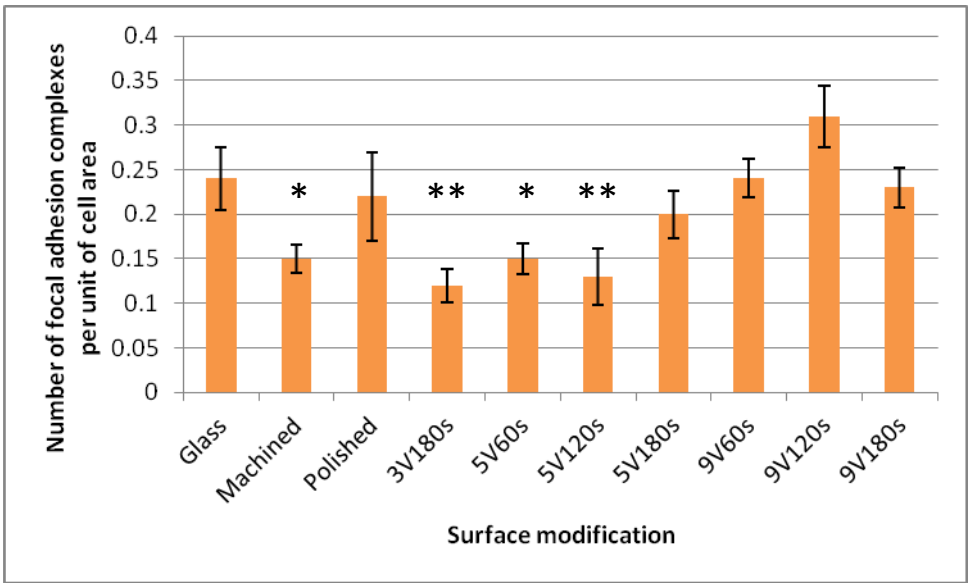

Figure 84: Bar chart demonstrating the number of focal adhesion complexes found per unit of cell area from anti-vinculin immunofluorescence after rat calvarial osteoblasts cultured for 24 hours on control and modified surfaces (data from 1 experiment representative of 3 independent experiments; n=10).

The mean number of focal adhesion complexes per unit cell area (per μm^2) was found to be significantly lower in the cells cultured on the machined, 3V180s, 5V60s and 5V120s treated surfaces (Figure 84, marked with *), than on the 9V120s treated surfaces ($p<0.05$) and the focal adhesions on the 3V180s and 5V120s (Figure 84, marked with **) treated surfaces were also significantly lower than on the polished surface.

3.3.3. Cell morphology on polycaprolactone

The morphology of rat calvarial osteoblasts was investigated on polycaprolactone moulds of the treated surfaces in order to investigate the effect of surface roughness, independent of any effects of changes to the surface chemistry of the oxide layer induced by the electrochemical modification process.

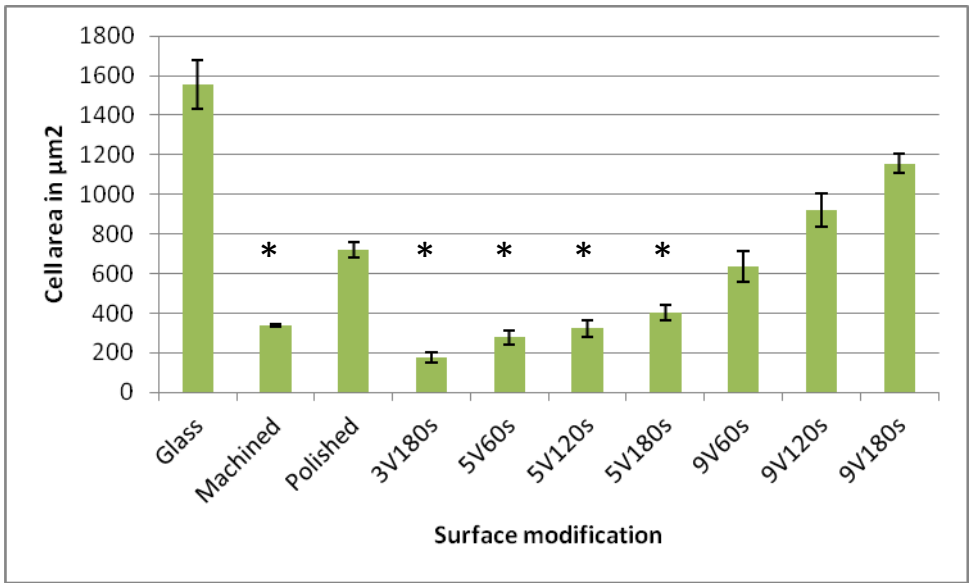

Figure 85: Graph demonstrating the area of rat primary calvarial osteoblasts cultured on polycaprolactone moulds of the treated surfaces (μm^2) for 24 hours, error bars representing standard error of the mean (data from 1 experiment representative of 3 independent experiments; n=10).

The mean cell area of rat osteoblasts cultured on polycaprolactone moulds of machined, 3V180s and 5V treated surfaces (Figure 85, marked with *) was significantly smaller than the mean cell area of those cultured on moulds of the 9V treated surfaces and on the glass control surface ($p<0.05$).

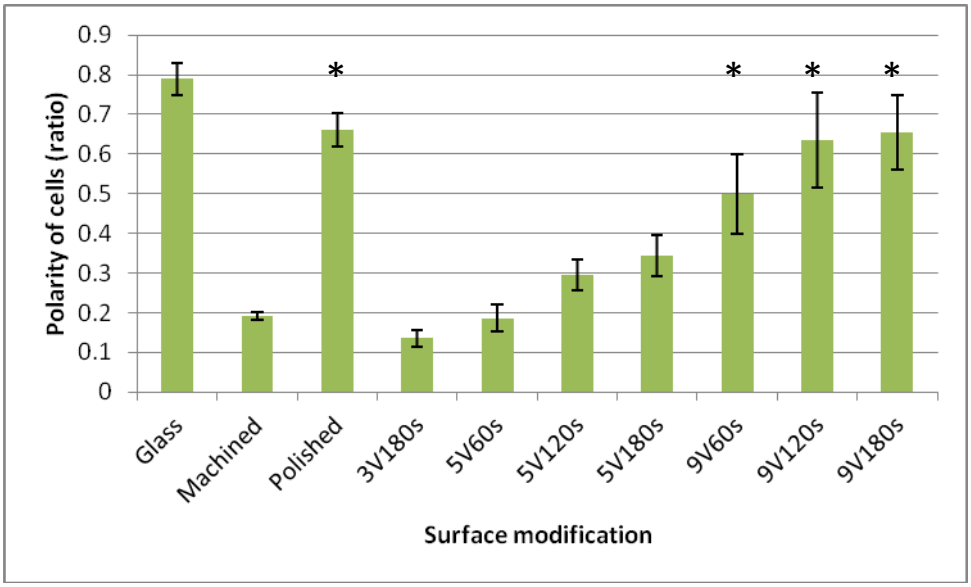

Figure 86: Graph showing the polarity of rat primary calvarial osteoblasts cultured on polycaprolactone moulds of the treated surfaces for 24 hours (as a decimal ratio), error bars expressing standard error of the mean (data from 1 experiment representative of 3 independent experiments; n=10).

There were also significant differences seen in the polarity of cells on these surfaces with the cells cultured on the moulds of the polished and 9V treated surfaces (Figure 86, marked with *) being significantly less polarised than those cultured on the moulds of 3V and 5V treated surfaces ($p<0.05$).

3.4. Cell adhesion and morphology of human mesenchymal stromal cells on Titanium alloy surfaces

3.4.1. Immunofluorescence with anti-vinculin

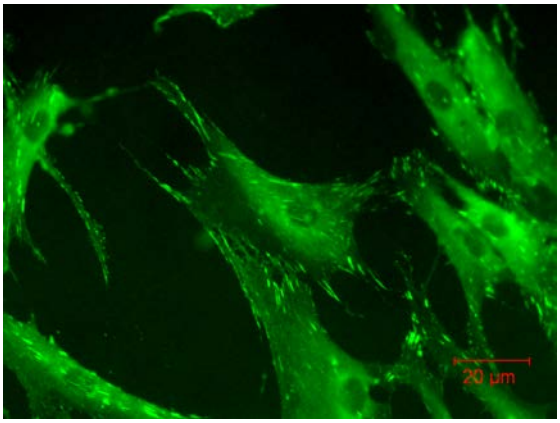

Figure 87: Anti-vinculin immunofluorescence of human mesenchymal cells cultured on a glass surface for 24 hours.

Human mesenchymal cells cultured on glass control surfaces (Figure 87) displayed a less uniform morphology than the rat calvarial osteoblasts. They generally displayed a well spread morphology with large focal adhesion complexes at the peripheries but some short filopodia were also observed.

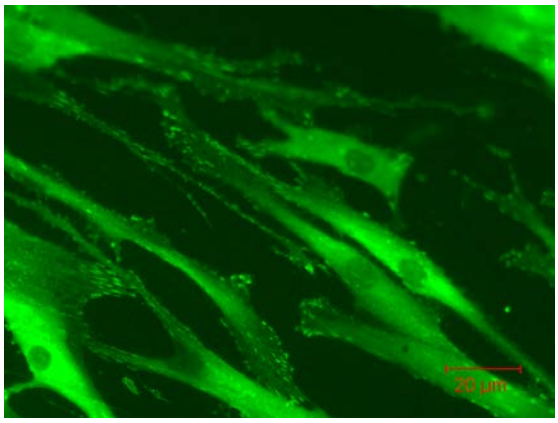

Figure 88: Anti-vinculin immunofluorescence of human mesenchymal cells cultured on a machined Ti6Al4V surface for 24 hours.

Human mesenchymal cells cultured on machined surfaces (Figure 88) also demonstrated significant contact guidance, with the cells polarised with their long axis parallel to the direction of the tooling marks. Focal adhesion complexes were observed mostly at the cell perimeters at the edges of the long axis.

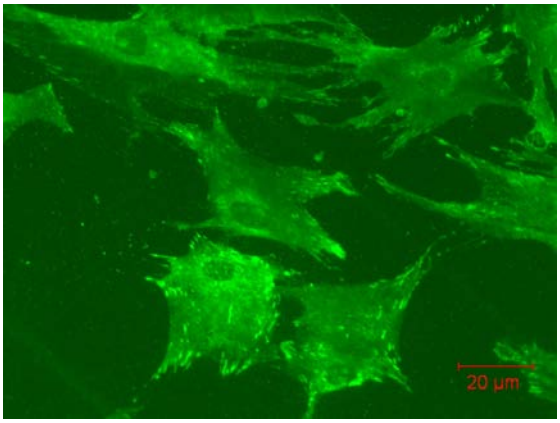

Figure 89: Anti-vinculin immunofluorescence of human mesenchymal cells cultured on a mechanically polished Ti6Al4V surface for 24 hours.

Cells cultured on the mechanically polished surfaces (Figure 89) demonstrated a similar morphology to those on the glass control surfaces, with relatively spheroid cells with few filopodia and large focal adhesion complexes.

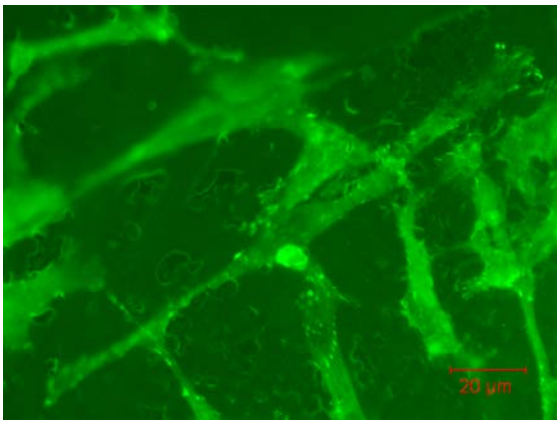

Figure 90: Anti-vinculin immunofluorescence of human mesenchymal cells cultured on a 3V180s treated Ti6Al4V surface for 24 hours.

The human mesenchymal cells cultured on 3V180s treated surfaces (Figure 90) were observed to have a much more elongated morphology with smaller focal adhesions. However the filopodia, although present, were less pronounced than those present on rat osteoblasts cultured on these surfaces.

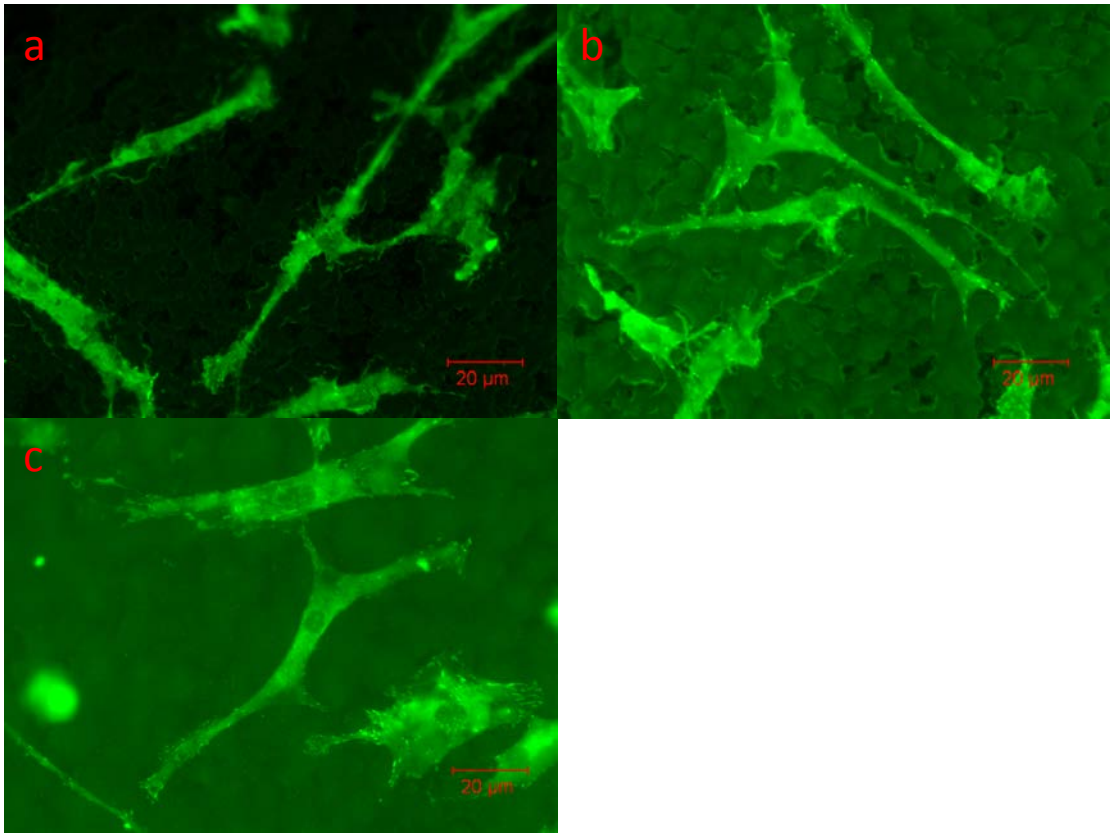

Figure 91: Anti-vinculin immunofluorescence of human mesenchymal cells cultured on a) 5V60s, b) 5V120s and c) 5V180s treated Ti6Al4V surfaces for 24 hours.

The cells cultured on the surfaces treated at 5V (Figure 91a, b and c) demonstrate decreasing polarisation and decreasing presence of filopodia with increased time of electrochemical treatment. Cells on all these surfaces were observed to have relatively small and fewer focal adhesions.

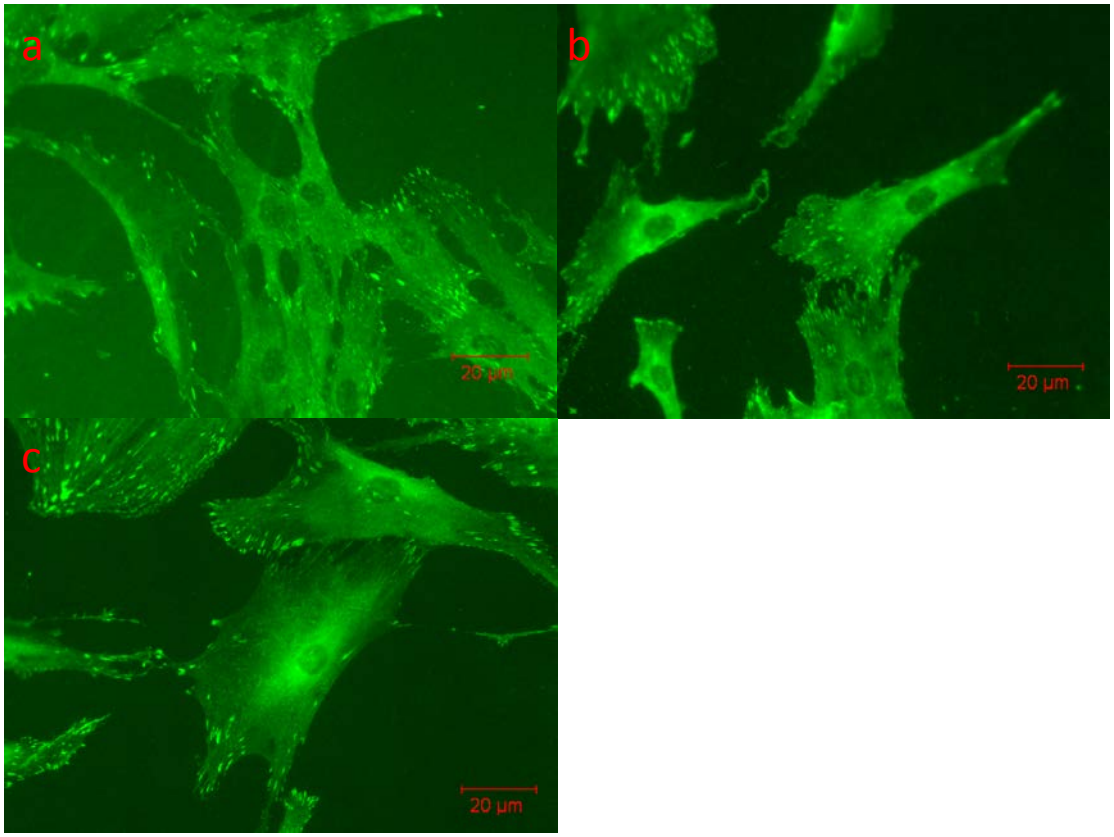

Figure 92: Anti-vinculin immunofluorescence of human mesenchymal cells cultured on a) 9V60s, b) 9V120s and c) 9V180s treated Ti6Al4V surfaces for 24 hours.

The human mesenchymal cells cultured on the surfaces treated at 9V (Figures 92a, b and c) all showed fewer filopodia, more numerous focal adhesion complexes and less elongated morphologies than those cultured on 3V and 5V treated surfaces.

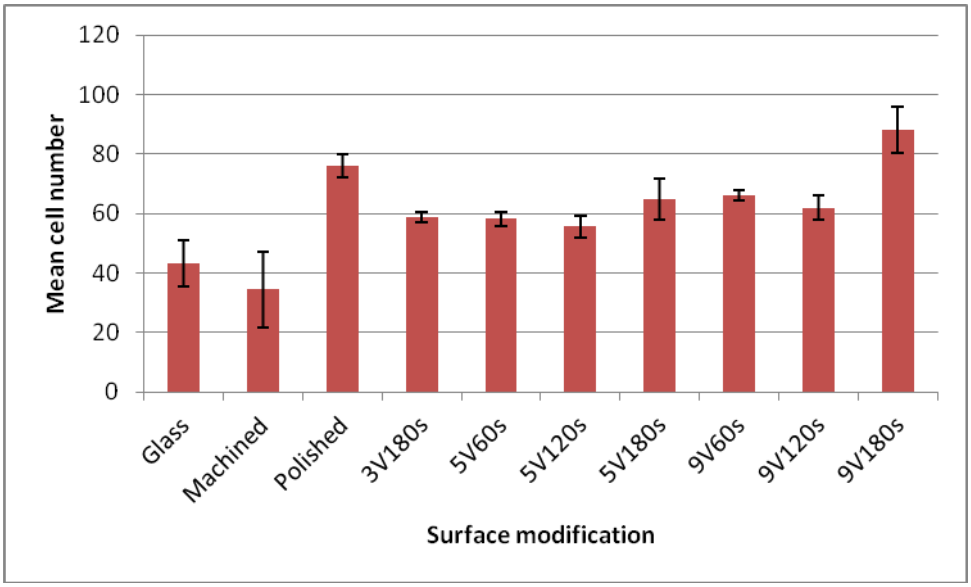

Figure 93: Bar chart illustrating the mean number of cells counted during immunofluorescence of human mesenchymal stromal cells cultured for 24 hours on the control and modified surfaces for 24 hours (results combined from 3 independent experiments).

As with the rat osteoblasts, no definite pattern was seen in the number of human mesenchymal cells on control or modified surfaces. The surfaces did not appear to systematically alter the proliferation or viability of the seeded cells.

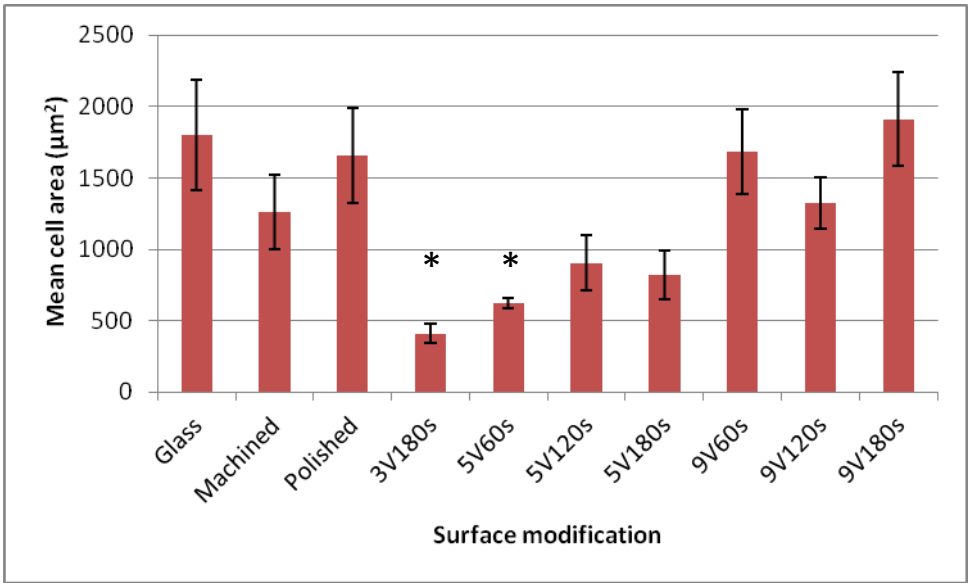

Figure 94: Bar chart demonstrating mean cell area (µm^2) of primary human mesenchymal stromal cells cultured on control and modified surfaces for 24 hours (data from 1 experiment representative of 3 independent experiments; n=10).

Human mesenchymal cell area is significantly smaller when cultured on 3V180s and 5V60s surfaces (Figure 94, marked with *) than on 9V180s treated surfaces ($p<0.05$).

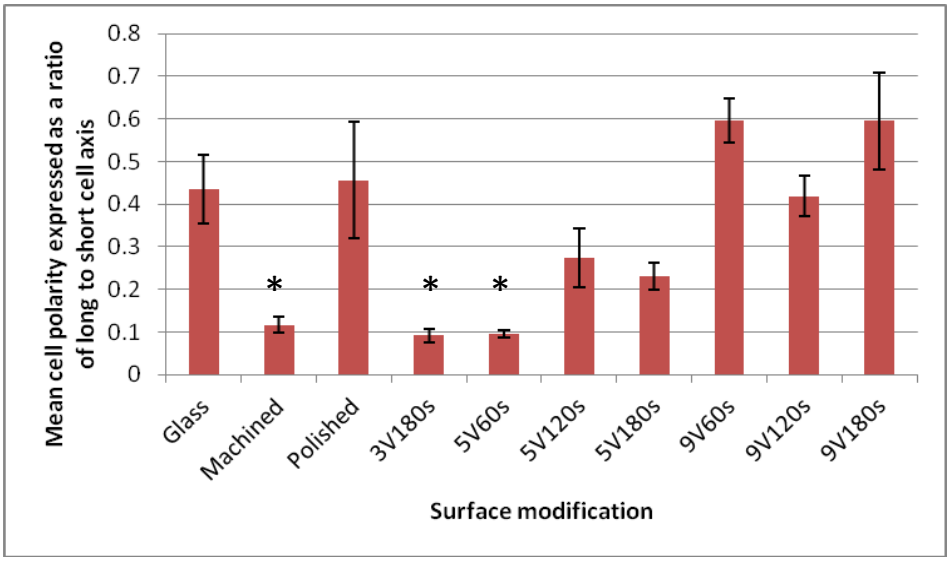

Figure 95: Bar chart recording cell polarity of human mesenchymal stromal cells cultured for 24 hours on control and modified surfaces as a ratio of long to short cell axis (data from 1 experiment representative of 3 independent experiments; n=10).

The graph above demonstrates that the polarity of the human mesenchymal cells is significantly more pronounced ($p<0.05$) when cultured on the 3V180s, 5V60s and machined surfaces (Figure 95, marked with *) than on the glass control, mechanically polished, 9V60s or 9V180s treated surfaces.

3.4.2. Focal adhesion quantification

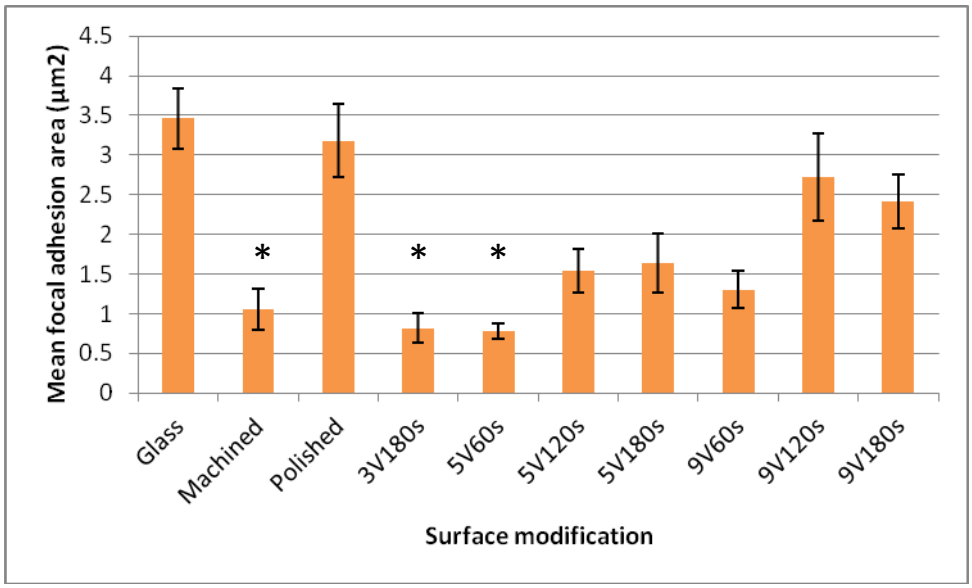

Figure 96: Bar chart illustrating mean area of focal adhesions measured from anti-vinculin immunofluorescence in human mesenchymal stromal cells cultured for 24 hours on control and modified surfaces (data from 1 experiment representative of 3 independent experiments; n=10).

The mean area of focal adhesion complexes in the human mesenchymal cells cultured on machined, 3V180s and 5V60s treated surfaces (Figure 96, marked with *) was significantly smaller ($p<0.05$) than those on the glass control, polished and 9V120s treated surfaces.

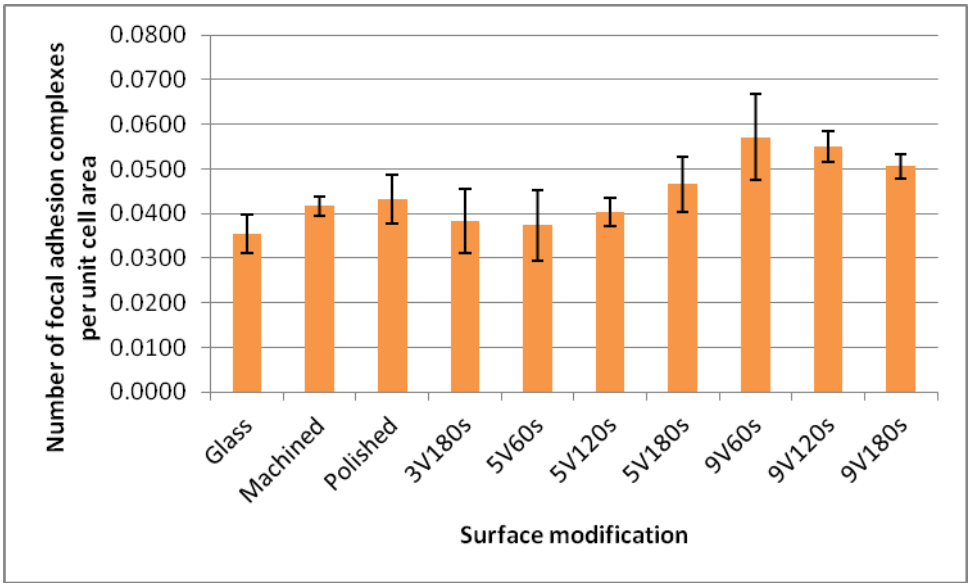

Figure 97: Bar chart demonstrating the number of focal adhesion complexes found per unit of cell area from anti-vinculin immunofluorescence after human mesenchymal stem cells were cultured for 24 hours on control and modified surfaces (data from 1 experiment representative of 3 independent experiments; n=10).

The graph above demonstrates that there are no significant differences in the number of focal adhesions per unit of cell area (per μm) in human mesenchymal cells cultured on the control and modified surfaces, although there is a non-significant trend towards more focal adhesions per unit cell area in the cells cultured on the surfaces treated at 9V.

3.5. Alkaline phosphatase assay

Alkaline phosphatase is a marker for matrix mineralisation and indicates commitment to osteoblast differentiation. Alkaline phosphatase activity was quantified using p-nitrophenol as a substrate after 21 days of culture in osteogenic media.

3.5.1. Rat osteoblasts

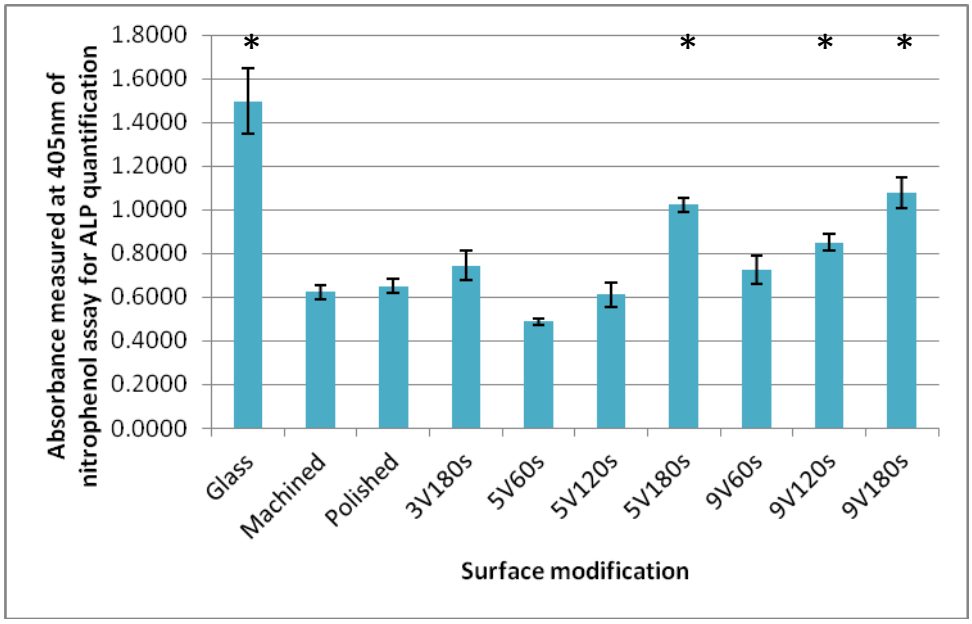

Figure 98: Bar chart displaying the absorbance measured at 405nm from p-nitrophenol assay for quantification of alkaline phosphatase activity of rat primary calvarial osteoblasts cultured for 21 days on glass control and modified surfaces (results of 1 experiment, representative of 3 independent experiments).

The above bar chart (Figure 98) displays the results of an alkaline phosphatase activity assay using p-nitrophenol substrate with cells grown on glass control and modified titanium alloy surfaces. Results are not normalised for cell number as the processing of the experimental surfaces for alkaline phosphatase quantification caused cells to peel off the surfaces and an accurate count was not possible. Counts of cell number during the immunofluorescence experiments, however, did not demonstrate systematic differences in cell number between the surfaces (Figure 80). Alkaline phosphatase activity was significantly greater on the glass control, 9V180s, 9V120s and 5V180s (Figure 98, marked with *) treated surfaces than on the machined, mechanically polished, 5V60s and 5V120s treated surfaces.

3.5.2. Human mesenchymal stromal cells

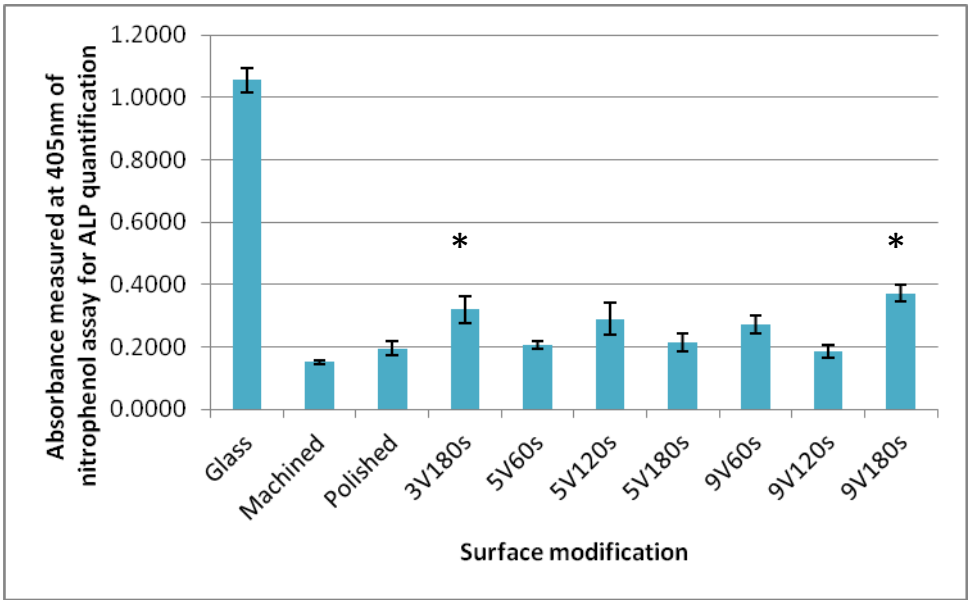

Figure 99: Bar chart displaying the absorbance measured at 405nm from p-nitrophenol assay for quantification of alkaline phosphatase activity of human mesenchymal cells cultured for 21 days on glass control and modified surfaces (results of 1 experiment, representative of 3 independent experiments).

The graph (Figure 99) above demonstrates that the highest alkaline phosphatase activity was seen in cells cultured on glass control surfaces ($p<0.05$). As with the rat osteoblasts, quantification of cell number following the experiment was not possible and no systematic differences in cell number with surface treatment were observed in immunofluorescence experiments (Figure 93). Of the cells grown on titanium alloy surfaces, there was significantly greater alkaline phosphatase activity seen with the cells on the 3V180s and 9V180s (Figure 99, marked with *) treated surfaces than on the machined and polished surfaces ($p<0.05$).

3.6. Bone nodule staining

Primary rat calvarial osteoblasts and human mesenchymal stromal cells were cultured for 28 days in osteogenic media then stained with alizarin red. This stains the calcium in the calcified bone nodules, allowing measurement of their area and following de-staining the intensity of alizarin red may be quantified using an optical plate reader. Taken together this allows the degree of calcified matrix formation by the osteoblasts to be quantified, thereby allowing investigation in vitro, of the long term growth and differentiation potential of bone precursor cells on the modified surfaces.

3.6.1. Rat osteoblasts

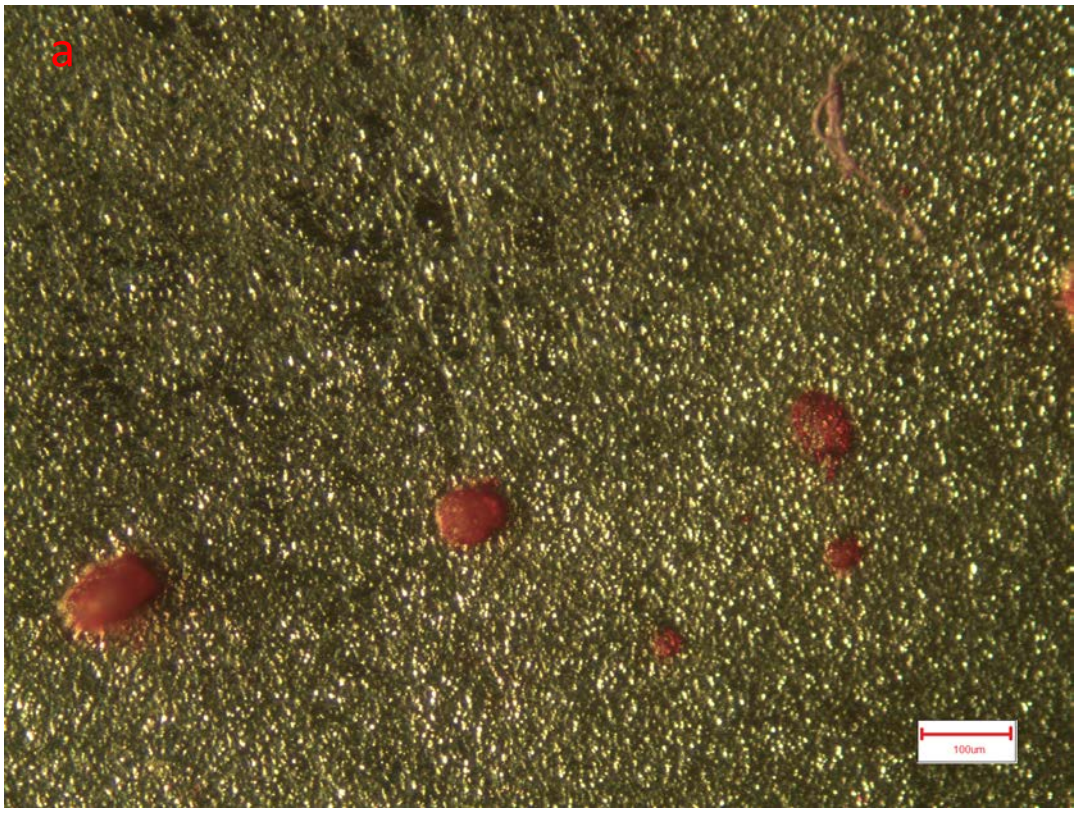

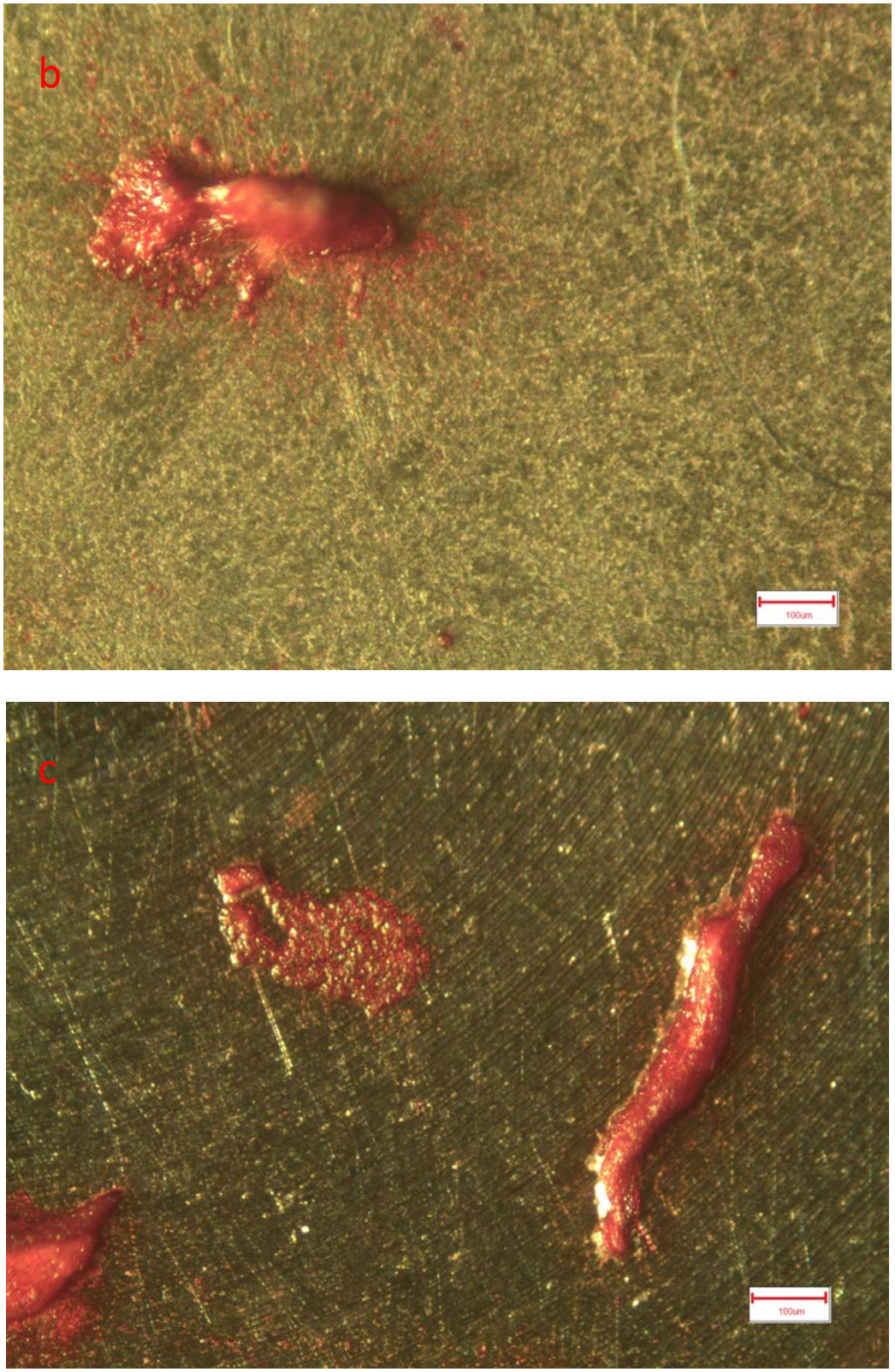

Figure 100: Incident light photomicrographs of bone nodules stained with alizarin red on a) 3V180s, b) 9V180s and c) machined surfaces.

Figure 100 demonstrates photomicrographs of bone nodules stained with alizarin red. The nodules on the 3V180s surface were observed to be small but frequent. Those on the 9V treated surfaces were larger, randomly oriented and less numerous. Those observed on the machined surface were seen to follow the machine tooling marks with their long axes aligned parallel to the grooves in the majority of cases, demonstrating organisation of matrix deposition on the macroscopic scale.

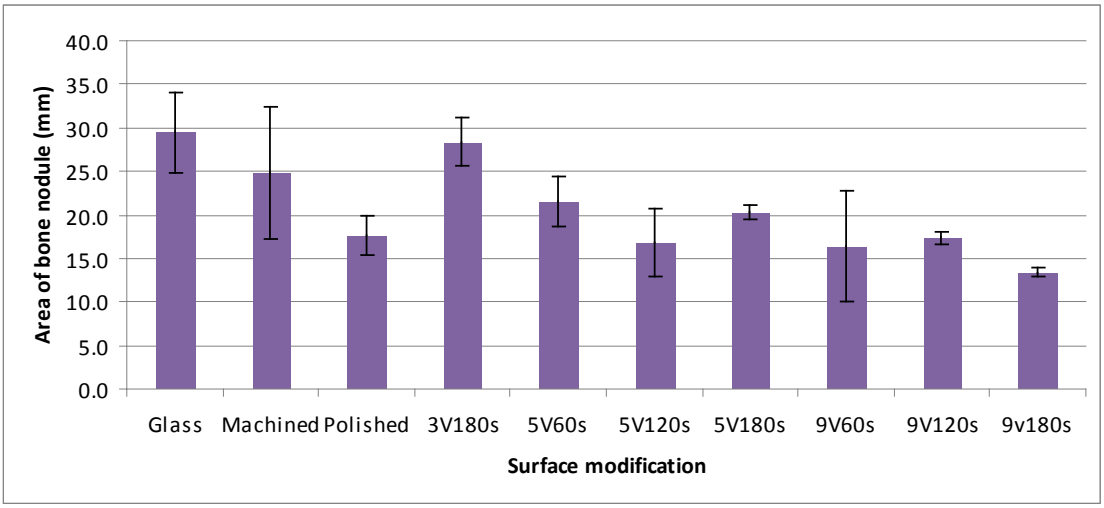

Figure 101: Area of bone nodule formed on treated surfaces following 28 days culture in osteogenic media, measured from digital photographs of surfaces (results of a single experiment representative of 3 independent experiments).

Analysis of variance with pairwise comparisons using Tukey's post-test comparison with 95% confidence intervals reveals no significant differences in the area of bone nodule staining on any of the surfaces, using primary rat calvarial osteoblasts after 28 days of culture in osteogenic media (Figure 101).

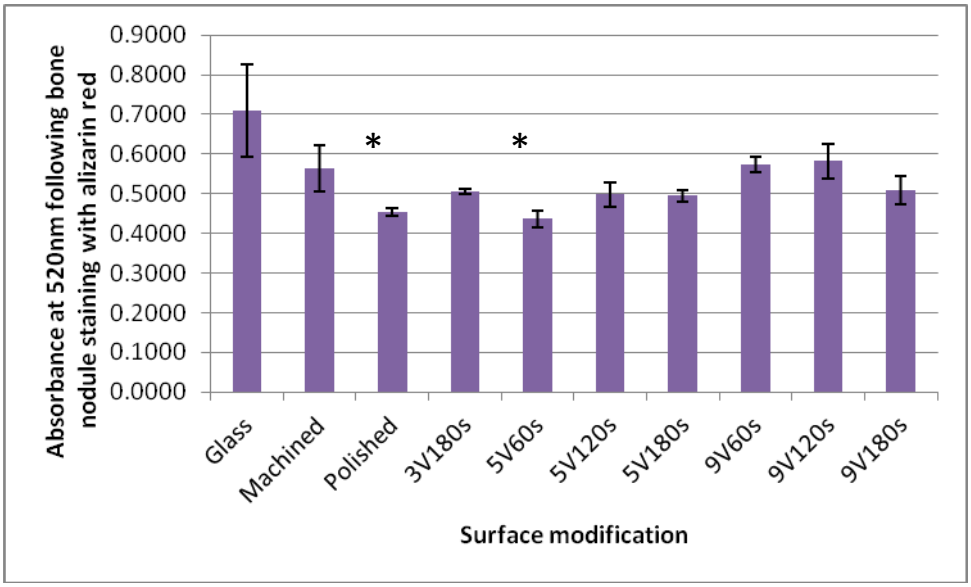

Figure 102: Absorbance at 520nm following culture of rat primary calvarial osteoblasts for 28 days and staining with alizarin red (results of the same single experiment as in Figure 101, representative of 3 independent experiments).

Absorbance of alizarin red staining is significantly lower on the mechanically polished and 5V60s (Figure 102, marked with *) treated surfaces than all other surfaces.

3.6.2. Human mesenchymal stromal cells

During culture in osteogenic media for 28 days the human mesenchymal cells did not form bone nodules, which were large enough for macroscopic image analysis. Rather, they formed a more homogeneous layer of mineralisation on the surfaces, amenable to analysis using absorptiometry.

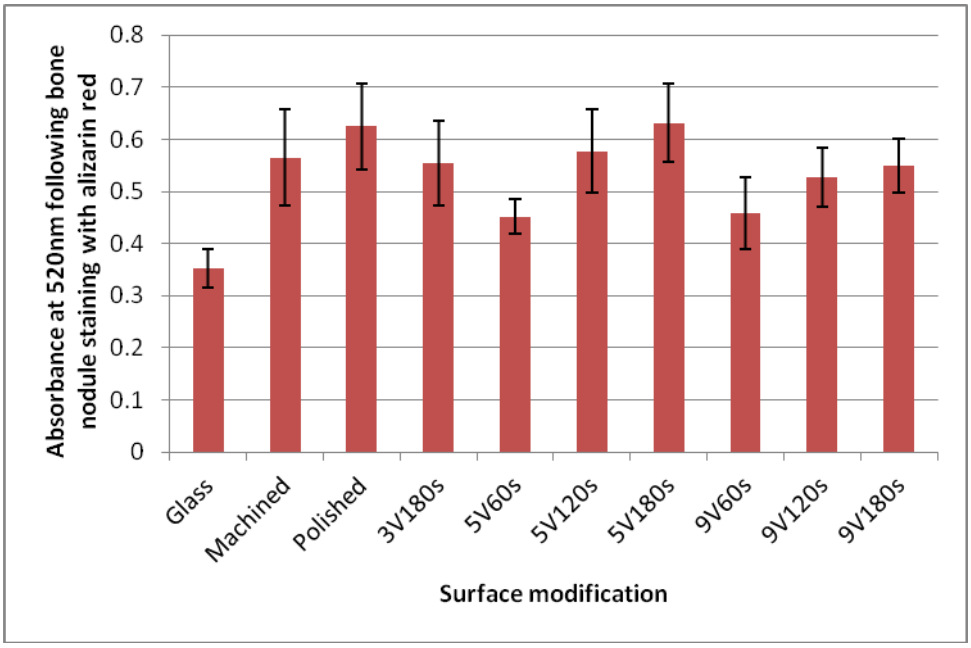

Figure 103: Absorbance at 520nm following culture of human mesenchymal cells for 28 days and staining with alizarin red.

Analysis of variance with pairwise comparisons using Tukey's post-test comparison with 95% confidence intervals reveals no significant differences in the quantity of alizarin red staining on any of the surfaces.

3.7. Discussion

In this series of experiments, the surface physical and chemical characteristics of the electrochemically treated surfaces were investigated and correlated with observations of the morphology and early adhesion behaviour, as well as the function in longer term culture, of rat osteoblasts and human mesenchymal cells on the surfaces.

Current profiles produced during the electrochemical modification of the surfaces demonstrated high initial currents decaying to a plateau due to the formation of the surface oxide film. At this point in the process it is not possible to increase the current by increasing the supplied potential, as extra potential is used to transport ions and electrons across the oxide layer. For this reason, the oxide layer increases in thickness with increasing supplied potential.

Residual grooves in the surfaces were evident even after the finest mechanical polish. Some of the features of the surfaces after electrochemical modification may be explained by pre-existing variations in the surface alloy, either from the manufacturing or from heat stress at the machined surfaces following sectioning of the titanium alloy rods into 1cm sections for workpieces. If these experiments were to be repeated, it may be possible to form more uniform surfaces to apply the electrochemical treatments to by performing a high voltage (9V) polished to all the surfaces, creating a very flat, almost featureless surface to begin with before each of the different electrochemical modifications were applied.

Light microscopy with optical profilometry was used to characterise the micron-scale features of the modified surfaces and atomic force microscopy and scanning electron microscopy were used to assess nanometre scale architecture. Optical profilometry demonstrated generally amorphous features on all modified surfaces but a trend towards fewer features with smoother transitions between features on the surfaces treated with higher voltages for longer times. This correlated with the AFM results of significantly lower R_A values at the nanometre scale on the 9V treated surfaces due to the smaller amplitude features, which were observed to be crystalline in nature on the SEM images. All the experimental surfaces were relatively smooth at the micron and nanometre scales in comparison to commercially available grit-blasted surfaces, which have been

observed by others to improve osteoblast growth and adhesion (Boyan et al 2002, Meyer et al 2005). However, the surfaces in this study all demonstrate a semi-structured nanometre pattern and nanometre scale structure (in the less than 100nm range) that has been shown to improve early osteoblast adhesion (Rani et al 2009, Tambasco de Oliveira et al 2007).

The chemical composition of the surface oxide layer of the modified titanium alloy surfaces was analysed using x-ray photoelectron spectroscopy. This method demonstrated a trend of decreased percentage content of aluminium and vanadium in the oxide layer with increasing voltage and time of electrochemical processing. This is similar to the graduated oxide layers produced by oxidation of titanium alloy substrates under physiological conditions (Milošev et al, 2000), producing an essentially TiO_2 layer on the surface of the alloy, providing a more favourable surface for the adhesion of osteoblasts. Aluminium is known to exhibit cellular toxicity, being implicated in the development of disorders such as Alzheimer's disease, Parkinson's disease and osteomalacia. The mechanism underlying many of these effects is accelerated cell death through disruption of second messenger systems (Exley and Birchall, 1992). Osteomalacia due to aluminium toxicity, or failure of normal mineralisation of bone matrix, is particularly seen in renal dialysis patients and in histology of bone from these patients, aluminium deposits are noted at the junction between mineralised and non-mineralised osteoid (Rapoport et al, 1987). Vanadium has been recognised as able to interfere with the normal function of the cell membrane sodium pump and has been noted to be toxic to osteoblast and osteosarcoma cell lines, likely due to increased oxidative stress (Cortizo et al, 2000). There is therefore evidence that aluminium and vanadium may interfere with normal osteoblast function and may partly explain the observation of increased early cellular adhesion on the modified surfaces treated at higher voltages and longer times. However, as the in vitro experiments were conducted over relatively short time spans, the initial effect of the surface chemistry on adhesion and early osteoblast behaviour may be most important.

The morphology of rat calvarial osteoblasts cultured for 24 hours on the experimental surfaces was investigated using immunofluorescence with antibodies for anti-vinculin, a cell membrane component protein, which is concentrated in focal adhesion complexes.

Along with cell number, area and polarity (or roundness), it was possible to measure area, number and distribution of focal adhesion complexes, which are the main points of anchorage of the cells to the underlying surface. The number of rat osteoblasts after 24 hours did not appear to be related to the experimental surface. Although the same number of cells was seeded onto each surface, it is possible that the effect of initial cell distribution or other minor variations in culture conditions had more effect on the final cell numbers than any effect from the culture surface. Cell area and cell polarity were observed to be affected by experimental surface with significantly smaller area and greater polarity of cells cultured on the 3V180s and 5V treated surfaces compared to the 9V treated, glass control and polished surfaces. This is explained by cells exhibiting increased adhesion points and enhanced spreading at early time points on the 9V, polished and glass control surfaces. This explanation is reinforced by the observation of the greater mean focal adhesion area and the greater number of focal adhesion complexes per unit of cell area on the 9V than the 3V and 5V treated surfaces. These are the complexes forming the main links between the cell membrane and the surface, with larger complexes and greater numbers of complexes indicating improved early adhesion of the cells to the 9V and polished surfaces. Previous studies have demonstrated that micron-scale features present regions for the attachment of focal adhesion complexes, thereby influencing the shape of cell filopodia and consequently cell attachment and motility (Bigerelle et al, 2002), whereas nanoscale features may be sensed by cell filopodia but do not necessarily provide further areas for attachment (Berry et al, 2006). It has been observed in previous studies that human endothelial cells show increased cell-surface adhesion on NiTi alloys, which have been heat treated in order to decrease the proportion of nickel in the surface alloy layers (Plant et al, 2005). This supports observations made in these experiments that reduction in the presence of the alloy metals (aluminium and vanadium) in the surface titanium oxide layer may promote osteoblast adhesion.

To assess the influence of surface topography, rat calvarial osteoblasts were also cultured for 24 hours on polycaprolactone moulds of the experimental surfaces. As the chemistry of the polycaprolactone surfaces were all identical, any differences in cell morphology observed on the surfaces was considered to be due to changes in topography. The results of these experiments demonstrated significantly increased cell

area and significantly decreased cell polarity on the mould of the 9V treated surfaces compared to the moulds of the 3V and 5V treated surfaces with the trend being more exaggerated than that observed for the experimental surfaces themselves. As the trends were observed to be in the same direction for growth on both titanium and polycaprolactone surfaces, this would suggest that the observed trend on the treated surfaces is mostly due to topography. However the trend was not identical on the titanium and polycaprolactone surfaces, suggesting a smaller observable effect on cell adhesion from surface chemistry.

Short term cell culture was repeated using human mesenchymal stromal cells to confirm whether the pattern observed in the rat osteoblasts was continued in human bone precursor cells. As with the rat osteoblasts, no systematic differences were produced in cell number by the different surface treatments, suggesting no short term effect of any of the surfaces on cell viability or proliferation. A similar pattern of cell area and polarity was seen with the human cells as with the rat osteoblasts, with smaller, more polarised cells observed on the 3V180s and 5V treated surfaces and machined surface compared to the polished and 9V surfaces. The polarisation of the cells on the machined surfaces was in line with the macroscopic grooves on the surface from cutting with the circular straw, producing contact guidance. The polarisation of the cells on the 3V and 5V treated surfaces was in randomly oriented directions, which was likely the result of poor early adhesion of the cells to these surfaces. Weight is leant to this conclusion by the significantly greater mean area of focal adhesions per cell on the 9V120s and 9V180s surfaces than on the 3V and 5V treated surfaces. There was also a trend towards a greater number of focal adhesions per unit of cell area in the cells cultured on the 9V surfaces, although in the human cells, unlike the rat osteoblasts, this did not reach significance. The focal adhesions in the human cells were on average smaller and less dense than those in the rat cells, this may have been due to the human cells being less metabolically active, less easily grown in a culture system or more heterogeneous than the rat cells.

Cell differentiation towards a more mature phenotype was assessed by longer term culture for 21 days. At the end of this time, an assay was conducted to quantify alkaline phosphatase activity. Alkaline phosphatase is an enzyme involved in the process of

matrix mineralisation and is therefore a measure of osteoblast differentiation and function. The pattern of increased early cell adhesion and growth on 9V treated surfaces after 24 hours in culture did not correlate with an increase in enzyme activity at 21 days. The greatest alkaline phosphatase activity was seen in the cells cultured on the 5V180s, 9V120s and 9V180s surfaces. A trend was also seen for increasing alkaline phosphatase activity with increasing time of electrochemical processing at both 5V and 9V. This may suggest a greater role for surface chemistry rather than topography at this later time point as greater processing time leads to greater oxide layer thickness. When the experiment was repeated with human mesenchymal stem cells, there was less enzyme activity overall, with higher alkaline phosphatase activity observed on the 3V180s and 9V180s treated surfaces, which does fit with the general pattern of greater activity on the surfaces treated for longer times. The reduced enzyme activity may have been due to the origin of the human mesenchymal cells, from older adults undergoing hip and knee replacement surgery. It may also have been due to the slower rate of maturation and differentiation of human cells, which might mean that this experiment would have been better performed at a later time point for the human cells, when their ALP activity may have been greater. This may have resulted in cell populations with generally decreased enzyme activity which may not have been evident in a younger donor population. The cell may also have been at a different stage of differentiation than the rat osteoblasts when placed in culture and as the experiment was only performed at one time point, any differences in enzyme activity at other time points would not have been observable.

Measurement of area of mineralised bone nodule formation was performed after 28 days in culture, in order to assess the ability of bone precursor cells on the experimental surfaces to fulfil their intended role of producing mineralised bone matrix. Previous research would suggest that differences in cell behaviour on modified surfaces is most evident on observations of early cell adhesion and these differences are often lost at later time points when cell behaviour and growth tends to converge to a mean (Yang T, 2005; Justesen 2009). This was also the observation from the bone nodule staining experiments. No significant differences were seen in the total area of bone nodules produced on any of the experimental surfaces with rat calvarial osteoblasts. This may have been because although the individual bone nodules on the 9V treated surfaces were larger in area, those on the 3V and 5V treated surfaces were more numerous. This assay

was not possible with human mesenchymal cells as they did not form discrete bone nodules, but rather a layer of diffuse mineralisation. The quantity of mineralised bone matrix was also measured using a colorimetric method to quantify the amount of alizarin red staining removed from the bone nodules with both rat calvarial osteoblasts and human mesenchymal cells. Significantly less staining was seen on the polished and 5V60s surfaces, with a trend towards greater staining on the 9V treated surfaces. This trend may be different to that observed in the area measurements as the volume or density of the bone nodules on the 9V treated surfaces may have been greater than on the 3V treated surfaces, therefore holding more stain. No significant differences were observed between the quantities of staining on the different surfaces for human mesenchymal cells and the previous trends towards improved osteoblast adhesion and growth on the 9V surfaces were reversed, with slightly greater staining seen on the 5V treated surfaces. These observations suggest that the early differences produced in adhesion by the experimental surfaces do not translate to a specific advantage in promoting osteoblast function and growth over the longer term in culture. This may be a feature of the experimental design as the mechanical forces present in vivo were not replicated within this cell culture system but play an important role in osseointegration of implants in vivo. Any longer term effects of the surfaces on bone formation may also be muted by the fact that once the initial layer of cells have formed a mechanically robust cytoskeleton, producing stable cell-surface adhesion, further layers of cells are laid down in mechanically and chemically similar environments on all surfaces.

Chapter 4. Results 2 – Investigation of osteoblast adhesion and communication behaviour

4.1. Introduction

The process of maturation of pre-osteoblasts is characterised by a cascade of gene activation. The differentiation of pluripotent stem cells into osteoblasts is controlled by several transcription factors. The earliest of these are Runx2 and the downstream effector osterix. Further downstream in the cascade, the *BGLAP* gene is upregulated, which produces osteocalcin (bone gamma-carboxyglutamate protein), a protein involved in matrix mineralisation. Quantitative real-time PCR was used to measure the relative expression of the osteogenic genes in order to provide a profile of differentiation for the cells cultured on the experimental surfaces to investigate the influence of electrochemically modified surfaces on the temporal regulation of osteogenic genes.

Cadherins are a group of transmembrane glycoproteins, which are present in a wide variety of cells but the presence of cadherin-2 and cadherin-11 is characteristic of mature osteoblasts. Their function in the cells is the formation of adherens junctions that link adjacent cells through their extra-cellular domains. They also form part of signal transduction pathways via their activation of the Wnt pathway and by the actions of the catenins on the cytoskeleton. Previous research has demonstrated the cadherin gene expression in osteoblast lineage cells is affected by the chemistry and morphology of titanium surfaces. Diamond-like carbon coating and hydrofluoride coating increased the expression of cadherin-13 (Kim et al 2006). There is no evidence in the current literature regarding the effect of surface chemistry or roughness on the quantity of cadherin protein present in the cell membrane. As well as quantifying cadherin gene expression differences in cells cultured on the treated surfaces, immunofluorescence for cadherin-11 demonstrates the distribution of the protein product in the cell. The following immunofluorescence experiments were performed with the purpose of quantifying the amount of cadherin present in the cell membranes, in the region of the cell where it is functional as part of the adherens junction complexes. This would provide insight into how cell-cell communication is linked to the observed differences in morphology observed in the cells cultured on the different treated surfaces.

Rho and Rac are subgroups of a family of small GTPases which are necessary for the production of cadherin-based adherens junctions and connexin-based gap junctions. They are also involved in the transduction of signalling between cell membrane receptors and the nucleus, thereby affecting gene expression and cytoskeletal orientation and tension. Both the Rho and Rac families exert their effects on adhesion of cells to substrates through the cytoskeleton and formation of focal adhesion complexes. They also promote adhesion to the extracellular matrix through clustering of integrins. Previous work has demonstrated that inhibition of RhoA reduces the contact guidance of mesenchymal cells and osteoblasts by nanometre grooves on titanium alloy substrates (Calzado-Martín et al. 2011). The RhoA and Rac1 assays were used in these experiments to quantify the activity of these GTPases on the osteoblasts cultured on the experimental surfaces. Inhibition of ROCK and Rac1 were investigated by assessing immunofluorescence for vinculin to study the effects on focal adhesion formation and therefore adhesion of cells to treated surfaces. In Chapter 3, electrochemically modified surfaces were shown to influence early adhesion and growth of osteoblasts. In this chapter, experiments are described that aim to provide mechanistic insight into how experimental surfaces regulate cell biology.

The aims of this section of experiments were:-

- To characterise the expression of genes involved in osteogenesis and cellular adhesion, by rat osteoblasts cultured on the treated surfaces
- To investigate the distribution of cadherin-11, a component of adherens junctions, in rat osteoblasts
- To measure activity levels of the small GTPases Rho and Rac, which are involved in cellular communication and intracellular signalling
- To investigate the effect of inhibiting Rho and RAC on cellular adhesion, as measured by immunofluorescence staining for vinculin, a component of focal adhesions

4.2. Regulation of gene expression in osteoblasts cultured on electrochemically modified surfaces

Real-time PCR was performed on cDNA extracted from cells cultured on the modified surfaces for 7 days in osteogenic media. This was intended to provide quantitative data about the activity of genes involved in osteoblast differentiation (Runx2, osterix, osteocalcin) and cell-cell communication (cadherin-2 and -11) on the different surfaces. However, despite 5 repeats of the experiment, the data remained very heterogeneous, as can be appreciated from the error bars on the graphs, which represent standard error of the mean. In each set of data, 2 repeats of the experiment were discarded as outliers and the mean of the other 3 repeats of each experiment are presented in the graphs below as a ratio of the measurement from the cells cultured on the glass surface, for the purposes of scale.

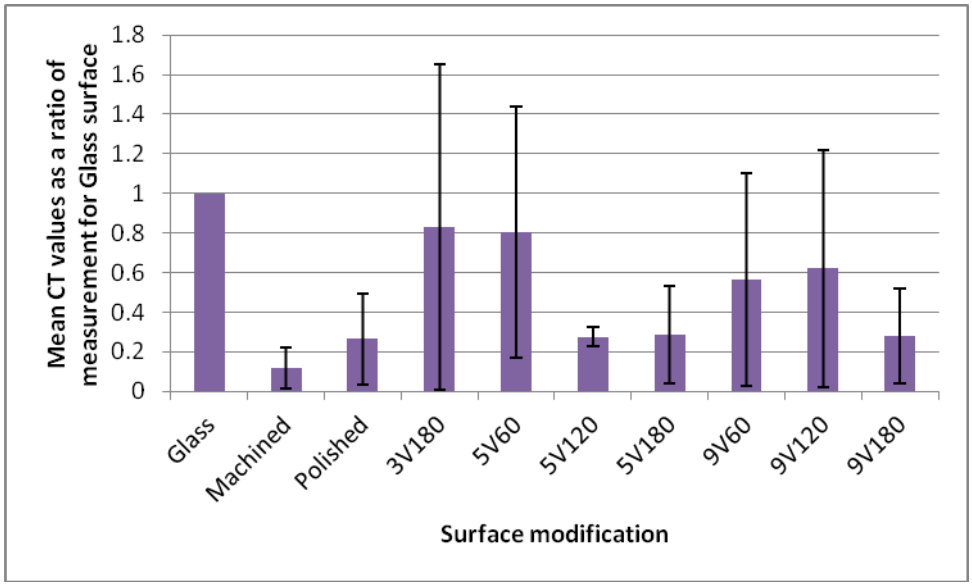

Figure 104: Graph of mean CT values for Runx2 taken from 3 separate real-time PCR runs (GAPDH used as housekeeping gene) after culture of cells on modified surfaces for 7 days in osteogenic media (error bars represent standard error of the mean).

Figure 104 illustrates the expression of the gene Runx2 relative to that of GAPDH. Runx2 is one of the earliest genes observed to be switched on in the cascade of differentiation of osteoblasts. No significant differences were observed in the expression of this gene in these experiments.

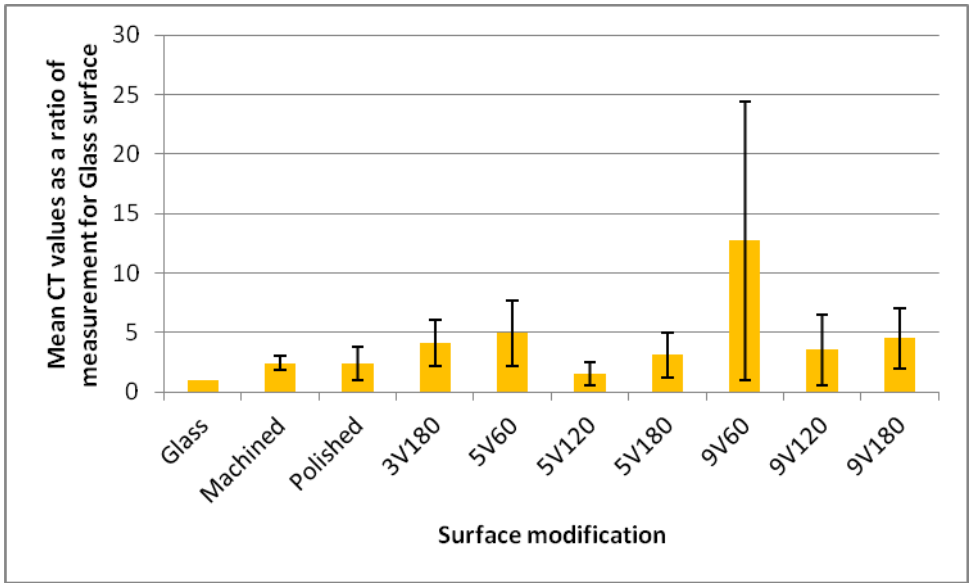

Figure 105: Graph of mean CT values for osterix taken from 3 separate real-time PCR runs (GAPDH used as housekeeping gene) after culture of cells on modified surfaces for 7 days in osteogenic media (error bars represent standard error of the mean).

Figure 105, above shows that no significant differences were observed in the activity of osterix extracted from the cells cultured on any of the experimental surfaces. Osterix is activated as a downstream effector of Runx2 in the differentiation of osteoblasts.

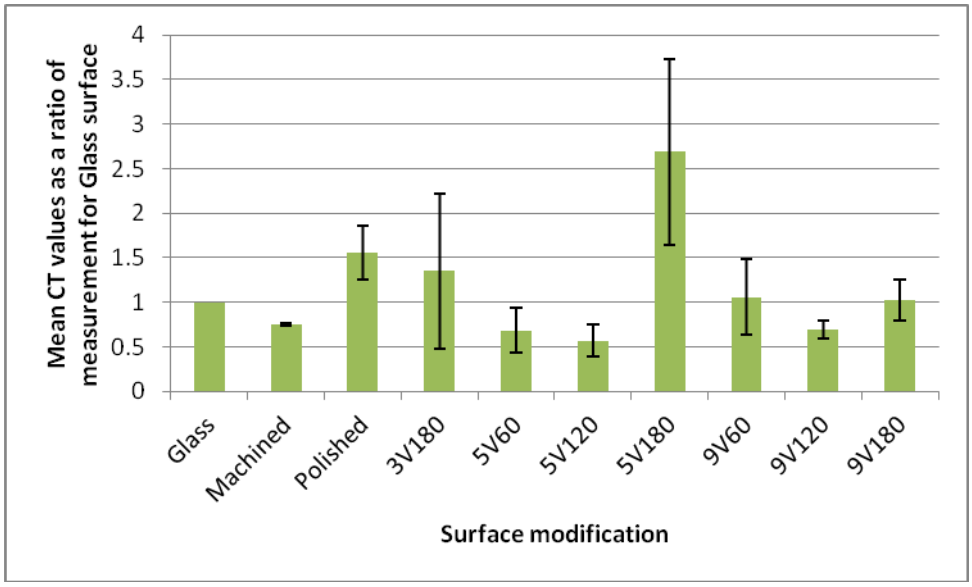

Figure 106: Graph of mean CT values for osteocalcin taken from 3 separate real-time PCR runs (GAPDH used as housekeeping gene) after culture of cells on modified surfaces for 7 days in osteogenic media (error bars represent standard error of the mean).

The above graph (Figure 106) demonstrates the gene expression of osteocalcin on the experimental surfaces. There were no observed statistically significant differences.

Osteocalcin is a non-collagenous matrix protein found and in bone and can be used as a marker of later stages of differentiation of osteoblasts and their production of matrix.

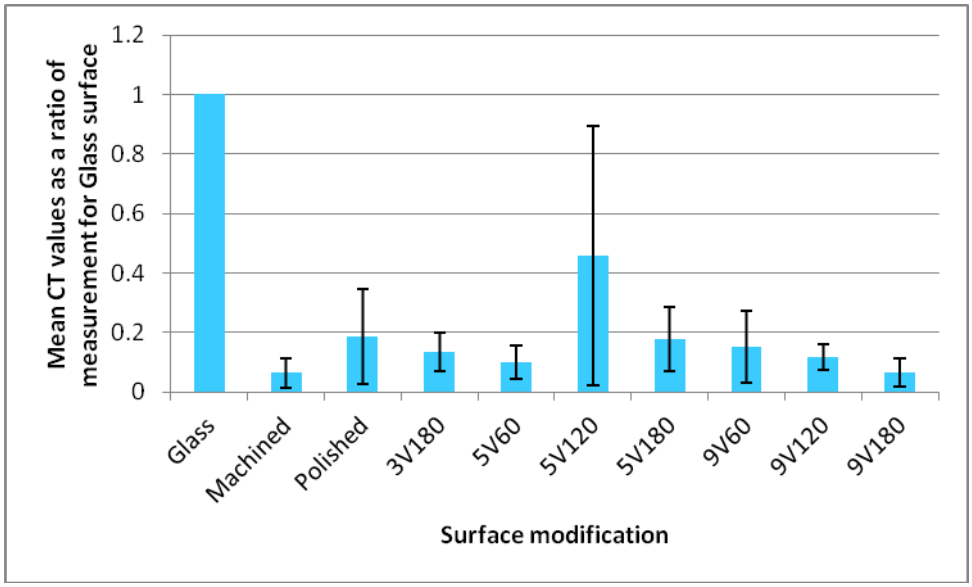

Figure 107: Graph of mean CT values for cadherin-2 taken from 3 separate real time PCR runs (GAPDH used as housekeeping gene) after culture of cells on modified surfaces for 7 days in osteogenic media (error bars represent standard error of the mean).

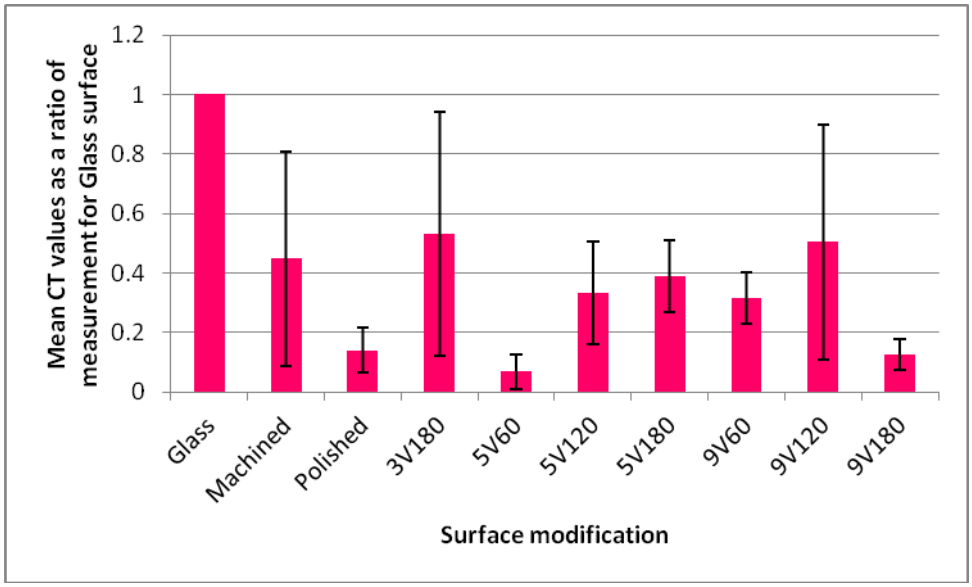

Figure 108: Graph of mean CT values for cadherin-11 taken from 3 separate real time PCR runs (GAPDH used as housekeeping gene) after culture of cells on modified surfaces for 7 days in osteogenic media (error bars represent standard error of the mean).

Figure 107 and Figure 108 above illustrate the expression of the genes cadherin-2 and cadherin-11, which are cell membrane proteins forming part of adherens junction complexes and therefore important to cell-cell communication. Although no significant differences were seen in cadherin-11 expression between the surfaces in these

experiments, there was significantly greater cadherin-2 measured on the glass and 5V120s treated surfaces.

4.3. Cadherin-11 immunofluorescence

The purpose of the following immunofluorescence experiments was to quantify the degree of staining for cadherin-11 in the cell membranes, where it is functional as part of the adherens junctions complexes, which are involved in cell-cell communication. These results were then correlated with the results of the anti-vinculin immunofluorescence experiments describing cell morphology.

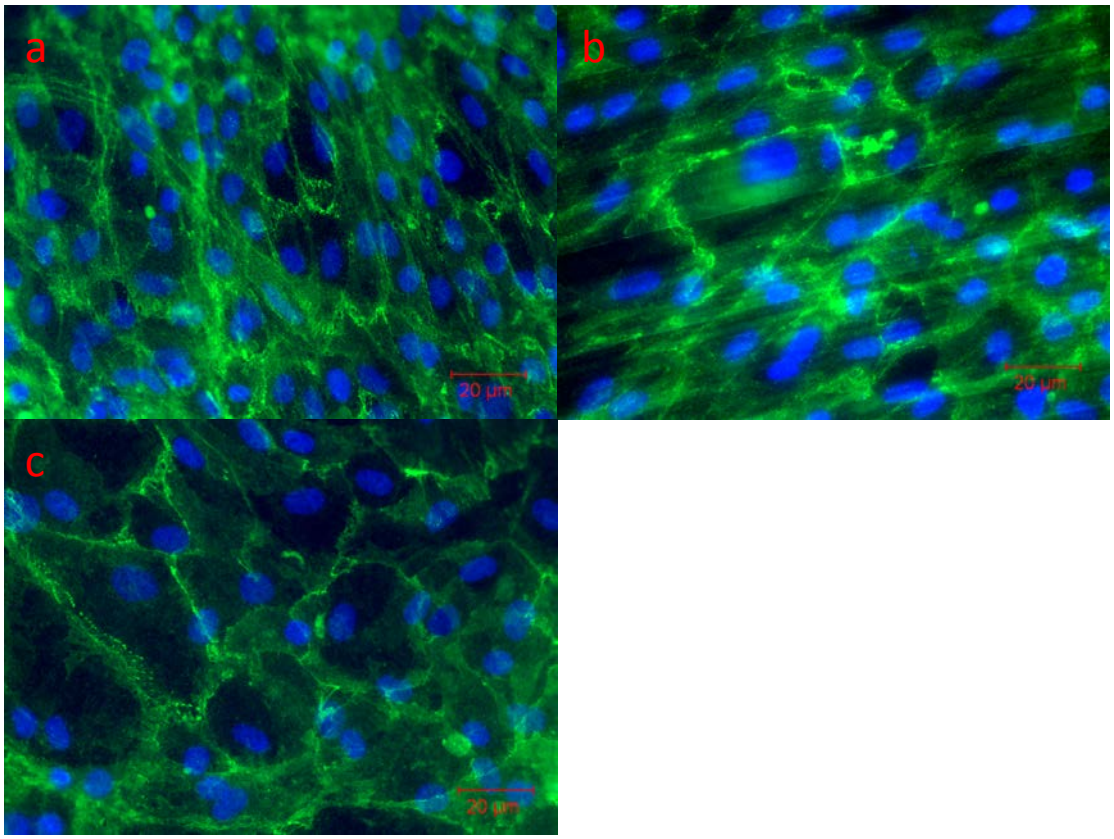

Figure 109: FITC Anti-cadherin-11 (green) and DAPI (blue) immunofluorescence of rat osteoblasts on glass (a), machined (b) Ti6Al4V and mechanically polished (c) surfaces

The cadherin-11 staining in the cell peripheries is most extensive and regular in the cells cultured on the polished surfaces (Figure 109c). This staining is also seen, to a lesser extent on the cells on the machined surface (Figure 109b). Cells cultured on glass (Figure 109a) display a well spread morphology, with large focal adhesions, indicating

strong cell-surface bonding but less peripheral staining of cadherin-11 was seen on the glass surfaces than the titanium surfaces.

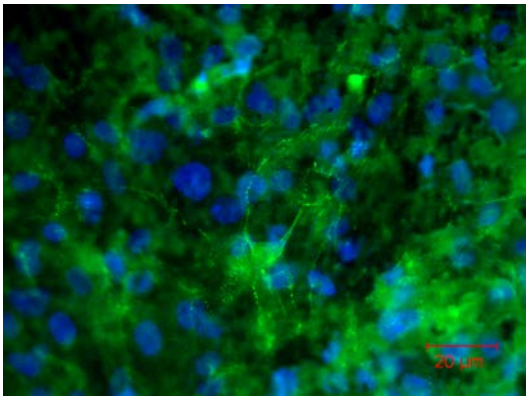

Figure 110: Anti-cadherin-11 and DAPI immunofluorescence of rat osteoblasts on a 3V180s treated Ti6Al4V surface

Very little peripheral staining was observed in the cells cultured on the 3V180s surfaces (Figure 110). Most of the staining was amorphous in nature and distributed throughout the cytoplasm, rather than discretely in the cell membrane.

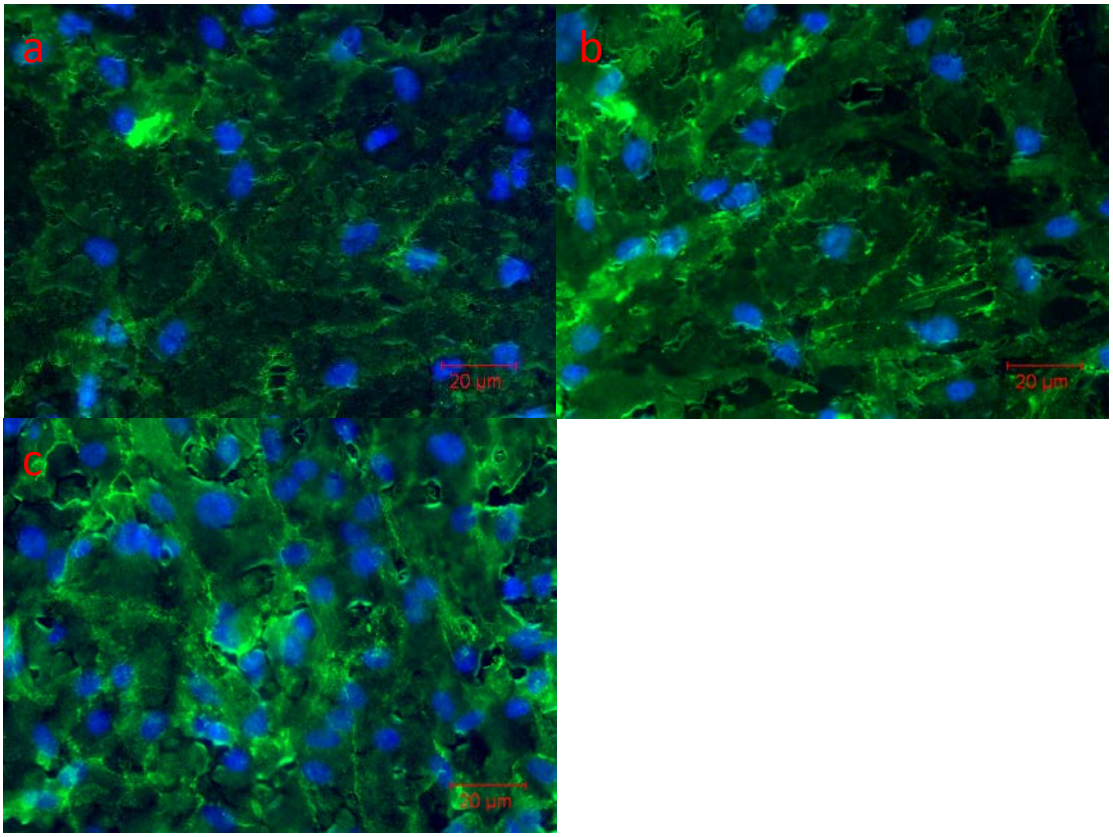

Figure 111 : Anti-cadherin-11 and DAPI immunofluorescence of rat osteoblasts on 5V60s (a), 5V120s (b) and 5V180s (c) treated Ti6Al4V surfaces

The cells cultured on the surfaces treated at 5V display increased cell membrane (Figure 111) staining compared to those on the 3V surfaces but it is not uniform around all the cells and there is still quite extensive staining visible in the cytoplasm.

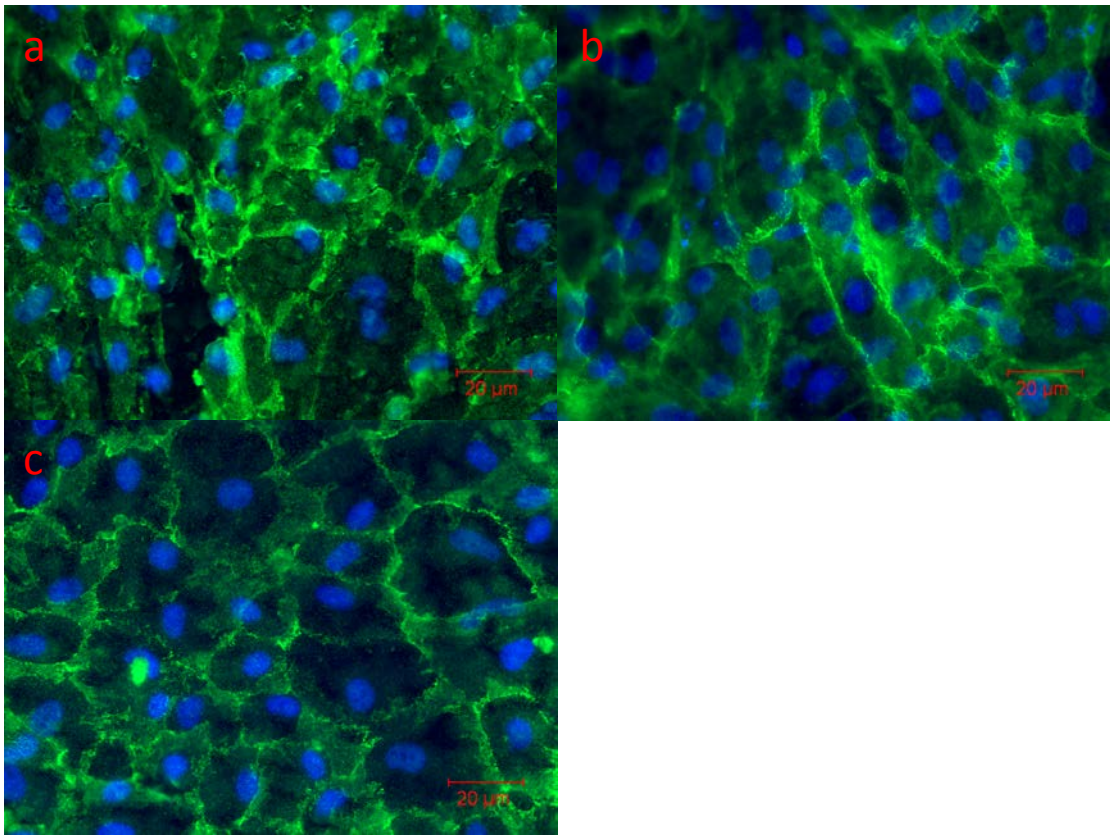

Figure 112: Anti-cadherin-11 and DAPI immunofluorescence of rat osteoblasts on 9V60s (a), 9V120s (b) and 9V180s (c) treated Ti6Al4V surface

The cells cultured on the surfaces treated at 9V (Figure 112) all display extensive, intense cadherin-11 staining, almost uniformly around their peripheries. The extent and uniformity of the staining is observed to increase with increasing time of surface treatment. This is also associated with an increase in regularity of size and shape of the cells.

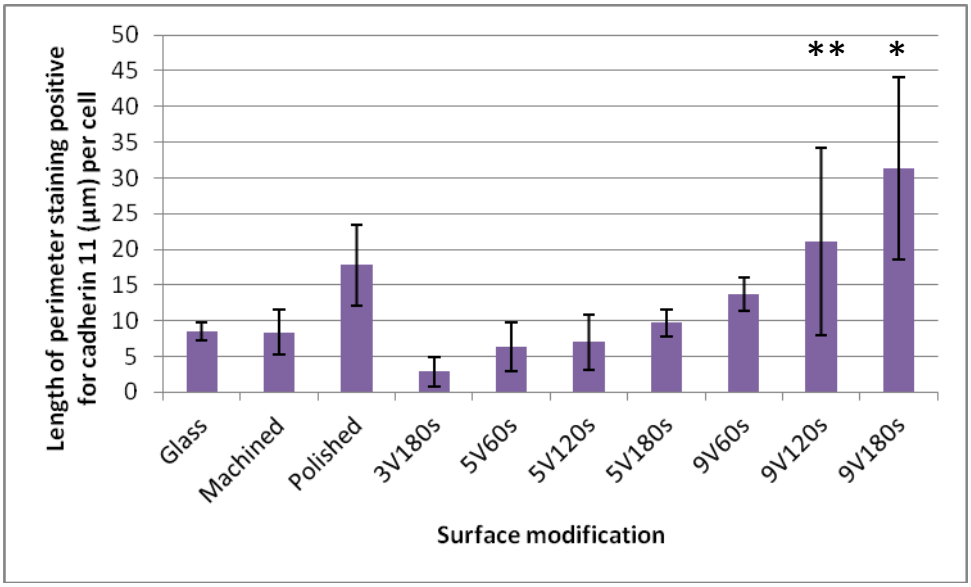

Figure 113: Graph of mean length of cell perimeter stained positive for cadherin-11 (µm) per cell, as a mean of 5 measurements taken from the results of one experiment, representative of three independent experiments in which rat osteoblasts were cultured for 7 days (error bars represent standard error of the mean).

There is a trend for increased cell perimeter staining for cadherin-11 in cells cultured on surfaces treated at higher voltages and for longer times. Using one-way analysis of variance, these differences are significant between the cells cultured on the 9V180s (*) and those on the glass, machined, 3V180s and 5V treated surfaces. There are also significant differences between the 3V180s and the 9V120s (**) and polished surfaces (Figure 113).

4.4. RhoA and Rac1

RhoA and Rac1 are members of the Rho family of small GTPases and are involved in cell-cell communication and signal transduction. The purpose of the following two experiments was to measure the activity of these GTPases in rat osteoblasts cultured on the control and treated surfaces. This was then correlated with the degree of cell-cell and cell-surface adhesion as measured by anti-vinculin and anti-cadherin-11 immunofluorescence.

4.4.1. RhoA assay

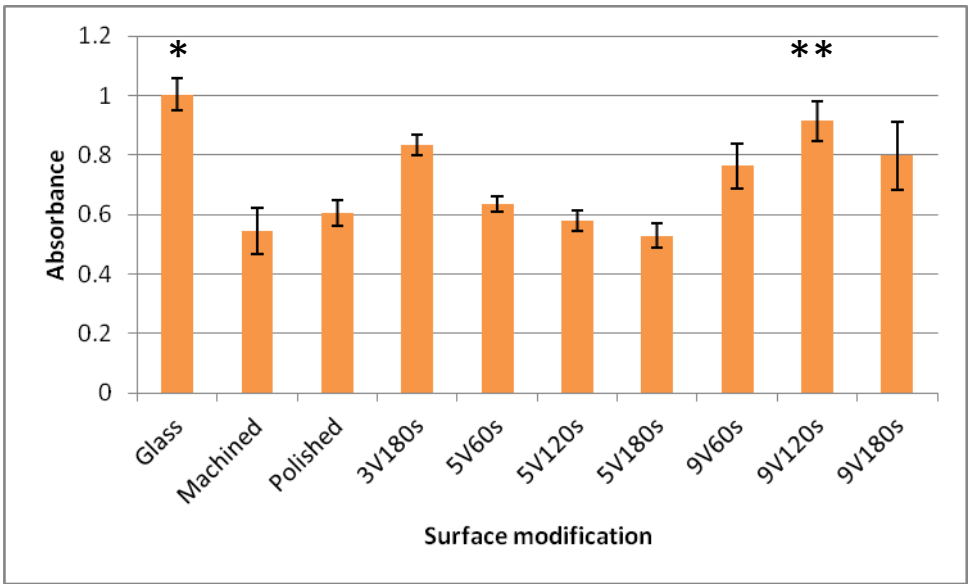

Figure 114: Graph of absorbance at 490nm, measuring RhoA activity in rat osteoblasts cultured in osteogenic media for 7 days. Results from 1 experiment, representative of 2 independent experiments (error bars represent standard error of the mean).

Significant differences are seen in RhoA activity on the glass surface (Figure 114, marked with *) and the machined, polished and 5V treated surfaces, significant differences are also seen between the 9V120s (Figure 114, marked with **) treated surface and the machined, 5V120s and 5V180s treated surfaces.

There is no direct correlation between the activity of RhoA and the quantity of staining for cadherin-11 or vinculin. However, there are trends in all data sets towards increased RhoA activity, increased focal adhesions (stained positive for vinculin) and increased cell membrane staining for cadherin-11 on the cells cultured on surfaces treated at 9V.

4.4.2. Rac1 assay

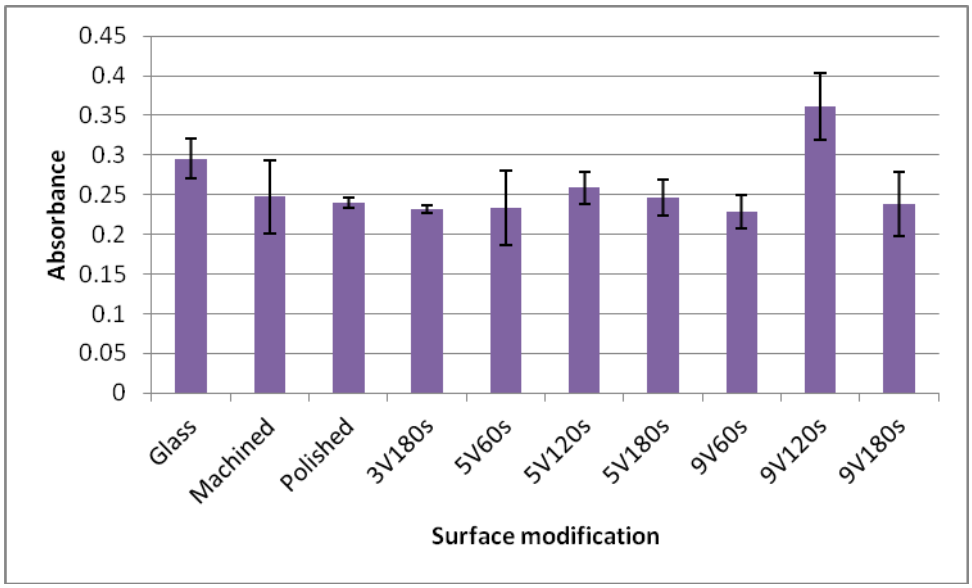

Figure 115: Graph of absorbance at 490nm, measuring Rac1 activity in rat osteoblasts cultured in osteogenic media for 7 days. Results from 1 experiment, representative of 2 independent experiments (error bars represent standard error of the mean).

No significant differences are seen in Rac1 activity between the cells on any of the surfaces on analysis with one-way ANOVA. There is therefore no correlation with the increased vinculin and cadherin-11 staining observed on the 9V surfaces (Figure 115).

4.4.3. ROCK inhibition

The aim of the following two experiments was to inhibit the action of ROCK and Rac1 in order to observe the effect on cell-surface adhesion as measured by mean focal adhesion area per unit of cell area after 24 hours in culture after addition of the inhibitor. This was intended to elucidate the importance of the role of the Rho family of GTPases in early cell-surface adhesion.

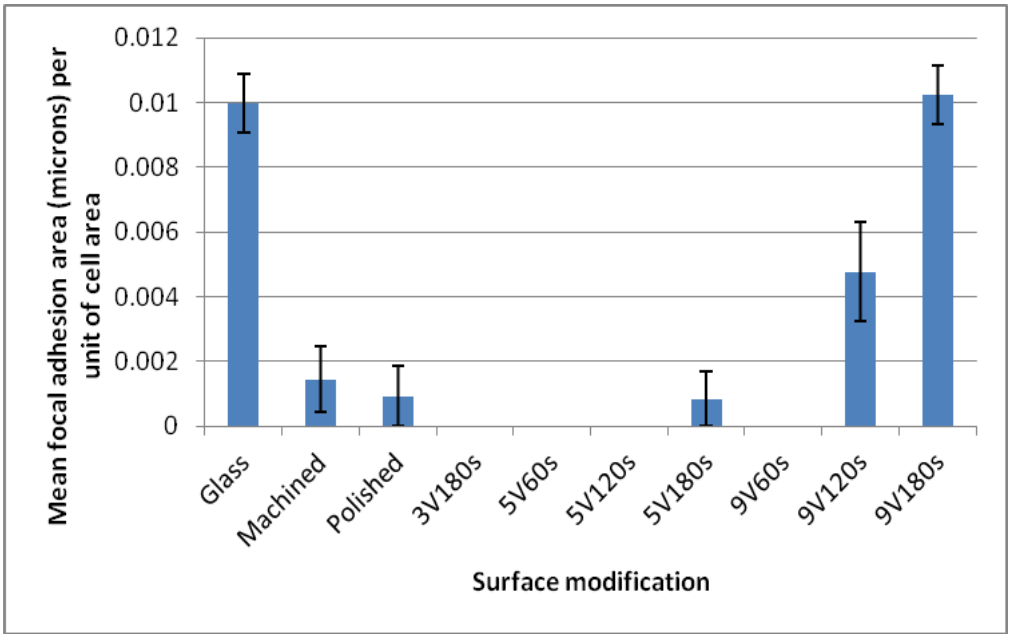

Figure 116: Graph of the mean focal adhesion area per unit of cell area measured on photomicrographs of anti-vinculin immunofluorescence stained surfaces following 48 hours of culture, 24 of which after addition of Y27632, a ROCK inhibitor.

Figure 116, above illustrates that the mean focal adhesion area per unit cell area for the cells cultured on glass, 9V180s and 9V120s treated surfaces was significantly greater than on the other surfaces, following addition of a ROCK inhibitor. The cells on all surfaces demonstrated lower mean focal adhesion area than when not exposed to ROCK inhibitor (see Results Chapter 1) but for the cells cultured on most of the 3V and 5V treated surfaces, the focal adhesions were not visible at all.

4.4.4. Rac1 inhibition

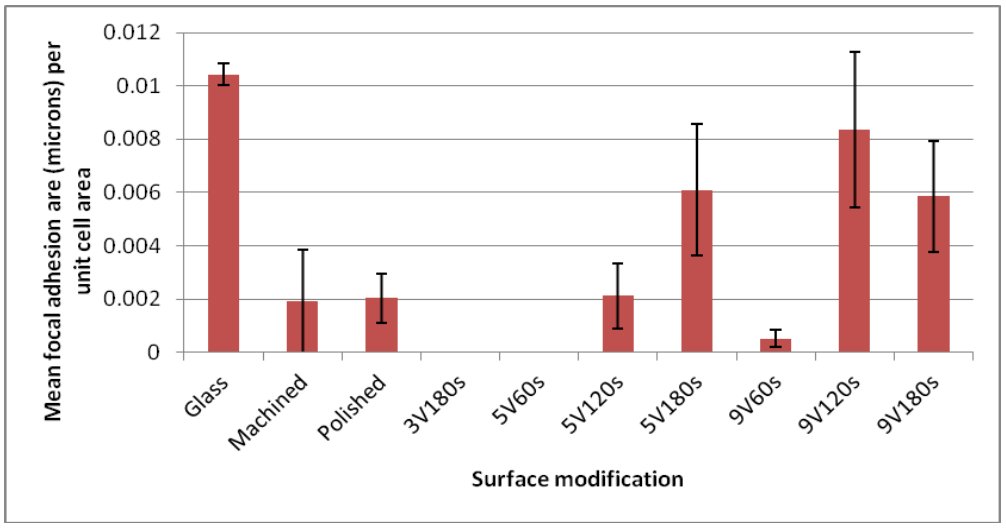

Figure 117: Graph of the mean focal adhesion area per unit of cell area measured on photomicrographs of anti-vinculin immunofluorescence stained surfaces following 48 hours of culture, 24 of which after addition of NSC23766, a Rac1 inhibitor.

Figure 117, above shows that the mean focal adhesion area per unit cell area was significantly greater for the cells cultured on the glass, 9V180s, 9V120s and 5V180s treated surfaces than those on the other surfaces after 24 hours exposure to Rac1 inhibitor. The mean focal adhesion area is reduced on all surfaces compared to that observed in culture without Rac1 inhibitor, but the inhibition of focal adhesion complexes is much more marked on the 3V180s and 5V60s surfaces than the others.

4.5. Discussion

The observations made in results chapter 1 regarding cell morphology and early adhesion on the experimental surfaces were investigated further using several methods. Genes involved in the early stages of osteoblast differentiation and cell-cell communication, were quantified using quantitative real-time PCR. Five repeats of the experiment were conducted with cDNA produced from mRNA isolated from cells on the experimental surfaces following 7 days of culture in osteogenic media.

Unfortunately, there was a large amount of variability in the data, even after exclusion of the two experimental repeats in which some of the amplifications were not successful and the others produced very much outlying data. This meant that the standard error of the mean for this data was very large, causing the observed trends generally not to reach the level of statistical significance. The genes selected to be studied in their roles in osteoblast differentiation were Runx2, osterix and osteocalcin. These genes were chosen to represent different stages of differentiation, with Runx2 being the earliest of these genes to be activated during the cascade of genes involved in the maturation of pre-osteoblasts through to committed bone forming cells. Osterix is a down-stream effector of Runx2 and therefore activated very slightly later and osteocalcin is a non-collagenous matrix protein produced by mature osteoblasts actively producing matrix. No statistically significant differences were observed in the quantity of any of these osteogenic genes between the cells cultured on any of the control or experimental surfaces. The large amount of variability in the data is likely to have masked any of these significant trends. The extraction of mRNA at only one time point may have masked subtle alterations in the timing of expression of these genes, thereby smoothing out any differences in timing of osteoblast differentiation. The time-point selected may have been too late to observe differences in Runx2, as this is likely to peak at day 2-3, but too early to demonstrate differences in osterix or osteocalcin (peak at 10 days and 21 days onwards respectively). Also, there is likely to have been some element of heterogeneity in the cell cultures with different cells at different stages of differentiation.

Two different genes coding for cadherin proteins were also studied using real-time PCR. The cadherins are a group of membrane-spanning proteins most evident in their role as part of adherens junction complexes which perform a role in cell-cell communication. Cadherins are common to all cells of mesenchymal origin but the two cadherins studied in this experiment were cadherin-2 and cadherin-11, which as a pair make up the major cadherin profile of osteoblast-lineage cells (Shin et al, 2000). Few significant differences were seen between the cadherin levels expressed in the cells cultured on the experimental surfaces. The relative levels of cadherin-2 were generally lower than those of cadherin-11. No significant differences were observed in the levels of cadherin-11. For cadherin-2, there was significantly greater expression on the glass and 5V120s treated surfaces. This is difficult to explain as a trend, in the context of the corroborating immunofluorescence experiments and may be a spurious result, produced by the large variability of the data. Rather than the total amount of gene activation of the cadherins, it is likely that the amount of active protein present in the cells and the position of this protein in relation to its place of action in the cell membrane are more important in determining the function of cadherins in these osteoblasts. This was therefore investigated further using immunofluorescence for cadherin-11.

When immunofluorescence analysis for cadherin-11 was performed on the cells after 7 days culture in osteogenic media, a definite trend was observed for greater cadherin-11 staining in the cell membrane of the osteoblasts cultured on surfaces treated at higher voltages and for longer times. Several of the comparisons of cadherin-11 staining between the 9V treated surfaces and the 3Vand 5V treated surfaces reached significance. Taking cell membrane staining for cadherin-11 as an indicator of increased cell-cell communication, it appears that 9V treated surfaces encourage this behaviour in the osteoblasts cultured on them. The trend for increased cadherin-11 staining also correlates well with the trends in cell area, cell polarity and focal adhesion area observed from immunofluorescence at 24 hours. Increasing cell area, decreasing cell polarity and increasing mean focal adhesion area are all associated with increased cell perimeter cadherin-11 staining. This would suggest that more successful early cell adhesion is associated with improved later cell-cell communication through adherens junctions. The relatively reduced cell membrane staining for cadherin-11 in the cells cultured on the glass surface was not expected, as these cells displayed markers of

enhanced early adhesion (see Chapter 3). It may be that this is an effect of surface chemistry, with cells cultured on titanium alloy surfaces in general displaying upregulated cadherin function. Previous work has demonstrated an upregulation of catenin (cadherin-associated protein) (Sohn et al, 2006) and cadherins (Kim et al, 2006) on titanium surfaces which have been treated with hydroxyapatite layers.

Rho and Rac (and the downstream effector ROCK), are small GTPases involved in signal transduction, cell motility and communication. There is evidence from the literature that inhibition of RhoA and ROCK decreases the contact guidance of osteoblasts on grooved titanium alloy surfaces (Calzado-Martin et al, 2011). Inhibition of Rho has been observed to reduce expression of gap junctions in corneal epithelial cells, although inhibition of ROCK increased gap junction expression (Anderson et al, 2002). The experiments in this chapter were designed to measure the activity of RhoA and Rac1 in the rat osteoblasts cultured on the experimental surfaces and explore the effects of inhibition of ROCK and Rac1 on cell morphology. After 7 days in culture, a trend could be observed for increased RhoA activity in the osteoblasts on the 9V, 3V180s and glass surfaces. In part, this trend correlates with those of increased focal adhesion formation and increased cadherin-11 cell membrane staining observed in the cells cultured on the 9V treated surfaces, which may be explained by an upregulation of intracellular signal transduction by the Rho-type GTPases (Narumiya et al, 1997) in response to greater cell-cell signalling and cell-surface adhesion. The increased RhoA activity on the 3V180s does not fit with this pattern, however. There are no significant differences between the surfaces for Rac1 expression, suggesting that in this culture model, its activity does not correspond to observed differences in cell-cell and cell-surface contact. It may be that its distribution in the cell is more important than the total quantity observed or that its phosphorylation may be more important than total quantity as the Rho family cycle between an active GTP-bound state and an inactive GDP-bound state controlled by regulatory proteins such as GEPs (Guanine Exchange Factors), GDIs (Guanine Dissociation Inhibitors) and GAPs (GTPase Activating Proteins). The inhibition of both ROCK and Rac1 resulted in a decrease in focal adhesion formation in osteoblasts cultured on all surfaces. The decrease was, however much more marked generally on the 5V and 3V treated surfaces rather than those treated at 9V, suggesting that the role of ROCK and Rac1 in focal adhesion formation and cell-surface adhesion

may be more important in cells with more tenuous adhesion. Previous work has elucidated the role of ROCK in mechanotransduction (Regent-Kloeckner et al, 2011; Tsai et al, 2012), which may explain this finding as well as the role that RhoA plays in rearrangement of the actin cytoskeleton (Hu et al, 2008).

Chapter 5. Results 3 – Investigation of osseointegration in an *in vivo* model

5.1. Introduction

Animal models are a regularly utilised experimental modality in the study of bone healing and osseointegration around orthopaedic and dental implants. Rodent models are the most often used, in common with other areas of medical research due to a combination of logistical factors such as availability, housing and costs. The use of rodents also fits in with the observation of the 'three Rs' of animal research – replace, reduce and refine. Rats are more often used in the literature than smaller rodents such mice and hamsters due to bone size in smaller animals limiting the choice of experimental implants. In the rat, the most commonly employed implant sites are the proximal tibia and distal femur, for reasons including bone diameter and ease of surgical access.

Several different shaped implants have been used by other groups and reported in the literature. Mushroom - shaped hollow implants were used by Butz's group, inserted into the distal femur of Sprague Dawley rats. Surrounding bone showed a correlation between mechanical properties and roughness of the implant surface (Butz et al. 2006a). Solid rods or wires were inserted horizontally into the distal femur in rats to compare the results of micro-CT with histomorphometry (Butz et al 2006b). A recent study used a partially threaded implant in the proximal tibia of rats to investigate implant fixation in bone compromised by disuse osteoporosis (Vandamme 2011) and a similar model of press-fit implants into the tibial diaphysis with rod shaped implants was used to study bioabsorbable implants by Raquez et al. in 2011.

Cylindrical press-fit rod implants have been used by several groups – in the proximal tibia of rats to compare different hydroxyapatite coatings (Oh et al 2005), to compare drilling with laser bone cutting in the proximal tibia (Kesler et al) and in the distal femur to assess biomolecular coatings (Reyes et al 2007). Press-fit rod or dowel-type implants to fit the distal femur or proximal tibia, as used in this study, are a common model in rodents and have been used successfully to investigate bone volume in apposition to implants in several previous studies. Ogawa et al. (2003) demonstrated

increased bone volume adjacent to acid-etched implants compared with smooth ones in a rat model.

The work of Castellani et al. in 2011, using a press-fit implant model in the rat distal femur formed a basis for our mechanical testing and histomorphometry analysis. The surgical technique by this group involved press-fit cylindrical implants, perpendicular to the axis of the bone, although they employed a mid-diaphyseal femoral approach, rather than the proximal tibia. The push-out mechanical testing protocol was very similar to that employed in the work presented here, although with a slightly faster displacement rate. This group also employed a micro-CT process for assessment of the area of bone in direct contact with the implant. The dehydration and resin embedding process was slightly different, with Technovit solutions, rather than polymethyl methacrylate and the sections taken longitudinally along the implant, rather than perpendicular to it.

The aims of the following series of experiments were:-

- to measure the mineralised bone formed in direct contact with the experimental implants by analysis of images taken of stained histology sections
- to correlate this with measurements of mineralised bone in contact with the implants on micro-CT images
- to measure the force required to break the bone-implant interface by mechanical 'push-out' testing

5.2. Histomorphometry

The purpose of this experiment was to quantify mineralised bone matrix in immediate contact with the surface of the experimental implants to study the effect on direct bone on-growth onto the implants with different electrochemical surface treatments. The tibias were explanted whole and sectioned using a diamond-edged circular saw into 300μm sections perpendicular to the axis of the implants, which were then polished down and stained with silver nitrate and giemsa stains. The sections were then visualised by optical microscopy and photomicrographs obtained, as illustrated in the figures below. These were then processed using image analysis software to arrive at a percentage of the implant area in each section, which was seen to be in direct contact with mineralised bone matrix. All full section images were made up from multiple

microscope images as the implant and surrounding bone were too large to be seen on one microscope field.

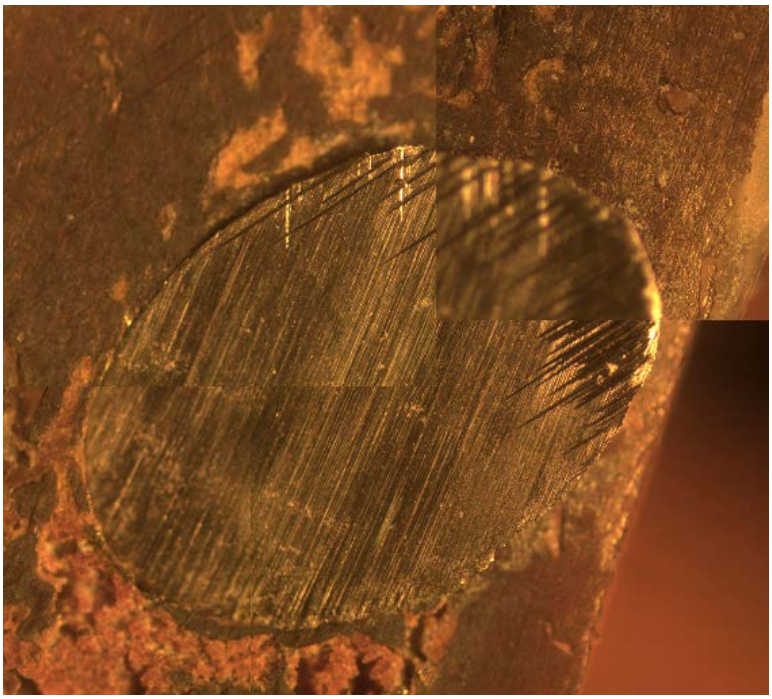

Figure 118: Light microscopy of histomorphometry section, stained with silver nitrate and Giemsa stain, of rat tibia bone surrounding rod with mechanically polished surface

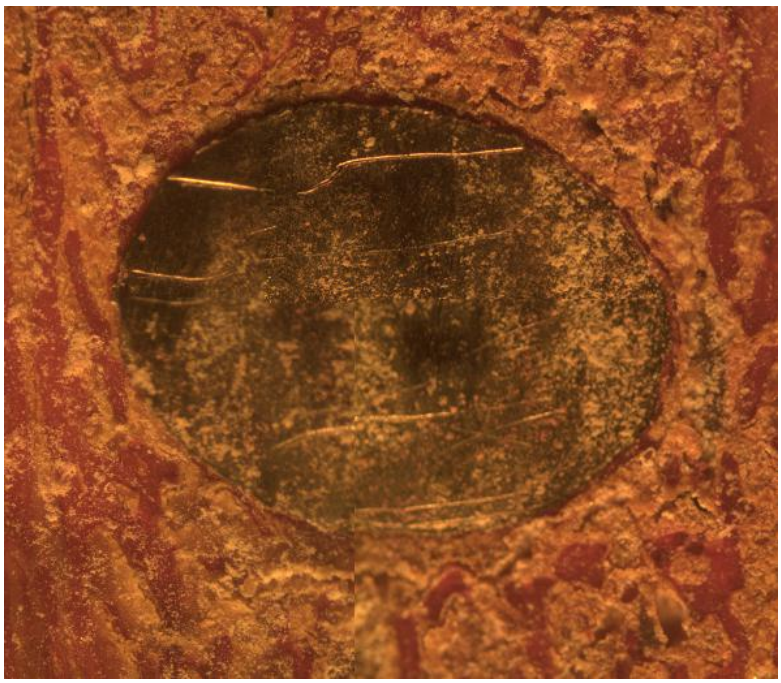

Figure 119: Light microscopy of histomorphometry section, stained with silver nitrate and Giemsa stain, of rat tibia bone surrounding rod treated with 3V180s surface

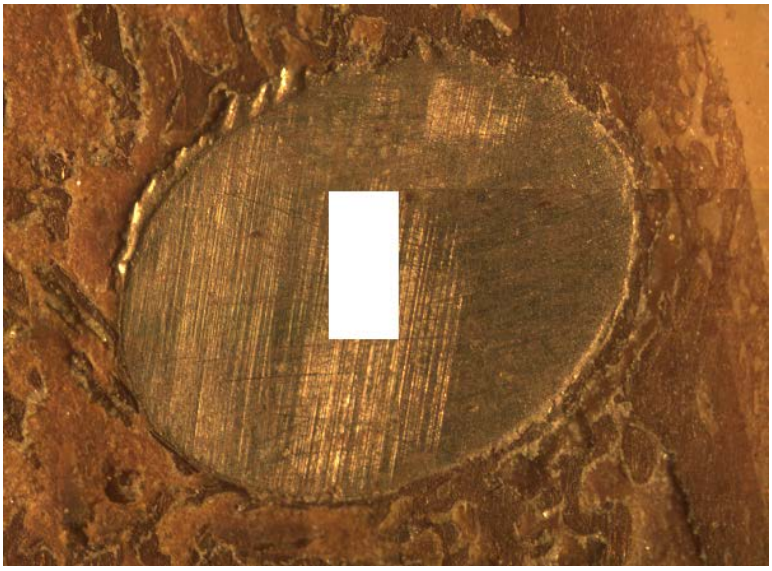

Figure 120: Light microscopy of histomorphometry section, stained with silver nitrate and Giemsa stain, of rat tibia bone surrounding rod treated with 5V180s surface

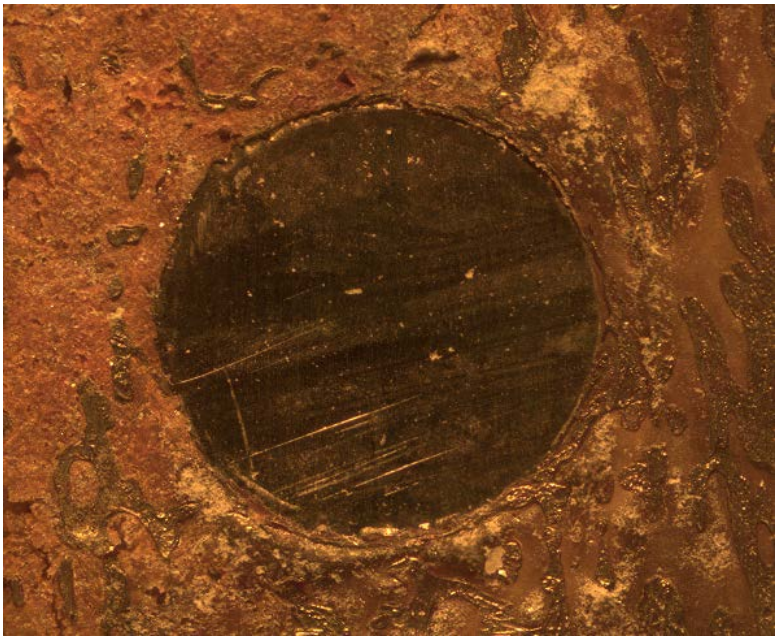

Figure 121: Light microscopy of histomorphometry section, stained with silver nitrate and Giemsa stain, of rat tibia bone surrounding rod treated with 9V180s surface

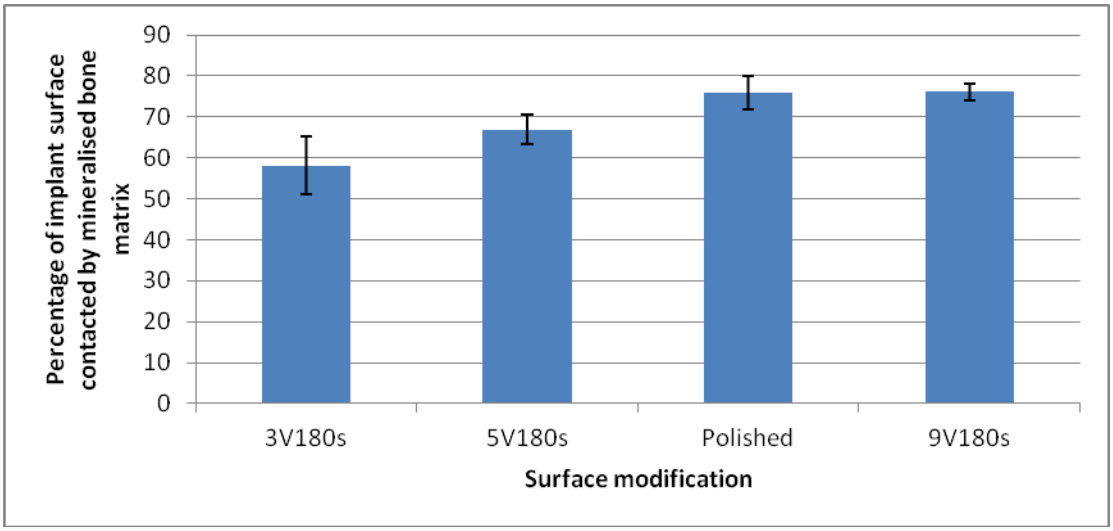

Figure 122: Bar chart displaying the percentage of implant surface in contact with mineralised bone matrix (n=5).

Figure 122, above demonstrates the percentage area of the experimental implants in contact with mineralised bone matrix, as calculated from the stained sections as illustrated in Figures 118-121. A trend can be seen of increased bone-implant contact for the sections taken of polished and 9V180s treated implants, compared to the 3V10s and 5V180s treated implants. This trend does not reach statistical significance however, on testing with one-way analysis of variance.

5.3. Mechanical testing

Other explanted tibias were taken fresh in saline-soaked gauze for immediate mechanical testing in an Instron push-out testing apparatus. The samples were mounted with the implants perpendicular to the base of the apparatus and were pushed out of the bone at 1mm/minute using a 2mm testing probe (Figure 123). This provided the yield strength in Newtons, a measure of the force required to break the bone-implant interface and cause the implant to move in the bone.

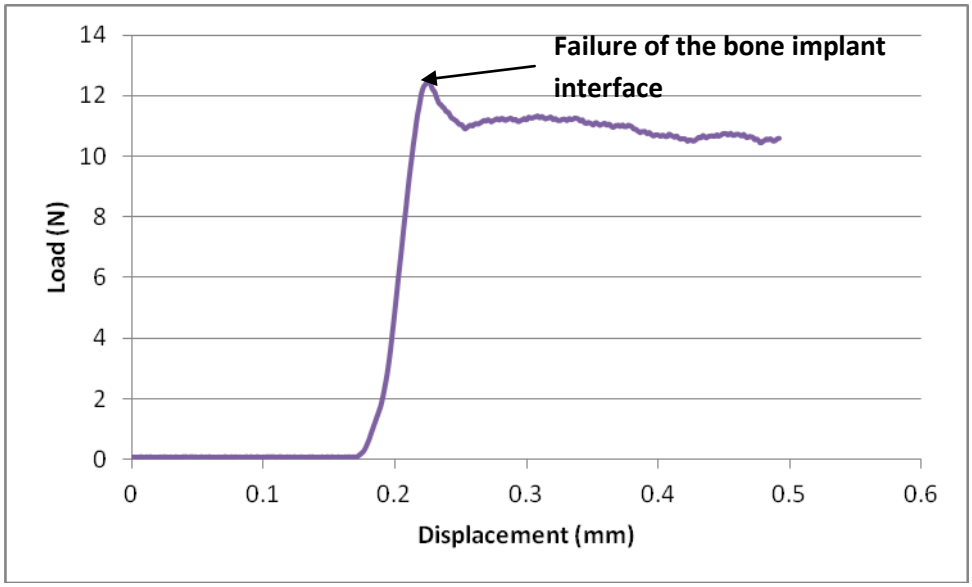

Figure 123: Example tracing of application of load (N) to failure against displacement (mm). Arrow indicates point of failure of the bone-implant interface.

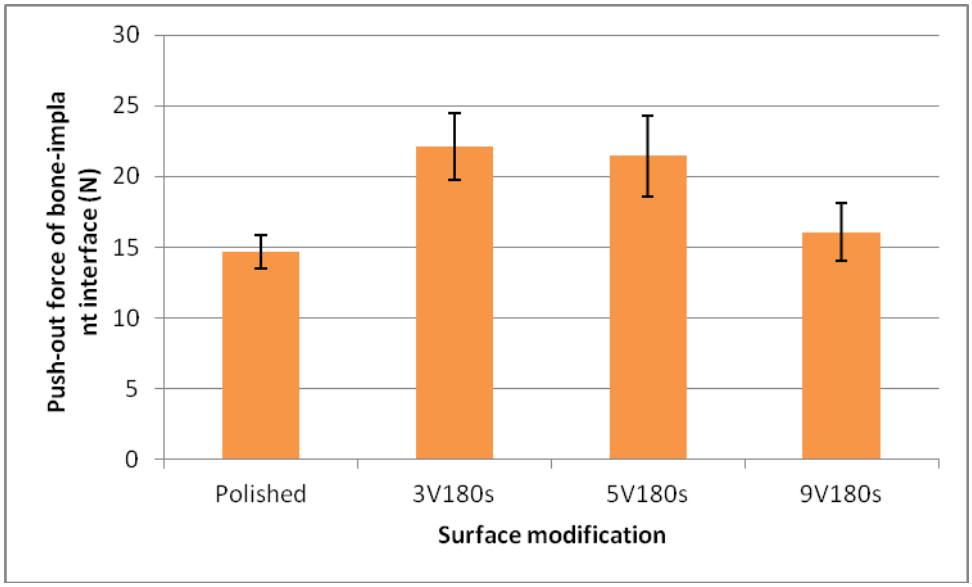

Figure 124: Bar chart illustrating the push-out force of the bone-implant interface during mechanical push-out testing for each of the modified surfaces.

Figure 124, above summarises the mean push-out force of the bone-implant interface for each of the experimental implants. The trend was for greater push-out forces to be observed for the 3V180s and 5V180s treated implants than the polished and 9V180s treated implants. Interfaces tested using this technique usually demonstrate a wide spread of results, which was also observed to be the case in this experiment. Due in part to the large confidence intervals observed in the data, the trend did not reach statistical significance on one-way analysis of variance.

5.4. Micro-CT

Some of the explanted tibia samples were sent for external imaging at SkyScan (Kontich, Belgium) with micro CT. This involved cross-sectional imaging using very thin CT slices, in an orientation perpendicular to the long-axis of the implant, providing orthogonal sections to those produced for histomorphometry. The images were processed using image analysis software to quantify the percentage of implant surface in direct contact with mineralised bone trabeculae. Figures 125a-d, below illustrate a sample of these images.

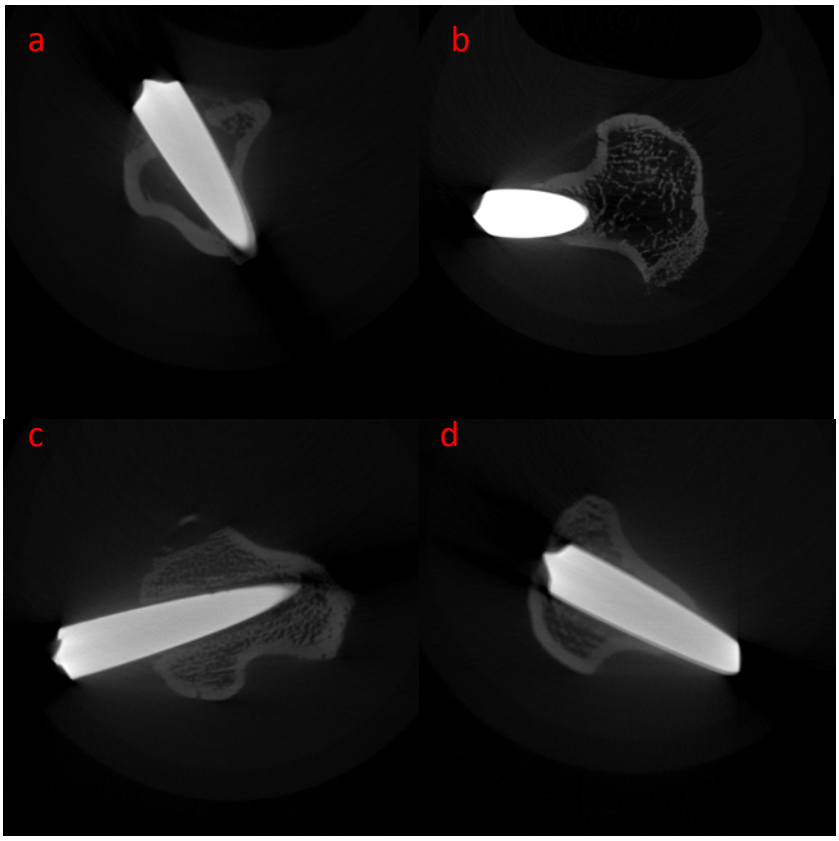

Figure 125 (a-d): Micro-CT slice longitudinally through experimental implant treated with a) mechanical polishing, b) 3V180s, c) 5V180s and d) 9V180s and surrounding bone.

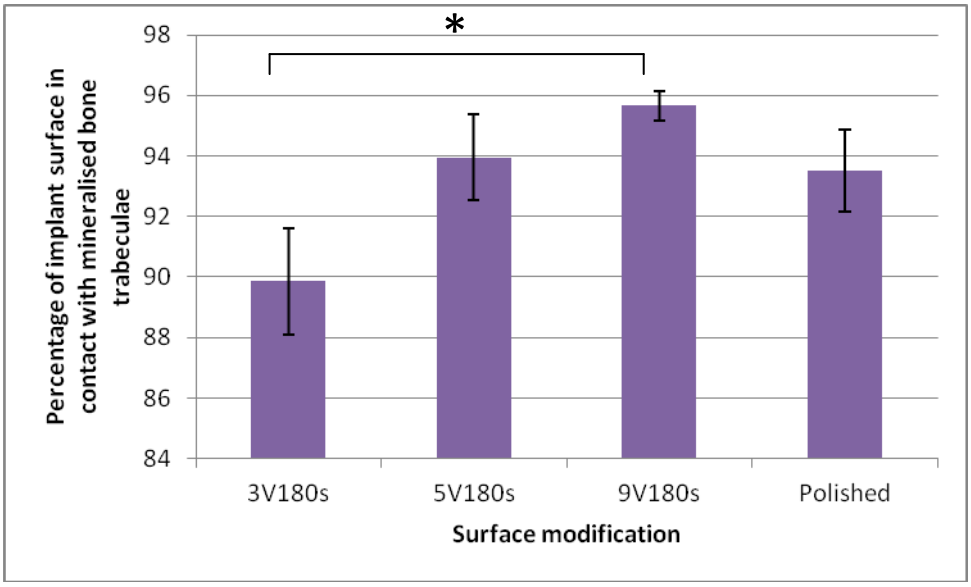

Figure 126: Graph displaying the percentage of the experimental implant surfaces in direct contact with trabeculae of mineralised bone on a sample of micro-CT slices (n=10). Asterisked bracket indicates a significant difference ($p<0.05$).

Figure 126, above demonstrates the percentage of the implant surface visualised on a sample of micro-CT slices, which is in direct contact with mineralised bone trabeculae. The trend in these results supports that demonstrated in the histomorphometry measurements, with a greater percentage of the 9V180s treated implant surface in direct contact with mineralised bone trabeculae than those treated at 5V180s and 3V180s. The difference in mineralised bone contact between the implants treated at 9V180s and 3V180s was found to be statistically significant at $p<0.05$ on one-way analysis of variance.

5.5. Discussion

An animal model was employed to investigate the osseointegration of the experimental implants in an in vivo model, in comparison with the behaviour of cells on the experimental surfaces in vitro.

Resin-embedded sections were analysed using histomorphometry to compare the percentage of the perimeter of the implants that was in direct contact with mineralised bone matrix. This provides a measure of the ability of the implant surface to induce growth and differentiation of mature bone tissue directly on the surface. With sections taken perpendicular to the long axis of the implant, several sections of each were available. A trend for increased percentage contact of mineralised bone matrix with the implant surface was observed on the polished and 9V180s treated implants compared to the 3V180s and 5V180s treated implants.

Although the trend did not reach statistical significance, its direction correlated with the early in vitro observations of improved osteoblast adhesion on these surfaces. The in vitro experiments over longer time periods, assessing bone nodule area and alkaline phosphatase activity, however did not demonstrate the same trend. The existing literature regarding osseointegration, using histomorphometry, is difficult to compare with this work, mainly due to the difference in roughness. Most literature relates to implants whose surfaces have roughness on the micron-scale, whereas the modified surfaces in this work have roughnesses on the nanometre scale. The differences between the surfaces in these experiments, with regard to surface morphology, is much less marked than that between the experimental surfaces in most reported literature (Kim et al, 2003). Direct comparison is also hindered by the multitude of different experimental models, with rabbit, miniature pig and goat used by several groups (Vercaigne 1998, Wennerberg 1997), with the natural history of bone healing in each species, particularly with regard to time taken, being very variable. This is reflected in the variable time-courses of the experiments, from 3 weeks to 12 months, with the longer term experiments tending to be performed in the larger animals, whose healing times most closely resemble that in humans (Grizon et al, 2002). The use of large animals, for long term experiments, however is both prohibitively expensive and potentially ethically

challenging. The implants themselves are of several different shapes, with different insertion techniques – drilling with press-fit, rectangular hollow implants and screw-shaped implants (Franchi et al, 2007).

Mechanical testing, by push-out using the Instron testing apparatus, demonstrated a trend for increased push-out force of the bone-implant interface for the 3V and 5V treated surfaces compared to the mechanically polished and 9V treated surfaces. Due to the large variability apparent in the data, this trend did not reach statistical significance. The push-out testing is very similar to that described in the work of Vercaigne and colleagues in 1997. This group used a goat model to evaluate plasma-sprayed implants and also encountered very large variations in the data, with only a weak correlation apparent between surface roughness and push-out force of the bone-implant interface. Other shapes of implants require different mechanical testing strategies, including shear testing but mechanical testing in general, as reported in the orthopaedic literature, displays high levels of test-retest variability, making it a difficult test modality to correlate with other methods of assessment (Liang et al, 2003). As the trend in push-out force at the bone-implant interface is not accompanied by increased area of mineralised bone matrix in contact with the implant, it is likely that it can be explained by increased mechanical interlocking of the rougher 3V and 5V treated surfaces. It may also be that explanting the tibias at another time point would yield different results as rapid early bone on-growth may be more than compensated for by increased cell proliferation and mineralisation later on other surfaces. A similar effect is possible for yield strength of the bone-implant interface if early cell proliferation is accompanied by less rapid mineralisation, but this is made up for later and greater ultimate yield strength is produced.

Micro-CT was also used to assess the percentage of contact of mineralised bone with the implant surface. The CT slices were taken longitudinally along the length of the implant due to the restrictions of the scanning process. By combining the results with those from histomorphometry a better impression of the distribution of mineralised bone in three dimensions can be gained because of the orthogonal nature of the sections in each method of measurement. A similar trend of increased bone-implant contact with the 9V180s treated implants compared to the 3V180s and 5V180s treated implants was

observed on micro-CT as was seen with histomorphometry, which was statistically significant, however contact was lower for the polished implants. The direction of measurement perpendicular to those taken for histomorphometry allows triangulation between the results of the two methods, as a good correlation in the results of the two techniques would be confirmation that the results are representative of the 3 dimensional architecture of mineralised matrix around the implants. The difference in volume of bone measured in contact with the implants in each technique may have been due to the inherent difficulty of measuring bone volume in the first few microns outside the implant because of metal artefact (Butz et al, 2006b), this has been minimised by the settings of this micro-CT apparatus, however would not be present at all in measurements from histomorphometry.

Comparison between histomorphometry, micro-CT and mechanical testing has been conducted in a similar way in other literature, although a large animal model was used (Xiao et al, 2011). Li and colleagues in 2010 used micro-CT in combination with mechanical testing and histomorphometry in a rat model to assess the effect of hydrofluoric acid treatment of titanium implants and found good correlation between the methods, although the comparison between surfaces was on the basis of chemical difference, not differences in roughness which may influence mechanical interlocking. Other groups have used micro-CT to analyse bone-implant contact longitudinally on a time-course in live animals, using a rat model, which would provide further valuable information, however was not feasible with the budgetary and time constraints of the current project (Lee et al, 2011).

Chapter 6. Discussion

6.1. Final Discussion

Titanium and its alloys are frequently used materials for orthopaedic and dental applications. In orthopaedics titanium is commonly used for arthroplasty, spinal fixation and fracture fixation due to its biocompatibility and favourable mechanical properties. This is a result of its resistance to corrosion in the body as titanium reacts rapidly in oxygen-containing environments to form an inert oxide layer on the surface. The biocompatibility of titanium alloy allows direct ongrowth of bone onto the implant without intervening soft tissue (Krause et al, 2000). This situation of osseointegration is unique among metal implants to titanium and its alloys. If early osteoblast adhesion is unsuccessful, leading to weak osseointegration of implants with bone, this can lead to formation of a layer of fibrous tissue on the surface with adhesion of fibroblasts. In the long term, implants which have not been successfully osseointegrated are more liable to failure by aseptic loosening (Boyan et al, 1998).

There is a large body of evidence in existence that demonstrates the effect of implant surface topography and chemistry on cell growth and differentiation. For orthopaedic applications, an optimum range of surface roughnesses improve early osteoblast adhesion and differentiation to a mature phenotype. Regular micron- and submicron-scale features affect early cell adhesion, proliferation and spreading, which is termed contact guidance, parallel grooves cause cells to grow in an elongated fashion in the direction of the grooves (Anselme et al, 2002). Micron-scale pillars tend to encourage attachment of the cells only on the tops of the pillars with exaggerated production of filopodia, unless the pillars are spaced far enough apart for cells to fit between them and effectively ‘ignore’ their effect on topography (Justesen et al, 2009). More mature, mineralised bone nodules have been observed on rougher plasma-sprayed and coarse grit-blasted surfaces in longer term cell culture (Boyan et al, 2002). A more mature osteoblast phenotype in terms of alkaline phosphatase activity, extracellular matrix synthesis, osteocalcin production and response to hormones and growth factors, can be seen on roughened titanium alloy surfaces (Lincks et al, 1998). Surface roughness also appears to improve longer term bone on-growth onto the implants, with porous coatings being common features on the surfaces of implants intended for uncemented fixation in

lower limb arthroplasty (Sychterz, Claus and Engh, 2002). These surfaces tend to be very rough with RA values in the high micrometre range, allowing macroscopic interlocking of bone trabeculae with the implant surfaces. Surface chemistry also affects cell growth on implant surfaces with surface energy, surface charge and addition of specific binding sites all influencing cell adhesion. Strategies such as the addition of calcium phosphate or hydroxyapatite crystals to the surfaces of titanium and titanium alloy have been successful in modulating cell signalling pathways in osteoblasts (Zreiqat et al, 2005) and improving cell-surface contact in vitro (Mendes, Moineddin and Davies, 2007). The functionalisation of surfaces with peptides and collagen molecules has also been shown to enhance osteoblast mineralisation in vitro and to improve bone-implant contact and mechanical properties of the bone-implant interface in vivo (Reyes et al, 2007). The differences in surface energy have been proposed as a mechanism underpinning the observed differences in osteoblast morphology on surfaces with different alloy thicknesses, as a direct correlation between alloy thickness and cell behaviour could not be confirmed (Muhonen et al, 2007).

Very few surface modification techniques have been exhaustively investigated in the literature from in vitro studies of early cell adhesion, through long term in vitro culture experiments investigating intermediate-term cell behaviour to in vivo experiments in an animal model to study the effect on osseointegration in a complex living system. Data presented here addresses this. There are also few methods of reproducibly creating nano- and micron-scale features on the outer and inner surfaces of complex 3-dimensional structures, which this electrochemical methodology provides.

The electrochemical etching technique used in this research was developed to allow control of micron and nanoscale surface features with the same technique. It allows patterning of the surface of implants without using photolithographic masks and is readily scalable and adaptable to different implant shapes. Surfaces created by lithography tend to have the disadvantages of being expensive, limited in the size and shape of surface they can be used on and difficult to scale up to industrial size processes. They have however, demonstrated the ability to upregulate surface adhesion, intracellular signalling and extracellular matrix protein production in osteoblasts (Dalby et al, 2007). The surfaces produced by electrochemical modification have been

characterised for morphology and chemistry of the oxide layer using optical microscopy, scanning electron microscopy, atomic force microscopy and x-ray photoelectron spectroscopy.

Electrical current profiles were used to ensure the internal validity of the electrochemical modification process, with the profiles compared to others for the same voltage and time conditions, each time a sample was made. They also allowed direct comparison between what was happening during treatment of 2D and 3D surfaces with the same modification conditions. This allow us to say with some confidence that the 3D surfaces produced at 5V and 9V received comparable current profiles to their 2D counterparts, although there was some difference seen just at the beginning of etching for the surfaces treated at 3V. In all cases, due to the specific requirements of the electrochemical cells used, the current density experienced by the 2D surfaces was higher. As the current profiles were very similar but not identical, the surfaces were compared visually using light microscopy.

Light microscopy and optical profilometry were used to compare profiles of the micron-scale features of the surfaces. The features on all surfaces were randomly distributed. A trend at this scale was seen for larger, more widely-spaced features on the surfaces treated at 3V and 5V than at 9V. This is likely to be due to inherent irregularities in the crystalline structure of the surface alloy, allowing some areas to be differentially etched to a greater degree than other areas. At higher voltages and longer time points, this effect would be less evident as the whole surface is etched to a greater depth, smoothing out some of the pre-existing irregularities. Light microscopy also demonstrated the comparable nature of the 2D and 3D surfaces produced with the same voltage and time conditions so parallels can be drawn between cell behaviour on the 2D surfaces and osseointegration of the 3D surfaces in vivo.

Atomic Force Microscopy and Scanning Electron Microscopy were used to characterise the experimental surfaces at a nano-scale level. Very similar patterns of features were identified at the nano-scale as at the micron-scale. Surfaces treated at lower voltages were observed on SEM imaging to have predominantly amorphous characteristics, whereas those treated at 9V showed crystalline features. It has been commented in

electrochemistry literature that industrial electropolishing of titanium and its alloys often results in a micron-scale 'rippling' effect, partially dependent on the composition of the alloy (Black and Hastings, 1998) and this appears to be reflected in our surfaces produced at lower voltages. This trend from larger, undulating features produced at low voltages to much smaller, finer and more regularly spaced features produced at 9V was reflected in the differences in RA values. The 9V-treated surfaces all had significantly lower mean RA values (around 5nm) than the 3V- and 5V-treated surfaces (20-35nm). However, all treated surfaces were significantly smoother than those used commercially in arthroplasty applications, which are usually grit-blasted or plasma sprayed. The surfaces prepared in the work presented here, would not provide the increased surface area necessary for macroscopic bone interlocking, however one of the advantages to them is that they can be used in addition to these other methods in order to add further biologically favourable characteristics to previously roughened surfaces. The RA results from the AFM correlate well with the observations of early cell adhesion experiments, with the 9V surfaces with lower RA values being associated with significantly larger, more circular cells with greater numbers and larger mean areas of focal adhesion complexes.

X-ray Photoelectron Spectroscopy demonstrated differences in the chemical composition of the oxide layer of the electrochemically treated experimental surfaces. Both the aluminium and vanadium content of the oxide layer decrease with increasing time and voltage used. This was apparent not just in the most superficial layer of the oxide but also at deeper layers. Aluminium has a well established toxic effect on osteoblasts and is clinically important in the etiology of bone disease in renal dialysis patients. Vanadium also has been shown in some in vitro studies to have a toxic affect on osteoblast-like cells through an oxidative stress mechanism (Cortizo et al, 2000). Although these experiments support a greater role for surface topography than surface chemistry in the determination of early osteoblast adhesion and morphology, the observations regarding chemical changes in the oxide layer opens up the possibility that this may exert an additional effect.

The observed topographical features were first investigated using osteoblast cell culture. Cell morphology, studied using immunofluorescence after short term cell culture was

used as a measure of early cell adhesion, along with number and area of focal adhesion complexes, the major areas of cell-surface contact. Both rat primary calvarial osteoblasts and human mesenchymal cells were used for short term culture experiments. No systematic differences were found in the number of cells counted on any of the experimental surfaces at 24 hours. This suggests that the surface does not have a major effect on early cell viability and adhesion and that these are more reliant on other factors, such as initial distribution of the cells. After 24 hours of culture, cell polarity was significantly higher for the cells cultured on the 3V and 5V treated surfaces and as a consequence, cell area was significantly smaller. The cells cultured on these surfaces were observed to have longer filopodia, less rounded morphology, with smaller and fewer focal adhesions. This would suggest that their attachments to the surfaces were more tenuous. Further measurement of the focal adhesion complexes revealed a smaller mean area of focal adhesions on these surfaces and significantly fewer focal adhesions per unit cell area. The differences in focal adhesions can explain most of the observed differences in cell morphology, indicating that these points of anchorage for the cell membrane onto the underlying surface are important determinants of early cell adhesion. The distribution of these points of anchorage on the different surfaces correlates to the changes seen in cell morphology. Previous studies have demonstrated the ability of nano-scale architecture, including pits and pillars, to induce changes to focal adhesion complex morphology and also changes to localisation of focal adhesion-associated proteins including integrins, vitronectin and paxillin (Lim et al, 2007).

The effect of surface topography was separated from surface chemistry by assessing cell morphology on polycaprolactone reproductions of the experimental surfaces. The same trends were observed in morphology of rat osteoblasts cultured on the polycaprolactone surfaces as on the original surfaces, with significantly smaller and more polarised cells found on the moulds of the 3V and 5V treated surfaces. The trends were, if anything, more smoothly progressive on the polycaprolactone surfaces than the experimental surfaces. This suggests that the effect of surface chemistry is smaller in magnitude than the effect of topography but operates in addition. The differences between the cell area and polarity on the 5V and 9V surfaces appears to be of larger magnitude on the experimental surfaces than the moulds, suggesting that the surface chemistry on the 9V surfaces is favourable to early cell adhesion in addition to the effects of its topography,

or the 5V surface chemistry is particularly unfavourable to cell adhesion, survival or growth. This is likely to be explained by the differential levels of aluminium and vanadium in the oxide layers as both elements have some toxic affects in vitro (Cortizo et al, 2000). Aluminium is also a causative factor in clinically important bone disease in humans, particularly renal dialysis patients (Parisien et al, 1988). Another possibility is that the different levels of oxides have an effect on protein adsorption, which in turn affects cell behaviour.

The effect of surface modification on longer term cell growth and differentiation was studied using an alkaline phosphatase activity assay and bone nodule staining. Alkaline phosphatase activity of rat osteoblasts demonstrated an increasing trend with increased voltage and increased time of modification with this difference being significant for the 9V180s and 9V120s surfaces compared to the 5V60s and 5V120s surfaces. This shows that the previously observed changes to early cell adhesion at 24 hours continue to be reflected after 14 days in culture with increased osteoblast differentiation towards a mature phenotype and expression of the major marker of matrix mineralisation. This would suggest that an increase in early cell adhesion gives cells a continuing advantage in the medium term regarding their extracellular matrix formation. Bone nodules were assessed with both measurement of total area with image analysis and using colorimetry to measure liberated alizarin red staining from the nodules. No significant differences were seen between surfaces for the total area of bone nodules measured, although there was a slight trend towards lower area of nodules on surfaces treated at higher voltages. The same trend was not observed with the colorimetric method of measurement. This may suggest that although the bone nodules on surfaces treated at higher voltages were smaller or less numerous, they may have protruded further from the surfaces and therefore have a greater volume, or been more densely mineralised, thereby offsetting the observed lower total area. Previous studies that have included longer term cell culture experiments have tended to show less marked differences between surfaces at later time points, even when obvious differences in early cell behaviour and morphology have been observed in the first 48 hours of culture (Martinez et al, 2009), suggesting that it may be pertinent to assess the quality of the bone alongside measures on quantity.

Osteoblast differentiation towards a mature phenotype was studied using real-time PCR for the quantification of expression of osteogenic genes. Despite multiple repeats of the experiment, however, the variability in the data was so large that no meaningful trends could be found. It is possible that more meaningful results may have been obtained by a different experimental approach, with multiple samples being taken from the same cell cultures rather than single samples across multiple experiments with different primary cells. The differences in activity between the different cell cultures may have overwhelmed any subtle differences in gene expression between cells on the different surfaces. It is unclear whether there is any real difference in the expression of the osteogenic genes studied, however it is possible that any differences between the surfaces is most evident in the amount and distribution of the relevant proteins, rather than the genes themselves.

To explore this possibility further and since the surfaces were shown to dictate differences in cell morphology; immunofluorescence was performed for cadherin-11, which is found consistently in osteoblasts (Kawaguchi et al, 2001). Cadherins are cell membrane spanning glycoproteins, components of adherens junctions which mediate cell-cell communication in cells of mesenchymal origin. Their gene expression and distribution of proteins in the cell is indicative of cell-cell communication. Previous research has demonstrated the roles of cadherin-2 and -11 as synergistic in skeletal development and response of bone to loading and the levels of co-expression of cadherins-2 and -11 is a marker of osteogenic lineage (Shin et al, 2000). Immunofluorescence was performed to quantify the degree of cell perimeter staining positive for cadherin-11, which demonstrated a trend for increasing cell perimeter cadherin-11 staining with increasing voltage and time of modification and significant differences seen between the surfaces treated at 9V and at 3V. Cadherin-11 has been shown to be involved in both cell-cell communication in adherens junctions and cell-surface adhesion through its action on filopodia formation, which has been demonstrated in neural crest cells (Kashef et al, 2009). Its role in cell adhesion also requires the downstream action of the small GTPases RhoA and Rac. Their role in the behaviour of osteoblasts cultured on the experimental surfaces was studied using activity assays and the application of inhibitors during short term culture, with the effect on focal adhesion formation measured using immunofluorescence. No significant

differences were seen in the Rac1 activity assay between the treated surfaces, demonstrating that it does not play a central role in explaining the observed differences in early cell adhesion. There was, however, significantly greater RhoA activity on the 9V treated surfaces but also, interestingly, the 3V treated surface. The increased RhoA activity would be expected on the 9V surfaces if it played a significant role in early cell-cell communication and cell-surface adhesion, but the higher activity on the 3V surface was unexpected. It may be a spurious result, as due to the cost of the assay, it could only be conducted twice. It may also be the case that the overall activity of RhoA was enhanced on the 3V surfaces but this did not relate to its presence in the cell membrane at junctional complexes, but represented a response to the more roughened surface. To explore this, immunofluorescence with anti-vinculin for focal adhesion complexes was performed following the inhibition of Rac1 and the downstream effector of RhoA – ROCK. Inhibition of either ROCK or Rac1 for 24 hours resulted in a reduction in focal adhesion formation, confirming that the finding of Kashef et al, in neural crest cells, also applies to the behaviour of osteoblasts on titanium alloy surfaces. The inhibition is more marked for ROCK than Rac1, which fits with previous work demonstrating the central role of ROCK as a target for RhoA in regulation of the actin cytoskeleton (Narumiya et al, 1997). Previous work has shown that inhibition of ROCK enhances proliferation of osteoblasts on calcium phosphate surfaces but these experiments did not specifically address the question of adhesion (Yang et al, 2011). The inhibition is also more marked on the 3V and 5V treated surfaces than those treated at 9V, suggesting that the roles of Rac1 and ROCK are more important if cell-surface adhesion is already tenuous and that well-adhered cells may have other compensatory mechanisms at work in their formation of focal adhesion complexes.

Osseointegration in an in vivo system was studied using a rat model, with press fit implants as used in previous studies. The bone-implant interface was assessed using micro-CT, histomorphometry and push-out testing.

The results of histomorphometry demonstrate a trend for increased bone-implant contact for the implants which were treated with mechanical polishing and at 9V180s. Although this did not reach statistical significance, it does correlate with the observations of Chapter 3 with respect to the evidence, from focal adhesion complex quantification, of

increased early cell adhesion on the polished and 9V treated surfaces. The observations from the use of micro-CT to quantify the bone-implant contact support those from histomorphometry and do confirm a significant difference in bone on-growth between the 9V180s and the 3V180s implants. Although less difference was observed between the cells on the experimental surfaces at 14 and 28 days in culture than at 24 hours, these differences do correspond to differences in bone-implant contact in vivo. This supports the findings of previous authors, that increased early cell adhesion and spreading convey an advantage in terms of determining longer term osseointegration. This may be due to more secure and extensive anchorage of osteoblasts preventing other cell types intervening at the interface, such as fibroblasts, which would form an undesirable fibrous layer on the implant surface, preventing the bone-bonding necessary for optimal long term fixation. It may also prevent colonisation of the implant surface by bacteria.

Mechanical push-out testing revealed a different trend to that noted in quantification of bone-implant contact by histological and imaging methods. The push-out force of the bone-implant interface was higher for surfaces treated at 3V and 5V than those treated at 9V. As this observation was not accompanied by a corresponding increase to mineralised bone around these implants, this is most likely to be due to a mechanical phenomenon of interlocking. The 3V and 5V surfaces were substantially rougher than those treated at 9V and the greater push-out force can be explained by interlocking of the trabeculae of the bone with the larger surface features. This is the same principle as that seen in the fixation of porous coated uncemented implants for arthroplasty, but on the micrometre scale, rather than with macroscopic interlocking.

6.2. Conclusions

- Electrochemical modification produces surfaces with a range of topographical features, with surfaces treated at lower voltages for shorter times having larger and fewer surface features and higher RA values.
- Chemical composition of the titanium alloy oxide layer is also altered by the electrochemical processing, with beneficial effects on osteoblast growth of decreased aluminium and vanadium content.
- Changes to the surface topography and chemistry of the titanium alloy implants results in changes to cell morphology in short term cell culture, with cell grown on surfaces treated at higher voltages demonstrating larger size, rounder shape and greater size and number of focal adhesion complexes.
- The changes in osteoblast behaviour become less marked in longer term culture, as measured by alkaline phosphatase activity and bone nodule area.
- Osteoblasts cultured on surfaces treated at higher voltages also display greater cell-cell communication via adherens junctions, as measured by cell perimeter staining for cadherin-11.
- Inhibition of the action of small GTPases of the Rho family disrupts the formation of focal adhesion complexes to a greater extent on surfaces treated at lower voltages and therefore in cells that are more tenuously adhered to the surfaces.
- A trend towards greater bone-implant contact was observed with implants treated at higher voltages using both histomorphometry and micro-CT imaging.
- This did not correlate with greater push-out force of the bone-implant interface, with this being greatest for implants treated at lower voltages, likely due to greater mechanical interlocking with the rougher surfaces.
- This electrochemical etching technique benefits from being easily scalable for industrial processing, can be used on any shape or size of implant, can produce different surfaces on different parts of an implant and can be used with existing surface treatment strategies such as grit blasting.

6.3. Limitations, future work

- It would have been preferable to have a method of direct comparison of surface features between the 2D and 3D surfaces. The small radius of curvature of the 3D implants, however, made any meaningful interpretation of surface characteristics very difficult, other than a qualitative visual inspection of small areas at a time.
- As several studies have found that the success of cell adhesion is at least in part determined by the adsorption of extracellular matrix proteins onto the surfaces, it would be useful to study the adsorption of proteins such as fibronectin on the experimental surfaces.
- The original aim of the cell culture experiments conducted on polycaprolactone was to include immunofluorescence to assess focal adhesion complexes in order to compare these with the data from early cell culture on the modified titanium surfaces. However, the auto-fluorescence of the polycaprolactone meant that this was not possible and conventional cell staining was used as an alternative but only cell morphology could be studied with this method.
- The high variability of the quantitative PCR results unfortunately resulted in there being few useful conclusions that could be drawn from the data. If time had permitted, other methods of assessing gene expression would have been beneficial in adding to our understanding of the molecular biology underpinning the observed trends in cell behaviour. Also a repetition of the PCR with multiple replicates from a single experiment may have been helpful.
- Larger than predicted variability in the data from mechanical testing, in particular resulted in these results not reaching statistical significance. Time constraints of the project prevented further animal experiments to increase the sample sizes. Retrieving the samples at a different time point may also have yielded results with more significant differences. The histomorphometry results were correlated with and supported by the micro-CT results, which demonstrated the same trend and did reach significance. However, mechanical testing has been shown in previous literature to be an approach which usually produces high variability of results and a much larger sample size may have

been required in order to demonstrate any significant difference between surfaces.

- Further work on combining these experimental surfaces with current implant surface treatment techniques, such as grit-blasting and plasma-spraying, would be a useful addition to the previous experiments. This would allow an assessment to be made of whether any further increase in biological compatibility can be obtained through a combination of treatment techniques. The electrochemical technique could also be combined with more complex macro-scale features, such as in trabecular metal used to manage bone loss in revision arthroplasty.
- Experiments to quantify the growth and proliferation of bacteria that are commonly implicated in deep prosthetic joint infections would also be a useful continuation of the work to determine whether any of the treated surfaces are more able to reduce the growth of these bacteria and the formation of biofilms.
- Combining areas treated with different voltage and time conditions on the same implant would be useful in order to assess whether differential bone-implant contact occurred and how this might relate to prevention of stress shielding around implants in a lower limb arthroplasty application.

References

Abrahamsson I, Berglundh T, Linder E, Lang N, Lindhe J. Early Bone Formation Adjacent to Rough and turned Endosseous Implant Surfaces. *Clinical Oral Implant Research.* 2004; 15: pp 381-392.

Albrektsson T, Brånemark P, Hasson H, Lindstrom J. Osseointegrated Titanium Implants. *Acta Orthopaedica Scandinavica.* 1981; 52: 155-179.

Al-Aql ZS, Alagi AS, Graves DT, Gerstenfeld LC, Einhorn TA. Molecular mechanisms controlling bone formation during fracture healing and distraction osteogenesis. *Journal of Dental Research*. 2008; 87: 107-118.

Anderson SC, Stone C, Tkach L, SunderRaj N. Rho and Rho-kinase (ROCK) signalling in adherens and gap junction assembly in corneal epithelium. *Investigative Ophthalmology & Visual Science.* 2002; 43(4): 978-86.

Anselme K. Osteoblast Adhesion on Biomaterials. *Biomaterials.* 2000; 21: 667-681.

Anselme K, Bigerelle M, Noel B, Iost A, Hardouin P. Effect of Grooved Titanium Substratum on Human Osteoblastic Cell Growth. *Journal of Biomedical Materials Research*. 2002; 60(4): 529-540.

Att W, Tsukimura N, Suzuki T, Ogawa T. Effect of Supramicron Roughness Characteristics Produced by 1- and 2-step Acid etching on the Osseointegration Capability of Titanium. *The International Journal of Oral and Maxillofacial Implants.* 2007; 22 (5): 719-728.

Bates P, Ramachandran M. Chapter 14: Bone injury, healing and grafting. Basic Orthopaedic Sciences (ed. Ramachandran M). (Hodder Arnold). 2007.

Bauer T, Schils J. The Pathology of Total Joint Arthroplasty. I: Mechanisms of Implant Fixation. *Skeletal Radiology*. 1999; 28(8): 423-432.

Benoit DSW, Schwartz MP, Durney AR, Anseth KS. Small functional groups for controlled differentiation of hydrogel-encapsulated human mesenchymal stem cells. *Nature Materials*. 2008; 7: 816-823.

Berry CC, Curtis ASG, Oreffo ROC, Agheli H, Sutherland DS. Human Fibroblast and Human Bone Marrow Cell Response to Lithographically Nanopatterned Adhesive

Domains on Protein Rejecting Substrates. *IEEE Transactions On Nanobioscience*. 2007; 6 (3): 201-209.

Berry C, Dalby M, Oreffo R, McCloy D, Affrosman S. The Interaction of Human Bone Marrow Cells with Nanotopographical Features in Three Dimensional Constructs. *Journal of Biomedical Materials Research Part A.* 2006; 79A: 431-439.

Bigerelle M, Anselme K, Noel B, Ruderman I, Hardouin P, Iost A. Improvement in the Morphology of Ti-based Surfaces: A new Process to Increase In Vitro Human Osteoblast Response. *Biomaterials.* 2002; 23: 1563-1577.

(a) Biggs M, Richards R, Gadegaard N, Wilkinson C, Dalby M. Regulation of Implant Surface Cell Adhesion: Characterization and Quantification of S-phase Primary Osteoblast Adhesions on Biomimetic Nanoscale Substrates. *Journal of Orthopaedic Research*. 2007; 2: 273-282.

(b) Biggs M, Richards R, Gadegaard N, Wilkinson C, Dalby M. The Effects of Nanoscale Pits on Primary Human Osteoblast Adhesion Formation and Cellular Spreading. *Journal of Materials Science: Materials in Medicine.* 2007; 18: 399-404.

Biggs MJP, Richards RG, Gadegaard N, Wilkinson CDW, Oreffo ROC, Dalby MJ. The use of nanoscale topography to modulate the dynamics of adhesion formation in primary osteoblasts and ERK/MAPK signalling in STRO-1+ enriched skeletal stem cells. *Biomaterials*. 2009; 30 (28): 5094-5103.

Bilezikian JP, Raisz LG, Rodan GA. *Principles of Bone Biology* 2nd ed. Academic Press 2002.

Birch MA, Johnson-Lynn S, Nouraei S, Wu Q-B, Ngalim S, Lu W-J, Watchorn C, Yang T-Y, McCaskie AW and Roy S. Effect of electrochemical structuring of Ti6Al4V on osteoblast behaviour in vitro. *Biomedical Materials*. 2012; 7: 1-14.

Black J, Hastings G. (Springer-Verlag 1998) *Handbook of Biomaterial Properties*.

Bowers KT, Keller JC, Randolph BA, Wick DG, Michaels CM. Optimization of surface micromorphology for enhanced osteoblast responses in vitro. *The International Journal of Oral and Maxillofacial Implants*. 1992; 7 (3): 302-310.

Boyan B, Batzer R, Kieswetter K, Liu Y, Cochran D, Szmuckler-Moncler S, Dean D, Schwartz Z. Titanium Surface Roughness Alters Responsiveness of MG63 Osteoblast-

like Cells to 1alpha hydroxyvitamin D. *Journal of Biomedical Materials Research.* 1998; 39:77-85.

Boyan BD, Bonewald LF, Paschalis EP, Lohmann CH, Rosser J, Cochran DL, Dean DD, Scharwtz Z, Boskey AL. Osteoblast-mediated mineral deposition in culture is dependent on surface microtopography. *Calcified Tissue International*. 2002; 71: 519-529.

Brånemark PI. Osseointegration and its experimental background. *The Journal of Prosthetic Dentistry.* 1983; 50 (3): 399–410.

Brydone AS, Dalby MJ, Berry CC, Meek RMD, McNamara LE. Grooved surface topography alters matrix-metalloproteinase production by human fibroblasts. *Biomedical Materials*. 2001; 6: 035005.

Buser D, Schenk R, Steinemann S, Fiorellini J, Fox C, Stich H. Influence of Surface Characteristics on Bone Integration of Titanium Implants. A Histomorphometric Study in Miniature Pigs. *Journal of Biomedical Materials Research*. 1991; 25: 889-902.

(a) Butz F, Aita H, Wang C, Ogawa T. Harder and Stiffer Bone Osseointegrated to Roughened Titanium. *Journal of Dental Research*. 2006; 85(6): 560-565.

(b) Butz F, Ogawa T, Chang T, Nishimura I. Three-Dimensional Bone-Implant Integration Profiling Using Micro-Computed Tomography. *The International Journal of Oral and Maxillofacial Implants.* 2006; 21(5): 687-695.

Calzado-Martin A, Mendez-Vilas A, Multigner M, Saldana L, Gonzalez-Carrasco JL, Gonzalez-Martin ML, Vilaboa N. On the role of RhoA/ROCK signaling in contact guidance of bone-forming cells on anisotropic Ti6Al4V surfaces. *Acta Biomaterialia*. 2011; 7(4): 1890-901.

Castellani C, Lindtner RA, Hausbrandt P, Tschegg E, Stanzl-Tschegg SE, Zanoni G, Beck S, Weinberg A-M. Bone-implant interface strength and osseointegration: biodegradable magnesium alloy versus standard titanium control. *Acta Biomaterialia*. 2011; 7: 432-440.

Castro CH, Stains CS, Cheng JP, Sheikh S, Mbalaviele G, Szenfeld VL, Civitelli R. Targeted expression of a dominant-negative N-cadherin in vivo delays peak bone mass and increases adipogenesis. *Journal of Cell Science*. 2004; 117: 2853-2864.

Cavalcanti-Adam E, Volberg T, Miculet A, Kessler H, Geiger B, Spatz J. Cell Spreading and focal Adhesion Dynamics are Regulated by Spacing of Integrin Ligands. *Biophysics*. 2007; 92: 2964-2974.

Cherian PP, Xia X, Jiang JX. Role of gap junction, hemichannels, and connexin 43 in mineralizing in response to intermittent and continuous application of parathyroid hormone. *Cell Communication and Adhesion*. 2008; 15(1): 43-54.

Chow JW. Role of nitric oxide and prostaglandins in the bone formation response to mechanical loading. *Exercise and Sport Science Review*. 2000; 28: 185-188.

Christenson E, Anseth K, van den Breucken J, Chan C, Ercan B, Jansen J. Nanobiomaterial Applications in Orthopaedics. *Journal of Orthopaedic Research*. 2007; 25: 11-22.

Chung DJ, Castro CHM, Watkins M, Stains JP, Chung MY, Szejnfeld VL, Willecke K, Theis M, Civitelli R. Low peak bone mass and attenuated anabolic response to parathyroid hormone in mice with an osteoblast-specific deletion of connexin43. *Journal of Cell Science*. 2006; 119: 4187-4198.

Civitelli R. Cell-cell communication in the osteoblast/osteocyte lineage. *Archives of Biochemistry and Biophysics.* 2008; 473: 188-192.

Clevers H. Wnt/β-catenin signaling in development and disease. *Cell*. 2006; 127: 469-480.

Colon G, Ward B, Webster T. Increased Osteoblast and Decreased Staphylococcus epidermidis Functions on Nanophase ZnO and TiO_2. *Journal of Biomedical Materials Research: Part A*. 2006; 78(3): 595-604.

Cortizo AM, Bruzzone L, Molinuevo S, Etcheverry SB. A possible role of oxidative stress in the vanadium-induced cytotoxicity in the MC3T3E1 osteoblast and UMR106 osteosarcoma cell lines. *Toxicology*. 2000; 147: 89-99.

Curran JM, Chen R, Hunt JA. The guidance of human mesenchymal stem cell differentiation in vitro by controlled modifications to the cell substrate. *Biomaterials*. 2006; 27 (27): 4783-4793.

Currey J. Chapter A1 – Cortical Bone. Handbook *of Biomaterial Properties.* Ed. Black J, Hastings G. 1998; Chapman and Hall. pp3-14.

Currey JD. The many adaptations of bone. *Journal of Biomechanics*. 2003; 36: 1487-1495.

Dalby MJ, Berry CC, Riehle MO, Sutherland DS, Agheli H, Curtis ASG. Attempted endocytosis of nano-environment produced by colloidal lithography by human fibroblasts. *Experimental Cell Research*. 2004; 295: 387– 394.

Dalby MJ, Gadegaard N, Tare R, Andar A, Riehle MO, Herzyk P, Wilkinson CDW, Oreffo R. The control of human mesenchymal cell differentiation using nanoscale symmetry and disorder. *Nature Materials*. 2007; 6: 997-1003.

Datta HK, Ng WF, Walker JA, Tuck SP, Varanasi SS. The cell biology of bone metabolism. *Journal of Clinical Pathology*. 2008; 61 (5): 577-587.

Dbouk H, Mroue R, El-Sabban M, Talhouk R. Connexins: a Myriad of Functions Extending Beyond Assembly of Gap Junction Channels. *Cell Communication and Signalling.* 2009; 7(4): 1-17.

Di Benedetto A, Watkins M, Grimston S, Salazar V, Donsante C, Mbalaviele G, Radice GL, Civitelli R. N-cadherin and cadherin 11 modulate postnatal bone growth and osteoblast differentiation by distinct mechanisms. *Journal of Cell Science*. 2010; 123: 2640-2648.

Diebold U. The surface structure of titanium dioxide. *Surface Science Reports*. 2003; 48: 53-229.

Dierkes C, Kreisel M, Schulz A, Steinmeyer J, Wolff JC, Fink L. Catabolic properties of microdissected human endosteal bone lining cells. *Calcified Tissue International.* 2009; 84: 146-155.

Ducy P, Schinke T, Karsenty G. The Osteoblast: a sophisticated fibroblast under central surveillance. *Science*. 2000; 289: 1501-1504.

Ehlen HWA, Buelens LA, Vortkamp A. Hedgehog signalling in skeletal development. *Birth Defects Research (Part C).* 2006; 78: 267-279.

Exley C, Birchall JD. The cellular toxicity of aluminium. *Journal of Theoretical Biology*. 1992; 159 (1): 83-98.

Forriol F, Shapiro F. Bone development: Interaction of molecular components and biophysical forces. *Current Orthopaedics and Related Research*. 2005; 432: 14-33.

Franchi M, Bacchelli B, Giavaresi G, De Pasquale V, Martini D, Fini M, Giardino R, Ruggeri A. Influence of different implant surfaces on peri-implant osteogenesis: histomorphometric analysis in sheep. *Journal of Periodontology*. 2007; 78 (5): 879-888.

Fulzele K, Riddle RC, Cao X, Wan C, Chen D, Faugere M, Aja S, Hussain MA, Brüning JC, Clemens TL. Insulin receptor signalling in osteoblasts regulates postnatal bone acquisition and body composition. *Cell*. 2010; 142 (2): 309-319.

Gerstenfeld LC, Cho TJ, Kon T, Aizawa T, Tsay A, Fitch J, Barnes GL, Graves DT, Einhorn TA. Impaired fracture healing in the absence of TNF-alpha signaling: the role of TNF-alpha in endochondral cartilage resorption. *Journal of Bone Mineral Research*. 2003; 18(9):1584-92.

Gispert MP, Serro AP, Colaco R, Saramago B. Bovine serum albumin adsorption onto 316L stainless steel and alumina: a comparative study using depletion, protein labelling, quartz crystal microbalance and atomic force microscopy. *Surface Interface and Analysis*. 2008; 40: 1529-1537.

Gordeladze JO, Reseland JE, Duroux-Richard I, Apparailly F, Jorgenson C. From stem cells to bone: phenotype acquisition, stabilization, and tissue engineering in animal models. *ILAR Journal*. 2010; 51 (1): 42-61.

Grimston SK, Screen J, Haskell JH, Chung DJ, Brodt MD, Silva MJ, Civitelli R. Role of connexin43 in osteoblast response to physical load. *Annals of the New York Academy of Sciences.* 2006; 1068: 214-224.

Grinnell F, Feld MK. Fibronectin adsorption on hydrophilic and hydrophobic surfaces detected by antibody binding and analyzed during cell adhesion in serum-containing medium. *Journal of Biological Chemistry*. 1982; 257: 4888-4893.

Hamadouche A, Witvoet J, Prcher R, Meunier A, Sedel L, Nizard R. Hydroxyapatite-coated versus grit-blasted femoral stems. *Journal of Bone and Joint Surgery (British volume).* 2001; 83-B (7): 979-987.

Halleen JM, Räisänen S, Salo JJ, Reddy SV, Roodman GD, Hentunen TA, Lehenkari PP, Kaija H, Vihko P, Väänänen HK. Intracellular fragmentation of bone resorption products by reactive oxygen species generated by tartrate-resistant acid phosphatase. *Journal of Biological Chemistry*. 1999; 274: 22907-22910.

Hallgren C, Reimers H, Gold J. The Importance of Surface Texture for Bone Integration of Screw Shaped Implants: An In Vivo Study of Implants Patterned by Photolithography. *Journal of Biomedical Materials Research*. 2001; 57: 485-496.

Hamilton D, Brunette D. The Effect of Substratum Topography on Osteoblast Adhesion Mediated Signal Transduction and Phosphorylation. *Biomaterials.* 2007; 28: 1806-1819.

Harada S, Rodan GA. Control of osteoblast function and regulation of bone mass. *Nature*. 2003; 423: 349-355.

Hirao M, Hashimoto J, Yamasaki N, Ando W, Tsuboi H, Myoui A, Yoshikawa H. Oxygen tension is an important mediator of the transformation of osteoblasts to osteocytes. *Journal of Bone and Mineral Metabolism*. 2007; 25: 266-276.

Howie DW, Middleton RG, Costi K. Loosening of matt and polished cemented femoral stems. *Journal of Bone and Joint Surgery – British volume*. 1998; 80-B: 573-6.

Howlett CR, Evans MDM, Walsh WR, Johnson G, Steele JG. Mechanism of initial attachment of cells derived from human bone to commonly used prosthetic materials during cell culture. *Biomaterials*. 1994; 15 (3): 213-222.

Hu J, Liu X, Ma PX. Induction of osteoblast differentiation phenotype on poly(L-lactic acid) nanofibrous matrix. *Biomaterials.* 2008; 29 (28): 3815-21.

Huelsken J, Behrens J. The Wnt signalling pathway. *Journal of Cell Science*. 2002; 115 (21): 3977-3978.

Ingber DE. Tensegrity: the architectural basis of cellular mechanotransduction. *Annual Review of Physiology*. 1997; 59: 575-599.

Isaacs JD, Shidiak L, Harris IA, Szomor ZL. Femoral insufficiency fractures associated with prolonged bisphosphonate therapy. *Clinical Orthopaedics and Related Research.* 2010; 468 (12): 3384-3392.

Justesen J, Lorentzen M, Andersen LK, Hansen O, Chevallier J, Modin C, Fuchtbauer A, Foss M, Besenbacher F, Duch M, Pedersen FS. Spatial and temporal changes in the morphology of preosteoblastic cells seeded on microstructured tantalum surfaces. *Journal of Biomedical Materials Research*. 2009; 89A: 885-894.

Kamioka H, Ishihara Y, Ris H, Murshid SA, Sugawara Y, Takano-Yamamoto T, Lim S. Primary cultures of chick osteocytes retain functional gap junctions between osteocytes

and between osteocytes and osteoblasts. *Microscopy and Microanalysis*. 2007; 13: 108-117.

Kanczler JM, Oreffo ROC. Osteogenesis and Angiogenesis: The potential for engineering bone. *European Cells and Materials*. 2008; 15: 100-114.

Karsenty G. Update on the transcriptional control of osteoblast differentiation. *BoneKEy*. 2007; 4 (6): 164-170.

Karsenty G, Wagner EF. Reaching a genetic and molecular understanding of skeletal development. *Developmental Cell*. 2002; 2: 389-406.

Kashef J, Kuhler A, Kuriyama S, Alfandari D, Mayor R, Wedlich D. Cadherin-11 regulates Protrusive Activity in Xenopus Cranial Neural Crest Cells Upstream of Trio and the Small GTPases. *Genes and Development.* 2009; 23: 1393-1398.

Kawaguchi J, Kii I, Sugiyama Y, Takeshita S, Kudo A. The Transition of Cadherin Expression in Osteoblast Differentiation from Mesenchymal Cells: Consistent Expression of Cadherin-11 in Osteoblast Lineage. *The Journal of Bone and Mineral Research.* 2006; 16(2): 260-269.

Keaveny TM. Chapter A2 – Cancellous Bone. *Handbook of Biomaterial Properties*. Ed. Black J, Hastings G. 1998; Chapman and Hall. pp 15-23.

Kesler G, Romanos G, Koren R. Use of Er:YAG Laser to Improve Osseointegration of Titanium Alloy Implants: A Comparison of Bone Healing. *International Journal Oral & Maxillofacial Implant.* 21 (3): 375-379.

Kim H, Kim S, Kim M. Varying Ti6Al4V Surface Roughness Induces Different Early Morphologic and Molecular Responses in MG63 Osteoblast-like Cells. *Journal of Biomedical Materials: Part A*. 2005; 74:366-373.

Kim CS, Sohn SH, Jeon SK, Kim KN, Ryu JJ, Kim MK. Effect of various implant coatings on biological responses in MG63 using cDNA microarray. *Journal of Oral Rehabilitation*. 2006; 33: 368-379.

Kim Y-H, Koak J-Y, Chang I-T, Wennerberg A, Heo S-J. A histomorphometric analysis of the effects of various surface treatment methods on osseointegration. *Journal of Oral and Maxillofacial Implants*. 2003; 18 (3): 349-356.

Kirmizidis G, Birch M. Microfabricated grooved substrates influence cell-cell communication and osteoblast differentiation. *Tissue Engineering : Part A*. 2009; 15: 1-10.

Knothe Tate ML, Adamson JR, Tami AE, Bauer TW. The osteocyte. *The International Journal of Biochemistry and Cell Biology*. 2004; 36: 1-8.

Komori T. Regulation of osteoblast differentiation by transcription factors. *Journal of Cellular Biochemistry*. 2006; 99: 1233-1239.

Koryta J, Dvorak J, Kavan L. (John Wiley and Sons 1993) *Principles of Electrochemistry:* 79-141.

Krause A, Cowles EA, Gronowicz G. Integrin-mediated signalling in osteoblasts on titanium implant materials. *Journal of Biomedical Materials Research.* 2000; 52: 738-747.

Kronenberg HM. Developmental regulation of the growth plate. *Nature*. 2003; 423: 332-336.

Kurana JS (ed.) (Humana Press) *Bone Pathology* 2nd ed. 2009.

Labek G, Thaler M, Janda W, Agreiter M, Stöckl B. Revision rates after total joint replacement: cumulative results from worldwide joint register datasets. *Journal of Bone and Joint Surgery (British volume).* 2011; 93-B (3): 293-297.

Lai C, Cheng S, Mbalaviele G, Donsante C, Watkins M, Radice G, Civitelli R. Accentuated Ovariectomy-Induced Bone Loss and Altered Osteogenesis in Heterozygous N-Cadherin Null Mice. *Journal of Bone and Mineral Research*. 2006; 21(12): 1897-1906.

Laing PG. The blood supply of the femoral shaft. *The Journal of Bone and Joint Surgery (British volume).* 1953; 35-B (3): 462-466.

Lee W, Kim D, Yi W, Cho Y, Kim H, Lee S, Choi S, Heo M. Volumetric analysis of in vivo bone-to-implant contact ratio using intrinsic thresholding. *International Journal of Computer Assisted Radiology and Surgery.* Conference: Computer Assisted Radiology and Surgery - 25th International Congress and Exhibition, CARS 2011 Berlin Germany. 2011; 6: S378-S379.

Lennon AB, McCormack BA, Prendergast PJ. The relationship between cement fatigue damage and implant surface finish in proximal femoral prostheses. *Medical Engineering and Physics.* 2003; 25(10): 833-41.

Li Y, Zou S, Wang D, Feng G, Bao C, Hu J. The effect of hydrofluoric acid treatment on titanium implant osseointegration in ovariectomized rats. Biomaterials. 2010; 31 (12): 3266-73.

Li Z, Zhou Z, Saunders MM, Donahue HJ. Modulation of connexion-43 alters expression of osteoblastic differentiation markers. *American Journal of Physiology: Cell Physiology*. 2006; 290: C1248-C1255.

Liang B, Fujibayashi S, Neo M, Tamura J, Kim H-M, Uchida M, Kokubo T, Nakamura T. Histological and mechanical investigation of the bone-bonding ability of anodically oxidized titanium in rabbits. *Biomaterials*. 2003; 24: 4959-4966.

Lim JY, Dreiss AD, Zhou Z, Hansen JC, Siedlecki CA, Hengstebeck RW, Cheng J, Winograd N, Donahue HJ. The regulation of integrin-mediated osteoblast focal adhesion and focal adhesion kinase expression by nanoscale topography. *Biomaterials.* 2007; 28: 1787-1797.

Lima F, Niger C, Herbert C, Stains JP. Connexin43 potentiates osteoblast responsiveness to fibroblast growth factor 2 via a protein kinase C-delta/runx2-dependent mechanism. *Molecular Biology of the cell*. 2009; 20: 2697-2708.

Lin C, Jiang X, Dai Z, Guo X, Weng T, Wang J, Li Y, Feng G, Gao X, He L. Sclerostin mediates bone response to mechanical unloading through antagonizing Wnt/beta-catenin signalling. *Journal of Bone and Mineral Research.* 2009; 24: 1651-1661.

Lincks J, Boyan BD, Blanchard CR, Lohmann CH, Liu Y, Cochran DL, Dean DD, Schwartz Z. Response of MG63 osteoblast-like cells to titanium alloy is dependent on surface roughness and composition. *Biomaterials.* 1998; 19: 2219-2232.

Lutjering G, Williams J. (Springer 2003) *Titanium*: 177-201.

Mendes VC, Moineddin R, Davies JE. The effect of discrete calcium phosphate nanocrystals on bone-bonding to titanium surfaces. *Biomaterials*. 2007; 28: 4748-4755.

Meuleman WRA, Roy S. Transient electrochemical processes during Cu-Ni deposition. *Transactions of the Institute of Metal Finishing*. 2003; 81**(**2): 55-58.

Meyer U, Büchter A, Wiermann HP, Joos U, Jones DB. Basic reactions of osteoblasts on structured material surfaces. *European Cells and Materials*. 2005; 9: 39-49.

Milošev I, Metikoš-Huković M, Strehblow H-H. Passive film on orthopaedic TiAlV alloy formed in physiological solution investigated by x-ray photoelectron spectroscopy. *Biomaterials.* 2000; 21: 2103–13.

Muhonen V, Heikkinen R, Danilov A, Jämsä T, Tuukkanen J. The effect of oxide thickness on osteoblast attachment and survival on NiTi alloy. *Journal of Materials Science: Materials in Medicine*. 2007; 18: 959-967.

Nakaoka R, Yamakoshi Y, Isama K, Tsuchiya T. Effects of surface chemistry prepared by self-assembled monolayers on osteoblast behaviour. *Journal of Biomedical Materials Research Part A*. 2010; 94A (2): 524-532.

Narumiya S, Ishizaki T, Watanabe N. Rho effectors and reorganization of actin cytoskeleton. *FEBS Letters.* 1997; 410: 68–72.

Naski MC, Ornitz DM. FGF signalling in skeletal development. *Frontiers in Bioscience.* 1998; 3: d781-794.

National Joint Registry Website. www.njrcentre.org.uk. 8th Annual Report (Data to December 2011). Last updated January 2013.

Ngalim S. Surface patterning Ti alloys to influence osteoblast growth and bone formation. MRes Dissertation, Newcastle University, 2007.

Noble BS. The osteocyte lineage. *Archives of Biochemistry and Biophysics*. 2008; 473: 106-111.

Norman TL, Thyagarajan G, Saligrama VC, Gruen TA, Blaha JD. Stem surface roughness alters creep induced subsidence and 'taper-lock' in a cemented femoral hip prosthesis. Journal of Biomechanics. 2001; 34(10): 1325-33.

Nouraei S. MRes Dissertation. Mask-less micron scale structuring of metals and alloys : principles and applications. University of Newcastle upon Tyne. School of Chemical

Engineering and Advanced Materials. Publisher: University of Newcastle upon Tyne, 2008.

Ogawa T, Nishimura I. Different Bone Integration Profiles of Turned and Acid-etched Implants Associated with Modulated Expression of Extracellular Matrix Genes. *International Journal of Oral and Maxillofacial Implants*. 2003; 18: 200-210.

Oh S, Tobin E, Yang Y, Carnes D, Ong J. In Vivo Evaluation of Hydroxyapatite Coatings of Different Crystallinities. *International Journal of Oral & Maxillofacial Implants.* 2005; 20 (5): 726-731.

Olsen BR, Reginato AM, Wang W. Bone Development. *Annual Review of Cell Developmental Biology*. 2000; 16: 191-220.

Palin E, Liu H, Webster T. Mimicking the Nanofeatures of Bone Increases Bone-Forming Cell Adhesion and Proliferation. *Nanotechnology.* 2005; 16:1828-1835.

Parfitt AM, Drezner MK, Glorieux FH, Kanis JA, Malluche H, Meunier PJ, Ott SM, Recker RR. Bone histomorphometry: standardization of nomenclature, symbols, and units. Report of the ASBMR Histomorphometry Nomenclature Committee. *Journal of Bone and Mineral Research.* 1987; 2(6): 595-610.

Parisien M, Charhon SA, Arlot M, Mainetti E, Chavassieux P, Chapuy MC, Meunier PJ. Evidence for a toxic effect of aluminum on osteoblasts: A histomorphometric study in hemodialysis patients with aplastic bone disease. *Journal of Bone and Mineral Research.* 1988; 3 (3): 259-267.

Pavalko FM, Norvell SM, Burr DB, Turner CH, Duncan RL, Bidwell JP. A model for mechanotransduction in bone cells: the load-bearing mechanosomes. *Journal of Cellular Biochemistry*. 2003; 88: 104-112.

Piotrowski O, Madore C, Landolt D. Electropolishing of tantalum in sulphuric acid-methanol electrolytes. *Electrochimera Acta*. 1999; 44: 3389-3399.

Plant SD, Grant DM, Leach L. Behaviour of human endothelial cells on surface modified NiTi alloy. *Biomaterials.* 2005; 26(26): 5359-67.

Qiu Q, Sayer M, Kawaja M, Shen X, Davies J. Attachment, morphology, and protein expression of rat marrow stromal cells cultured on charged substrate surfaces. *Journal of Biomedical Materials Research*. 1998; 42: 117-127.

Radl R, Aigner C, Hungerford M, Pascher A, Windhager R. Proximal femoral bone loss and increased rate of fracture with a proximally hydroxyapatite-coated femoral component. *Journal of Bone and Joint Surgery – British Volume.* 2000; 82(8): 1151-1155.

Rani VVD, Manzoor K, Menon D, Selvamurugan N, Nair SV. The design of novel nanostructures on titanium by solution chemistry for an improved osteoblast response. *Nanotechnology.* 2009; 20: 1-11.

Rapaport J, Chaimovitz C, Abulfil A, Mostovlavsky M, Gazit D, Bab I. Aluminium-related osteomalacia: clinical and histological improvement following treatment with desferrioxamine. *Israel Journal of Medical Sciences*. 1987; 23 (12): 1242-1246.

Rasanen P, Paavolainen P, Sintonen H, Koivisto A, Blom M, Ryynanen O, Roine R. Effectiveness of Hip or Knee Replacement Surgery in Terms of Quality-Adjusted Life Years and Costs. *Acta Orthopaedica.* 2007; 78(1): 108-115.

Regent-Kloeckner M, Bouin A-P, Balland M, Verdier C, Laurent V, Bouvard D, Planus E, Albiges-Rizo C. ICAP-1 and beta1 integrin modulate adhesion strength and traction force to sense matrix rigidity and control cell migration. *Molecular Biology of the Cell*. Conference: Annual Meeting of the American Society for Cell Biology, ASCB 2011 Denver, CO United States. Conference Publication. 2011; 22 (24).
Reiger P. (Chapman and Hall 1994) *Electrochemistry 2nd Ed:* 1-54.

Reinhold MI, Naski MC. Direct interactions of Runx2 and canonical Wnt signaling induce FGF18. *Journal of Biological Chemistry.* 2007; 282 (6): 3653-3663.

Reis RL, Monteiro FJ, Hastings GW. Stability of hydroxyapatite plasma-sprayed coated Ti6Al4V under cyclic bending in simulated physiological solutions. Journal of Material Sciences: Materials in Medicine. 1994; 5: 457-462.

Reyes C, Petrie T, Burns K, Schwartz Z, Garcia A. Biomolecular Surface Coating to Enhance Orthopaedic Tissue Healing and Integration. *Biomaterials.* 2007; 28: 3228-3235.

Rho JY, Ashman RB, Turner CH. Young's modulus of trabecular and cortical bone material: Ultrastructural and microtensile measurements. *Journal of Biomechanics*. 1993; 26 (2): 111-119.

Robinson JA, Chatterjee-Kishore M, Yaworsky PJ, Cullen DM, Zhao W, Li C, Kharode Y, Sauter L, Babij P, Brown EL, Hill AA, Akhter MP, Johnson ML, Recker RR, Komm BS, Bex FJ. Wnt/β-catenin signalling is a normal physiological response to mechanical loading in bone. *The Journal of Biological Chemistry.* 2006; 281 (42): 31720-31728.

Rochefort GY, Pallu S, Benhamou CL. Osteocyte: the unrecognised side of bone tissue. *Osteoporosis International*. 2010; 21: 1457-1469.

Rollins V. Surface Defect Inspection – at the double. *Materials World*. 2001; 9: 1-2.

Schmidhammer R, Zandieh S, Mittermayr R, Pelinka L, Leixnering M, Hopf R, Kroepf A, Redl H. Assessment of Bone Union/Nonunion in an Experimental Model Using Microcomputed Technology. *The Journal of Trauma.* 2006; 61: 199-205.

Schmidt C, Kaspar D, Sarkar M, Clacs L, Ignatius A. A Scanning Electron Microscopy Study of Human Osteoblast Morphology on Five Orthopaedic Metals. *Journal of Biomedical Materials Research.* 2002; 63: 252-261.

Shin CS, Lecanda F, Sheikh S, Weitzmann L, Cheng S-L, Civitelli R. Relative abundance of different cadherins defines differentiation of mesenchymal precursors into osteogenic, myogenic or adipogenic pathways. *Journal of Cellular Biochemistry*. 2000; 78: 566-577.

Simmons C, Valiquette N, Pilliar R. Osseointegration of Sintered Porous-Surfaced and plasma Spray-Coated Implants: An Animal Model Study of Early Postimplantation Healing Response and Mechanical Stability. *Journal of Biomedical Materials Research*. 1999; 47: 127-138.

Sohn S-H, Jun H-K, Kim C-S, Kim, K-N, Chung S-M, Shin S-W, Ryu J-J, Kim M-K. Biological responses in osteoblast-like cell line according to thin layer hydroxyapatite coatings on anodized titanium. *Journal of Oral Rehabilitation*. 2006; 33(12): 898-911.

Struers Knowledge – Grinding and Polishing. www.struers.com. Last updated January 2010.

Stylios G, Wan T, Giannoudis G. Present Status and Future Potential of Enhancing Bone Healing using Nanotechnology. *Injury*. 2007; 38S1:S63-S74.

Svehla M, Morberg P, Zicat B, Bruce W, Sonnabend D, Walsh W. Morphometric and Mechanical Evaluation of Titanium Implant Integration: Comparison of Five Surface Structures. *Journal of Biomedical Materials Research*. 2005; 51: 15-22.

Sychterz C, Claus A, Engh C. What we have Learned about Long-Term Cementless Fixation from Cementless Fixation from Autopsy Retrievals. *Clinical Orthopaedics and Related Research.* 2002; 405: 79-91.

Tambasco de Oliveira P, Zalzal SF, Beloti MM, Rosa AL, Nanci A. Enhancement of in vitro osteogenesis on titanium by chemically produced nanotopography. *Journal of Biomedical Biomaterials Research Part A.* 2007; 80A (3): 554-564.

Teitelbaum SL. Bone resorption by osteoclasts. *Science*. 2000; 289: 1504-1508.

Tsai SW, Liou HM, Lin CJ, Kuo KL, Hung YS, Weng RC, Hsu FY. MG63 osteoblast-like cells exhibit different behavior when grown on electrospun collagen matrix versus electrospun gelatin matrix. *PloS one*. 2012; 7 (2): pp e31200).

Turner CH, Rho J, Takano Y, Tsui TY, Pharr GM. The elastic properties of trabecular and cortical bone tissues are similar: results from two microscopic measurement techniques. *Journal of Biomechanics*. 1999; 32: 437-441.

Väänänen HK, Zhao H, Mulari M, Halleen JM. The cell biology of osteoclast function. *Journal of Cell Science*. 2000; 113: 377-381.

Vandamme K, Holy X, Bensidhoum M, Logeart-Avramoglou D, Naert I, Duyck JA, Petite H. In vivo molecular evidence of delayed titanium implant osseointegration in compromised bone. *Biomaterials.* 2011; 32: 3547-3554.

Vercaigne S, Wolke JGC, Naert I, Jansen JA. Histomorphometrical and mechanical evaluation of titanium plasma-spray-coated implants placed in the cortical bone of goats. *Journal of Biomedical Materials Research*. 1998; 41: 41-48.

Ward BC, Webster TJ. The effect of nanotopography on calcium and phosphorus deposition on metallic materials in vitro. *Biomaterials*. 2006; 27: 3064-3074.

Watkins M, Grimston SK, Norris JY, Guillotin B, Shaw A, Beniash E, Civitelli R. Osteoblast connexin43 modulates skeletal architecture by regulating both arms of bone remodelling. *Molecular Biology of the Cell.* 2011; 22: 1240-1251.

Weiner S, Traub W. Bone structure: from ångstroms to microns. *The FASEB Journal*. 1992; 6: 879-885.

Weiner S, Traub W, Wagner D. Lamellar bone: Structure – Function Relations. *Journal of Structural Biology*. 1999; 126: 241-255.

Weiner S, Wagner HD. The material bone: structure-mechanical function relations. *Annual Review of Materials Science*. 1998; 28: 271-298.

Wennerberg A, Ektessabi A, Albrektsson T, Johansson C, Andersson B. A 1-year follow-up of implants of differing surface roughness placed in rabbit bone. *The International Journal of Oral and Maxillofacial Implants*. 1997; 12 (4): 486-494.

Wennerburg A, Hallgren C, Johansson C, Danelli S. A histomorphometric evaluation of screw-shaped implants each prepared with two surface roughnesses. *Clinical Oral Implants Research*. 1998; 9: 11-19.

Xiao J, Zhou H, Zhao L, Sun Y, Guan S, Liu B, Kong L. The effect of hierarchical micro/nanosurface titanium implant on osseointegration in ovariectomized sheep. *Osteoporosis International.* 2011; 22 (6): 1907-1913.

Yang S, Tian YS, Lee YJ, Yu FH, Kim HM. Mechanisms by which the inhibition of specific intracellular signalling pathways increase osteoblast proliferation on apatite surfaces. *Biomaterials.* 2011; 32 (11): 2851-2861.

Yang T. Novel biomaterial surfaces to regulate bone cell activity. MRes Dissertation, Newcastle University, 2005.

Yim EKF, Darling EM, Kulangara K, Guilak F, Leong KW. Nanotopography-induced changes in focal adhesions, cytoskeletal organization and mechanical properties of human mesenchymal stem cells. *Biomaterials*. 2010; 31: 1299-1306.

Zhu J, Zhang Y-T, Alber MS, Newman SA. Bare bones pattern formation: A core regulatory network in varying geometries reproduces major features of vertebrate limb development and evolution. *PLoS One*. 2010; 5 (5): e10892.

Zreiqat H, Valenzuela SM, Nissan BB, Roest R, Knabe C, Radlanski RJ, Renz H, Evans PJ. The effect of surface chemistry modification of titanium alloy on signalling pathways in human osteoblasts. *Biomaterials*. 2005; 26: 7579-7586.